UNIVERSITY OF COPENHAGEN
FACULTY OF SCIENCE

May 16, 2019

Ph.D. thesis

Ida Margrethe Ringgaard

Sensitivity of Arctic sea ice change on climate in the coupled climate model EC-Earth

Academic advisors: Eigil Kaas[1], Shuting Yang[2], Jens Hesselbjerg Christensen[1,2,3]

(1) Physics of Ice Climate and Earth, Niels Bohr Institute, Univsersity of Copenhagen

(2) Danish Meteorological Institute

(3) NORCE, Norwegian Research Centre AS, Bergen, Norway

This thesis has been submitted to the PhD School of The Faculty of Science, University of Copenhagen

Acknowledgements

This PhD thesis is the culmination of more than three years of hard work. Three years full of extremely interesting discussions across scientific fields, great collaboration across institutes, hard work, great new friends, a lot of laughter and a few frustrated tears. I feel very privileged to have been part of the Ice2ice project. Working with people across scientific fields have taught me so much and have opened my eyes to the wonders of ice and mud. I am especially grateful for the large focus on the PhD students, encouraging us to collaborate across fields and building lasting friendships by having us arrange PhD Bootcamps where we solely decided the subjects and outcomes. This was a very unique opportunity which I am very grateful for. It made my stay abroad in Bergen easy to adapt to, since I already knew everyone.

My three supervisors Shuting Yang, Eigil Kaas and Jens Hesselbjerg Christensen have been outstanding in helping me through this PhD project, always ready to help and discuss. I would especially like to thank Shuting for all her technical help understanding and running EC-Earth, and discussing potential solutions when the model crashed.

I could not have done this without the help of my wonderful family and friends, bringing me out into the real world occasionally. I would like to thank Pia and Anna (and Freja) who helped to proof-read this thesis. Finally, I couldn't have done it without my boyfriend Alexander who cheered me up, brought me food and chocolate, and kept my motivation high by telling me how wonderful it is to be a Doctor.

As a last note, the research leading to these results has received funding from the European Research Council under the European Community's Seventh Framework Programme (FP7/2007-2013) / ERC grant agreement 610055 as part of the ice2ice project.

Abstract

The climate system has throughout time been sensitive to changes in the Arctic sea ice. During the last glacial period, the climate experienced abrupt climatic changes (Dansgaard-Oeschger events), likely due to a rapid retreat of the Nordic Seas sea ice. Present climate experiences a sea ice loss as well, where the regional sea ice loss in the Barents-Kara Seas has been linked to cold European winters. In the future, Arctic sea ice is projected to disappear. This PhD project aimed at investigating the sensitivity of the climate to changes in the Arctic sea ice. For this, the atmosphere-ocean coupled climate model EC-Earth was used. Focus was on the impact of the regional sea ice loss in the Barents-Kara Seas, as well as the pan-Arctic sea ice loss projected in the RCP8.5 emission scenario. Testing the sensitivity to sea ice changes in a coupled climate model required a method for constraining sea ice. Two methods using the surface sensible heat flux to nudge sea ice were tested, one of them conserving energy. This latter method required a fine balance to avoid model instabilities, a balance that we did not succeed in finding for longer simulations. Our results showed that Barents-Kara sea ice loss might be linked to a cooling over parts of Europe in winter, but the response was weak and only present for the temporal mean winter temperatures. The coldest winters did not show a statistically significant cooling over Europe for any amount of sea ice loss in the Barents-Kara Seas. The RCP8.5 scenario simulation was run for 1350 years (1850-3200) using EC-Earth-PISM, where EC-Earth is coupled to an interactive Greenland Ice Sheet. During the simulation, the Arctic transitioned from having a perennial sea ice cover to an ice-free Arctic Ocean. The overall evolution of the RCP8.5 simulation resembled that of the CMIP5 ensemble, although the loss of the Arctic sea ice appeared to lead to a shift in trends for some key parameters: the precipitation variability increased, the AMOC stabilized after an initial reduction and the Arctic Ocean stratification strengthened. However, as changes in sea ice coincided with increasing global temperature and anthropogenic Greenhouse Gas emissions, more work is required to separate the effects.

Resumé

Klimaet har gennem tiden været følsomt for ændringer i den Arktiske havis. I sidste istid ændrede klimaet sig pludseligt flere gange (Dansgaard-Oeschger events), sandsynligvis på grund af en hurtig tilbagetrækning af havis i de Nordiske Have. I det nuværende klima sker der også tilbagetrækning af havisen. Det regionale havis tab i Barents-Kara havene er blevet associeret med kolde europæiske vintre. Projektioner for fremtidens klima viser et is-frit Arktisk. Formålet med dette ph.d.-projekt var at undersøge klimaets sensitivitet i forhold til ændringer i den Arktiske havis. Til dette blev den koblede atmosfære-ocean klima model EC-Earth brugt. Fokus var på virkningen af det regionale havis tab i Barents-Kara havet, såvel som det fulde Arktiske havis tab, simuleret i RCP8.5-emissionsscenariet. For at teste sensitiviteten af ændringer i havisen i en koblet klimamodel, kræver det en metode til at tvinge modellen mod et bestemt mål. To metoder, der anvender den sensible varmeflux til at nudge havis, blev testet. Den ene metode var energi-bevarende, men der krævedes en fin balance mellem at nå målet og ikke forårsage at modellen blev ustabil. Vi lykkedes ikke med at finde denne balance for længere simuleringer. Vores resultater viser, at Barents-Kara havets istab kan være forbundet med koldere vintre over Europa, men signalet var svagt og kun til stede for 100-års middel vintertemperaturer. De koldeste vintre viste ikke en statistisk signifikant afkøling over Europa for nogen form for havis reduktion i Barents-Kara havene. RCP8.5 scenario simuleringen blev kørt i 1350 år (1850-3200) ved hjælp af EC-Earth-PISM, hvor EC-Earth er koblet til en interaktiv Grønlandsk Indlandsis . Under simuleringen ændrede Arktis sig fra at være dækket af havis hele året, til at være is-frit hele året. Den overordnede udvikling af RCP8.5-simuleringen lignede CMIP5-ensemblet, selvom tabet af den Arktiske havis tilsyneladende første til et skift i trends for nogle nøgleparametre: variabiliteten for nedbør steg, AMOC stabiliserede sig efter en indledende reduktion og stratifikationen i det Arktiske Ocean blev stærkere. Da ændringer i havisen skete samtidig med stigende global temperaturer samt stigende udledninger af drivhusgasser, kræves der mere arbejde for at separere effekterne.

Contents

List of original manuscripts

Manuscript I
Ringgaard, Ida M., Yang, Shuting, Kaas, Eigil and Christensen, Jens H. *Nudging sea ice in the coupled climate model EC-Earth*. Manuscript ready for submission.

Manuscript II
Ringgaard, Ida M., Yang, Shuting, Kaas, Eigil and Christensen, Jens H. *Barents-Kara sea ice and European winters in EC-Earth*. Manuscript resubmitted to Climate Dynamics after revisions.

Manuscript III
Ringgaard, Ida M., Yang, Shuting, Kaas, Eigil and Christensen, Jens H. *Climate change associated with sea ice loss in extended EC-Earth-PISM RCP8.5 simulation*. Manuscript in preparation.

Chapter 1

Introduction

In the recent past, increasing anthropogenic Greenhouse Gas (GHG) emissions have caused the climate to change drastically (IPCC (2013)). Exemplifying this is the global mean temperature, which has increased by $\sim$1°C since the beginning of the pre-industrial period. Another is the thinning and retreating Arctic sea ice cover. The Arctic is a notoriously difficult place to obtain observations. Therefore, the Arctic sea ice cover in its entirety has only been observed continuously since 1979, when satellites began to orbit the poles. Since 1979 the September Arctic sea ice area has been observed to decline by 12.8 percent per decade relative to the 1981-2010 average (NSIDC: http://nsidc.org/arcticseaicenews/2018/10/). The decline is projected to continue, leading to an ice-free Arctic Ocean in September by the middle of this century. Ice loss is not only occurring in the ocean, but also on land. The Greenland Ice Sheet (GIS) is also experiencing accelerated mass loss (Kjeldsen et al. (2015)). These changes to the Arctic cryosphere not only affect the animals and plants living in the Arctic, but also the climate it self. A reduced sea ice cover allows more heat to be absorbed by the ocean, accelerating the global warming. A reduced sea ice cover will affect the large-scale ocean circulation as well. This is partly driven by the formation of cold, saline deep water at the poles, sinking to the bottom of the ocean and flowing southward. The deep water is formed at the sea ice edge, where the cold water is injected with saline brine from sea ice formation. As cold, saline water is denser than cold fresh water, the former sinks to the bottom of the ocean. The northward retreat of the Arctic sea ice drags the location of the deep water formation northward, causing the deep water formation to weaken dramatically when the sea ice gone (Brodeau and Koenigk (2015)). These few examples highlight the importance of sea ice and its variability on our climate system.

The climate changes we are experiencing now are not unique in the sense of the climate changing, but in the rate of the changes and that they are driven by anthropogenic GHG emissions. Paleo records such as ice cores and marine sediment cores show how temperature, CO_2, sea ice etc. have changed over the course of the Earth's life time. Ice core records covering the last glacial period show short-term events of rapid warming known as Dansgaard-Oeschger (D-O) events (Dansgaard et al. (1993)). The most pronounced of these events occurred during the Marine Isotope Stage 3 (MIS3), approximately 25.000-60.000 years ago. During these events, the temperature on Greenland rapidly increased by up to 15°C within decades (Kindler et al. (2014)). These D-O events have since been observed in other paleo records as well, indicating global implications of these events (Stocker and Johnsen (2003)). An obvious question is then: what caused these rapid temperature changes and can they occur in a warmer climate like the present and the projected climate?

Coinciding with the abrupt temperature changes in Greenland were a rapid retreat of the Nordic Seas sea ice cover (Dokken et al. (2013), Sadatzki et al. (2019)). This implies a potential link between the Arctic sea ice and the Greenland Ice Sheet, a link that has not been given much attention before. This we aim at rectifying in the ERC grant synergy project Ice2ice, which this PhD thesis is a part of. The key hypothesis of Ice2ice is that "*Arctic and sub-Arctic sea ice cover excerts important controls on past and future Greenland temperature and ice sheet variations*" (Ice2ice website: ice2ice.w.uib.no). A potential chain of mechanisms for D-O events is suggested in Dokken et al. (2013): a rapid collapse of the Nordic Seas sea ice cover could have led to a break down of the oceanic stratification, releasing heat to the atmosphere and thus leading to the rapid temperature increases observed in the Greenlandic ice cores. This hypothesis is investigated in the Ice2ice project by combining the knowledge from marine sediment and ice core proxy records with climate models. One of the recent results of the Ice2ice project is a study pinpointing the rapid Nordic Seas sea ice retreat as the driver of the abrupt temperature changes seen on Greenland, thus supporting the hypothesis of Dokken et al. (2013) (Sadatzki et al. (2019)). This was achieved by combining temperature proxy records from Greenland with a marine sediment core in the Nordic Seas, constraining the relative timing of the sea ice retreat, increased ocean mixing and increased temperature on Greenland. This hypothesis was further supported by a model study, simulating the MIS3 period using the Norwegian Earth System Model (NorESM), (Guo et al. (2019, manuscript in preparation)). The MIS3 simulated sea ice cover was slightly larger than present day, but it did not cover the Nordic Seas, as the marine sediment cores indicate. Therefore, to force the model to form a sea ice cover large enough to cover the Nordic Seas with perennial sea ice, they added fresh water to the simulation, a so called 'hosing' experiment. This resulted in a sea ice cover from the North Pole down to Spain, most likely too large, but ensuring a sea ice covered Nordic Seas. When stopping the supply of fresh water, the sea ice rapidly retreated almost back to the starting point. This led to a temperature increase over Greenland of approximately 9°C, similar in magnitude to the temperature changes observed in the ice cores during the MIS3.
The study by Guo et al. (2019, manuscript in preparation) showed three important things. First, NorESM was able to simulate the rapid sea ice retreat and temperature increase. Second, the rapid retreat of the Nordic Seas sea ice cover could trigger temperature rates similar in magnitude to observed D-O rates. Third, NorESM had difficulties in replicating the sea ice cover correctly, making it necessary to be able to push the model toward a target state.

Dokken et al. (2013) and Sadatzki et al. (2019) focused on the importance of sea ice variations in the past, showing what large changes a retreat of sea ice across the Nordic Seas can cause. But what happens when the Arctic sea ice retreats even further North? And what happens when it is completely gone? During MIS3 and the D-O events, the central Arctic Ocean was still covered by perennial sea ice, but future climate simulations project a year-round ice-free Arctic Ocean sometime during the 22nd or 23rd century (Dai et al. (2019)). This shift in sea ice states will most likely have a large impact on climate, although not necessarily similar to the D-O events.

The above shows that past climate has been sensitive to sea ice changes. We will test this sensitivity further in this PhD thesis. The overall goal of this PhD thesis is to analyze the sensitivity of the climate to sea ice changes in the coupled climate model EC-Earth. This is investigated for small as well as large changes, and for present day conditions as well as the future. This PhD thesis is based on three manuscripts, attached in Appendices A, B and C.
Manuscript I (Study I) is Ringgaard et al. (2019a). This manuscript is ready for submission. Ring-

gaard et al. (2019a) investigate methods to constrain sea ice in a coupled climate model, while maintaining energy conservation. As was shown in the study by Guo et al. (2019, manuscript in preparation), the sea ice cover in NorESM did not match the proxy reconstructions. Therefore, they needed to push the model to form more sea ice. This was accomplished by adding fresh water to the system. This strengthened the stratification, allowing for the surface mixed layer to cool enough to form sea ice, without mixing into the warmer subsurface waters. However, this method is neither energy or water conserving. Several studies have looked into constraining sea ice in coupled models (e.g. Screen (2018)). Most methods do not conserve energy, and those that do, are only valid for shorter time periods (Petrie et al. (2015), Semmler et al. (2016)) or are confined to the sunlit part of the year (Blackport and Kushner (2016)). A longer discussion on this can be found in section 3.1. In Manuscript I we developed and tested two methods for nudging sea ice in a coupled climate model.

Manuscript II (Study II) is Ringgaard et al. (2019b). This paper is currently in review in Climate Dynamics. This manuscript feeds into the ongoing discussion on a potential link between sea ice loss in the Barents-Kara Seas (BAKA) and the observed wintertime cooling over Eurasia (see section 3.2). A hypothesis is that sea ice reductions in BAKA induce a negative NAO, leading to advection of cold Arctic air over Eurasia in winter (Petoukhov and Semenov (2010), Kretschmer et al. (2016)). Petoukhov and Semenov (2010) found a non-linear response to linear BAKA sea ice loss, where only moderate sea ice reductions led to cold Eurasian winters, whereas larger sea ice reductions led to warming. Our aim in Manuscript I was to investigate the sensitivity of the climate system to regional sea ice changes under present day conditions, by investigating this potential link.

Manuscript III (Study III) is Ringgaard et al. (2019c). This is still in preparation, as further analysis is required. Here, we focused on the climatic shifts between sea ice states. More precisely, we analyzed different climate states, comparing pre-industrial and present day conditions to the period just after the Arctic September sea ice is gone, just after the Arctic winter sea ice is gone (i.e. when the Arctic becomes ice-free year-round) and when the GIS has started to shrink at the end of the simulation. This was analyzed using a 1350 years long (years 1850-3200) future scenario simulation (RCP8.5). By focusing on these specific periods, we investigated how sensitive the climate is to large changes in the Arctic sea ice cover.

The thesis is structured as follows. Chapter 2 presents some background information on the Arctic Ocean, sea ice, past and future climate as well as climate models. Chapter 3 presents the motivation for each of the three manuscripts. Chapter 4 presents the climate model we have used (EC-Earth). The results for each of the three manuscripts are briefly presented in chapter 5, followed by a discussion of each of the three manuscripts, as well as a more general discussion in chapter 6. The conclusions are presented in chapter 7.

Chapter 2

Background

2.1 The Arctic Ocean and sea ice

2.1.1 The Arctic Ocean

The Arctic Ocean is a semi-enclosed ocean, covering the area around the North Pole (fig. 2.1a). It is connected to the other world oceans at several gateways, where the main entrance points are: the shallow Bering Strait to the Pacific Ocean, the Canadian Archipelago to Baffin Bay and Labrador Sea, and the Fram Strait and the Barents Sea Opening to the North Atlantic Ocean. The Arctic Ocean differs from the other world oceans by having a perennial sea ice cover. As ice has a large albedo it will reflect between 30% and 40% of the incoming solar radiation, potentially reflecting up to 95% (Knauss (1997)). Open water has a much lower albedo (~6%, but varies between 3-30% depending on the angle of the incoming solar radiation, Knauss (1997)). Thus, more heat is absorbed in an ice-free ocean. The sea ice cover also works as a lid on the ocean, shielding the ocean from the winds above, thus contributing to a stable ocean underneath. This stratification in the Arctic Ocean is mainly associated with the halocline (layer with a large salinity gradient), contrary to the thermocline (layer with a large temperature gradient) in the other oceans. The vertical structure of the Arctic Ocean is comprised of a fresh, cold surface layer, separated from the warmer, more saline Atlantic Water (AW) underneath (fig. 2.1b; Aagaard et al. (1981), Rudels et al. (1996), Rudels et al. (2004)). The fresh surface layer is fed by river runoff, positive net precipitation, fresh water inflow through Bering Strait and seasonal ice melt. The halocline is located in the cold surface layer above the thermocline. Hence, it is often referred to as the cold halocline. The cold halocline is maintained through lateral advection of saline, brine-enriched water from the shallow shelves.

Despite the very strong radiative cooling of the ocean surface in winter, the existence of the Arctic sea ice cover is greatly dependent on the cold halocline. If the Arctic Ocean stratification was mainly dominated by a thermocline like the other world oceans, sea ice could not form. The reason for this lies in the different properties of fresh and salt water (Knauss (1997)). Fresh water increases its density with decreasing temperature, until it reaches a temperature of 4°C. Continuing to cool decreases the fresh water density, hence the densest fresh water is 4°C, not 0°C. This prevents the cold surface water sinking as it cools even further, thus allowing for sea ice formation. In contrast to this, saline water with a salinity larger than 24.7 psu does not have this threshold of maximum density. Instead, its density continues to increase with decreasing temperature. This means, that

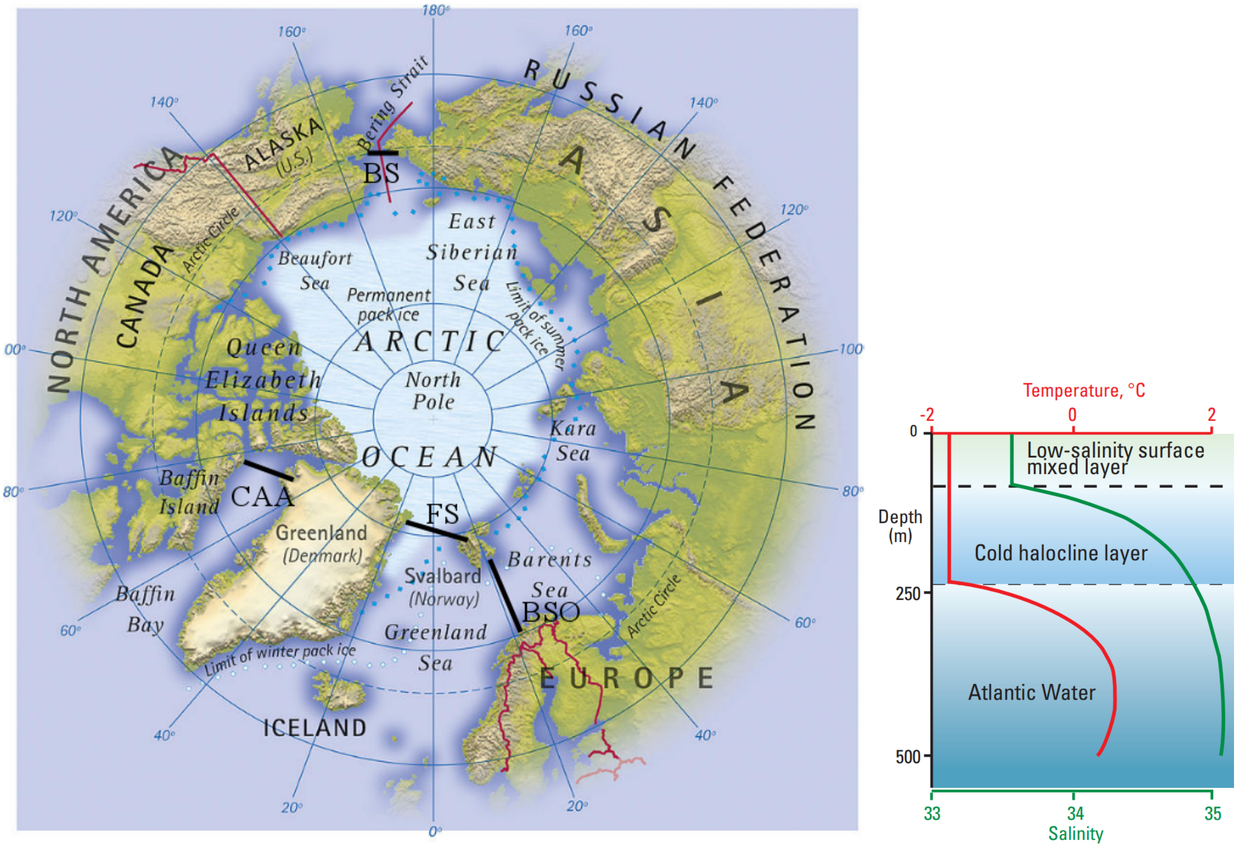

(a) **(b)**

Figure 2.1: (a) Map of the Arctic Ocean, its regional seas and the four main gateways: Barents Sea Opening (BSO), Fram Strait (FS), Canadian Archipelago (CAA) and Bering Strait (BS). Figure from `https://pasarelapr.com/detail/arctic-ocean-map-23.html`. (b) Schematic of the structure of the upper Arctic Ocean. Modified from figure 3-40 in AMAP (1998).

as the surface sea water cools, it becomes heavier and sinks, causing warmer waters to rise and replace it at the surface. To form sea ice in the Arctic Ocean would require the entire Arctic Ocean to cool to the freezing point, before any ice could be formed. This is not the case. Instead, the cold halocline separates the fresh, cold surface layers from the saltier water below. Cooling this fresh layer to the freezing point will not make it heavier than the saline water underneath, thus it will not sink, and therefore it can be cooled enough to form sea ice.

2.1.2 Sea ice

The central Arctic Ocean is covered by a perennial sea ice cover (fig. 2.2). This is generally thicker and stronger than the seasonal first-year ice formed in winter southward of the perennial cover. Sea ice is frozen ocean water, making it salty and therefore different from land ice. Simply put, as the ocean water freezes, salt is being pushed into small unfrozen pockets within the ice. As salt water has a lower freezing temperature than fresh water, these brine pockets can survive for some time, leaking brine into the ocean beneath. If the ice freezes slowly, almost all of the brine can be released to the ocean underneath (Knauss (1997)). This process is referred to as brine rejection and results in multi-year ice being less salty than first-year ice.

The Arctic sea ice cover persists year round, but there a large seasonal variations. In summer, it melts and thins, forming open-ocean areas. After reaching a minimum extent and volume in September (fig. 2.2(right)), the ice grows and thickens during autumn and winter, reaching a maximum extent in March and a maximum volume in May (fig. 2.2(left)). When the sea ice begins to melt in spring along the sea ice edge, cold brine-enriched water is released to the water beneath. As high saline water is denser than less saline water, and cold water is denser than warm water, this cold, brine-enriched water will sink toward the bottom of the ocean. This is known as deep water formation and is one of the main drivers of global ocean circulation (see section 2.2.2). The extent of the sea ice cover is defined in two ways: the sea ice area (SIA) and the sea ice extent (SIE). The SIE only distinguishes between a grid cell being ice covered or ice-free, whereas SIA uses the actual percentage of a grid cell covered by sea ice. Hence, SIE will be larger than SIA.

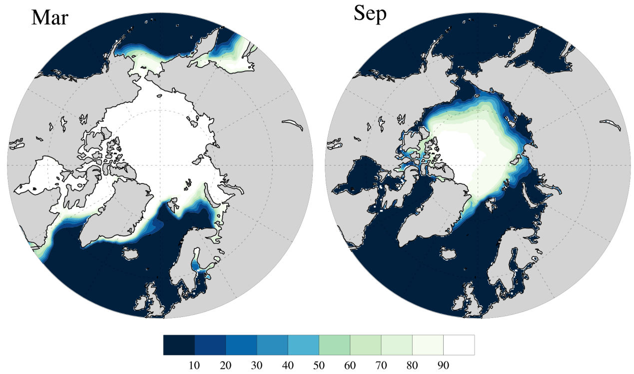

Figure 2.2: Mean sea ice concentration (SIC; in %) for March (left) and September (right) for the period 1979-2009. Data from OSISAF (2017).

2.2 General circulation of the atmosphere and the ocean

Below is a brief introduction to the general circulation of the atmosphere and the ocean with focus on the Polar and mid-latitude regions, together with some of the atmospheric/oceanic phenomenons discussed in this thesis.

2.2.1 The atmosphere

The global atmospheric circulation is driven by general differences in diabatic heating at low latitudes and cooling at high latitudes (Randall (2015)). However, more regional patterns of diabatic heating, due to shortwave absorption and condensation of water vapor, and radiative cooling, blurs the picture. Diabatic heating within the atmosphere typically occurs via vertical convective mixing from below of sensible heat (enthalpy). Convective mixing also transfers water vapor upward, which after possible subsequent horizontal transport condenses and releases latent heat, often taking place at latitudes far away from the area of evaporation. The atmosphere is radiatively cooled in the infrared (long wave) domain and heated in the solar part of the spectrum (short wave). The net effect of radiation is cooling. The zonal mean general circulation is dominated by three meridional cells in each hemisphere: a strong (in particular in winter) Hadley cell (Equator to 30°N), a much weaker Ferrel cell (30°N-60°N) and an even weaker Polar cell (60°N-90°N). The Hadley and the Polar Cells are direct cells, meaning that air rises over heated areas and sinks over cooled areas. Due to subtle dynamics involving baroclinic waves and related convergence of eddy momentum the Ferrel Cell is an indirect cell, meaning that the air sinks over heated areas and rises over cooled areas. The atmospheric meridional circulation is illustrated figure 2.3 by the streamfunction in isentropic coordinates (θ, left panels) and in pressure coordinates (p, right panels). The two representations are quite different but complement each other in the sense that the pressure-based version directly gives the meriodional and vertical mass transport in the atmosphere while the θ version provide info on both (static stability weighted) meridional mass transport, and the total diabatic heating in the atmosphere: vertical motion in this coordinate system is a direct measure of diabatic heating (upward motion) and cooling (downward motion). The Hadley Cell is clearly visible in both coordinate systems with rising air in the summer-hemisphere tropics and subsidence in the winter-hemisphere subtropics, but the Ferrel Cell is only present for p-coordinates. For θ-coordinates, the direct cells extends all the way to the poles. This discrepancy occurs due to the θ-coordinate using the pseudo density as weight.

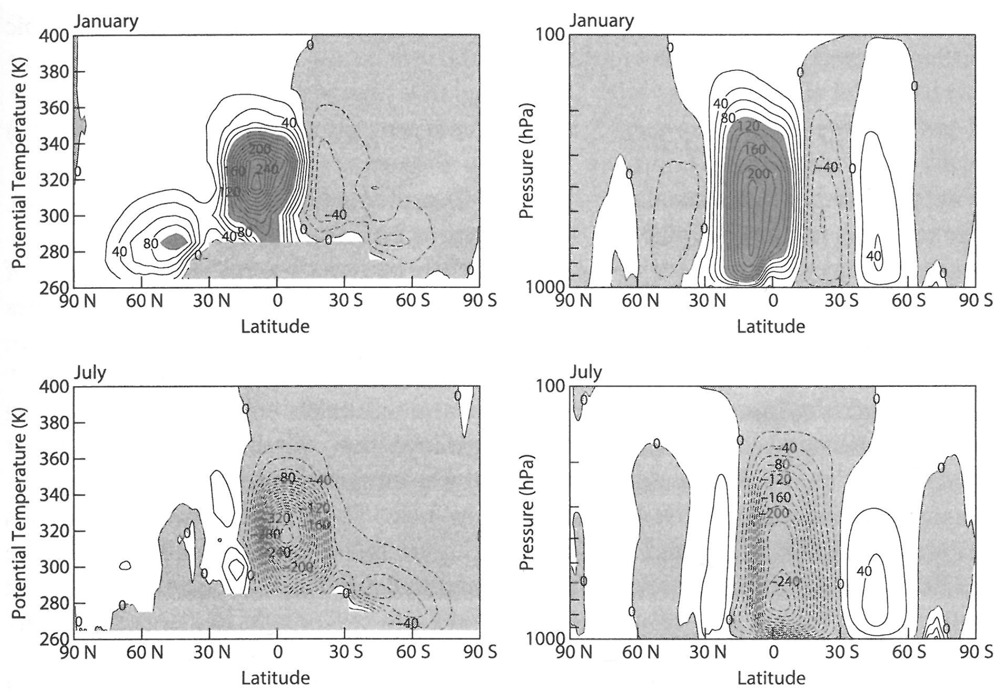

Figure 2.3: The streamfunction of the mean meridional circulation in θ-coordinates (left panels) and p-coordinates (right panels) for January (top row) and July (bottom row). Solid contours indicate positive values (cyclonic) and dashed contours indicate negative values (anticyclonic). Units are 10^9kg s^{-1}. Figure from Randall (2015).

In the upper troposphere on the boundaries between the three cells are strong westerly jet streams: the subtropical jet between the Hadley and the Ferrel Cell at approximately 30°N, and a hint of a second maximum around 50°N to 60°N, between the Ferrel and the Polar Cell (Randall (2015)). This boundary is known as the polar front and the jet is known as the polar front jet. The jet streams can be visualized as fast-flowing meandering rivers of wind flowing from west to east. They are driven by temperature differences between Equator and the poles, and are therefore strongest in winter. The jet stream can be more or less stable, with an unstable jet stream being more wavy, i.e. it has larger undulations and can induce large planetary waves. In the stratosphere above the polar front jet is the polar night jet, also blowing from west to east. The polar night jet encircles the stratospheric polar vortex which is a low pressure system in the stratosphere, constraining the cold Arctic air in the North. Similar to the jet stream, the strength of the polar vortex depends on the meridional temperature difference, resulting in seasonal variations (strongest in winter) as well as interannual variations. It can be weakened by for example upward propagating waves (Kim et al. (2014)). A weakening of the polar vortex is associated with weaker westerlies or even easterlies, allowing for cold stratospheric air to descend (Kolstad et al. (2010)). This results in a rapid warming in the stratosphere, leading to these events being referred to as sudden stratospheric warmings. These events are often accompanied by cold-air outbreaks at the surface in the mid-latitudes, causing cold Arctic air to flow toward the mid-latitudes. A weakened polar vortex is often followed by a negative Arctic Oscillation (Kim et al. (2014)).

The Arctic Oscillation and the North Atlantic Oscillation

The Arctic Oscillation (AO) refers to an atmospheric pressure pattern in the Northern Hemisphere (Thompson and Wallace (1998)). In the positive AO phase, the prevailing low pressure system in the upper atmosphere above the Arctic is strengthened by lower than normal anomalies, i.e. the low pressure intensifies, often associated with a stronger polar vortex. Together with a positive anomaly over the central Atlantic, this creates a stronger north-south pressure gradient, resulting in stronger westerlies. The negative phase of the AO refers to the opposite: a high pressure anomaly over the Arctic, a low pressure anomaly over the central Atlantic and the North Pacific and weaker westerlies. This allows for cold Arctic air in the lower part of the atmosphere to escape southwards due to Ekman drift. Ekman drift refers to the phenomenon where the surface winds are at an angle to the left of the geostrophic winds. High up in the atmosphere, the pressure gradient force and the Coriolis force are in geostrophic balance. At the surface, the frictional force become important as well, resulting in the pressure gradient force having to balance the sum of the Coriolis force and the frictional force. Hence, the surface wind is not in geostrophic balance.
The North Atlantic Oscillation (NAO) refers to a different pressure pattern (Hurrell et al. (2013)). This pattern consists of the prevailing low pressure system near Iceland and the high pressure system over the Azores. A positive NAO refers to a stronger pressure gradient, were the Icelandic low becomes even lower and the Azorian high intensifies as well. This strengthens the westerlies, and the resulting weather resembles that of the positive AO. The negative NAO refers to the opposite case, were the Icelandic low and the Azorian high weakens, leading to a weakening of the westerlies and allowing cold Arctic air to travel south. Cold Eurasian winters are often associated with a negative NAO, see section 3.2.
In Manuscript III a third pressure pattern is mentioned. This is the Scandinavian pattern which is characterized by a high pressure anomaly over Scandinavia, leading to cold air being advected down toward Europe from the Arctic (Barnston and Livezey (1987)).

2.2.2 The ocean

The ocean circulation is driven by the wind as well as changes in density due to temperature and salinity (Knauss (1997)). It is dominated by the large currents transporting heat from Equator toward the Poles. The branch of this system affecting Europe the most is the *Atlantic Meridional Overturning Circulation* (AMOC). This is sometimes referred to as the thermohaline (thermo = temperature and haline = salt) circulation, but this name is misleading. The AMOC is not only driven by changes in temperature and salinity, but also the wind. It reaches from the Southern Ocean to the North Atlantic, branching into the Nordic Seas and the Arctic Ocean. There are two thermohaline circulation 'schools': the 'push' school and the 'pull' school (Huang (2010)). The 'push' school proposes that the AMOC is driven by *deep water formation* at high latitudes: as the surface water cools and is enriched with brine, it becomes denser and eventually sinks to the bottom. This creates a density gradient between the cold, heavy bottom water at high latitudes and warm, less dense water in lower latitudes. This pushes an oceanic circulation into trying to

equalize the pressure gradient. Hence, the circulation is being pushed by the deep water formation. The 'pull' school propose that the oceanic circulation is being pulled by either deep mixing or the wind. Deep mixing transforms the cold deep water into warmer water. As this rises to the surface, it leaves room for new cold water to replace it, thus pulling in new cold abyssal water. A subset of the 'pull' school is that the oceanic circulation is driven by the wind, not deep mixing. Ekman upwelling in certain locations pull up deep water to the surface where, where it is mixed and becomes less dense.
The deep water is primarily formed along the edge of the sea ice cover, as the largest ocean to atmosphere heat fluxes are located here. This is partly due to cold, dry air outbreaks flowing over the sea ice, partly due to the sea ice protecting the ocean from the atmosphere (Vaage et al. (2018)). The main region of deep water formation in the North Atlantic is the Labrador Sea (Knauss (1997)). However, this does not necessarily mean that the Labrador Sea deep water formation dominates the AMOC variability. In fact, a recent study showed that it does not. In the summer of 2014 the Overturning in the Subpolar North Atlantic Program (OSNAP) observing system was launched. As the name suggests, its main purpose was to observe the Atlantic overturning circulation. The newest results show that the deep water formation in the Irminger Sea and the Iceland Basin have the largest impact on the AMOC, not the Labrador Sea (Lozier et al. (2019)).

2.3 Observed climate changes

The climate has changed over the past decades. These changes are evident in all parts of the climate system, from the atmosphere, to the ocean, the cryosphere and the biosphere. These changes have been attributed to the increased anthropogenic GHG emissions (IPCC (2013)). Climate changes are often taken relative to a base line before anthropogenic GHG emissions began. This base line is referred to as the pre-industrial period. Key changes in the atmosphere, the ocean and the Arctic sea ice are discussed below.

2.3.1 The atmosphere

The most obvious change due to increased GHG emissions is the increasing global mean temperature shown in figure 2.4a. This has increased approximately 1°C since the pre-industrial period, leading to the current climate change being known as Global Warming. This implies that the temperature increases equally everywhere and that temperature is the only parameter changing. However, this is not the case, as is illustrated by the map of observed temperature anomalies in 2018 relative to the period 1981-2010 in figure 2.4b. Here it can be seen that there are large regional differences, both intra-continental and globally. The most pronounced spatial temperature difference pattern is the Arctic Amplification (AA). This refers to the difference in observed surface temperature between the Arctic and the rest of the Earth (fig. 2.4(b)). The Arctic temperature increases much faster than the globally averaged surface temperature. The main driver of AA is the Arctic sea ice loss, with the largest contributor being the temperature feedback and the second largest being the ice-albedo feedback (Serreze et al. (2009), Screen and Simmonds (2010), Pithan and Mauritsen (2014)). The temperature feedback refers to the feedback mechanism where sea ice loss cause the ocean surface and the lower atmosphere to warm. As the emitted Long Wave Radiation (LWR) from the Earth's surface will increase with increasing temperature ($LWR \sim T^4$), a temperature change starting from a cold background state will emit less LWR than a similar temperature change at a warm background state. Thus, a certain temperature change in the tropics

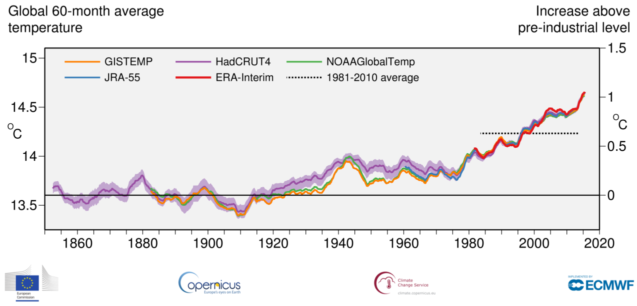

(a)

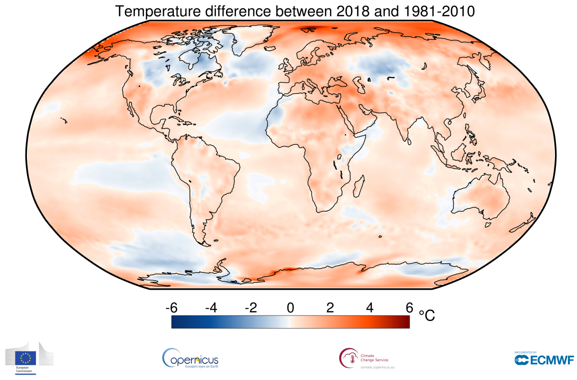

(b)

Figure 2.4: (a) The observed global mean 2m air temperature and (b) the observed 2m air temperature anomaly for 2018, both relative to 1981-2010. Figures from: `climate.copernicus.eu`.

results in a larger outgoing LWR than in the Arctic, leading to further warming of the Arctic. The ice-albedo feedback refers to the fact that sea ice has a larger albedo than the open ocean. Therefore, as the sea ice retreats, less of the incoming solar radiation will be reflected. Instead, it will be absorbed by the ocean, heating it up and leading to more sea ice melt, continuing the negative feedback loop. The increased polar temperature relative to the global mean is primarily seen over the Arctic, not over the Antarctic. Hence the name Arctic Amplification.
As AA increases, the temperature difference between the North Pole and Equator decreases. A weaker north-south temperature gradient will most likely lead to weaker westerlies and a weaker polar jet (Francis and Vavrus (2015)). A weaker jet is wavier (a slow running river meanders more) which allows for cold Arctic air to flow more southward, resulting in cold air outbreaks (see section 2.2.1). A weaker jet might also lead to more persistent weather systems as the air moves slower and takes longer to move on.

As warm air can contain more water than cold air, the precipitation patterns have likely changed as well due to the observed increase in temperature. However, large internal variability and a relatively short precipitation record have made it difficult to assess anything with certainty (IPCC (2013)).

2.3.2 The ocean

The ocean is generally less observed than the atmosphere, partly for historic reasons, partly because satellites can only be used for observations of the ocean surface. Most of the observational ocean records are relatively short and not uniformly distributed around the world oceans. Measurements of the ocean interior consists of either relatively few transects or single point observations made from a research ship, or autonomous instruments (e.g. the ARGO floats; Dean Roemmich | Scripps Institution of Oceanography et al. (2009)). Observations of the ocean have shown that the oceanic heat content has increased over the recent past (Abraham et al. (2013), IPCC (2013)). Some studies have found that the AMOC is slowing down (Smeed et al.), but the observational record is too short to determine if this is caused by the increased temperature.

One phenomenon that have been attributed to the increased oceanic temperature is the *atlantifica-*

tion of the Barents Sea and the Eurasian Basin in the Arctic Ocean (Aarthun and Eldevik (2012), Polyakov et al. (2017)). This phenomenon refers to the transition during sea ice retreat: the vertical oceanic structure shifts from being similar to that in the Arctic Ocean, to a structure similar to that in the Atlantic Ocean. This leads to a weakening of the stratification, increasing vertical mixing and shoaling of the Atlantic Water.

2.3.3 The Arctic sea ice

Since satellite observations of the Arctic sea ice began in 1979, the sea ice has been observed to decline. The mean Sea Ice Extent (SIE) for the years 1981-2010 has a seasonal cycle that varies between approximately 6 and 15.5×10^6 km^2 (NSIDC). For the period 1979-2016, the annual mean Northern Hemisphere (NH) SIE has decreased by 2.0×10^6 km^2 (Onarheim et al. (2018)). The September SIE is shown in figure 2.5, illustrating the sea ice decline. In a recent study, Stroeve and Notz (2018) reviewed the current state of the Arctic sea ice. They found that the Arctic sea ice has changed significantly over the last 40 years. The SIE was declining in all months, with a record of 16 consecutive months from January 2016 to July 2018 with SIE more than 2σ below the 1981-2010 long-term mean SIE. Much attention have been on the record low summer SIE of 2012 (3σ below the 1981-2010 long-term average), but autumn, winter and spring have seen a more significant sea ice loss since 2016. Record low SIE were reached for 8 out of the 12 months (January-June and November-December) between 2016 and 2018.

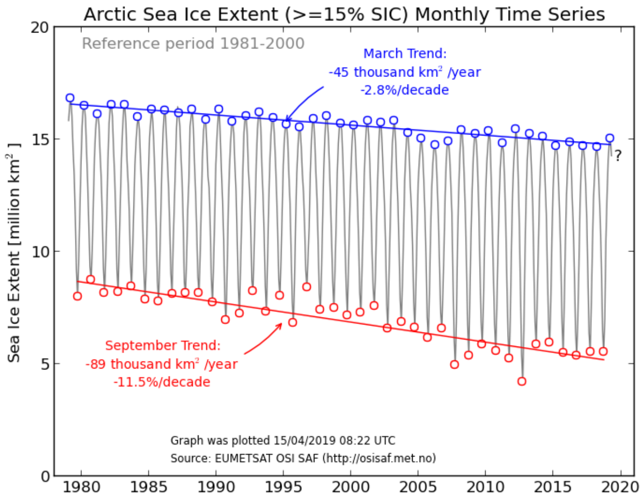

Figure 2.5: Monthly mean Arctic sea ice extent (>=15% SIC) in million km^2. Source: OSISAF (2017).

The sea ice loss was concentrated in specific regions, depending on the season. The largest decrease was observed in summer, with the NH September SIE having decreased by 3.2×10^6km^2 over the period 1979-2016. Summer sea ice loss was concentrated in the perennial sea ice cover, with the East Siberian Sea, the Chukchi Sea, the Beaufort Sea, the Laptev Sea and the Kara Sea experiencing the largest summer sea ice loss and explaining 89% of the inter-annual September SIE variance (Onarheim et al. (2018)). Onarheim et al. (2018) referred to these areas with largest variance and negative trend in summer SIE as the 'summer mode'. The corresponding 'winter mode' cover the seasonally ice-free areas with no sea ice in summer, hence the largest sea ice loss occurred in winter. For 1979-2016, the NH March SIE had decreased by 1.5×10^6km^2. The largest contributor to this was the Barents Sea (27%), followed by the Sea of Okhotsk (27%), Greenland Sea (23%) and Baffin Bay/Gulf of St. Lawrence (22%). These regions explained 81% of the inter-annual March SIE variance. As the climate continues to warm in the future, there seems to be a transition of regions from 'summer mode' to 'winter mode'. The climatic impact due to sea ice loss

depends on the location of the sea ice loss (Koenigk et al. (2016), Pedersen et al. (2016), Screen (2017b)). This will be discussed further in section 6.5.
Not only the extent, but also the thickness and age of the ice are decreasing. Stroeve and Notz (2018) estimated that the mean ice thickness in the Arctic Ocean had decreased by 28 cm per decade, or 40% from 1979-2017. The part of the Arctic Ocean covered by perennial ice had decreased from 58% in 1984 to 28% in 2018. Ice older than 5 years only covered about 2% in 2018, compared to 30% in 1984. The sea ice loss had resulted in a melt-onset 12 days earlier and freeze-up 28 days later in 2018 compared to 1979, extending the melt season. With the increase in younger and thinner ice, the same incoming energy will melt more ice. Due to this, the Arctic sea ice cover has increased the likelihood of rapid ice loss events in summer over the last 40 years. Additionally, the larger areas of ice-free ocean increases the likelihood of rapid ice growth events during autumn, due to the larger areas of ice-free areas (Stroeve and Notz (2018)).

Drivers of the observed sea ice changes

An explanation for the observed decline in sea ice is the observed increase in air temperatures caused by increased anthropogenic CO_2 emissions (IPCC (2013)). This correlation between the observed sea ice decline and the anthropogenic CO_2 emissions was shown by Notz and Stroeve (2016). For the period 1953 to 2015, they found a linear relationship between CO_2 emissions and the September sea ice area, where a metric ton of anthropogenic CO_2 emissions lead to a loss of 3 ± 0.3 m^2 of September sea ice area. They used a conceptual model to explain that the Arctic sea ice loss is less impacted by changes in atmospheric and oceanic changes, and more by the surface energy balance at the sea ice edge. The relationship between sea ice loss and increasing CO_2 emissions has been established by several studies (see Notz and Stroeve (2016)). Niederdrenk and Notz (2018) estimated the sea ice sensitivity to 1°C of annual mean global warming to a loss of 3.3-4 million km^2 of September Arctic sea ice area and 1.6 million km^2 of March Arctic sea ice area.
The global warming might determine the overall trend of the sea ice loss, but on shorter time scales internal variability plays a part as well (Swart et al. (2015)). In a study by Ding et al. (2019) it was shown that the internal atmospheric variability contributed about 40-50% to the observed Arctic sea ice decline. This indicates that the observed sea ice loss is the result of the combined effects of long-term external forcing in the form of increased anthropogenic CO_2 emissions and short-term internal variability.

2.4 Paleo climate

It is not the first time in Earth's history that the climate has changed. As discussed in section 1, temperature reconstructions reveal several large temperature changes during the last glacial. These abrupt temperature increases have been proposed to be caused by a rapid retreat of sea ice (see section 2.4.3). Understanding these past changes and the impact they had on climate can help us to understand the current climate changes. This understanding can be obtained by analyzing reconstructions from proxy (or paleo) records.

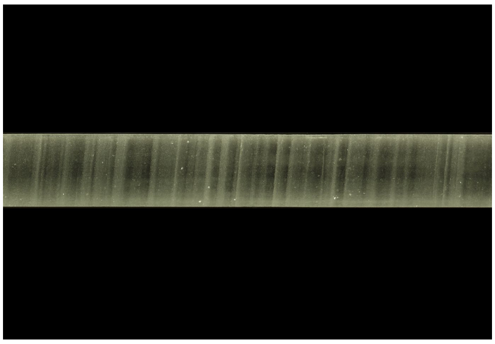

(a)

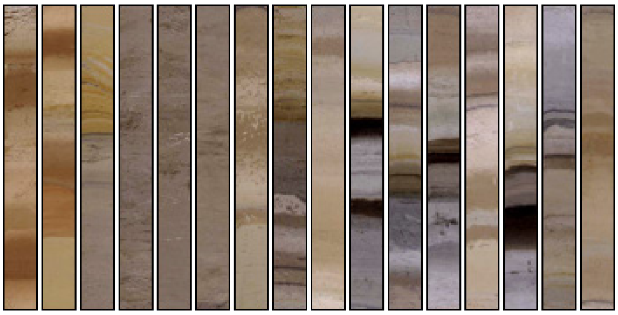

(b)

Figure 2.6: (a) Ice core. Source: `https://www.nbi.ku.dk/english/www/willi/dansgaard/arven-fra-dansgaard/`. (b) Marine sediment cores. Source: `https://earthobservatory.nasa.gov/features`.

2.4.1 Proxy records

Our knowledge about the climate in the recent past is based on observations of temperature, precipitation, sea ice extent etc. Systematic observations started slowly in the end of the 19th century, increasing in spatial and temporal resolution up through the 20th and 21st centuries. Today satellites enable continuous monitoring of even the most remote areas. Some parameters are measured directly, some are inferred from other parameters. The latter approach is referred to as using proxy records. This approach is also used to gain knowledge of past climate. Below is a brief introduction to proxy records, with focus on ice core records from Greenland and marine sediment cores.

Ice cores

Ice cores contain information about past climate through the chemical construction of precipitation falling on the GIS and through the air trapped in bubbles in the ice. As time goes, the precipitation fallen on the surface of the GIS will be buried by new precipitation. This condenses the snow into ice, capturing and preserving the specific chemical fingerprint of the precipitation of that time as well as the air captured in caveats in the ice. The GIS is 2-3 kilometers thick, preserving ice as old as 120,000 years (Kindler et al. (2014)). This provides us with a record covering the current interglacial (the Holocene), the last glacial and the end of the last interglacial (the Eemian). The age of the ice core record is limited as the ice at some point reaches bedrock. Due to the weight of the ice sheet, the ice at the bottom will reach the freezing/melting point and start to melt.
As the ice cores do not preserve temperature, this can be inferred from the ratio of oxygen isotopes in the ice (Paterson (1994)). Precipitation consists of water (H_2O). The most abundant oxygen isotope is ^{16}O, but a smaller fraction is made up of the heavier ^{18}O isotope. Cold air can contain less water vapor, thus condensating more vapor into precipitation relative to warmer air. As ^{18}O is slightly heavier than ^{16}O, relatively more ^{18}O will have condensated into precipitation before reaching the GIS in a cold climate (or in winter relative to summer). This means that the ratio $\delta^{18}O = {}^{18}O/{}^{16}O$ is lower for cold air than for warm air. Besides temperature, several additional parameters are measured in the ice cores as well.

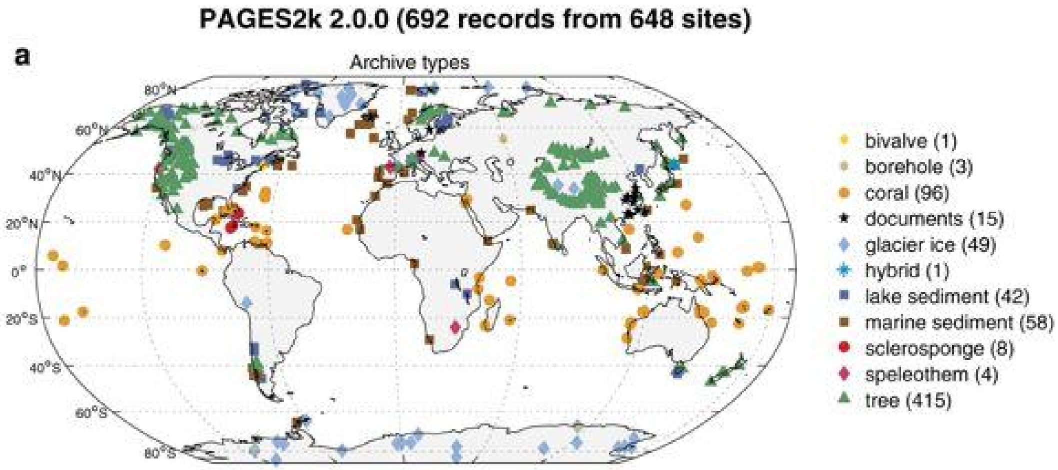

Figure 2.7: Location of various proxy records. Figure from PAGES2k Consortium (2017).

Marine sediment cores

Marine sediment cores are taken from the bottom of the ocean floor (Ruddiman (2008)). They contain the shells of the animals living in the water column above, molecular biomarkers of the biota and transported material such as ice-rafted debris. From these cores we can obtain information of past ocean states such as the temperature in specific layers of the water column (inferred from the number of a specific species), the strength of the ocean mixing (anhysteric remanent magnetization, ARM) and the presence of sea ice represented by the PIP_{25} (Müller et al. (2011)). PIP_{25} is a combination of open-water biomarkers and ice-algae biomarker IP_{25}. High abundance of open-water biomarkers indicate open-water conditions, high values of IP_{25} indicate sea ice. Combining these proxies results in a record of the sea ice cover, ranging from open-water over seasonally ice-covered to perennial sea ice cover (Sadatzki et al. (2019)).

Proxy records are an extremely useful tool to obtain information about the past, but it has its limitations. First of all, it is expensive and often difficult to obtain the records. The deep ice cores on Greenland require a few years of drilling in the summer season to reach the bottom of the ice sheet, 2-3 kilometers down. This leads to a second limitation, namely the sparse unevenly spatial distributions of the proxy records. This is illustrated in figure 2.7, showing the location of various kind of proxy records, covering the last 2000 years: they range in length from 50 to 2000 years. Clearly some areas are covered quite well (e.g. Western USA), some areas are not (e.g. the ocean). A third limitation with proxy records are their inability to show cause and effect. Proxy records show the sum of the processes that have occurred, but they do not show what caused what. Comparing proxies from the same ice core reveals similar changes. However, this only shows a correlation, not what drives what. The same issue is valid when comparing with proxy records from different ice or sediment cores, including the new issue of having to pinpoint the relative timing between the two records. Pinpointing the timing between proxy records provides us with a potential lead/lag relationship, but it does not show causality.

2.4.2 Past climate change

Paleo records show that the Earth have experienced several cold periods (glacials or ice ages) separated by warmer periods (interglacials). The current interglacial (the Holocene) began about

11,700 years ago, marking the end of the last glacial. During the last glacial the air temperature on Greenland was lower than today and large ice sheets covered North America (the Laurentide Ice Sheet) and Scandinavia (the Fenno-Scaninavian Ice Sheet), in addition to the GIS that still persists today. The water trapped in these ice sheets caused the global sea level to be lower than today. A reconstructed temperature record from the NGRIP ice core on Greenland covering the period 10 to 120 kyr b2k (thousand years before 2000 AD) is shown in figure 2.8. Besides the low temperatures on Greenland relative to present day, another feature is evident: abrupt warmings occurred several times during the approximately 110,000 years it lasted. These events are referred to as Dansgaard-Oeschger events (Dansgaard et al. (1993)).

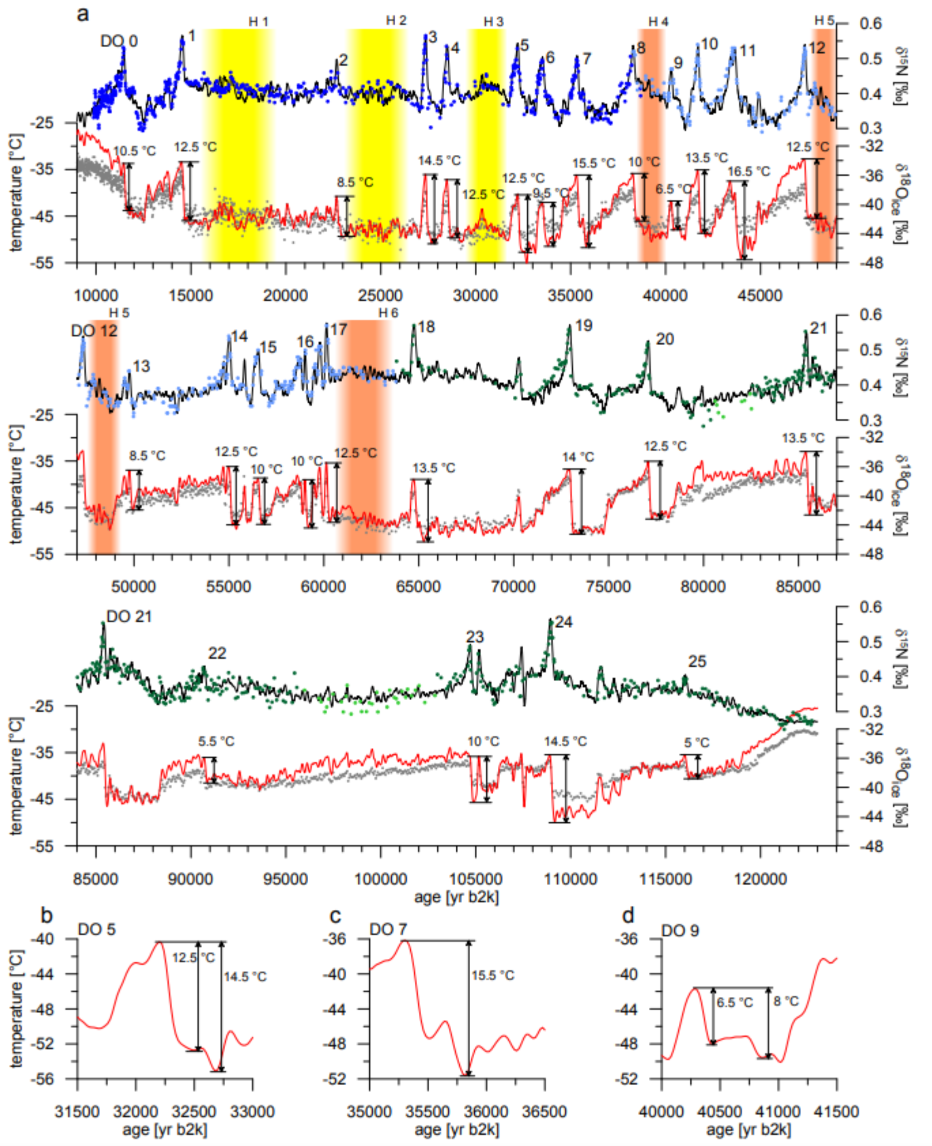

Figure 2.8: NGRIP temperature reconstruction (red line) from 10 to 120 kyr b2k (thousand years before 2000 AD). Please note that time goes from right to left. Grey points are $\delta^{18}O$ measurements. Blue and green dots are $\delta^{15}N$ measurements from various sources and the black solid line is modelled $\delta^{15}N$. Yellow (orange) areas indicate stadials with a Heinrich event with no long-term warming observed (with long-term warming observed). Numbers indicate D-O events. Figure from Kindler et al. (2014).

2.4.3 Dansgaard-Oeschger events

The Dansgaard-Oeschger (D-O) events recorded in the Greenlandic ice cores varied in duration and magnitude of the warming events. They were characterized by a rapid warming (10-15°C over a few decades or centuries; see lower panel in figure 2.8), followed by a gradual cooling back to the starting point. Based on this, the climate is said to transition from a cold stadial to a warmer interstadial and back again into a stadial.

Changes in Nordic Seas sea ice was proposed by Dokken et al. (2013) to be a potential cause of these abrupt warmings (the 'Dokken hypothesis'). Comparing the temperature proxy records from NGRIP with a marine sediment core in the Nordic Seas, they found that the Nordic Seas were covered by sea ice during the cold stadials, but ice-free during the warm interstadials. They proposed that warm subsurface water built up under the Nordic Seas sea ice cover during stadials, weakening the stratification. At some point, the stratification collapsed, causing the warm water to be mixed into the surface waters, rapidly melting the sea ice cover. The now ice-free ocean surface released vast amounts of heat to the colder atmosphere, resulting in a rapid warming. Jensen et al. (2018) support this hypothesis by showing in a eddy-resolving idealized general circulation model that a rapid retreat of the sea ice on the Nordic Sea could occur due to small changes in the temperature of the inflowing water, leading to a breakdown of the stratification.

Using an idealized topography, Jensen et al. (2018) showed that rapid sea ice retreat as a driver of the abrupt D-O events is possible. Increasing the model complexity, Guo et al. (2019, manuscript in preparation)) showed that the Dokken hypothesis was also possible in a fully coupled climate model. Using the climate model NorESM, they simulated the Marine Isotope Stage 3 period (MIS3; approximately 30-60 thousand years ago), as this period covers several D-O events. The sea ice cover in their glacial simulation did reach further south than present day conditions, yet it did not cover the Nordic Seas. In order to simulate the cold stadial conditions during the glacial, fresh water was added to the simulation, a so called hosing experiment. More precisely, they added 0.33 Sv of fresh water uniformly in the region between 50°N and 70°N for 500 years. After the 500 years the fresh water forcing stopped, and the simulation continued for 300 years. Adding fresh water strengthened the halocline between the fresh surface layer and the saline water underneath, hence strengthening the stratification. This shielded the cold fresh surface layer from the warm saline water underneath, allowing for sea ice to form. As a results, they achieved a sea ice cover from the Arctic Ocean down to the Bay of Biscay, representing a cold stadial. To force the model to transition into a warm interstadial, they stopped the fresh water forcing. This resulted in a rapid retreat of the sea ice cover, back to the starting point. During this rapid retreat, they showed that the temperature on Greenland increased rapidly, in a rate similar to the observed rate during the D-O events. Hence, a rapid retreat of sea ice was able to induce an abrupt warming on Greenland.

The two model studies discussed above show that a rapid sea ice retreat is a valid candidate as the driver of the D-O events. A recent paleo study by Sadatzki et al. (2019) showed that changes in the Nordic Seas sea ice cover actually did leed to changes in the Greenlandic air temperature. By comparing the same two cores as in Dokken et al. (2013), but using PIP_{25} as a sea ice proxy, they could pinpoint the timing of the different transitions. They found that the Nordic Seas sea ice started to retreat due to increasingly warm subsurface water underneath. Following this was a reinvigoration of the ocean circulation and consequently the D-O events.

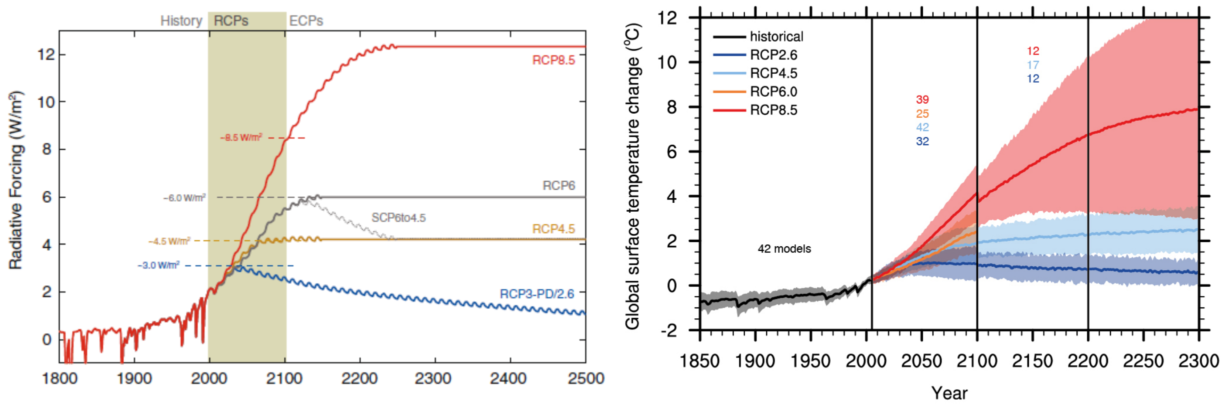

(a) (b)

Figure 2.9: (a) Radiative forcing (in W m^{-2}) for the four RCP scenarios. Figure from Meinshausen et al. (2011). (b) Global annual mean surface air temperature anomalies (relative to 1986-2005) from the CMIP5 ensemble for the historical simulations, followed by the four RCP scenarios. Solid lines are multi-model mean, shading indicate 5% to 95% range. Number in figure indicate number of models. Discontinuities are due to not all models continuing after year 2100. Figure from IPCC (2013).

2.5 Future climate

As opposed to the past and present climate, the future climate cannot be observed. For this we have to rely on climate models. In order for us to be able to compare different models, these modeling efforts have been combined in Model Intercomparison Projects (MIP's) where all the models use the same initial conditions as well as various scenarios for the future. There exist many different MIP's, but in this thesis we will only discuss the Coupled Model Intercomparison Project Phase 5 (CMIP5; Taylor et al. (2012)). CMIP5 was used for the IPCC AR5 (IPCC (2013)) and consists of more than 50 coupled climate models. The future scenarios depend on projections of GHG emissions and are represented by four Representative Concentration Pathways, as explained in section 2.5.1.

2.5.1 Representative Concentration Pathway (RCP)

To assess future climate projections across climate models, four scenarios have been defined. These scenarios are called Representative Concentration Pathway (RCP) and represent 4 sets of projections for GHG emissions, aerosols, air pollutant emission and land use for the 21st century (Meinshausen et al. (2011), IPCC (2013)). They represent four potential paths for the climate to follow in the future: RCP2.6, RCP4.5, RCP6.0 and RCP8.5. The numbers refer to the projected radiative forcing in Wm^{-2} by year 2100, relative to pre-industrial levels. The radiative forcing for each of the four pathways are shown in figure 2.9a. RCP2.6 peaks at 3 Wm^{-2} around year 2050, declining to about 2.6 Wm^{-2} by 2100. This is the scenario with the lowest GHG emissions, likely keeping global warming below 2°C. To achieve this, most models require net negative emissions. RCP4.5 and RCP6.0 represent two intermediate scenarios where the radiative forcing stabilizes at approximately 4.5 Wm^{-2} and 6.0 Wm^{-2} after 2100. The worst-case scenario is RCP8.5, where the radiative forcing is projected to reach 8.5 Wm^{-2} by 2100, continuing up to 12 Wm^{-2} by year 2250, after which it stabilizes. The 'baseline scenario' (or the 'business-as-usual' scenario) is between RCP6.0 and RCP8.5, where RCP8.5 represent the high-end of projected emissions. After

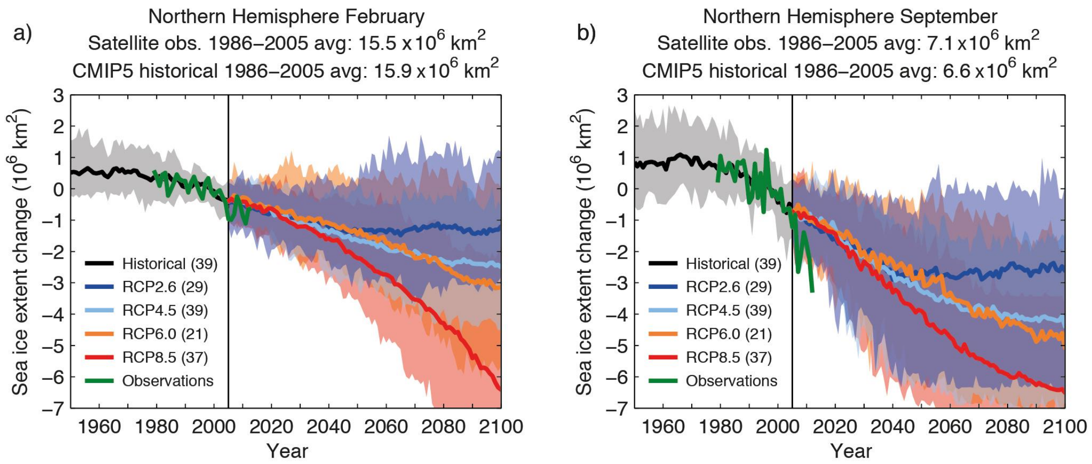

Figure 2.10: Changes in sea ice extent (SIE) relative to 1986-2005 for the CMIP5 ensemble for Northern Hemisphere a) February and b) September. Shown are the historical CMIP5 simulations, ending in year 2005. Following this is the four RCP scenarios. Number in legends refer to the number of models available. Green lines show the observed SIE for the period 1979-2012. Solid lines are multi-model mean, shading indicate 5% to 95% range. Figure from IPCC (2013).

year 2100 the RCP's are extended, referred to as Extended Concentration Pathways (ECP), see figure 2.9a. For RCP2.6, emissions were kept constant, continuing the decline in GHG emissions. RCP4.5 and RCP6 transitions from constant emission by 2100 to constant concentrations by 2150. RCP8.5 has constant emissions up until year 2150, after which it transitions to stabilize concentrations by 2250.

2.5.2 Projected changes by the CMIP5 ensemble

The CMIP5 ensemble of the historical period and the four RCP scenarios as presented in IPCC (2013) can be seen in figures 2.9b and 2.10 for the global mean temperature anomaly and the sea ice extent anomaly, both relative to the period 1986-2005. There clearly is a large difference between the four scenarios. The low emission scenario RCP2.6 projects a mean temperature change of 1.0°C with a range of 0.3-1.7°C for the period 2081-2100, whereas the high emission scenario RCP8.5 projects a mean temperature of 3.7°C with a range of 2.6-4.8°C. Continuing on till year 2300 increases the difference, as well as the uncertainty range. The sea ice cover also shows large differences, ranging from the potential of an ice-free Arctic in summer by the middle of this century for the RCP8.5 scenario, to keeping the Arctic summer sea ice in RCP2.6. The RCP8.5 scenario has the highest GHG emissions, but even with this, the CMIP5 models fail to simulate the rate of the observed sea ice loss in September on the Northern Hemisphere, shown by the green curve in figure 2.10(b).
Although the global mean temperature rises, it does not mean the temperature rises equally everywhere. Figure 2.11(a) shows the temperature anomalies for RCP2.6 and RCP8.5 for the period 2081-2100 relative to 1986-2005. The Arctic Amplification is clearly seen, as the Arctic temperature increases more than at the low- and mid-latitudes. The precipitation change is not uniformly distributed either (fig. 2.11(b)). In general, are the currently wet areas projected to become wetter, and the dry areas projected to become drier.

In the ocean two main features are projected for the future, besides the overall warming (Koenigk et al. (2013)). First of all, the deep convective mixing is projected to go extinct as the sea ice disappears. As deep water is formed due to sinking of the cold, saline water, the mixed layer depth can be used as an indicator of deep water formation. Brodeau and Koenigk (2015) showed that the depth of the mixed layer shoaled as the Arctic sea ice edge retreated northward. This indicates that the deep water formation will weaken and subsequently disappear entirely. The weakening of the deep water formation might be part of the reason for the second feature, which is the projected weakening of the AMOC. The CMIP5 ensemble projects a 36% reduction in the strength of the AMOC by year 2100 (Cheng et al. (2013)).

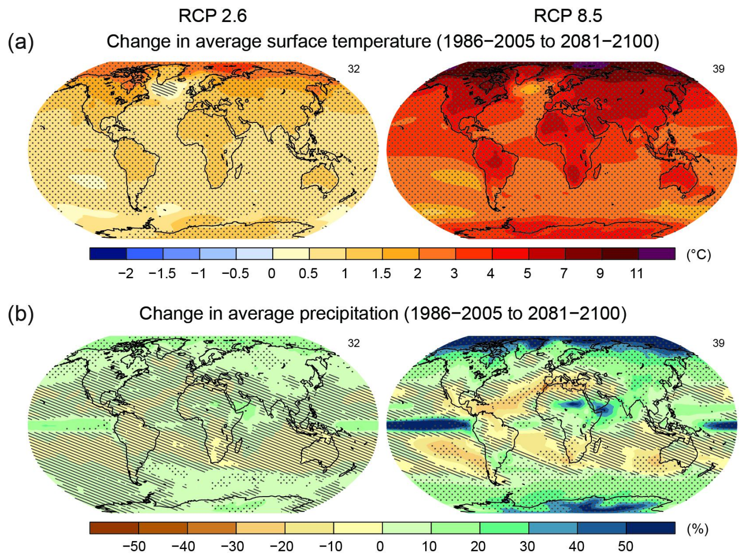

Figure 2.11: Projected late 21st century annual mean (a) surface temperature change and (b) precipitation change for RCP2.6 (left panels) and RCP8.5 (right panels). Changes taken for the period 2081-2100 relative to 1986-2005. Figure from IPCC (2013).

The RCP future scenarios start in year 2005. The radiative forcing and CO_2 emissions are still quite similar to the latest observations, although the RCP8.5 has started to take off. For year 2017, the annual mean projected radiative forcing for the four scenarios (3.05 W m^{-2}, 3.05 W m^{-2} , 3.04 W m^{-2} and 3.12 W m^{-2} for RCP2.6, RCP4.5, RCP6 and RCP8.5, respectively; `http://www.pik-potsdam.de/~mmalte/rcps/`) are similar to the observed (3.06 W m^{-2}; `https://www.esrl.noaa.gov/gmd/aggi/aggi.html`). The same goes for the annual mean CO_2 emissions in 2018: 407.5 ppm, 406.6 ppm, 405.4 ppm and 409.9 ppm for RCP2.6, RCP4.5, RCP6 and RCP8.5 projections) (http://www.pik-potsdam.de/ mmalte/rcps/)), respectively, and 408.3 ppm for the observed (`https://www.esrl.noaa.gov/gmd/aggi/aggi.html`).

2.5.3 A 1350 year long RCP8.5 scenario simulation

Study III analyses specific time slices in a 1350 year long RCP8.5 scenario simulation performed with EC-Earth coupled to the interactive ice sheet model PISM, i.e. EC-Earth-PISM. The specific model setup is described in section 4. Most future projections of climate simulate until the end of the 21st century. A few (∼8 model simulations) continue until year 2300, but to our knowledge, a simulation until year 3200 have not been performed before. Here, key parameters are presented in figure 2.12, and compared to the general CMIP5 RCP8.5 ensemble. As the GHG emissions continue to rise (fig. 2.9a), so does the global mean temperature (red curve in fig. 2.12). The global mean temperature increases from present day conditions (1986-2005, same reference period as in IPCC (2013)) of 13.4°C to 25.4°C by year 3200 at the end of the simulation, an increase of

Table 2.1: 30-year mean of the global mean surface (2m) air temperature (T_{2m}; in °C) and its change relative to P1, the sea ice area for March (September) (in million km^2), the Greenland Ice Sheet volume (in million km^2) and global mean precipitation (P; mm day^{-1}) for each of the five periods.

	Years	**T_{2m} (ΔT)** [°C]	**SIA Mar (Sep)** [million km^2]	**GIS volume** [million km^3]	**P** [mm day^{-1}]
P1	1850-1879	12.7	7.84 (15.4)	3.59	2.84
P2	1986-2005	13.4	6.38 (14.5)	3.59	2.85
P3	2060-2089	16.2	0.164 (10.4)	3.59	3.00
P4	2154-2183	20.5	0 (0.418)	3.52	3.24
P5	3170-3199	25.4	0 (0)	1.38	3.60

$\sim$12°C (see table 2.1). The CMIP5 ensemble does not continue after year 2300. The global mean temperature for the period 2281-2300 in our simulation has increased by 9.6°C, relative to the period 1986-2005 (table 2.1). This is within the range of the CMIP5 ensemble for the same period (7.8$\pm$2.9°C, IPCC (2013) table 12.2).

The rate of the warming is largest now and until around year 2250, coinciding with the rapid decrease in NH sea ice area (SIA, blue curves). Using a minimum SIA threshold of one million km^2, this simulation predict an ice-free Arctic in summer by year 2060 and in winter by 2154. The global mean temperature stabilizes after the Arctic becomes ice-free year-round. This coincide with the stabilization of the GHG concentrations for the ECP8.5, as can be seen in figure 2.9a. Not only the global temperature and sea ice are affected by the increasing GHG emissions. The Greenland Ice Sheet is currently relatively stable, but our simulation predicts an increase in melt, resulting in a linear decrease in the GIS volume from around year 2060 to the end of the simulation (green curve). This results in a GIS loss of 62% by year 3200 (table 2.1).

The general evolution of Arctic SIA shown in figure 2.12 is within the range of the CMIP5 model ensemble mean shown in figure 2.10(a) and (b), as the Arctic becomes ice-free in September by 2060 (Koenigk et al. (2013)). EC-Earth is part of the CMIP5 ensemble, but the simulation shown here differs from the CMIP5 model setup by being coupled to the Ice Sheet Model PISM (Svendsen et al. (2015); see section 4). Through the coupling to PISM the GIS is allowed to shrink in size, adding the extra fresh melt water to the ocean (2.13). The ice disappears at the coastal regions first, contracting back to the Southeastern part of Greenland.

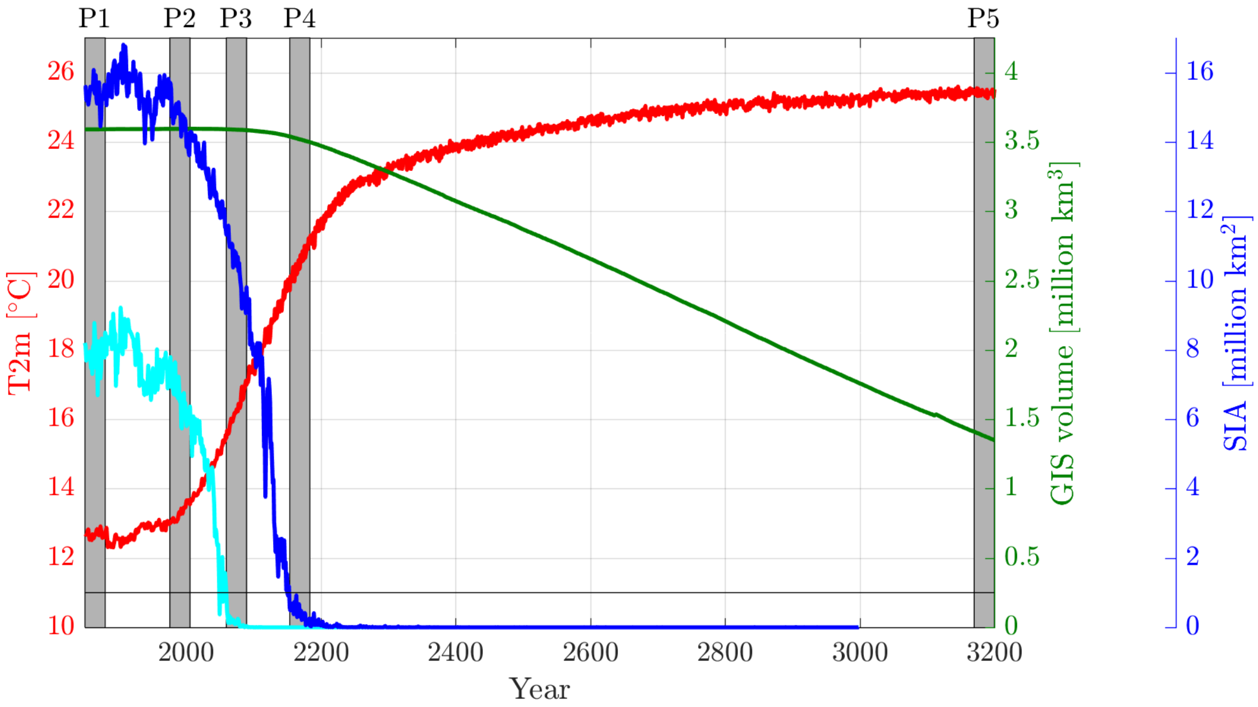

Figure 2.12: Annual global mean surface (2m) air temperature (red; in °C), annual Greenland Ice Sheet Volume (green; in million km^3) and mean NH SIA (in million km^2) for March (dark blue) and September (light blue) in the EC-Earth-PISM RCP8.5 simulation. Horizontal line indicate SIA equal to one million km^2. The 5 grey boxes indicate the 5 periods defined in Manuscript III (see table 2.1 and section 5.3). The temperature for year 2571 has been removed, as there was a spurious spike in temperature for this year. The spike occurred due to an error in the forcing setup.

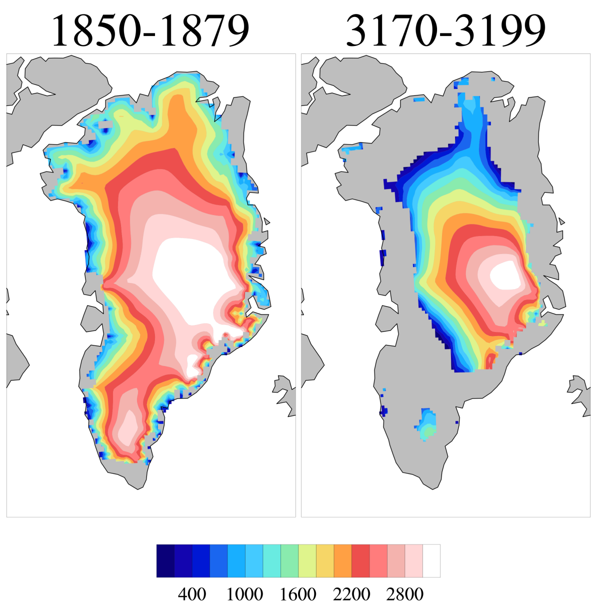

Figure 2.13: Mean ice sheet elevation [m] for years 1850-1879 (left) and 3170-3199 (right) in the RCP8.5 simulation. Figure courtesy of Rasmus Anker Pedersen.

2.6 Climate models and nudging

2.6.1 General Circulation Models (GCM)

Simulating the climate requires numerical models capturing the complexity of the climate system. The complexity of the models vary from one dimensional column models, over box models to the most complex climate models, the General Circulation Models (GCM). GCM's enclose the Earth in a 3D grid, with a certain horizontal and vertical resolution (see figure 2.14). For each grid cell and at each time step in the model, the physical processes controlling the climate are computed. GCM's can model just the atmosphere (AGCM), just the ocean (OGCM) or couple the atmosphere and the ocean (AOGCM). Each of them has their advantages. Modeling just the atmosphere or the ocean reduces the required computer power compared to the fully coupled system. AGCM's are used for weather prediction, often in a regional higher resolution setup and with prescribed observed ocean surface conditions. This is partly for historical reasons (atmospheric modeling began before oceanic modeling), partly because they are faster than fully coupled model and partly because of the relatively short time scales used in weather prediction. Often, predictions cover days, potentially weeks. During this time span the oceanic feedbacks to atmospheric changes are negligible.

The importance of atmosphere-ocean coupling

AGCM's have been widely used for climate modeling as well. For example, several studies have used AGCM's to investigate the impact of sea ice changes on the climate system (e.g. Petoukhov and Semenov (2010), Screen (2013), Pedersen et al. (2016)). In these, sea surface temperature (SST) and a target sea ice cover are prescribed to the model. This allows for the atmospheric processes to be isolated and analyzed. However, this does not allow for oceanic feedbacks to the atmospheric changes. Deser et al. (2015) showed that by neglecting the ocean and its feedbacks to the atmosphere, remote impacts of the climatic changes are not captured. By designing three experiments using an AGCM coupled to either a non-interactive ocean (prescribing ocean surface conditions), a slab ocean (only capturing the thermodynamic ocean processes) or to a full-depth dynamical ocean model, they conclude that only the latter captures the equatorial symmetry observed due to changes in the sea ice cover. They further suggest that AGCM's underestimate the spatial coverage of the predicted future warming. Supporting the importance of coupling climate components are the studies by Petrie et al. (2015) and Screen (2018). Both studies suggests that AOGCM's generally agree more across models on predicted atmospheric response than AGCM's. This stresses the importance of using coupled climate models for climate simulations.

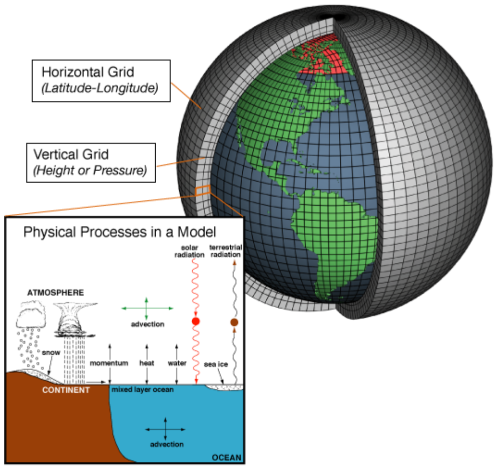

Figure 2.14: Schematic of a General Circulation Model. Source: `https://celebrating200years.noaa.gov/breakthroughs/climate_model`

2.6.2 Nudging

Nudging is a simple form of data assimilation. Data assimilation is the process of improving a models initial conditions using observations or short-range forecasts Kalnay (2012). The more accurate the initial conditions, the more accurate the forecast.
Nudging, or *Newtonian Relaxation* pushes the model solution toward the observations by adding a term to the prognostic equations (Kalnay (2012)). For example:

$$\frac{dT}{dt} = \frac{dT_b}{dt} + \frac{T_{obs} - T_b}{\tau} \tag{2.1}$$

where T is the variable, T_b is the 'background' or 'first guess', T_o is an observations and τ is an empirical relaxation time scale, determining how fast the T converges toward the observation. Other assimilation methods include the statistical information about the observations (appropriately called *statistical interpolation schemes*). The overall idea is the same as for the nudging: determine the corrected value T by combining information about the 'first guess' and the observations. These methods all have the same caveat: they do not conserve energy. Using temperature as an example and returning to eq. 2.1, $\frac{dT_b}{dt}$ is the temperature change the model computes based on the background state. This is energy conserving. Adding $\frac{T_{obs}-T_b}{\tau}$ requires a change in energy (positive or negative), but it is not taken from somewhere. It appears out of thin air. Thus, assimilation is not energy conserving.

Chapter 3

Motivation for each study

The motivations for Manuscript I, Manuscript II and Manuscript III discussed below summarizes the motivations discussed in each manuscript.

3.1 Study I: Nudging sea ice in the coupled climate model EC-Earth

Constraining sea ice in climate models is used to minimize the bias between model and target, or to analyze the effect of a specific sea ice state. In AGCM's this can be achieved by simply prescribing the target sea ice configuration. However, as discussed in section 2.6.1, the coupling between the atmosphere and the ocean is crucial for capturing the global signal by allowing for feedbacks between the atmosphere and the ocean. Therefore, coupled GCM's are needed to get the full picture of these changes on the climate system.

Constraining sea ice in coupled GCM's is not as straightforward as in AGCM's or OGCM's. Coupled GCM's exchange information between the atmosphere and the ocean/sea ice/land beneath. As the Earth is a closed system, energy, water and mass must be conserved in the total Earth system. Therefore, any exchange between the components must be countered somewhere else in the system. Constraining sea ice (or any parameter) should aim at not breaking this conservation. As it turns out, constraining sea ice while conserving energy is tricky. Sea ice can be constrained by directly nudging sea ice concentration (SIC) and thickness (Tietsche et al. (2013), Smith et al. (2017)). By increasing the amount of sea ice, water in the form of ice is added to the model. Hence, water conservation is broken. Removing sea ice, removes the energy in the sea ice from the climate system as well. In addition to violating the energy and water conservation, constraining sea ice directly includes other issues such as dividing the new ice into ice thickness categories (Kimmritz et al. (2018)). Therefore, constraining sea ice directly in coupled models are not ideal.

Several other methods have been developed to constrain sea ice, some of them discussed in Screen (2018). There do exist energy-conserving methods for constraining sea ice in coupled climate models. By changing the initial sea ice thickness, Petrie et al. (2015) and Semmler et al. (2016) succeeded in reducing sea ice throughout the year due to the increased heat flux through the ice and increased melt. However, this is a time limited solution, since the system will return to the unperturbed state again relatively fast. Energy will also be conserved if the sea ice albedo is modified (Blackport and Kushner (2016), Blackport and Kushner (2017)). This changes the amount of solar radiation absorbed by the sea ice, allowing for more or less sea ice to be melted. The caveat of this

method is its seasonal dependency; it only works in the sunlit part of the year.
These two methods, although being energy and water conserving, are not ideal for longer climate simulations or in cases where sea ice needs to be constrained during winter. To avoid this, methods involving the surface heat flux have been used to constrain sea ice. Deser et al. (2015) added an additional long wave radiation flux (LWR) to the sea ice model to reach a target sea ice cover. This LWR flux varied seasonally, but not spatially, and was designed to reach the mean Arctic sea ice concentration predicted by the CCSM4 RCP8.5 model simulation by the end the twenty-first century. This 'ghost flux' (naming from Screen (2018)) is only seen by the sea ice module. A similar approach was taken by McCusker et al. (2017) and Oudar et al. (2017). McCusker et al. (2017) computed the amount of heat needed to melt or form sea ice, then added this to the sea ice module. In the study by Oudar et al. (2017) the modified surface heat flux (LWR+turbulent heat fluxes) was seen by the ocean module and through this communicated to the sea ice. The last three approaches are quite similar and all conserve water, but not energy.

So far, methods for constraining sea ice in coupled climate models only work on short time-scales, in certain parts of the year, or they do not conserve energy. Study I aimed at developing a method for constraining sea ice while still conserving energy and water. This was based on methods modifying the surface heat flux. In particular the method in Oudar et al. (2017) as they modified the non-solar heat flux received by their ocean component, NEMO, the ocean component in EC-Earth as well. Thus, the flux adjustment (naming from Screen (2018)) observed by the ocean were subsequently communicated to the sea ice module.

Taking a step back, lets consider how to modify sea ice without modifying the total energy of the system. Following the approach in Oudar et al. (2017), an extra heat flux was added/removed from the ocean in order to reach a target. To conserve energy, this heat flux must come from somewhere. One place to get it is the atmosphere. The simplest way possible was to simulate a change in the surface sensible heat flux (SSHF). SSHF exchanges heat between the atmosphere and the land/ocean surface and is defined in eq. 3.1:

$$SSHF = C_H|V|(T_s - T_{air}) \tag{3.1}$$

where C_H is a bulk transfer coefficient for heat, V is the wind speed, T_s is the skin temperature and T_{air} is the air temperature (Wallace and Hobbs (2006)). Increasing the SSHF from the ocean to the atmosphere would lead to an increase in the atmospheric temperature. Since SSHF only changes the amount of energy exchanged between the atmosphere and the surface, it conserves energy. Therefore, it is a good candidate when we want to nudge sea ice and maintain conservation. This is the topic of Study I: *can SSHF be used to indirectly nudge sea ice, while maintaining energy conservation?* The results are presented in section 5.1.

Two sea ice targets were initially used for testing the nudging methods. The first target had Arctic sea ice extending from the North Pole to 70°N and no sea ice south of this latitude. This created an idealized sea ice cover, with a sharp edge at 70°N. This target was not realistic, but allowed us to test how well the methods worked when pushed to form sea ice (in the Nordic Seas) and to melt sea ice (Baffin Bay/Labrador Sea). The second target had sea ice down to 50°N. This sea ice cover was even less realistic than the previous one, but it allowed us to test how our methods worked for sea ice targets far away from the models own sea ice cover. Moreover, this approach would allow us to test similar conditions as in the (Guo et al. (2019, manuscript in preparation)), but without adding fresh water.

The energy-conserving sea ice nudging method developed in Study I was initially intended for nudging sea ice in the Barents-Kara Seas in Study II (see below). As shown in the results (sec. 5.1), the energy-conserving method (M2) required a fine balance between reaching the target sea ice and the model becoming unstable. This balance turned out to be dificult to find, thus Study II was performed using the not energy-conserving method M1, instead of the energy-conserving method M2.

3.2 Study II: Barents-Kara sea ice and European winters in EC-Earth

Study II investigated the potential link between Barents-Kara (BAKA) sea ice loss and cold European winters. As discussed in section 2.3.2, the Barents Sea has experienced the largest winter sea ice decline in the Arctic since 1979. The Kara Sea was one of the largest contributors to September sea ice loss, and it is predicted to be the first of the perennial ice-covered seas to become ice free in September (Onarheim et al. (2018)). During the same time period, the global mean temperature has increased (fig. 2.4a). Coinciding with the increase in global temperature and decline in sea ice, several severe winter events have been observed over Eurasia (2005/2006 (Scaife and Knight (2008),), 2009/2010, 2010/2011 (Cattiaux et al. (2010), Guirguis et al. (2011), Cohen et al. (2010))) and North America (2009/2010, 2013/2014 (Van Oldenborgh et al. (2015)), 2018/2019). This apparent counter-intuitive behavior has led to several hypotheses on the potential link between the Arctic sea ice decline and abnormally cold winter events in Eurasia and North America. Several studies have focused on the BAKA, since these are the regions with the largest changes in sea ice. This link has been investigated in numerous observational and modeling studies, and it was also the focus of Study II.
Yang and Christensen (2012) stated that cold winters are still likely to occur, despite the global warming, and Mori et al. (2014) suggested that due to BAKA sea ice reductions, the probability of severe winters in central Europe have more than doubled. Outten and Esau (2012) used the ERA-Interim reanalysis to show a co-variability between the Arctic sea ice and Eurasian temperatures. Another observational study using ERA-Interim as well as satellite sea ice data from OSI-SAF, indicated that autumn Barents Sea sea ice was the best predictor for the winter NAO (low sea ice $\rightarrow$ negative NAO; Koenigk et al. (2016)). As a negative AO/NAO is associated with weaker westerlies and cold winter events over Europe, this implied a potential link between the Barents Sea sea ice and cold winters over Europe. This potential link was investigated further by Ruggieri et al. (2016) using reanalysis data as well. They suggested that late autumn and early winter BAKA sea ice anomalies caused a negative AO-like pattern by late winter, through enhanced blocking over BAKA, inducing upward wave propagation and leading to negative late winter temperature anomalies over Europe. The potential link was further supported by Kretschmer et al. (2016) who, based on causal effects network analysis of reanalysis data, proposed that the BAKA sea ice loss is a main driver of European winter circulation. The same pathway from BAKA sea ice reductions to negative AO/NAO like patterns, leading to cold continental mid-latitudes, was shown by Nakamura et al. (2015) using an AGCM. Petoukhov and Semenov (2010) also used an AGCM to reduce SIC step-wise in BAKA, finding a non-linear response to the linear sea ice loss. For moderate sea ice reductions (40-80% of the climatological SIC), enhanced anticyclonic anomalies over the Arctic

Ocean resembling a negative NAO induced weaker westerlies. This led to cooling over Europe. In contrast, smaller and larger sea ice reductions induced cyclonic anomalies over the Arctic Ocean, stronger westerlies and warming over Europe.

There is no consensus in the scientific community about the potential link between Arctic sea ice decline, in particular BAKA sea ice decline, and extreme cold winter events over Eurasia. Several studies proposed that the observed cold winter events in the recent past were driven by internal atmospheric variability and not by the Arctic sea ice loss. McCusker et al. (2016) analyzed sea ice and temperature trends from an AGCM and an AOGCM. They found, the Eurasian cooling from the period 1979-1989 to 2002-2012 was exceptional, the BAKA sea ice loss was not, thus the BAKA sea ice loss did not drive the Eurasian cooling events. Screen (2017a) concluded that although the Arctic sea ice loss did intensify negative NAO events, the European winter cooling was missing. They suggested that the missing cooling was due to the dynamical cooling associated with the negative NAO was exceeded by the thermodynamic warming caused by the sea ice loss it self.

The amount of literature on this potential link between Arctic sea ice loss and teleconnections to the mid-latitudes, especially cold winter events, is growing rapidly. The above is only a fraction of it. Two comprehensive reviews of this subject are given in Vihma (2014) and Meleshko et al. (2018). Vihma (2014) suggested that the circulation pattern response to sea ice loss might favor a negative NAO, but potentially only for a relatively small sea ice loss. Larger sea ice loss will not induce cold winters in the future as the global mean temperature rises. Meleshko et al. (2018) suggested that there is a potential link, but the internal atmospheric variability and the differences in models hamper this conclusion. Further limitations are due to the relatively short observational record. Despite the vast amount of literature on the subject, coordinated model experiments are needed, together with a longer observational record.

Several of the studies mentioned here either used reanalysis or AGCM's. As discussed in section 2.6.1, AGCM's do not simulate the atmosphere-ocean feedbacks, they underestimate the spatial coverage and the strength of climatic changes and they do not capture remote impacts. Further, AGCM's do not agree across models as well as AOGCM's do. All this implies that coupled GCM's are required to investigate teleconnections between different components of the climate.

Study II investigates this widely discussed potential link between BAKA sea ice loss and cold European winters. Our study was based on the Petoukhov and Semenov (2010) study, but in contrast to this, we used a *coupled climate model*, not an atmosphere-only climate model. This allowed us to capture the feedbacks related to the sea ice changes, as well as the remote impacts, not just the local. Part of this study was to investigate if we also observed the non-linear response to linear sea ice loss, where moderate sea ice reductions were linked to cold winters, but larger reductions were not.

Constraining sea ice in coupled climate models is not straightforward, as discussed in section 3.1. Study II builds on Study I, as methods for constraining sea ice in coupled GCM's were explored in Study I and used in Study II.

3.3 Study III: Climate change associated with sea ice loss in extended EC-Earth-PISM RCP8.5 simulation

In the recent past, observations have shown a declining Arctic sea ice. Present day observations indicate that sea ice plays a large role in the climate system. However, the observational record is relatively short (since 1979 for sea ice using satellites), so to gain more information on the potential influence of sea ice on the present and future climate, proxy records on past climate can be studied. As discussed in section 2.4.3, several large abrupt D-O events occurred during the last glacial, proposed to be driven by changes in sea ice. Although these abrupt events occurred in a climate very different from the present and the projected climate, it indicates that sea ice variability can influence the climate dramatically. Future projections of the climate predict the Arctic to become ice-free in summer by the middle of this century and ice-free year-round before year 2200 (for the RCP8.5 scenario). If the retreat of the Nordic Seas sea ice caused abrupt warming of up to 15°C within a decade, how does it affect the climate when all the Arctic sea ice disappears? And what happens on a longer timescale when the Greenland Ice Sheet starts to melt, increasing the fresh water input to the Arctic Ocean? These are our research question for Study III: *how does the climate react to different sea ice states? More precisely, how does the disappearance of Arctic summer sea ice and Arctic winter sea ice impact the climate. And how does it react to the increased FW flux from the disappearing Greenland Ice Sheet?*

Chapter 4

Model

In this PhD project, the global coupled atmosphere-ocean general circulation model EC-Earth was used (Hazeleger et al. (2010), Hazeleger et al. (2012)). EC-Earth is developed by the European EC-Earth consortium (EC-Earth Consortium), consisting of 27 research institutions from 10 European countries. This consortium is coordinated by the Swedish Meteorological and Hydrological Institute (SMHI). EC-Earth consists of the atmospheric component IFS (European Centre of Medium Range Forecast (ECMWF) Integrated Forecast System; ECMWF (2010)), the ocean component NEMO (Nucleus for European Modelling of the Ocean; (Madec and the NEMO team (2008))) and LIM (Louvain-la-Neuve sea Ice Model) as the sea ice component. LIM is embedded in NEMO and both are on the ORCA1 tripolar grid (1°x1° horizontal resolution). These components are coupled through the OASIS-3 coupler (Valcke (2013)).
EC-Earth can be used for a wide range of configurations. The simplest is the single-column model, which is used to study physical processes and their parameterizations. Focusing on a single column isolates the small-scale processes from the large-scale forcing. Single-column models can consists of a single model component (i.e. the atmosphere) or the fully coupled system (e.g. Hartung et al. (2018)). In addition to the single-column configuration, EC-Earth can be run as an atmosphere-only model (AGCM), an ocean-only model (OGCM) or a fully coupled climate model. Finally, EC-Earth can be run as an Earth System Model by adding atmospheric chemistry and aerosols, ocean-bio-geo-chemistry, dynamic vegetation and the Greenland Ice Sheet to the fully coupled system. EC-Earth-PISM is validated against the standard EC-Earth in Madsen et al. (2019, manuscript in preparation).
Changing the initial conditions, forcing and, if necessary the topography, EC-Earth can simulate present day climate as well as paleo climate and future climate. EC-Earth have been used for projecting future climate as part of the Coupled Model Intercomparison Project Phase 5 (CMIP5; Taylor et al. (2012)). In this project, up to 50 climate models from around the world are setup to run the same simulations with the same initial conditions and forcing files. These include a historical simulation and the four future RCP emission scenarios. Combining many different climate models lead to more robust results, as any shortcomings of the individual models are averaged out. The CMIP5 ensemble were used in the IPCC AR5 (IPCC (2013)) for the future climate projections and some of the key parameters are discussed in section 2.5.2.

In Manuscript III, EC-Earth is coupled to the interactive Parallel Ice Sheet Model (PISM; Albrecht et al. (2012)). This setup, EC-Earth-PISM, is described in the DMI report Svendsen et al. (2015). EC-Earth and PISM exchange relevant parameters after each modelled year. PISM sends fresh water input (melt, runoff, basal melt and calving), ice discharge, the land ice mask, and the ice sheet topography to EC-Earth. The land ice mask defines which grid cells are ice covered and which are not, hence determining which processes occur in each grid cell. Updating the land ice mask every time step allow for the ice sheet to change in size and extent. In the standard EC-Earth setup, the height and size of the GIS are predefined and cannot change during the simulation. The topographic changes of the ice sheet affect the surface pressure in EC-Earth. Having an interactive GIS allows for EC-Earth to capture the climatic responses to a shrinking GIS, for example by adding melt water to the ocean and by allowing for weather systems to pass over the lower GIS, not around it.

Two different versions of EC-Earth were used in this project. The RCP8.5 scenario simulation (Manuscript III) used EC-Earth V2.3. This older version consists of IFS cycle 31r1 with T159L62 ($\sim$ 125km horizontal resolution), NEMO2.0 (ORCA1, 42 vertical layers) and LIM2 (Fichefet and Maqueda (1997)). This EC-Earth version is part of the CMIP5 ensemble. EC-Earth V2.2 performs well compared to observations, although the Arctic is 2°C too cold in the twentieth century and there is too much sea ice, both in thickness and extent (Hazeleger et al. (2012), Sterl et al. (2012), Koenigk et al. (2013)). The version of EC-Earth used for Study III (i.e. EC-Earth-PISM) were coupled to the Ice Sheet Model PISM (horizontal resolution of 20km).
For the Barents-Kara study and the nudging study (Manuscripts II and I, respectively) EC-Earth V3.2 was used. It consists of IFS cycle 36r4 with a spectral resolution of T255 (equivalent to $\sim$80 km) and 91 vertical levels, NEMO3.6 (ORCA1, 75 vertical levels) and LIM3 with 5 ice thickness categories (Vancoppenolle et al. (2012)). The sea ice is divided into thickness categories to account for the subgrid-scale variations in ice thickness as ice behaves differently depending on its thickness (ridging/rafting, heat conduction etc.). V3.2 was briefly validated against ERA-Interim reanalysis data in Manuscript II, similar to the validation of V2.2 in Hazeleger et al. (2012). Overall, the temperature and mean sea level pressure biases were smaller and shifted toward positive values in V3.2 compared to V2.2. The temperature bias over the Arctic had shifted from being cold to a slightly less warm bias.

Chapter 5

Results

In the following are the results from the three original manuscripts presented.

5.1 Study I: Nudging sea ice in the coupled climate model EC-Earth

The following is a summary of the two nudging methods presented in Manuscript I. For the full description of the methods please see Manuscript I.

5.1.1 Method 1

Pushing the model toward a target sea ice cover required energy (ΔHF), either to melt sea ice or to cool the ocean to form sea ice. This energy was added to the SSHF (eq. 5.1), simulating a larger or smaller heat exchange between the atmosphere and the ocean, thus forcing the model to melt or form sea ice.

$$SSHF_{new} = SSHF + \Delta HF \tag{5.1}$$

Three parameters defined the magnitude and direction of ΔHF:

1. The size of the total heat flux received by the ocean $HF_{Total} = SWR + LWR + SLHF + SSHF$ where SWR was the Short Wave Radiation, LWR is Long Wave Radiation and SLHF is the Surface Latent Heat Flux.

2. The difference between the simulated SIC and the target SIC, $\Delta SIC = (SIC_{Model} - SIC_{Target})$. The larger the difference, the larger the nudging.

3. In the case where the model and the target SIC were opposing each other, e.g. forming sea ice in summer, an extra term $(-1) \cdot HF_{Total}$ was added. This term cancelled out the total heat flux received by the ocean, i.e. did not allow for energy to be added to the ocean in summer when the target was to form sea ice. If they were not opposing each other, this term was $0 \cdot HF_{Total} = 0$.

Combining these three terms gave the equation for ΔHF:

$$\Delta HF = ABS(HF_{Total}) \cdot \Delta SIC + \begin{Bmatrix} 0 \\ -1 \end{Bmatrix} \cdot HF_{Total} \tag{5.2}$$

Equations 5.1 and 5.2 were referred to as Method 1. In order for the model to form sea ice due to the target SIC, Method 1 send more energy from the ocean to the atmosphere, allowing the ocean to cool enough to form sea ice. The resultant increased energy in the atmosphere should be redistributed by the atmospheric component.

To test Method 1, a model simulation (M1) were nudged toward a target SIC of 100% covering the entire ocean north of 70°N. South of 70°N the target SIC was 0. Comparing to a control run with no nudging (CTRL) for one model year, Method 1 succeeded in melting sea ice south of 70°N and forming sea ice north of 70°N, close to the target SIC (fig. 5.1a). The associated ΔHF was on the order of 300-400Wm^{-2} above the ice-free areas targeting a full sea ice cover (fig. 5.1b). It appeared that melting sea ice required less energy than forming sea ice, illustrated by the two areas Baffin Bay and Barents Sea, respectively. This occurred as sea ice formation required the ocean had to cool to the freezing point first and then form sea ice. Melting sea ice only required receiving heat to increase the ice temperature until the melting point.
Forming sea ice in Barents Sea should be achieved by an increased SSHF from the ocean to the atmosphere. Therefore, an increase in the atmospheric temperature was expected. Similarly, a decrease in atmospheric temperature should be observed over Baffin Bay. This was not the case. The atmospheric temperature profiles for the first 6 time steps (2700s x 6 = 4.5 hours) revealed a warming of the lower atmosphere for both Barents Sea and Baffin Bay (fig.5.2a). This counter-intuitive behavior led us to check the energy balance, and Method 1 turned out not to be energy conserving after all. The reason for this was that SSHF only is a diagnostic variable, not a prognostic. Returning to the atmospheric module IFS, SSHF was computed for each time step and send to the ocean module NEMO. IFS did not use the SSHF it computed. The information equivalent to SSHF had been used indirectly already in IFS. Hence, modifying SSHF was not 'seen' by the atmosphere directly, only indirectly by the changes in the ice/ocean surface.

5.1.2 Method 2

Method 2 was based on Method 1. As revealed in Method 1, the atmosphere did not 'see' the change ΔHF added to SSHF. Redistributing ΔHF manually in the atmosphere to simulate the change in SSHF ensured that Method 2 was energy conserving. Redistributing the energy in the atmosphere was achieved by modifying the instantaneous total atmospheric energy E$_{tot}$ (eq. 5.3), where g was the gravitational acceleration, E_{kin} the kinetic energy, L the latent heat of vaporization, q_v the specific humidity, c_p the specific heat capacity at constant pressure, T temperature, z_s surface height, and p_s the surface pressure. As observed, modifying E_{tot} only changed the temperature T of the atmosphere (eq. 5.4).

$$E_{tot} = -\frac{1}{g}\int_{p_s}^{0} (E_{kin} + Lq_v + c_pT)\, dp + p_s z_s \tag{5.3}$$

$$\Delta E = \Delta HF = -\frac{1}{g}\sum_{klev=1}^{Nlev} c_p \Delta T_{klev} \Delta p_{klev} \tag{5.4}$$

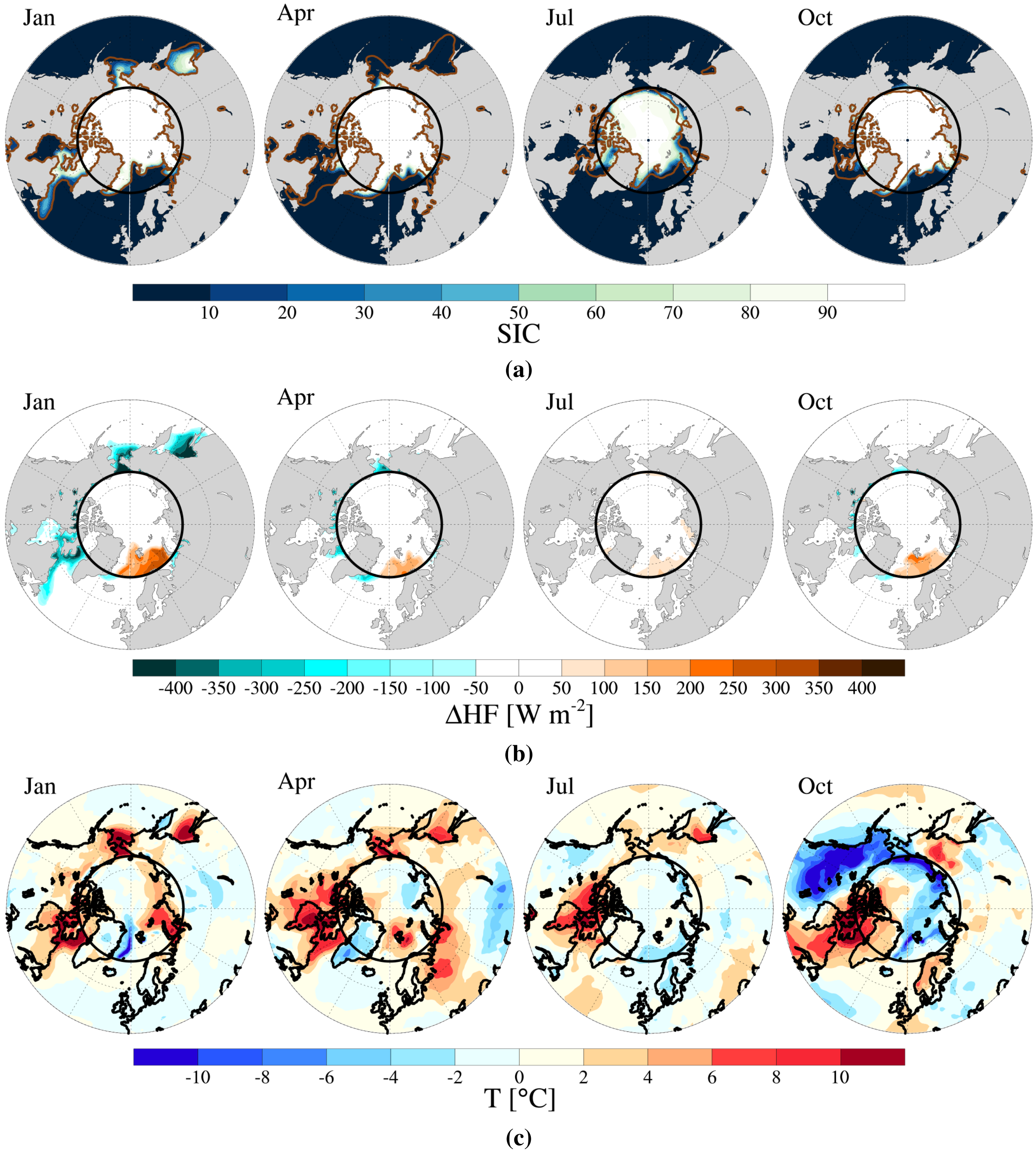

Figure 5.1: M1 monthly mean (a) sea ice concentration (in %), (b) ΔHF (in W m^{-2}) and (c) temperature anomaly (M1-CTRL; in °C)) for January, April, July and October. The dark brown line in (a) indicate the climatological sea ice edge (SIC>=15%) from CTRL. Black line indicate the target sea ice edge.

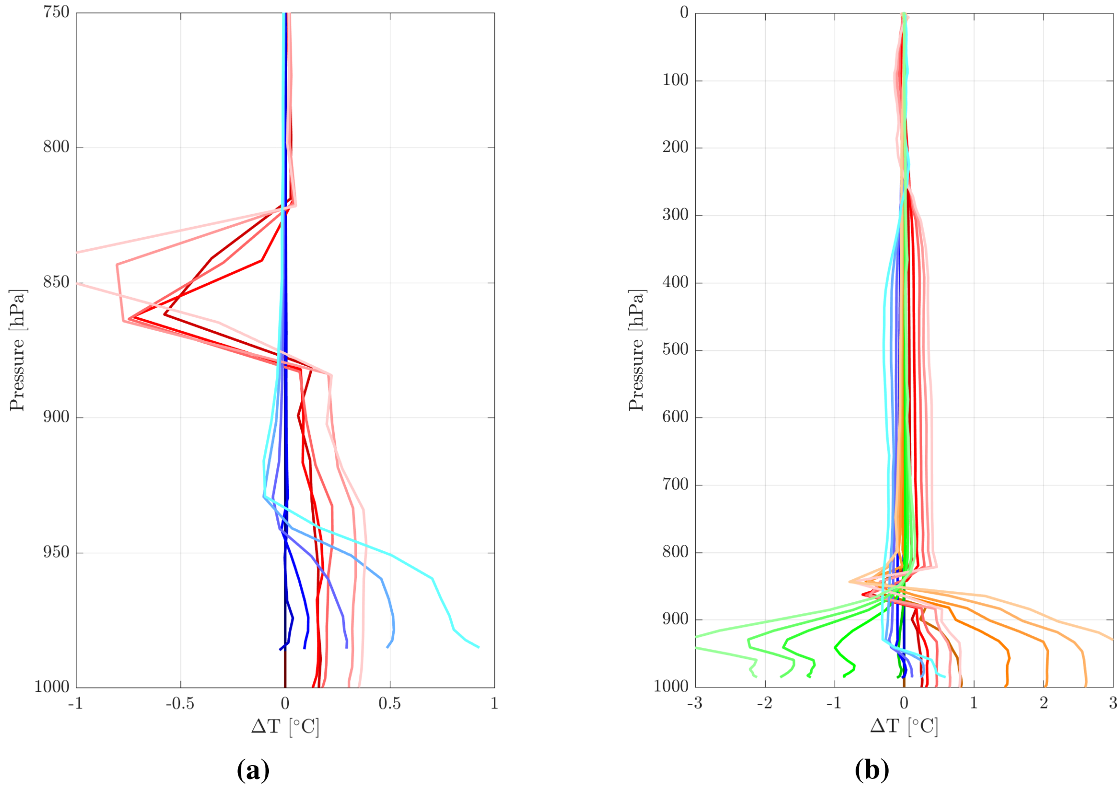

Figure 5.2: (a) Temperature anomaly (M1-CTRL; in °C) at each model level for the first 6 time steps at single grid point in the Barents Sea (red and orange) and Baffin Bay (blue and green). The lighter the color, the later in the simulation. (b) The same but for (M2-CTRL). ΔHF is either distributed in the entire air column (red and blue) or only in the bottom 700 hPa (orange and green). Please note the different y-axis.

p_{klev} was the pressure at each model layer and $Nlev$ was the total number of vertical layers. Defining the $\Delta T = A \cdot T_{prof}$ as the product of a vertical profile (T_{prof}) and an amplitude A, eq. 5.4 was rewritten (eq. 5.5), with the amplitude A given in eq. 5.6.

$$\Delta HF = -\frac{1}{g}\sum_{klev=1}^{Nlev} c_p A T_{prof}(klev)\Delta p(klev) = -\frac{1}{g} A c_p \sum_{klev=1}^{Nlev} T_{prof}(klev)\Delta p(klev) \tag{5.5}$$

$$A = -\frac{g\Delta HF}{c_p \sum_{klev=1}^{Nlev}(T_{prof}(klev)\Delta p(klev))} \tag{5.6}$$

In the following, a predetermined profile $T_{prof} = \frac{1}{1+exp(-x)}$) was used to avoid any sharp transitions between layers. As SSHF was send to the ocean at the end of each time step, the redistribution of the ΔHF was done by updating the air temperature at the beginning of the following time step (eq. 5.7).

$$\frac{dT}{dt} = \frac{dT}{dt} + \Delta T \tag{5.7}$$

Using the same experimental setup as for M1 but using Method 2 (experiment referred to as M2), the effect of the energy conservation was clear. Two experiments were performed, the main M2

where ΔHF was distributed through the entire atmospheric column, and M2_{700hPa} where ΔHF was distributed only in the lower atmosphere, up to 700 hPa. The reason for the latter was to simulate the real world as close as possible, where the surface heat flux would only be felt by the lower part of the atmosphere.
M2 succeeded in forming sea ice in Barents Sea to about the same extent as for M1 (fig. 5.3a). It also succeeded in melting sea ice south of 70°N. As the atmosphere now received the ΔHF, an increase in surface temperature was expected above Barents Sea and a decrease in temperature over Baffin Bay. This was observed for January and February when looking at the monthly mean surface temperatures (fig. 5.3b). For the following months, the air temperature seemed to depend more on whether the target sea ice cover was reached. The temperature changes ranged between ± 10°C. Focusing on the first 4.5 hours, the air temperature above the Barents Sea increased by approximately 1°C and by less than 1°C over Baffin Bay. The temperature decreased higher up in the atmosphere (fig. 5.2b). For M2_{700hPa} it was clear that the extra energy was added/removed from the bottom of the atmosphere. Above the Barents Sea, the temperature increased to approximately 4.6°C in the first day. Above Baffin Bay, the temperature decreased more than 7°C during the same time. By redistributing ΔHF in the entire atmospheric column (M2), the target sea ice cover was almost reached. Moreover, the air temperature did not become too unrealistic, as for M_{700hPa}. However, the model crashed after the first model year due to instabilities. While using weaker nudging allowed the model to run for longer, it prevented reaching the sea ice target. This showed that M2 required a fine balance between reaching the sea ice target and avoiding instabilities.
As Method 2 should work for a variety of sea ice targets, a larger sea ice target was tried. Experiment M2_{50N} had a target SIC = 100% down to 50°N (area shown in figure 5.3). The surface temperature anomaly and SIC for the second modeled year showed that the atmosphere heated up so much (more than 10°C almost everywhere), that it counteracted the effort to form sea ice (fig. 5.3).
Thus, Method 2 worked for some sea ice targets close to the observed sea ice cover and for shorter time periods. However, it was a very fine balance between reaching the target sea ice cover and avoiding model instabilities.

To sum up, Method 1 succeeded in reaching a sea ice cover close to the target. This method was not energy conserving, but it conserved water. Method 2 was conserving energy, but turned out not to be usable, as the model became unstable and crashed. Therefore, Method 1 seemed to be the more reliable method of the two.
NEMO does not receive the sensible heat flux separately, but the sum of the long wave radiation, latent and sensible heat fluxes. This is referred to as the non-solar radiation flux, and is the same parameter used by Oudar et al. (2017) to perturb sea ice indirectly. Thus, our Method 1 is very similar to the flux adjustment in Oudar et al. (2017), only differing in the method used for computing the magnitude of ΔHF.

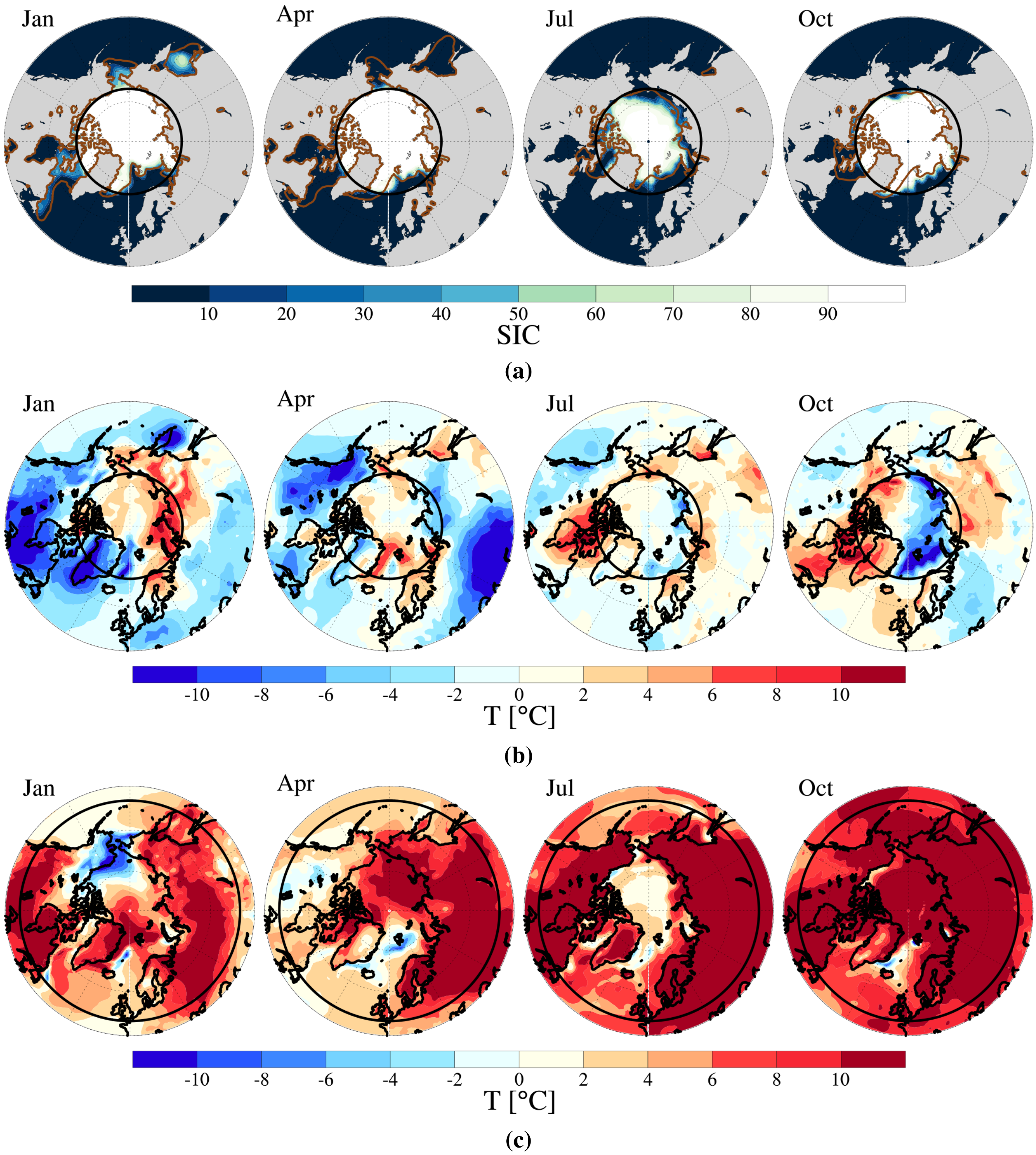

Figure 5.3: M2 monthly mean (a) sea ice concentration (in %) and (b) temperature anomaly (in °C) for (M2-CTRL) and for (c) ($M2_{50N}$-CTRL) for January, April, July and October. (a) and (b) are from the first model year, (c) is for the second model year. The dark brown line in (a) indicate the climatological sea ice edge (SIC>=15%) from CTRL. Black line indicate the target sea ice edge.

5.2 Study II: Barents-Kara sea ice and European winters in EC-Earth

This chapter summarizes the experimental setup and the results from Manuscript II.

5.2.1 Experimental design

To investigate the impact of sea ice loss in BAKA, five model simulations were performed. These all originated from the same initial conditions, taken from a freely running model simulation (CFree). All five perturbation experiments were 100 years long, only differing in their amount of sea ice in BAKA (black box in figure 5.4(a)). Each model simulation was nudged toward a certain percentage in SIC, relative to the climatology of CFree. C100 was the control run, with sea ice concentration (SIC) in BAKA nudged toward 100% of CFree SIC climatology. The remaining four perturbed experiments were C80, C60, C40 and C20, with BAKA SIC nudged toward 80%, 60%, 40% and 20% of CFree SIC climatology, respectively. Nudging was performed year-round; in November-April toward the designated SIC percentage and in May-October toward 100% of CFree SIC climatology. Method 1 was used to constrain sea ice, discussed in section 5.1.1. Results are shown for the three winter subseasons December-January (DJ; early winter), January-February (JF; mid winter) and February-March (FM; late winter).

5.2.2 Results

Mean responses

Reducing BAKA sea ice modified the mid winter mean surface (2m) air temperature, as shown in figure 5.4. Relative to the control simulation (C100, fig. 5.4(a)), the mean surface temperature increased by more than 1°C over the perturbed region as well as over large parts of Eurasia and the Arctic. Focusing on Europe, a non-linear temperature response was associated with the linear SIC reduction going from C80 to C20: minor BAKA sea ice reductions showed no statistically significant change in temperatures over Europe (C80, fig. 5.4(b)), moderate reductions showed significant cooling over a small area over eastern Europe (C60; fig. 5.4(c)) and major reductions (C40 and C20, fig. 5.4(d) and 5.4(e)) showed a statistically significant warming over Europe. Averaging the temperature over two regions of Europe (Europe (EU) and Central Europe (CEU), see regions in figure 5.4(a)), the significant cooling observed in C60 disappeared (fig. 5.5). The average temperature was lower in C60 for both areas, but not significantly lower. Only the warming in C20 and C40 was significantly different from C100. However, the temperature difference between C60 and C40 (i.e. minimum and maximum) was significantly different. This pattern was seen for all three winter subseasons.

The associated mean circulation responses shown in figure 5.6 did not indicate the same non-linearity. Instead, they revealed an increasing low mean sea level pressure (MSLP) anomaly over the perturbed region relative to C100, going from C80 to C20, saturating around C40. This low pressure anomaly was consistent with a 'heat low', caused by the increased upward surface heat flux from the larger area of open ocean. The intensification of the low pressure anomaly occurred in mid and late winter, illustrated by the root-mean-square-error (RMSE) of the MSLP response relative to C100 (fig. 5.7). The RMSE was computed for the area North of 50°N.

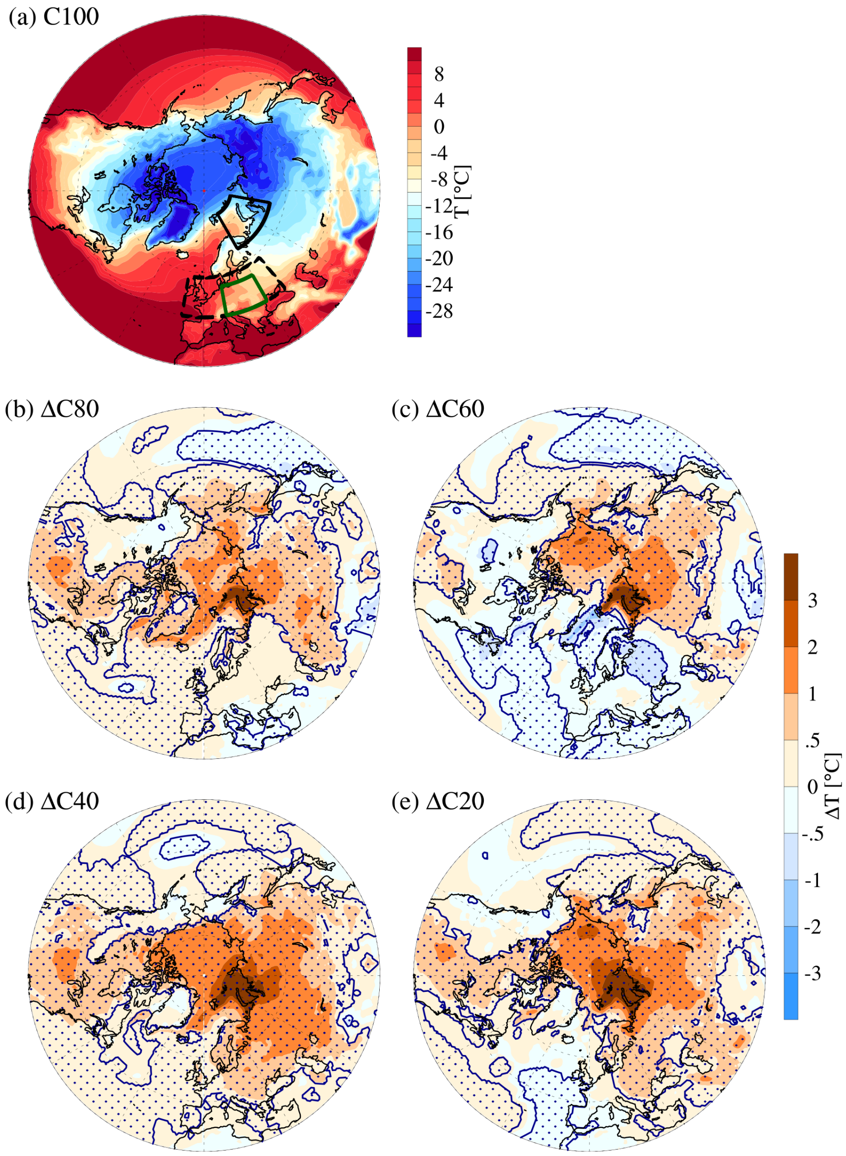

Figure 5.4: (a) Mid winter (JF) mean absolute surface (2m) air temperature (in °C) for C100. The difference in mean JF surface air temperature for (b) ΔC80, (c) ΔC60, (d) ΔC40 and (e) ΔC20. Black box indicates BAKA region [30-80°E, 65-80°N], black dashed box indicates Central Europe (CEU) region [-10°E-40°E, 45°N-58°N] (Screen et al. (2015a)) and green box indicates EU region [10°E-30°E, 45°N-55°N] (Petoukhov and Semenov (2010)).

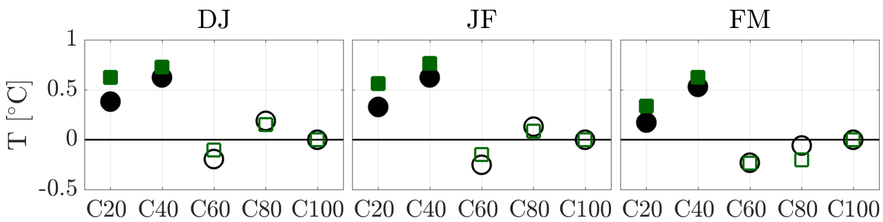

Figure 5.5: The area mean of the 100-year mean surface air temperature anomaly (in °C) for two areas over Europe for each of the five perturbed simulations. The two regions CEU (black circles) and EU (green squares) are shown in figure 5.4(a). Filled markers indicate temperatures significantly different from C100 at a 5% level. The temperature difference between C60 and C40 (i.e. minimum and maximum) is significantly different at a 5% level for both EU and CEU for all three subseasons.

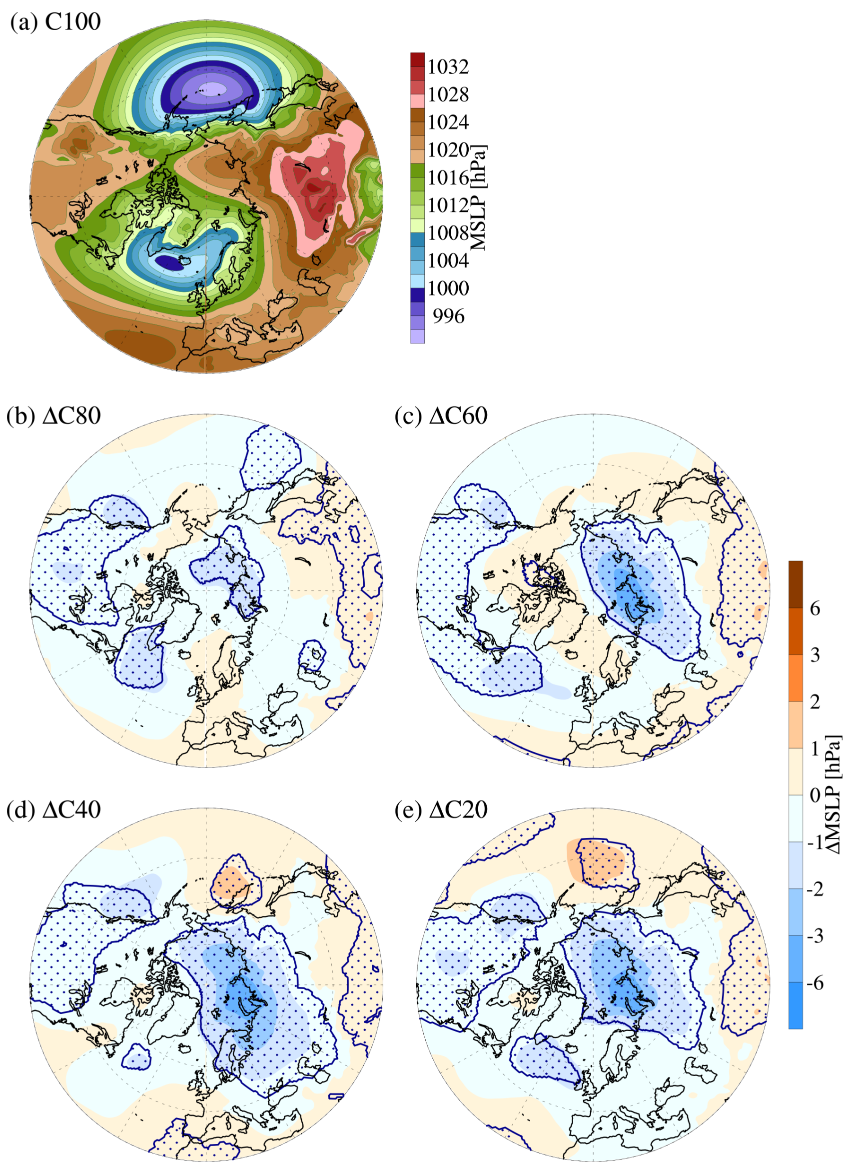

Figure 5.6: (a) Mid winter (JF) mean absolute mean sea level pressure (in hPa) for C100. The difference compared to C100 for (b) ΔC80, (c) ΔC60, (d) ΔC40 and (e) ΔC20. Dots indicate significance at 5% level.

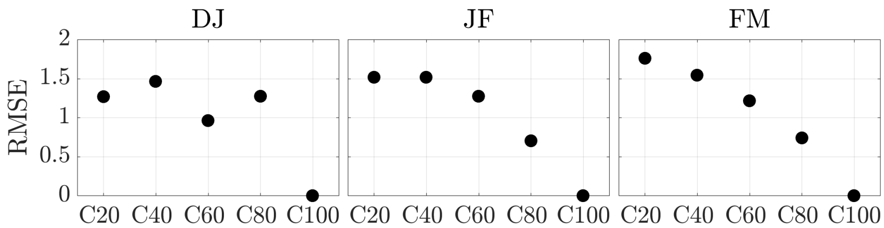

Figure 5.7: The root-mean-square-error (RMSE) of the mean sea level pressure (in hPa) for each perturbed experiment relative to C100. RMSE was computed for the area North of 50°N.

Abnormally cold European winters

As the focus in Study II was the coldest winters, analyzing 100-year mean winter responses were not the best indicator. Therefore, the 5% coldest mid winters in each grid cell were investigated (figure 6 in Manuscript II). The surface temperature pattern was similar to that of fig. 5.4, although less coherent patches. The area averaged temperature response were not statistically significant different from C100 in any of the four perturbed simulations for neither CEU nor EU (black circles and green squares in fig. 5.8). This patchy pattern arose since the 5% coldest winters in one grid point not necessarily coincided with the 5% coldest winters in the neighboring grid point. This was illustrated by figure 8 in Manuscript II: here, the number of the winter month with the coldest temperature occurring during the 100-year C60 simulation in each grid cell was shown (i.e. chronologically lining up 4 winter months each year for 100 years = 400 months). Larger coherent areas were evident, but proceeding to the second coldest winter month, the coherent areas disappeared (not shown). Continuing to the 5% coldest winters only worsened the picture. In order to associate certain circulation patterns with the European temperature patterns, the 5% coldest winters averaged over CEU were used instead.

Focusing on Europe, the composite of the 5% coldest winters for CEU were created. The composites for C20 to C80 are shown relative to the cold composite for C100 in figures 5.9(b)-(e). The composite for C100 (fig. 5.9(a)) showed cold temperatures over Europe, as expected since the composites were created based on this. Looking at the four reduced SIC simulations, they all exhibited a similar cooling over Europe in early and mid winter (>1°C), as well as a warming over the Arctic throughout the winter (fig. 5.9(b)-(e)). The cooling for the four perturbed experiments were not significantly different from that of C100 (blue circles in figure 5.8). However, the temperature differences between C80 and C40 (i.e. minimum and maximum) were statistically significant for JF and FM for EU, but not for CEU.
The associated circulation responses are shown for the same cold winter months in figure 5.10. The cold winters over Europe were associated with a high pressure system over Scandinavia, the Scandinavian pattern (fig. 5.10(a)). Reducing BAKA SIC increasingly expanded this high pressure anomaly, creating an increasingly stronger Scandinavian pattern. This indicated that sustaining cold European winters with decreasing BAKA sea ice required increasingly stronger positive MSLP anomalies and associated stronger easterlies. The intensification of the Scandinavian pattern was quantified in figure 5.11 by projecting the MSLP pattern for each of the four sea ice reduced experiments onto C100 (eq. 5.8).

$$P = \frac{\sum_{\phi}\sum_{\lambda}(\Delta MSLP_{C80} \cdot \Delta MSLP_{C100} \cdot \cos\phi\Delta\phi\Delta\lambda)}{\sum_{\phi}\sum_{\lambda}(\Delta MSLP_{C100} \cdot \Delta MSLP_{C100} \cdot \cos\phi\Delta\phi\Delta\lambda)} \tag{5.8}$$

where, λ and ϕ are the longitudinal and latitudinal coordinates, $\Delta MSLP$ is the temporal mean of the detrended MSLP anomaly (i.e. fig. 5.10). The sum is taken over the green box in figure 5.10. Similar to the mean response, this seemed to saturate around C40.

Comparing the mean responses to the coldest winter composites showed important differences: where the mean response showed a non-linear temperature response, implying that moderate BAKA sea ice reductions were linked to cooling over Europe, this was not seen for the coldest winters. Here, the response seemed to be more linear, with an intensification of the Scandinavian pattern.

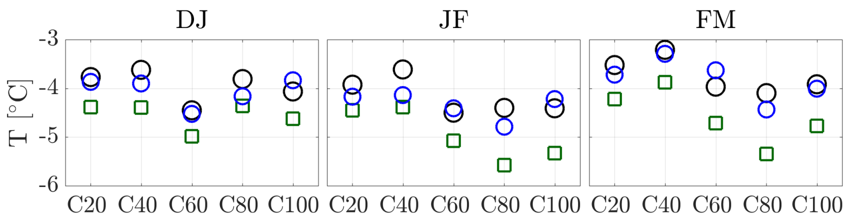

Figure 5.8: The area mean surface air temperature (in °C) of the 5% coldest winter months in each grid cell (black circles (CEU) and green squares (EU)) and the mean of the 5% coldest winter months in CEU (blue circles). None of the perturbed simulations are significantly different from C100 at a 5% level, but the temperature difference between C80 and C40 is significantly different in JF and FM for EU.

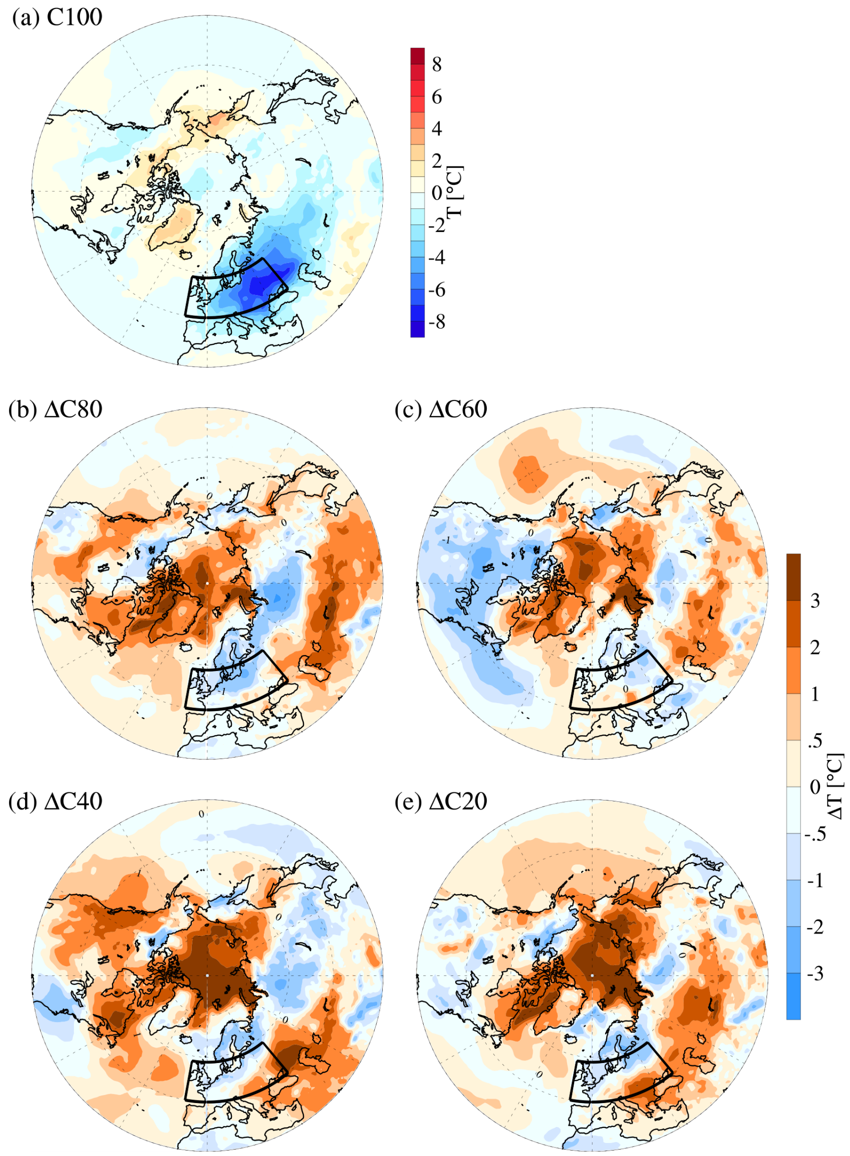

Figure 5.9: Mid winter (JF) composite of the surface air temperature (in °C) for the 5% coldest winters in CEU (black box). (a) Temperature difference in C100 ($T_{C100} - T_{C100,clim}$) and the response as changes of anomalies in (b) ΔC80, (c) ΔC60, (d) ΔC40 and (e) ΔC20.

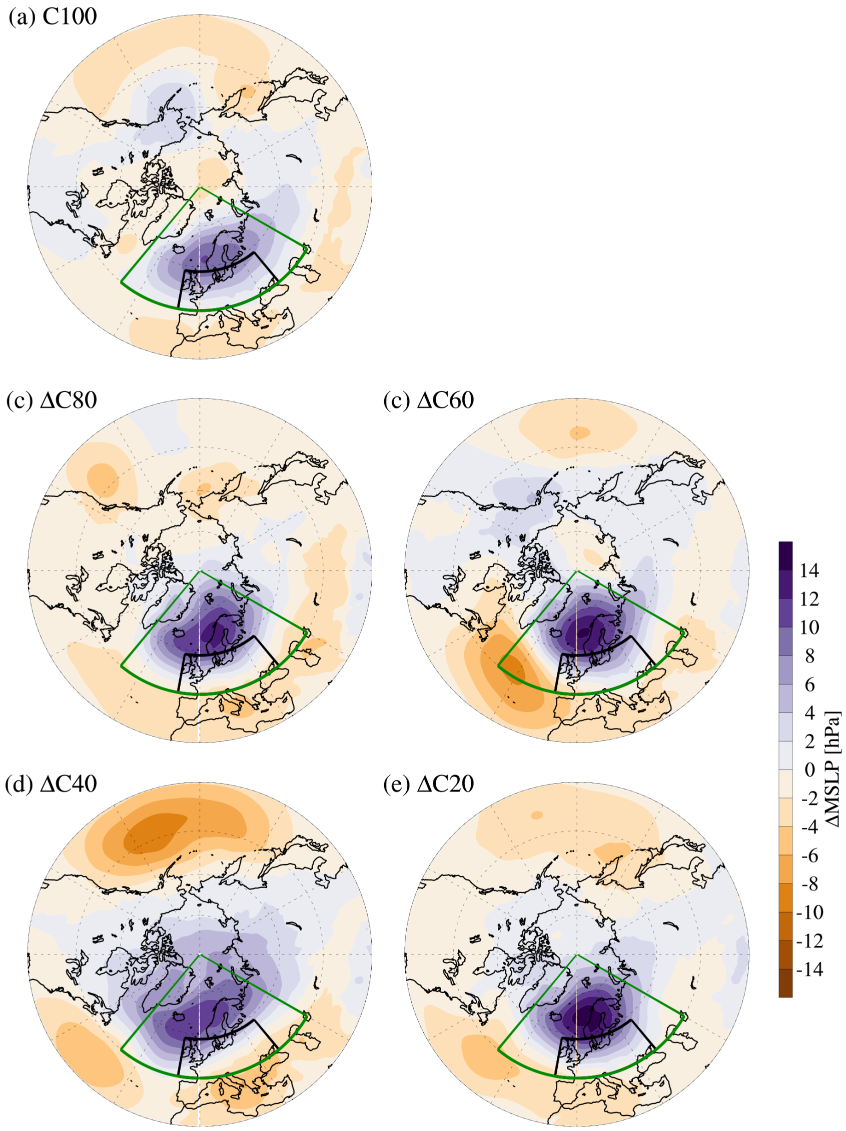

Figure 5.10: Mid winter (JF) composite of mean sea level pressure (in hPa) difference wrt the climatology of C100 for the 5% coldest winters in CEU (black box) for a) C100, (b) C80, (c) C60, (d) C40 and (e) C20. Green box indicate the region used to compute P in figure 5.11 [40°W-60°E, 45°N-90°N]. Black box indicate CEU.

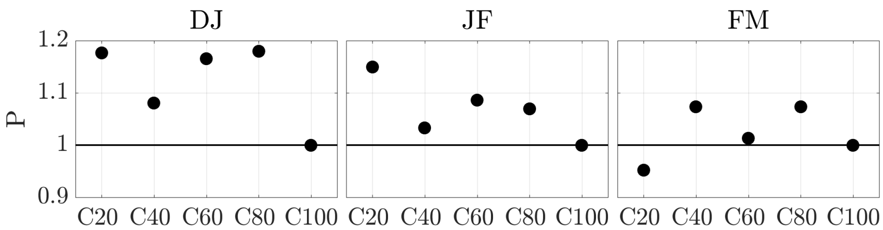

Figure 5.11: P of the sea ice reduced MSLP patterns relative to the C100 MSLP pattern in fig. 5.10(a). P is unitless. The method for computing P is shown in eq. 5.8. P=1 indicate that the Scandinavian pattern in C20 to C80 is equal to the one in C100. P>1 indicate a stronger Scandinavian pattern relative to C100, and P<1 indicate a weaker Scandinavian pattern.

5.3 Study III: Climate change associated with sea ice loss in extended EC-Earth-PISM RCP8.5 simulation

5.3.1 Experimental design

Manuscript III was based on a 1350 year long simulation, consisting of a historical simulation from 1850 to 2005, followed by the RCP8.5 future emission scenario from 2006 to 3200. The overall evolution of this RCP8.5 simulation was briefly discussed in section 2.5.3. The focus of Study III was on the shifts in sea ice states and how these affected the climate. To investigate this, five periods were chosen, each 30 years long: the pre-industrial period (P1, 1850-1879), present day (P2, 1976-2005), just after the Arctic summer sea ice disappears (P3, 2060-2089), just after the Arctic winter sea ice disappears (P4, 2154-2183) and the end of the simulation when the GIS had lost roughly 2/3 of its volume (P5, 3170-3200). The five periods are shown in figure 2.12. Results are shown as responses relative to the pre-industrial period and have been detrended, unless otherwise stated.

5.3.2 Results

The overall evolution of the RCP8.5 simulation was briefly discussed in section 2.5.3. Manuscript III is still ongoing work, as additional analyzes are required. The results presented below are therefore the preliminary results from Manuscript III.

Changes to the atmospheric surface climate

The detrended surface (2m) air temperature were patterned scaled by dividing it with the global mean temperature anomaly relative to P1 (fig. 5.12). This eliminated the overall warming signal from the global temperature increase and revealed spatial differences. The most pronounced change was the Arctic Amplification (AA), where the Arctic temperature increase was larger than the global temperature increase. This was more proninced when computing the AA index $((\overline{T_{Arc}^{P2}} - \overline{T_{Arc}^{P1}})/(\overline{T_{Glo}^{P2}} - \overline{T_{Glo}^{P1}}))$ in figure 5.14. AA was strongest for P2, while sea ice still existed in in the Arctic Ocean. After this, AA gradually weakened as the Arctic gradually became ice-free year round. The AA persisted throughout the simulation, despite a thousand years of ice-free Arctic Ocean.

The rising global temperature changed the temperature variability, here represented by the standard deviation (SD) in figure 5.13. The SD was projected to decrease at high latitudes and increase over low and mid latitudes. The high latitude decrease in SD was mostly confined to areas formerly covered by sea ice, as the air temperature over sea ice can become much lower than over the open ocean. The decrease in SD over high latitudes and increase over low and mid latitudes affected the extreme temperatures as well. The extreme temperatures were investigated for four specific regions (regions shown in figure 5.15a) and represented by the 5th and 95th percentile temperatures in figure 5.15b. The coldest and warmest temperatures over Greenland were converging, whereas they were diverging for Southeast Asia and South America. This indicated less extreme temperature events for Greenland and more extreme events for Southeast Asia and South America. The extreme temperatures over Central Europe (CEU) did not change substantially as the Arctic sea ice disappeared (P1 to P3), only afterwards (P4 and P5) was there a tendency for less extreme winter temperatures and more extreme summer temperatures. Overall, there appeared to be a shift in the

extreme temperatures after P3, i.e. when the Arctic Ocean transitioned from a perennial sea ice cover to a seasonal sea ice cover. The projected changes for the pattern scaled precipitation patterns were similar to those of the CMIP5 ensemble: wet-got-wetter, dry-got-drier and the variability of the precipitation increased for wet areas and decreased for dry areas (see figures 5.16 and 5.17 as well as figure 2.11(b) for the CMIP5 projected precipitation changes). In addition to this overall pattern, the RCP8.5 simulation projected a drier Europe in summer and a drier Amazon in autumn as the Arctic sea ice disappeared. The latter would have a large impact on the Equatorial rain forest. A sharpening in precipitation around Equator was indicated in figure 5.16, illustrated clearer by the zonal area-integrated precipitation in figure 5.18a. Here, the intensification in precipitation around Equator and the decline in precipitation on the poleward flanks were evident. This sharpening around Equator also indicated an equatorward shift of the Intertropical Convergence Zone (ITCZ). To investigate this potential equatorward shift of the ITCZ, two parameters for the location of the ITCZ were used: the latitude of the maximum precipitation (ϕ_{max}) and the precipitation centroid (ϕ_{cent}) (Frierson and Hwang (2012), Adam et al. (2016)). The latter was the latitude where equal amounts of precipitation fell to the north and to the south. In figure 5.18a, ϕ_{max} and ϕ_{cent} appeared to both converge toward each other and toward Equator. This convergence going from P1 to P5 was clearer in figure 5.18b, showing ϕ_{max} and ϕ_{cent} for each time period.
Changes to the extreme precipitation for Greenland, CEU, South America and Southeast Asia generally revealed an increase in extreme precipitation, both for high and low precipitation (fig. 5.19). This was especially clear for Southeast Asia.

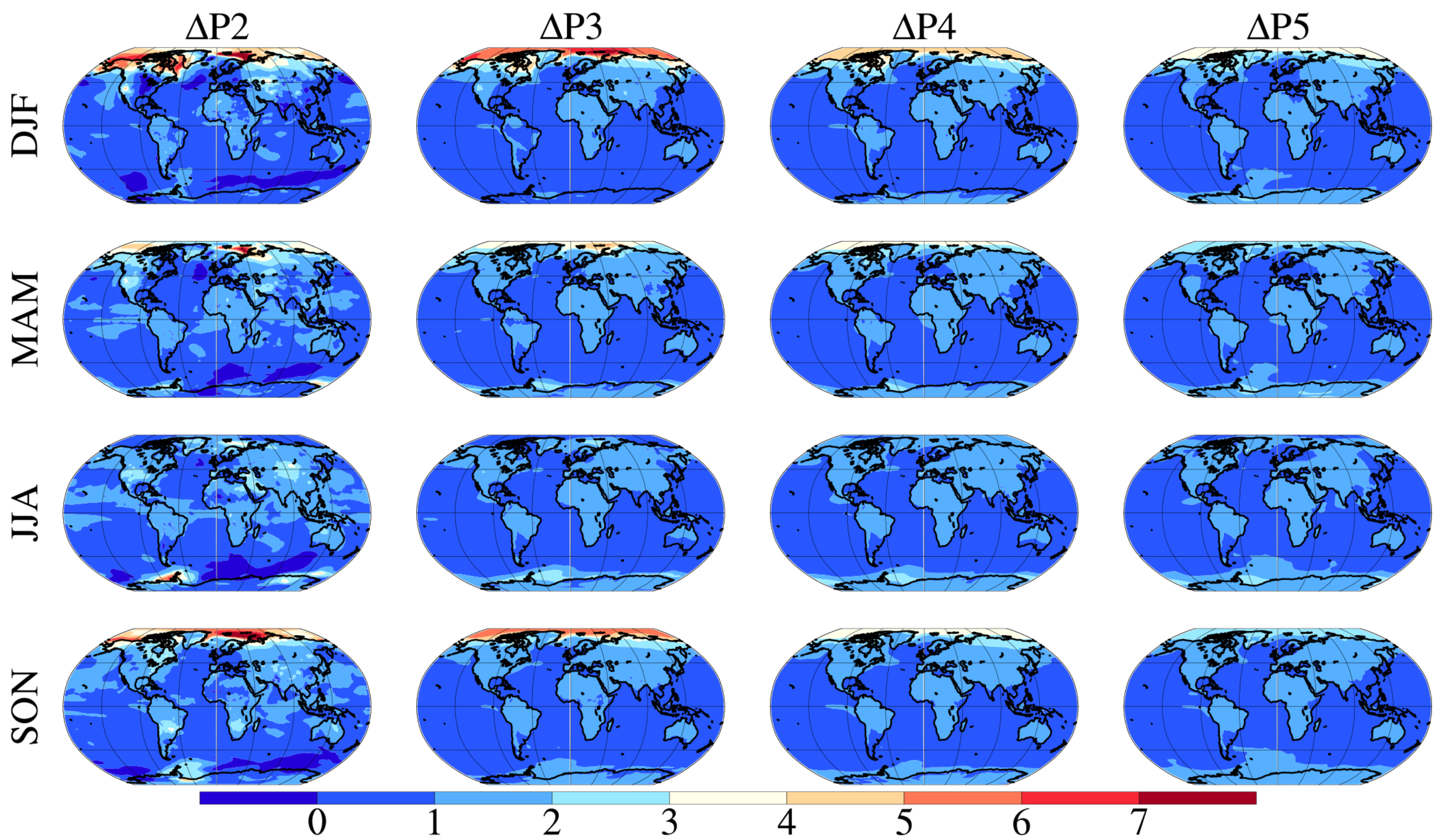

Figure 5.12: Pattern scaled surface air temperature (in °C/°C) for each season (rows) and each time period relative to P1 (columns).

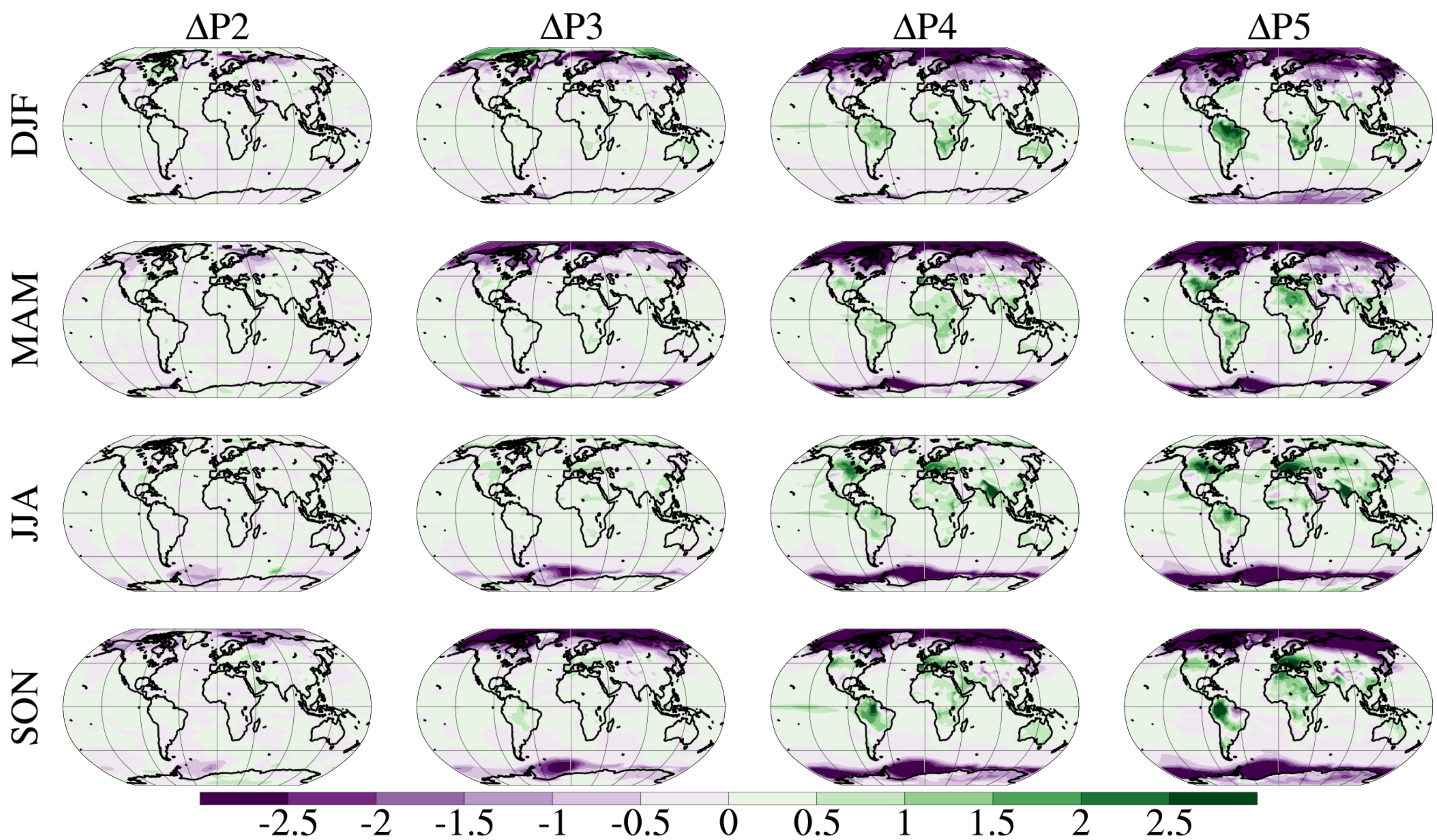

Figure 5.13: Standard deviation difference of the detrended surface air temperatures (in °C) for P2 to P5, relative to P1, for each season (rows) and each time period relative to P1 (columns).

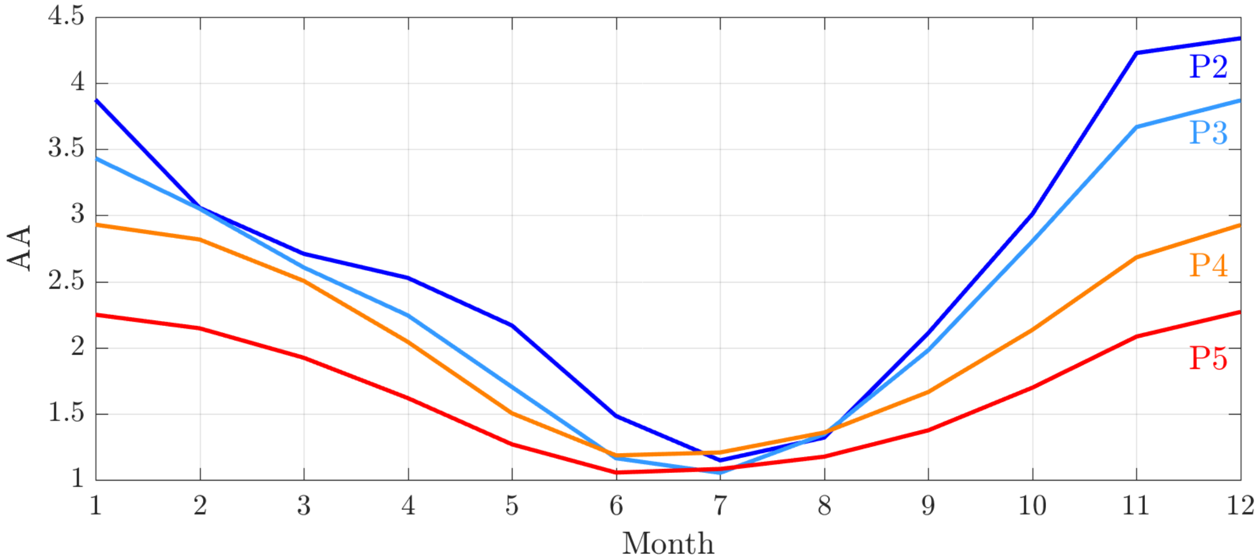

Figure 5.14: Arctic amplification, relative to P1 (1850-1879) for P2 (dark blue), P3 (light blue), P4 (orange) and P5 (red). AA is computed as: $(\overline{T^{P2}_{Arc}} - \overline{T^{P1}_{Arc}})/(\overline{T^{P2}_{Glo}} - \overline{T^{P1}_{Glo}})$.

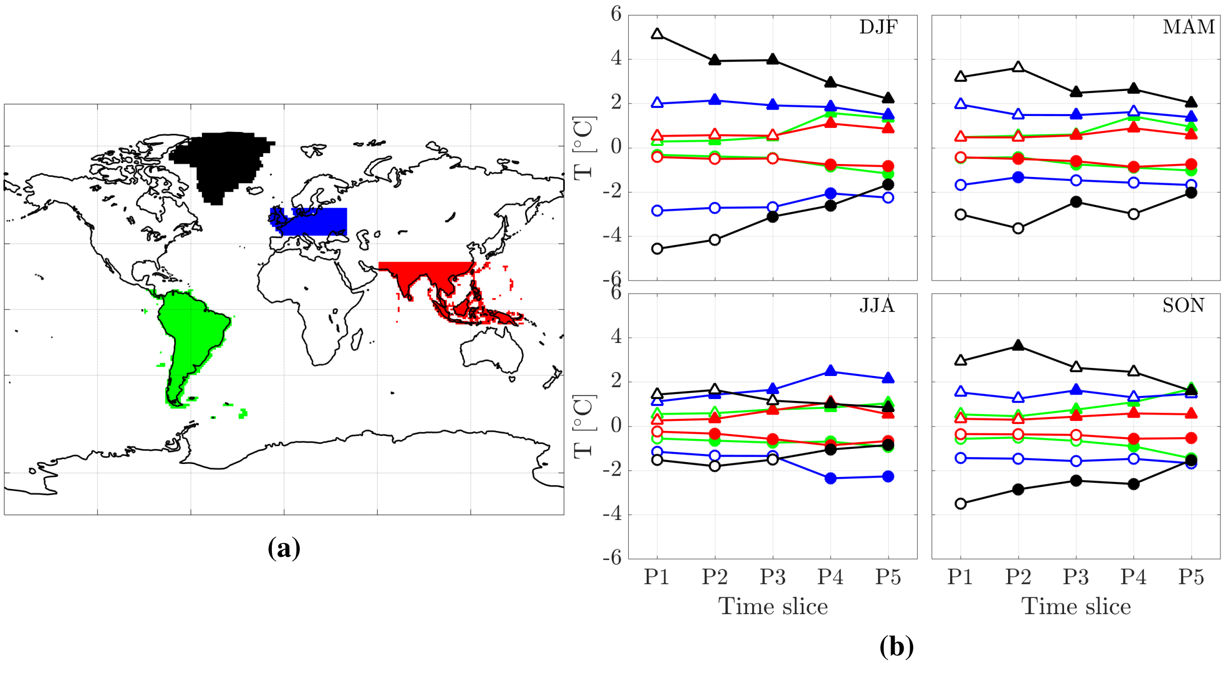

Figure 5.15: (a) Map showing the four areas Greenland (black), Europe (blue), Southeast Asia (red) and South America (green). (b) The 5th (circles) and 95th (triangles) percentiles of the area mean detrended seasonal temperature (90 months). Colors correspond to areas in (a).

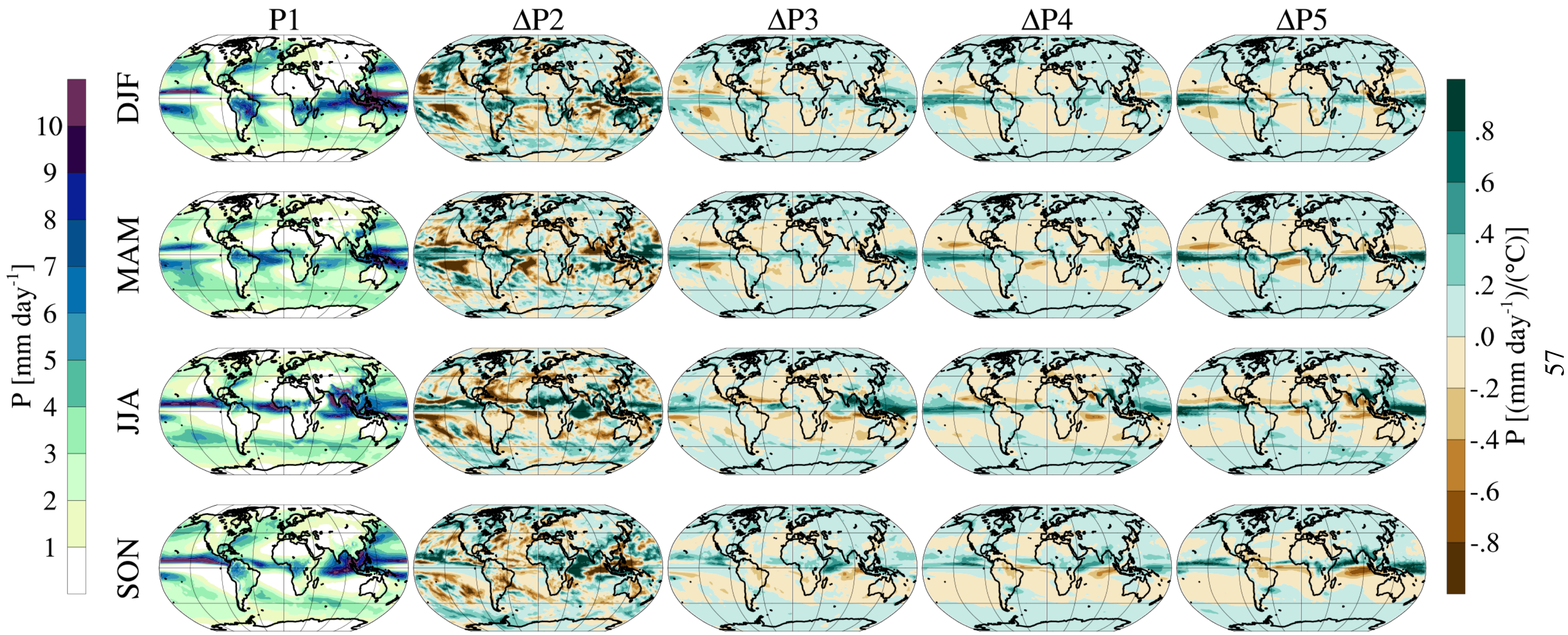

Figure 5.16: Absolute precipitation for P1 (in mm day^{-1}) (left column) and the pattern scaled precipitation (in (mm day^{-1})/(°C)) for P2 to P5 and for each season (four right columns).

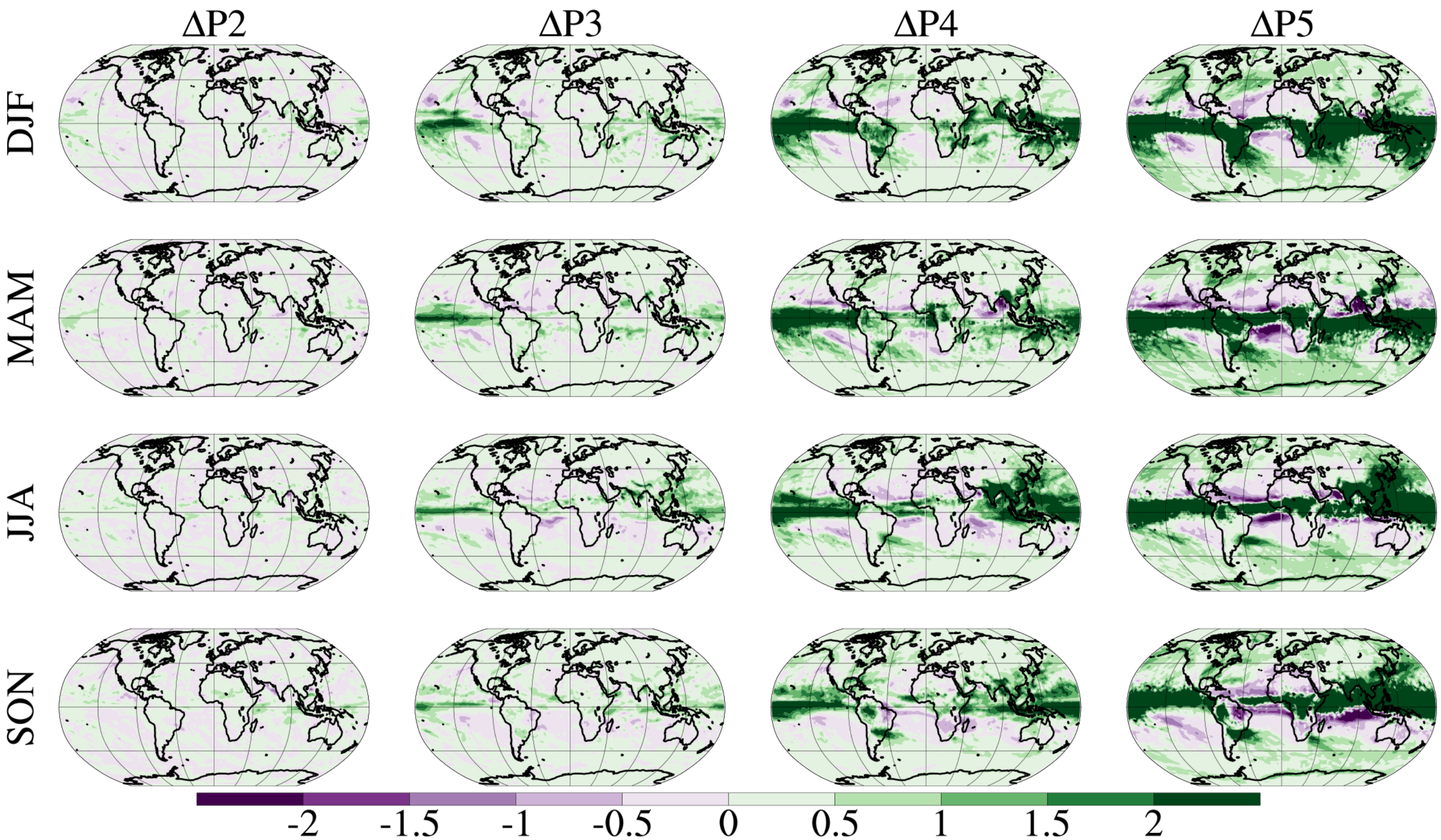

Figure 5.17: Standard deviation difference of the detrended precipitation (in mm day^{-1}) for P2 to P5, relative to P1, for each season (rows) and each time period relative to P1 (columns).

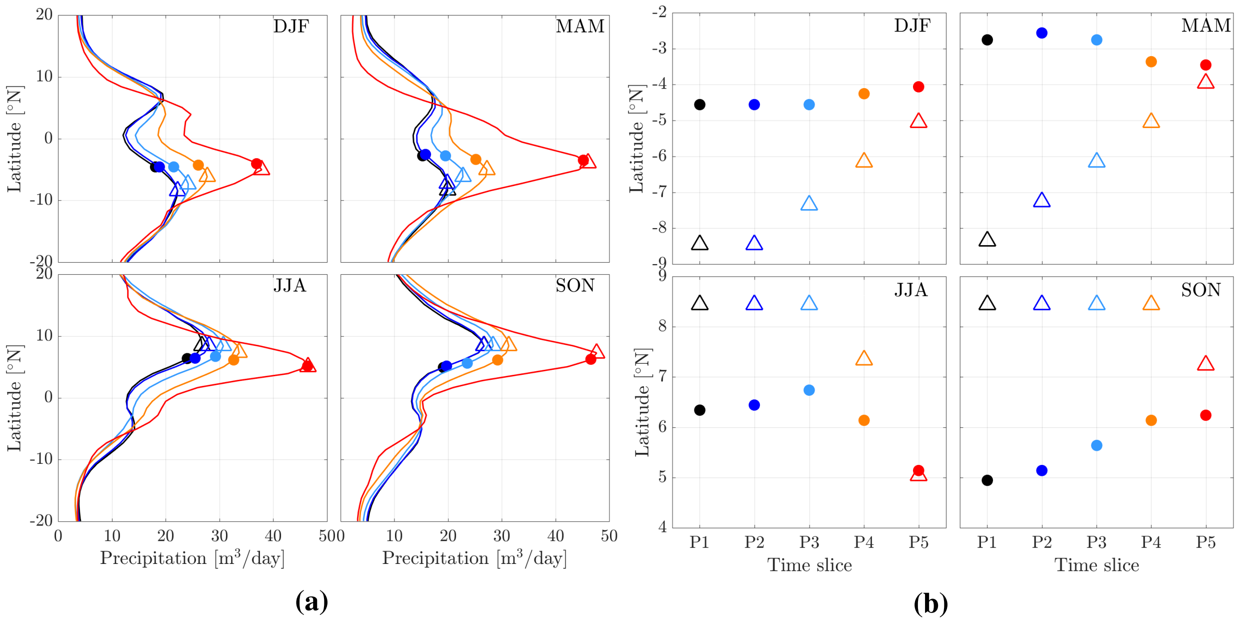

Figure 5.18: (a) Zonal area-integrated detrended precipitation. Circles show the latitude of the precipitation centroid (ϕ_{cent}, latitude of the median precipitation) and triangles show the latitude of the maximum precipitation (ϕ_{max}). (b) The latitude of the precipitation centroid (ϕ_{cent}, circle) and maximum precipitation (ϕ_{max}, triangles) for each time slice.

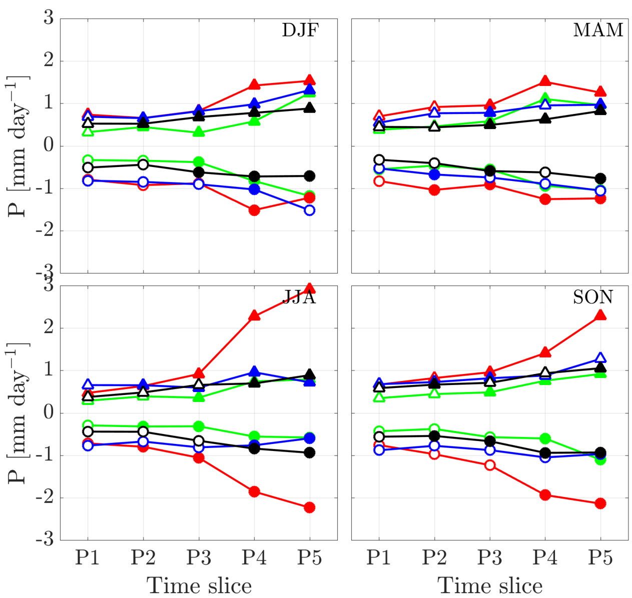

Figure 5.19: The 5th (circles) and 95th (triangles) percentile of the area mean detrended seasonal precipitation (in mm day^{-1}). Colors correspond to areas in fig. 5.15a.

Changes to the atmospheric circulation

The mean sea level pressure (MSLP) changes for P2 to P5 relative to P1 are shown in figure 5.20. Going from P1 to P5, the changes revealed a linear intensification of the Aleutian Low in winter and spring. In autumn, the low pressure anomaly over the Central Arctic intensified, together with and increase in MSLP north of the Azores High. This partially resembles a positive AO. A positive AO is associated with a stronger jet stream, stronger westerlies and a warmer and wetter Northern Europe.

The detrended MSLP variability changes going from P1 to P5 revealed an increase in SD over northern mid and high latitudes and a decrease in SD over southern mid and high latitudes. The changes were most pronounced for P4 and P5. An exception to this was over Europe, where the SD were projected to decrease in autumn and winter.

Atmospheric circulation can also be illustrated by the streamfunction (ψ). This is defined in equation 5.9:

$$g\frac{\partial \psi_p}{\partial p} = \bar{v}^{\lambda} 2\pi a \cos\phi \tag{5.9}$$

where g is the gravitational acceleration, p is the pressure, v is the zonal mean of the meridional velocity and ϕ is the latitude. The streamfunction for winter and summer showed the two Hadley Cells (the strongest one located in the winter hemisphere) and the two weaker Ferrel Cells (fig. 5.21). The strongest Hadley Cell had a rising branch in the tropics in the summer hemisphere and a sinking branch in the subtropics in the winter hemisphere. Going from P1 to P5, this Hadley Cell weakens (from 200×10^9kg s^{-1} to $\sim$$170\times10^9$kg s^{-1} in winter and from 240×10^9kg s^{-1} to $\sim$$200\times10^9$kg s^{-1} in summer). The rising branch appeared to be displaced toward equator, becoming slimmer, whereas the sinking branch appeared to widen toward the poles. A poleward displacement of the Ferrel Cells were associated with the loss of sea ice.

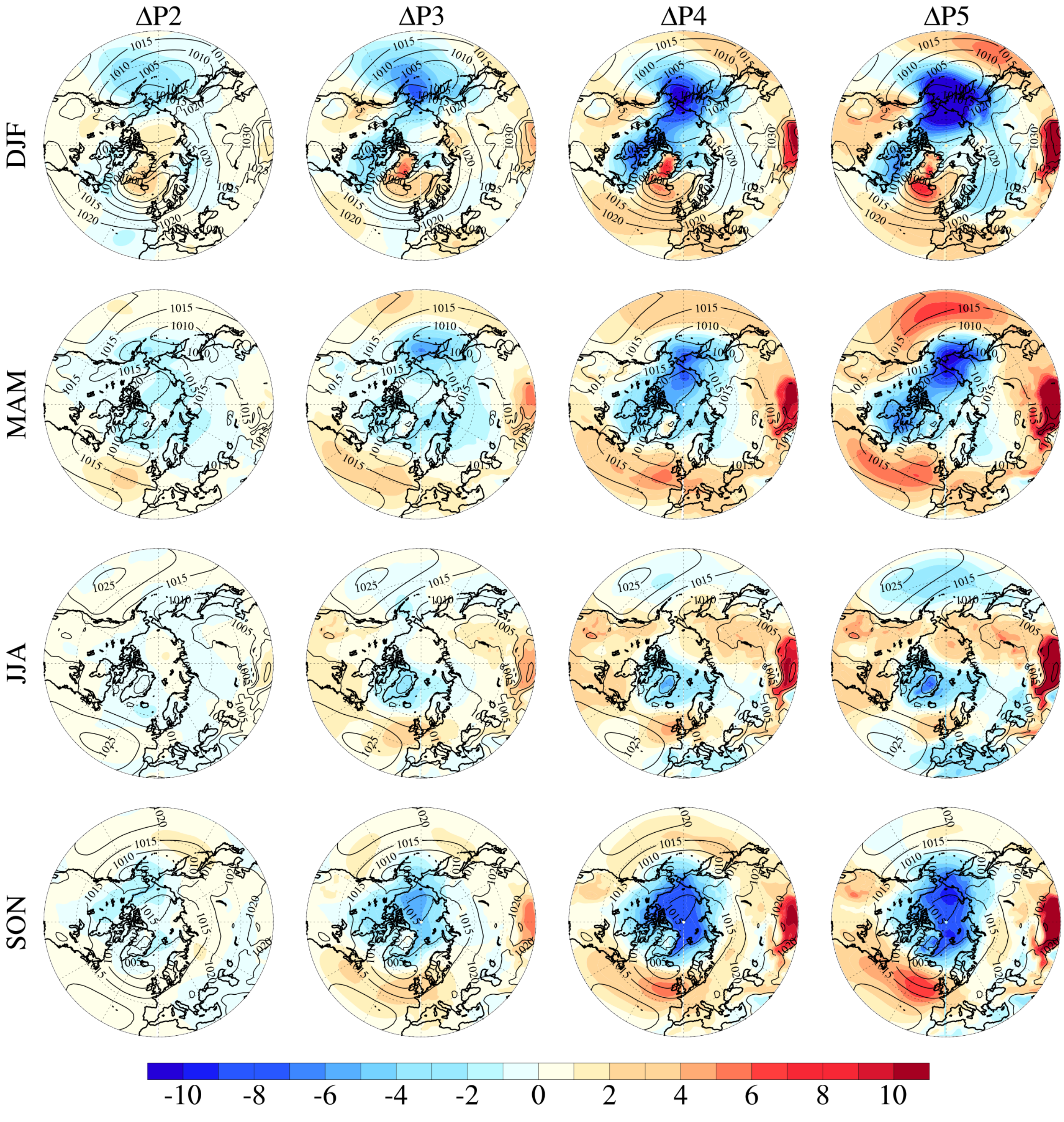

Figure 5.20: Mean sea level pressure (in hPa) for P1 (contours) and the changes for P2 to P5 relative to P1 (shading) for each season.

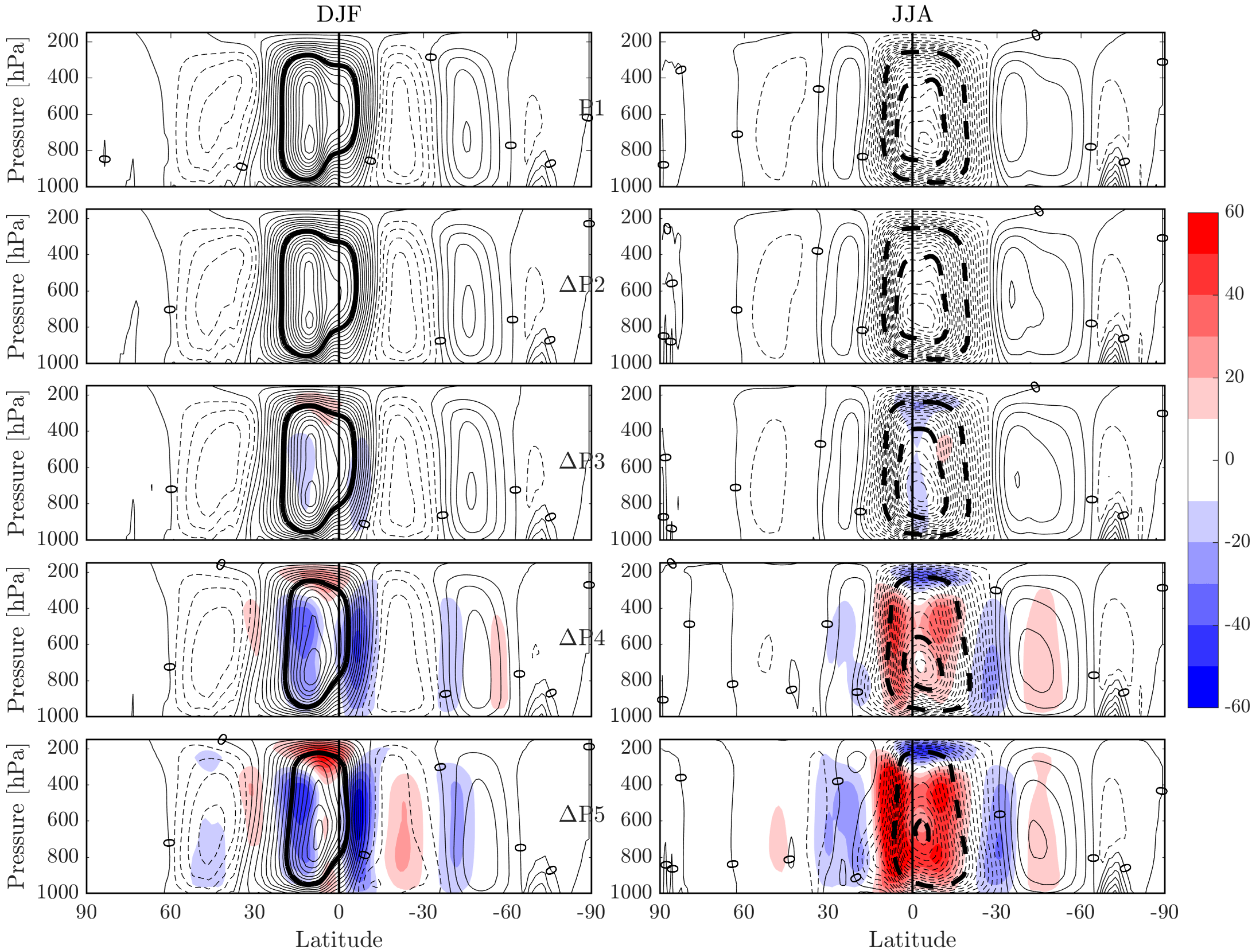

Figure 5.21: Stream function (in 10^9kg s^{-1}) for P1 (top row) for DJF (left column) and JJA (right column). The four rows below show the stream functions for P2 to P5 (contours) and the difference relative to P1 (shading; in 10^9kg s^{-1}). The interval for the thin contour lines is 10×10^9kg s^{-1} and 100×10^9kg s^{-1} for the thick contour lines. Positive is counterclockwise flow (solid lines + red shading) and negative is clockwise flow (dashed lines + blue shading).

Changes in the ocean stratification

The RCP8.5 simulations projected oceanic changes as well. The structure of the Arctic Ocean and the Barents Sea (regions shown in figure 5.22) were represented by the area mean temperature and salinity profiles with depth (figures 5.23 and 5.24). There were no substantial change between P1 and P2. Generally, the temperature and salinity changes were quite similar for both Arctic Ocean and Barents Sea: after P2, the temperature increased and the salinity decreased. The warm, saline subsurface 'bump' around 500m depth indicated the Atlantic Water (AW). The core of this appeared to decrease in depth from P1 to P5. Despite the overall similar development in Arctic Ocean and Barents Sea, there were significant differences between Arctic Ocean and Barents Sea. In the Arctic Ocean, the halocline deepened and strengthened, and the surface salinity decreased by up to 5 psu from P1 to P5. A stronger halocline implied a stronger stratification. This was illustrated by the Brunt-Väisälä frequency (N^2) in the right column of figure 5.23. N^2 showed increased stability (i.e. increase in N^2) going from P1 to P5, implying a stronger stratification. In the Barents Sea, the stratification strengthened as well, but only for P4 and P5. P3 revealed a weaker stratification due to a weaker halocline (fig. 5.24). This increased vertical mixing, together with the shallowing of the AW, andicated an atlantification of the Barents Sea.

Changes in the ocean circulation

The strength of the ocean circulation was represented by the AMOC. This was projected to weaken from the pre-industrial period until a complete loss of Arctic sea ice (i.e. P1 to P4; fig. 5.25). A gradual recovery from P4 to P5 was indicated between 10°N and 25°N, while there were no indications of a recovery further north. A weaker AMOC suggested a decrease in oceanic heat transport. However, this was not observed. The total heat transport into the Arctic ocean (the sum of the transport through the four main gateways shown in figure 5.22: Barents Sea Opening (BSO), Fram Strait (FS), Canadian Archipelago (CAA) and Bering Strait (BS)) revealed an increase in northward heat transport (fig. 5.26 top row). This was mainly due to an increase in northward heat transport through BSO which the southward heat transport through FS and CAA could not oppose. The heat transport increased until P3, after which it gradually stabilized at a lower level. The increased northward heat transport did not coincide with an increase in volume transport, indicating that the change in heat transport were due to changes in the ocean temperature (fig. 5.26 middle row). The liquid fresh water export out of the Arctic Ocean increased after P2.

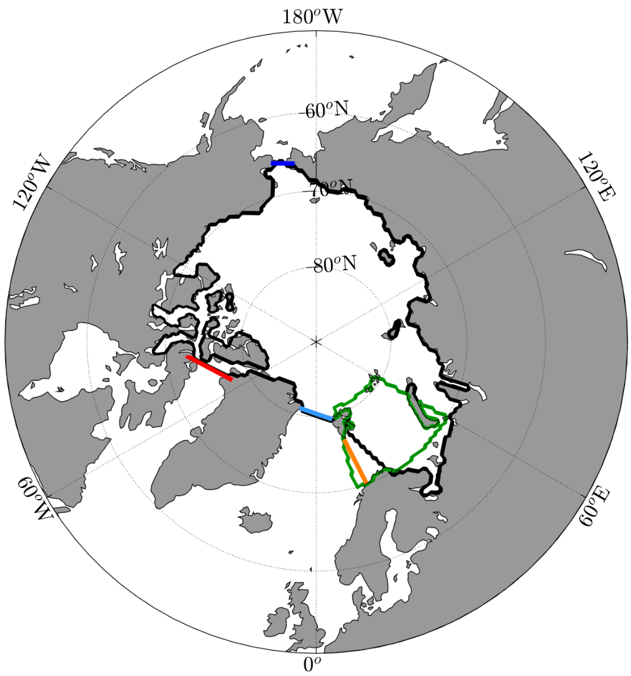

Figure 5.22: Map of the regions used for the Arctic Ocean (black) and the Barents Sea (green) and the four gateways: Fram Strait (FS; light blue), Barents Sea Opening (BSO; orange), Canadian Archipelago (CAA; red) and Bering Strait (BS; dark blue).

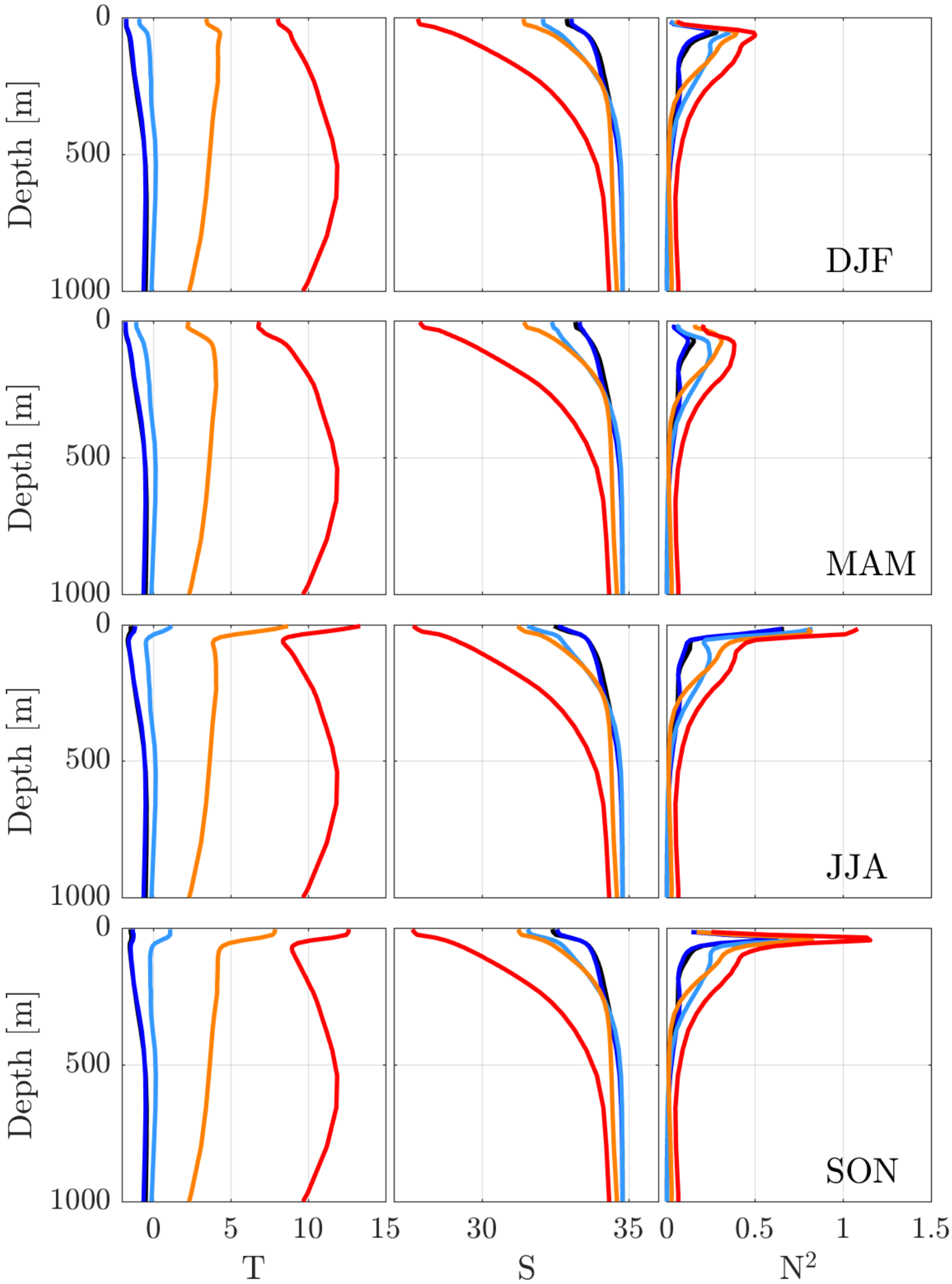

Figure 5.23: The upper 1000m of the area mean temperature (left; in °C), salinity (middle; in psu) and Brunt-Vaisala frequency (right; N^2; in hr^{-1}) for the Arctic Ocean. P1 (black), P2 (blue), P3 (yellow), P4 (orange), P5 (red).

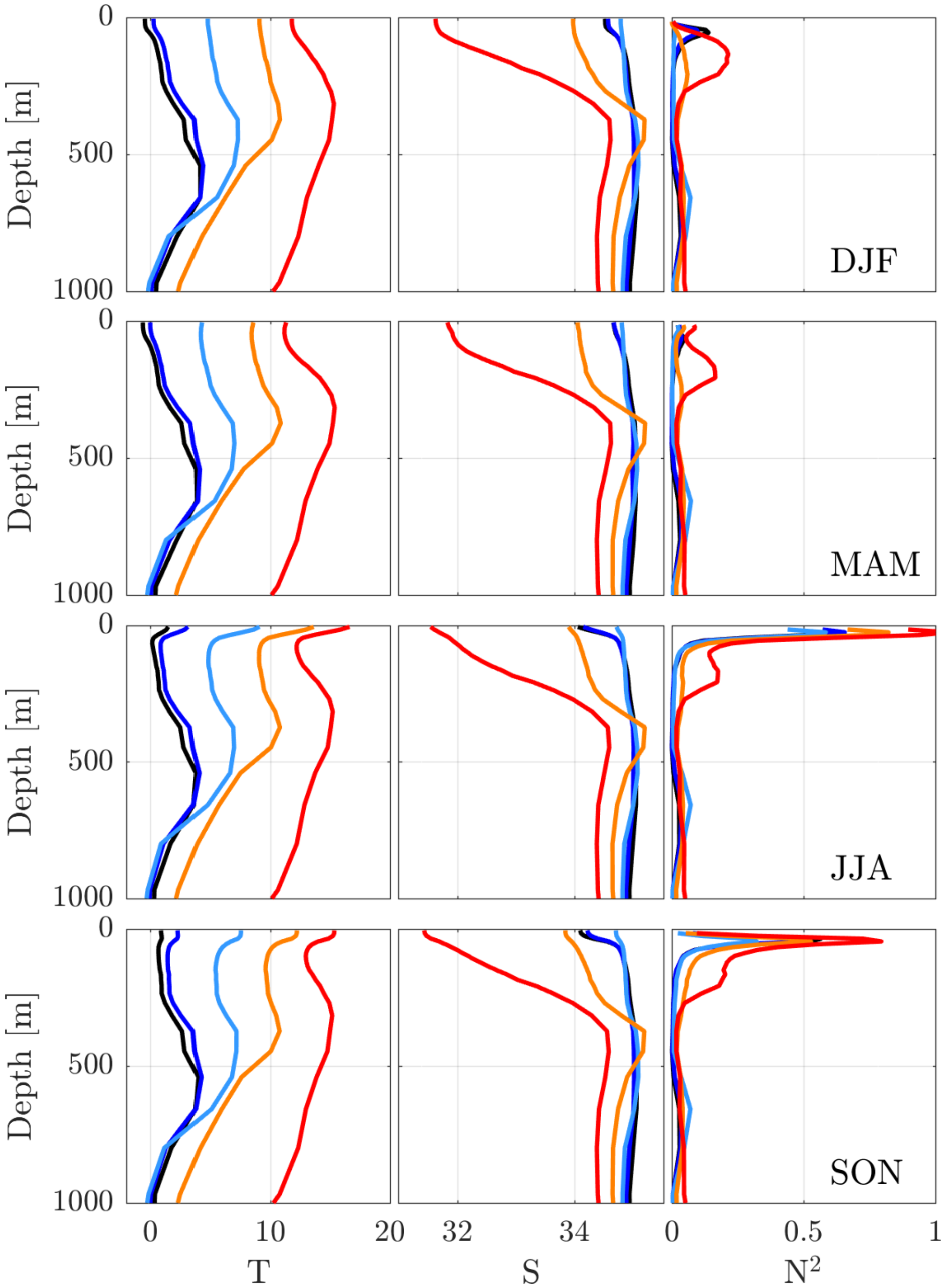

Figure 5.24: The upper 1000m of the area mean temperature (left; in °C), salinity (middle; in psu) and Brunt-Vaisala frequency (right; N^2; in hr^{-1}) for the Barents Sea. P1 (black), P2 (blue), P3 (yellow), P4 (orange), P5 (red).

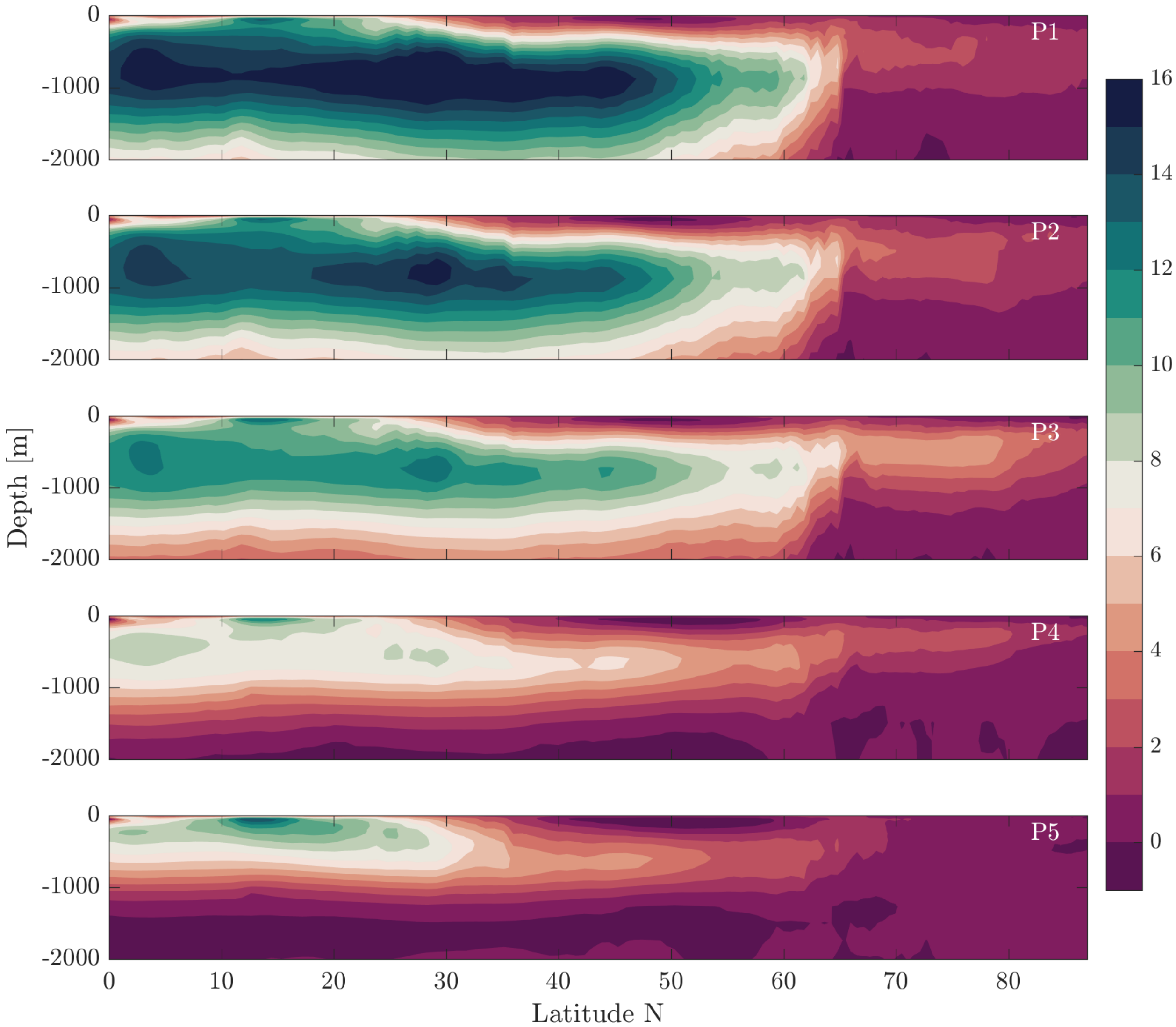

Figure 5.25: 30-year mean of the AMOC (in Sv) for each period.

The Arctic Ocean is projected to become fresher (fig. 5.23). The largest contributor to this freshening is most likely the increased precipitation. Table 5.1 show the annual mean net fresh water flux from the atmosphere to the ocean (precipitation-evaporation; P-E) and the river runoff. Of these two, the P-E is the largest contributor. Other potential fresh water sources for the Arctic Ocean are GIS melt and fresh water transport into the Arctic Ocean. The latter was disproved in figure 5.26 (bottom row), showing a net fresh water export out of the Arctic Ocean. Although the GIS is projected to decrease dramatically in size by year 3200, only the northern most tip of Greenland borders the Arctic Ocean region used (fig. 5.22). Hence, most of the GIS melt water will not end up in the Arctic Ocean.

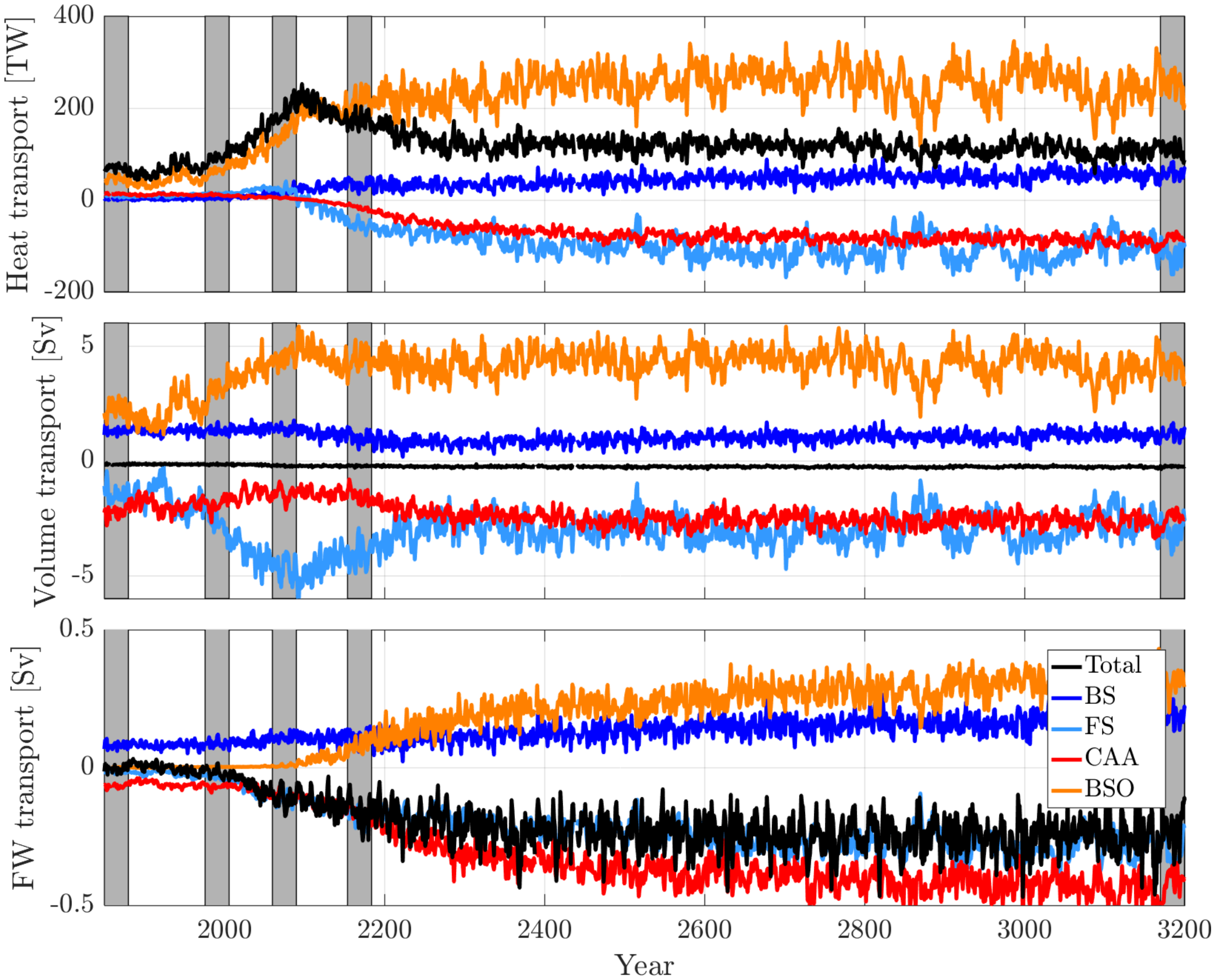

Figure 5.26: Monthly mean transport of heat (top; in TW), volume (middle; in Sv) and fresh water (bottom; in Sv) through Fram Strait (FS), Barents Sea Opening (BSO), Bering Strait (BS) and the Canadian Archipelago (CAA). Positive is into the Arctic Ocean. Grey bars indicate the five periods.

Table 5.1: Annual mean river runoff and net freshwater flux (Precipitation-Evaporation; P-E) for the Arctic Ocean (in x10^{15} kg year^{-1}), for each of the five time regimes. Arctic Ocean region defined in figure 5.22.

	River runoff [x10^{15} kg year^{-1}]	**P-E** [x10^{15} kg year^{-1}]
P1	0.177	1.78
P2	0.183	1.77
P3	0.247	2.02
P4	0.439	2.53
P5	0.837	3.11

Chapter 6

Discussion

The results of each of the three studies are discussed separately. Following this are discussions of 1) the capability of climate models to simulate sea ice, 2) the impact of different regional sea ice loss on the climate system and 3) on abrupt climate change.

6.1 Study I: Nudging sea ice in the coupled climate model EC-Earth

Study I aimed at developing a method for nudging sea ice in coupled climate models, while maintaining energy conservation. The approach replicates the realistic process of heat transfer between the atmosphere and the ocean by surface heat fluxes. As the sensible heat flux only modifies the temperature, we chose that as our nudging parameter. However, modifying the sensible heat flux between the atmosphere and the ice/ocean surface, proved to be a difficult. Melting/forming sea ice required such large amounts of heat to be redistributed in the atmosphere, that the simulated atmosphere cooled/warmed too much, consequently causing the model to become unstable within a few years.

As discussed in Manuscript I, there were some potential ways to avoid the large warming/cooling caused by the large amount of ΔHF being redistributed in the atmosphere. These included using a weaker nudging, go-with-the-flow of only nudging toward more sea ice in the freezing period or collecting ΔHF in a buffer, slowly releasing it over time. These three methods all required finding a fine balance between nudging the model enough to reach the target, and not too much, causing the model to become unstable and crash.

Instead of redistributing the heat in the atmosphere, it could be redistributed in the ocean. Adding heat would disturb the stratification, but it would disturb the oceanic stratification in the Arctic less than it would the atmospheric stratification. This discrepancy occurs because the stratification in the Arctic Ocean is predominantly determined by the salinity, not the temperature. Further, since the ocean heat capacity is much larger than that of the atmosphere, equal amounts of heat will not lead to equal amounts of temperature change. This approach have the potential to work, but we did not test it.

Staying in the ocean, one approach is to modify the mixing coefficient, forcing the vertical mixing to weaken (and thus strengthening the stratification) when targeting more sea ice and to strengthen the mixing when targeting less sea ice, allowing for warmer subsurface water to mix into the surface mixed layer. The mixing coefficients used in ocean modeling are normally empirically chosen and lay within a range of values (Knauss (1997)). Therefore, an approach is to modify the mixing coefficients slightly, keeping them within the observed range. We did not test this approach either. Finally, a potential approach is to redistribute the ΔHF in the entire global atmosphere or in the deep ocean. Doing so, the energy would not warm the atmosphere or ocean too much in a single region, leading to an unstable model. However, putting the energy in a non-physical location erodes the idea of conserving the energy. The idea behind maintaining energy conservation is to simulate the climate as close to the observed as possible. In experiment M2, the energy was redistributed in the atmospheric column directly above the area of nudging, replicating the real-life process of heat flux exchanges. In my opinion, if we are to put the energy somewhere non-physical, we might as well send it out to space, where it does not affect anything. This way, the effect of the sea ice changes can be isolated, ignoring the effect from the redistributed energy. This approach corresponds to our Method 1, which again resembles the flux adjustment in Oudar et al. (2017).

6.1.1 Testing Method 2 on Study II

After finishing Manuscript II we returned to the energy-conserving Method 2 developed in Study I. The original plan was to use this method for the BAKA experiments in Manuscript II. Method 2 was therefore used to nudge sea ice in the BAKA (same region as used in Study II, see section 5.2) toward the models own sea ice climatology in this region. This was similar to the experiment C100 presented in section 5.2 and was referred to as $M2_{C100}$. Comparing the SIC to the target sea ice edge (fig. 6.1a) showed that for the first model year, Method 2 succeeded in reaching the sea ice target. The freely running models sea ice edge was further south. The temperature response relative to the freely running model in fig. 6.1b showed that the temperature changes due to the nudging were not unrealistic, as was the case for M_{50N}. The $M2_{C100}$ simulation was continued for 100 years. The first few years succeeded in reaching the target sea ice cover quite well. However, after approximately 3 years, the surface temperature began to decrease and the sea ice extended further south (figure 6.2). This was quite unexpected, as nudging was only performed in BAKA and the target sea ice state was relatively close to the models own sea ice state. The sea ice outside BAKA was not constrained, allowing for the observed southward extension. Further work is required to investigate this shift toward cooling and subsequent extension of the sea ice cover.

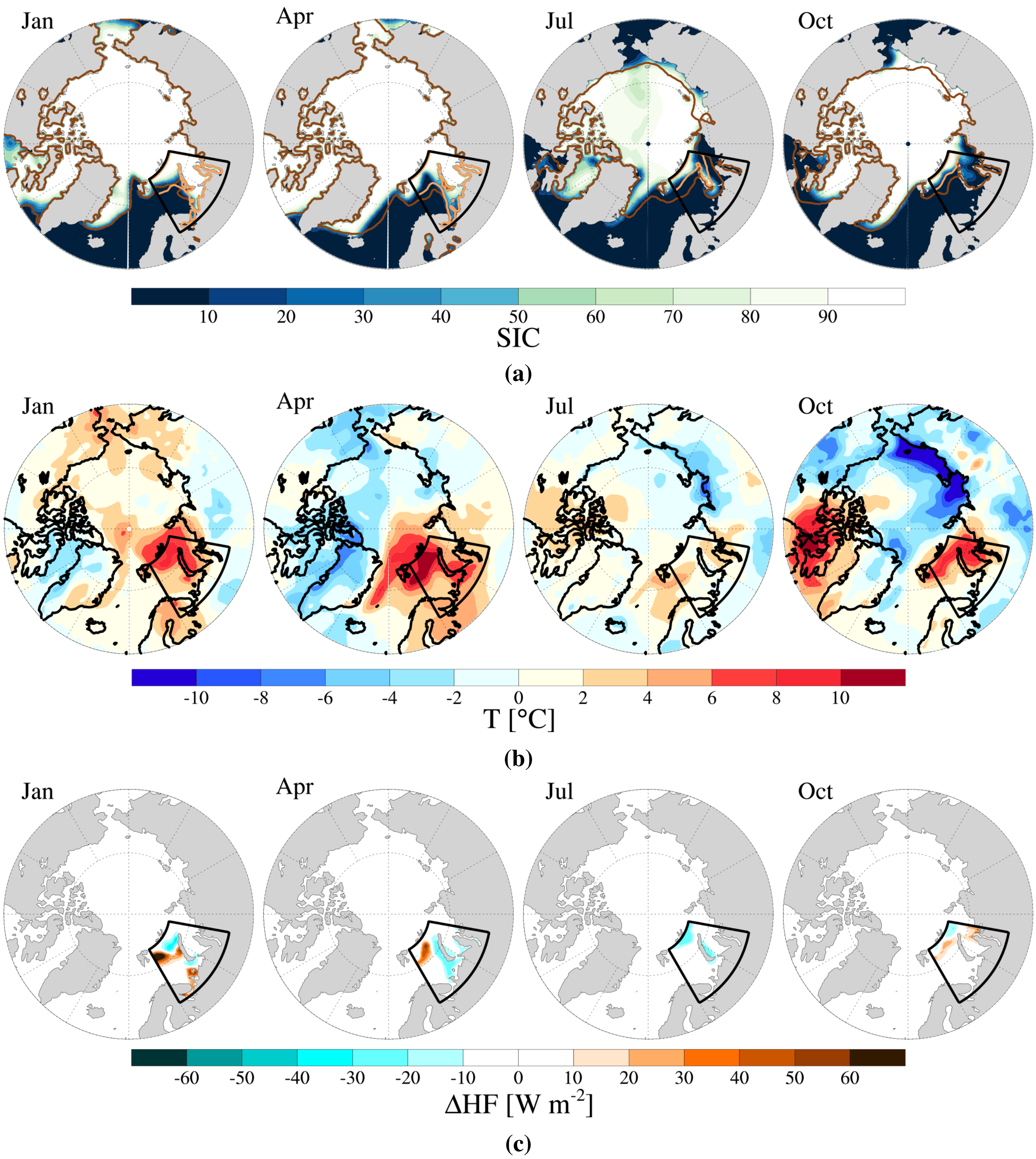

Figure 6.1: M2$_{C100}$ monthly mean (a) sea ice concentration (in %), (b) temperature anomaly (M2$_{C100}$-CTRL; in °C) and (c) ΔHF (in W m^{-2}) for January, April, July and October. The dark brown line in (a) indicate the climatological sea ice edge (SIC>=15%) from CTRL, the light brown line indicate the target sea ice edge.

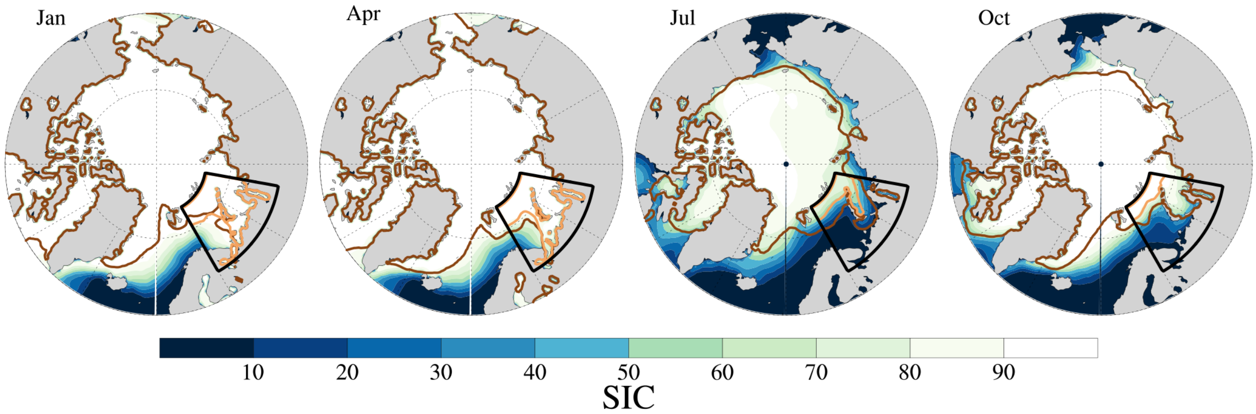

Figure 6.2: M2$_{C100}$ 100-year monthly mean sea ice concentration (in %) for January, April, July and October. The dark brown line in (a) indicate the climatological sea ice edge (SIC>=15%) from CTRL, the light brown line indicate the target sea ice edge.

6.2 Study II: Barents-Kara sea ice and European winters in EC-Earth

Study II investigated the link between cold European winters and reduced sea ice in the BAKA. Our results showed that the mean response differed from the response in the 5% coldest winters. The mean response was a lack of warming over Europe for a minor sea ice reduction (80%), a statistically significant cooling over a relatively small area of eastern Europe for moderate sea ice reductions (60%) and a statistically significant warming over Europe for major sea ice reductions (20-40%). The significant cooling was only observed for a small area, resulting in C60 not being statistically significant different from the control simulation C100 when averaging over CEU or EU. The corresponding mean circulation response, represented by the mean sea level pressure (MSLP), was a 'heat low' over the nudged area, i.e. a low pressure anomaly over BAKA. This low pressure anomaly intensified with sea ice reduction. The weak non-linear behavior observed for the temperature is similar to the findings in Petoukhov and Semenov (2010), whose design this study was based on. They also observed a cooling over Europe for moderate (40-80%) sea ice reductions in BAKA. However, they also see a non-linear response in the atmospheric circulation, with a shift from a cyclonic circulation to anticyclonic and back to cyclonic circulation. Our results differ from this, as they only show the intensified low pressure anomaly over BAKA. The discrepancies between our study and that of Petoukhov and Semenov (2010) might be due to two things. 1) They used an AGCM whereas we used an AOGCM. An AGCM does not reproduce the atmosphere-ocean feedbacks which are vital to obtain the remote effects of any changes, as discussed in section 2.6.1. 2) Study II used an atmospheric model resolution of T255 (approximately 80 km), whereas Petoukhov and Semenov (2010) used T42 (approximately 300 km, 2.8°). As a higher model resolution resolves finer scales, it can simulate the physical processes more adequately. Both these model related issues improve the models ability to simulate the real climate, hence we interpret our results to be a better representation of the response to BAKA sea ice reductions.

The response for the 5% coldest winters did not show a statistical significant cooling for any of the four reduced sea ice simulations, relative to C100. The MSLP response showed an intensi-

fication of the Scandinavian pattern with sea ice reduction, implying that the coldest winters did not get colder as BAKA sea ice was reduced, but that the associated high pressure system must be stronger to generate the same cold winters. This discrepancies between the mean and the extreme cold winters were due to the former being the mean over 2 months for 100 years (i.e. 200 months), the second being the subset of the 5% coldest winters (i.e. 10 months). The mean response was dominated by the heat low above BAKA due to the reduced sea ice. The coldest winters only occurred when cold air was advected down from the Arctic to Europe, which was bound to happen some winters.
Comparing our results to other studies is not straightforward as the combination in Study II (modifying only BAKA sea ice loss and using a coupled climate model) is relatively unique. Most model studies have used AGCM's, prescribing the sea ice changes. Those that use AOGCM's have mostly investigated a pan-Arctic sea ice loss, not an isolated BAKA sea ice loss. Some of the latter were analyzed in the study by Screen (2018). They compared six coupled climate models, all simulating projected Arctic sea ice loss [Blackport and Kushner (2016), Blackport and Kushner (2017), Deser et al. (2015), McCusker et al. (2017), Oudar et al. (2017) and Smith et al. (2017)]. They found that the six model simulations agreed on the intensification of the wintertime Aleutian Low, an increase in the MSLP over Eurasia, a weakening of the Icelandic low and a reduction in strength and southward shift of the mid-latitude westerlies in winter. The intensification of MSLP over Eurasia is similar to our MSLP response for the coldest winter months, but it differs from our temporal mean MSLP response. The coldest winter response was an intensification of the Scandinavian pattern, whereas the mean response was a low pressure anomaly over BAKA. The intensification of the Aleutian Low was not observed either in the mean nor the coldest winters. This is most likely due to the difference in regions of the sea ice loss (BAKA vs. pan-Arctic). See section 6.5 for further discussion. Hence, our circulation response for the coldest winters was similar to those in the six coupled model studies. Of these six studies only the study by Blackport and Kushner (2016) investigates the link between Arctic sea ice loss and cold Eurasian winters. They found a weak cooling over Eurasia as a response to a high pressure anomaly off the coast of Eurasia in some, but not all, of their eight simulations, strongest for the transient period when the models climate state was adjusting to the new sea ice albedo (they modified the sea ice albedo to nudge sea ice toward their target). This circulation pattern is similar to our findings, though the location of the high pressure anomaly differs. Even though Blackport and Kushner (2016) focused on cold Eurasian winters, they did not relate it to BAKA sea ice loss. McCusker et al. (2016) did this, but they too simulated the observed pan-Arctic sea ice loss, not only the BAKA sea ice loss. Comparing the simulated temperature trend over central Eurasia between years 1979-1989 to 2002-2012 with the trend in BAKA sea ice decline over the same periods, they concluded that the observed cooling was exceptional, but the sea ice decline in BAKA was not. Hence, BAKA sea ice loss was not the main driver of the observed Central European cooling trend. Instead, the cooling was suggested to be internally driven by a trend toward anticyclonic circulation over BAKA. This is in contrast to our findings: cold CEU winters of the same magnitude as for the control simulation C100. McCusker et al. (2016) underestimated the observed cooling trend over Eurasia, actually simulating a warming trend instead. A potential cause of the different results is the difference in the magnitude of the sea ice loss. McCusker et al. (2016) simulated the observed BAKA sea ice loss 1979-1989 to 2002-2012, amounting to a loss of 11%. In our study, SIC reductions begin at 20% (i.e. C80).

Several observational studies have found a link between BAKA sea ice decline and cold Eurasian winters (see section for 3.2 for further discussion); some even state that BAKA sea ice reduction is one of the main drivers of mid-latitude winter circulation and Eurasian cooling (Kretschmer et al. (2016)). A common pathway by which BAKA sea ice can influence Eurasian winter temperatures is: enhanced heat flux resulting from the reduced sea ice induces planetary waves from the troposphere into the stratosphere and back again; this induces a negative AO/NAO like pattern, leading to weaker westerlies and consequently cold air advection in Eurasia. This pathways have been suggested by both observational studies as well as model studies (Kretschmer et al. (2016), Ruggieri et al. (2016), Garcia-Serrano et al. (2015), Kretschmer et al. (2018)). Some studies do not find a link, leading them to state that the observed cooling over Eurasia is driven by internal atmospheric variability. These include observational studies (Sorokina et al. (2016)) as well as model studies (McCusker et al. (2016), Screen (2017a), Ogawa et al. (2018)).

6.2.1 Background state

Some studies suggest that the impact from sea ice loss depends on the background climate state, either in the form of the SST over the Northwest Atlantic (Balmaseda et al. (2010)), the Atlantic multi-decadal oscillation (Osborne et al. (2017)) or the mean climate state (Smith et al. (2017)). Yet, McCusker et al. (2017) did not find that the background state modulates the response. Instead, they showed that the response to sea ice loss was the same for CO_2 concentration on a pre-industrial level, as well as twice the CO_2 concentration. However, the discrepancies cannot be assigned to the differences between AGCM and AOGCM: where the two studies by (Balmaseda et al. (2010)) used AGCM's and the McCusker et al. (2017) study used an AOGCM, the Smith et al. (2017) study was based on comparing simulations from an AGCM and AOGCM.
To test if a preconditioning was present in our study, composites consisting of the 5% coldest/warmest winter months for the NA SST were analyzed. Our results showed no significantly colder temperatures over Europe for either warm or cold NA SST (not shown). Hence, our results did not indicate that the NA SST preconditions cold winters over Europe.

6.2.2 Potential drivers

The mean temperature response over CEU in figure 5.4 suggested a link between the BAKA sea ice reductions and cold European winters. Kretschmer et al. (2016) supported this further by naming the BAKA sea ice loss as a main driver of mid-latitude winter circulation. Nonetheless, other studies have named the Siberian snow cover as a main driver of the AO, with the response amplified by BAKA sea ice loss (Gastineau et al. (2017)). This was supported by Cohen et al. (2007) and Cohen et al. (2012) who found that increased Siberian snow cover in autumn induced a negative AO in the following winter. Cohen et al. (2014) suggested that increased Eurasian snow cover and reduced Arctic sea ice interfered positively to weaken the polar vortex, inducing a negative AO/NAO-like pattern. Allen and Zender (2011) showed that the Siberian snow cover was underestimated in their AGCM's. Correcting for this, they were able to reproduce the observed AO variability of the last decades. This implied that Siberian autumn snow cover variability was important for the winter AO/NAO.
We tested this hypothesis in our model simulations, by analyzing the snow cover extent for the 5% coldest winter months for CEU (i.e. the same months used to create the composites in figure 5.9; figure not shown). None of the sea ice reduced simulations showed a significantly different Siberian snow cover extent relative to C100. Hence, our results did not indicate a link between

increased Siberian snow cover and cold Eurasian winters.

6.3 Study III: Climate change associated with sea ice loss in extended EC-Earth-PISM RCP8.5 simulation

Focusing on five different sea ice states, Study III found that the overall evolution of the 1350-year long RCP8.5 scenario simulation was similar to that of the CMIP5 ensemble. There appeared to be a shift in the rate of change for some of the key parameters between the five sea ice states. In particular before and after P3, when the Arctic Ocean became seasonally ice-free. In the atmosphere the rate of the warming and the Arctic Amplification (AA) were the most pronounced.
The 30-year trend of the increasing global temperature is compared to the 30-year trend for four areas and for the five sea ice states in figure 6.3a. Here, the trend of the global mean temperature increases until P3, after which it decreases. Three of the four areas (Europe, Southeast Asia and South America) follow the global mean trend, whereas the temperature trend on Greenland is 2.7 times higher than the global mean trend for P3. It is still higher than the global mean for P4 (1.7 times), after which it decreases. The AA also peaked around P2 and P3. The AA was maintained throughout the simulation, despite the disappearance of the sea ice. However, computing the AA of P5 relative to P4, i.e. removing the dependence on sea ice, there is no substantial change in the north-south temperature gradient (fig. 6.4). This is appear to be contrary to the results by Langen and Alexeev (2007): in an AGCM simulation of an aquaplanet (no land or sea ice), they showed that polar amplification developed, i.e. without any influence from sea ice changes. The apparent contradiction with our result can be explained by the results from Caballero and L. Langen (2005). They showed, the poleward energy transport will reduce the Equator-Pole temperature gradient (ΔT), but only for a low background temperature (T_m<15°C) and a large ΔT. For T_m>15°C and

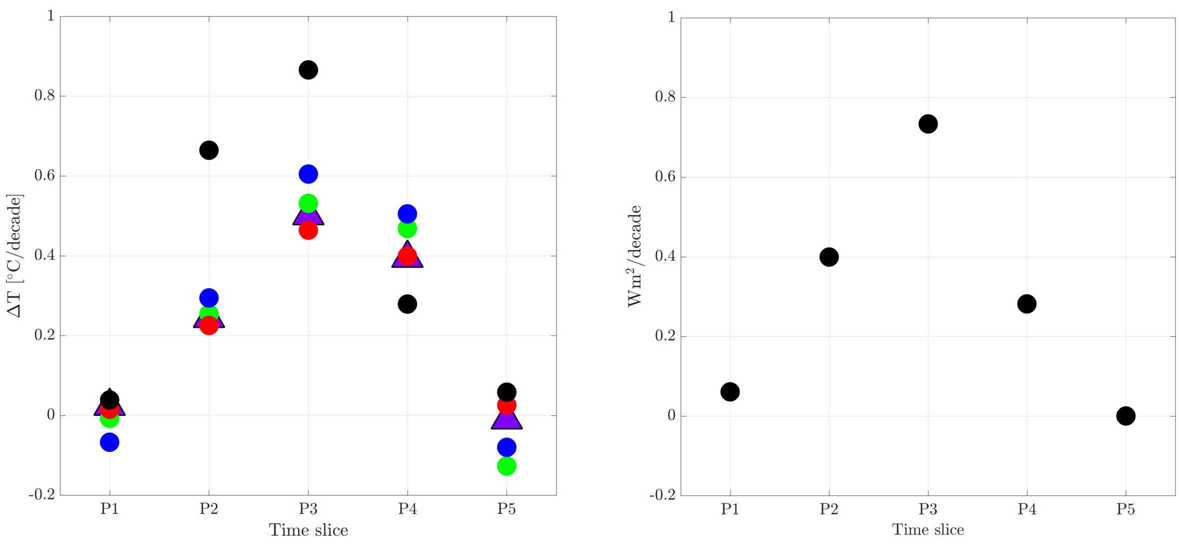

(a) **(b)**

Figure 6.3: (a) Trend of the annual mean absolute temperature for each 30-year time regime [°C/decade] for the global mean (purple triangle), Greenland (black), Europe (blue), Southeast Asia (red) and South America (green). (b) Trend of the total anthropogenic GHG forcing for the RCP8.5 scenario for each of the five time periods.

ΔT<30°C, the increased northward energy transport will not lead to a decrease in ΔT. Hence, as the background temperature for P4 and P5 is larger than 15°C, the ΔT will not be reduced further by northward energy transport and the AA will therefore not change substantially between P4 and P5.
In the ocean this, shift around P3 and P4 was seen as well. The warming of the Arctic Ocean intensified only after the Arctic became seasonally ice-free. The heat transport into the Arctic Ocean increased and peaked at P3, after which it decreased slightly and stabilized. The same occurred for the AMOC: it weakened as the Arctic sea ice declined and stabilized after all sea ice was lost. In the Barents Sea and parts of the Eurasian Basin an 'atlantification' have been observed in recent years (Aarthun and Eldevik (2012), Polyakov et al. (2017); see section 2.3.2). This atlantification (weakening of the stratification and shallowing of the Atlantic Water) was observed in the present RCP8.5 simulation as well, until the Arctic summer sea ice was gone. After this, the stratification increased again due to a freshening and warming of the Barents Sea. This implied that the atlantification will only occur during a sea ice retreat, after which the increased river runoff, precipitation and heat transport into the Barents Sea will strengthen the stratification.
The strengthened oceanic stratification in the Arctic Ocean could potentially lead to a positive stratification-based climate feedback mechanism. In winter, the ocean releases heat to the atmosphere and directly to space in the atmospheric window, assuming some cloud free periods. Due to the strong salinity-based oceanic stratification, the upper most ocean easily cools due to lack of significant convective mixing with the warmer water masses below. Thereby the surface will be colder than under less stratified conditions. Thus, the whole Arctic atmosphere-ocean system will lose less energy to space than under less stratified oceanic conditions. In other words, the ocean/atmosphere will likely rather quickly reach a cold (but still unfrozen) energetic equilibrium. Further analysis of this hypothesis is required, however, in future work.

As discussed above, several key parameters appear to be dependent on the sea ice state. Especially, the shift from a perennial sea ice cover to a seasonal sea ice cover appear to be important. This shift might not only be related to the retreating sea ice cover. The RCP8.5 scenario simulation is forced with increasing GHG emissions. Comparing the 30-year global mean temperature trend to the 30-year trend of the GHG forcing for each time period (fig. 6.3b), shows a common peak at P3. This suggests that the observed shift in trend of some parameters is most likely affected by the change in global mean temperature and GHG emissions, as well as the sea ice state. However, some of the features observed to shift are most likely due to the shift in sea ice state: the AA has been shown to be mainly driven by the sea ice loss (Serreze et al. (2009), Screen and Simmonds (2010), Pithan and Mauritsen (2014)), and the increased warming and freshening of the Arctic Ocean only occurred after the protecting sea ice cover disappeared.

6.3.1 The Earth in a warmer climate

The RCP8.5 simulation in Study III simulated the climate until year 3200, where sea ice have been lost for a thousand years; thus, the climate would no longer be sensitive to sea ice change. Regardless, it is still interesting to compare the projected climate to reconstructions of climate from paleo records, hence the brief discussion below on this topic.
By year 3200, under the assumptions of the RCP8.5 scenario, the global mean temperature will be 12.7°C higher than pre-industrial temperatures, there will be no sea ice and the Greenland Ice Sheet will have lost 62% of its volume. It is fair to say that this will be a very different cli-

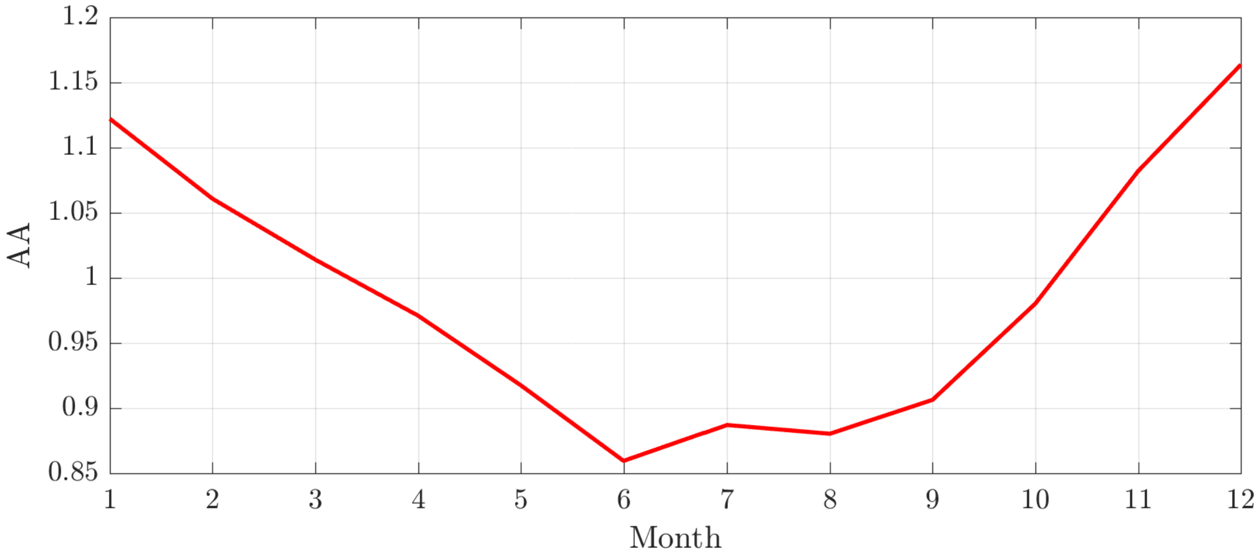

Figure 6.4: Arctic amplification in P5 relative to P4 $(\overline{T_{Arc}^{P5}} - \overline{T_{Arc}^{P4}})/(\overline{T_{Glo}^{P5}} - \overline{T_{Glo}^{P4}})$.

mate than today. An interesting question is then, if this future climate is unprecedented in Earth's history. Figure 6.5 shows temperature trend reconstructions from the past 65 million years, the four future GHG emission scenarios and the global mean temperature from the RCP8.5 simulation in Manuscript III. This temperature curve clearly illustrates two things: (1) the occurrence of warm periods in the past and (2) that the projected temperature change by year 2300 is unprecedented in the past 50 million years. During the Medieval Warm Period (years 950-1250) certain areas experienced warming similar in magnitude to the warming observed during the past decades. However, the warming only occurred over smaller regions, not over as wide regions as have been observed since the mid-20th century (IPCC (2013), chapter 5). Going back to the last interglacial, the IPCC AR5 (IPCC (2013), chapter 5) states *"with medium confidence that global mean annual temperatures were never more than 2°C higher than pre-industrial"*. Continuing back in time, the mid-Pliocene 3.3 to 3.0 million years ago experienced temperatures higher than pre-industrial by 1.9 and 3.6°C and CO_2 concentrations between 350 ppm and 450 ppm. This is comparable in magnitude to the annual mean 2018 CO_2 concentration of 408.3 ppm (`https://www.esrl.noaa.gov/gmd/aggi/aggi.html`). The early Eocene (52-48 million years ago) were even warmer, with temperatures 9-14°C higher than the pre-industrial period and CO_2 concentrations of approximately 1000 ppm (IPCC (2013) chapter 5). The projected CO_2 concentration in the RCP8.5 scenario stabilizes after year 2250 at approximately 2000 ppm (Meinshausen et al. (2011)).

Although the global mean temperature in the past possible have been equivalent or higher, the rate of change is not. Gingerich (2019) compared the modern rates of carbon emission to those of the Paleocene-Eocene Thermal Maximum (PETM; 56 millions years ago). During the PETM, the global temperature increased by 5-8°C to the highest temperatures recorded since the extinction of the dinosaurs, leading to widespread mass extinction. Gingerich (2019) showed that the modern carbon emission rates are 9-10 times faster than that during the PETM.

The above show that although the projected temperature by the RCP8.5 scenario is not unprecedented in history (and even here we have to go 56 millions year back in time), the rate of climate change is.

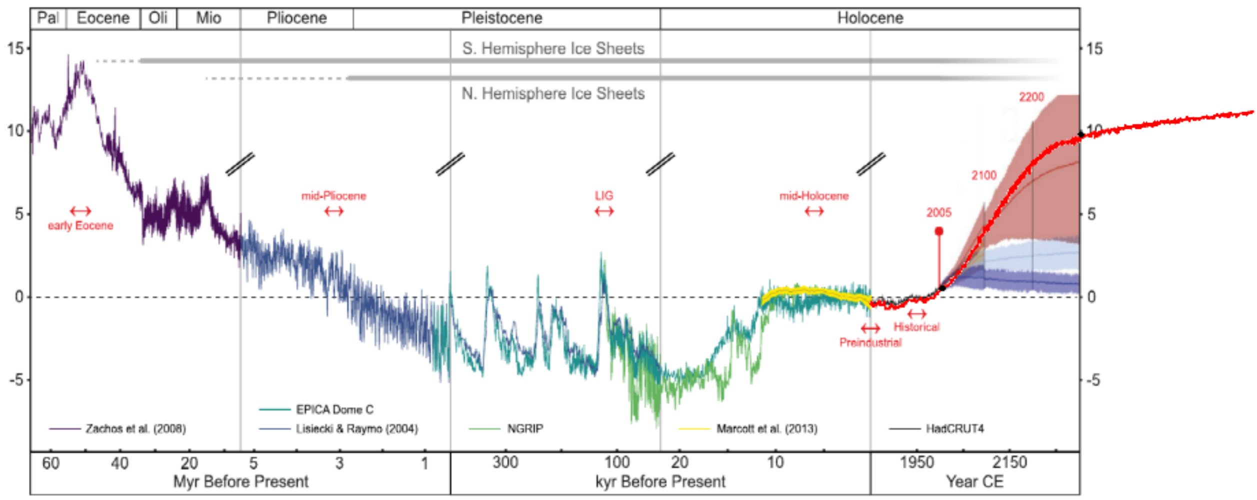

Figure 6.5: Reconstructed temperature trends for the past 65 million years and the four future GHG emission scenarios. Temperatures are relative to the period 1961-1990. Red curve on top is the global mean temperature anomaly from the RCP8.5 simulation in Manuscript III. Figure modified from Burke et al. (2018).

6.4 Sea ice in climate models

From the discussions above it is clear, the climate is sensitive to sea ice changes in relatively small regions (Study II) as well as pan-Arctic sea ice loss in a warmer climate (Study III). This sensitivity to large sea ice changes has also been observed for the past climates (Sadatzki et al. (2019)), underlining why it is important to be able to realistically model the changes in sea ice cover. Mori et al. (2019) showed that AGCM's underestimate the observed Eurasian cooling due to an underestimation of the response to BAKA sea ice loss. This was further supported by a study (Jansen et al. (2019, manuscript submitted)) who compared abrupt temperature changes in the four GHG emission scenarios to reanalysis data. They found, all four scenarios underestimated the observed abruptness of the temperature change. Temperature is not the only parameter that the climate models underestimate. Comparing the CMIP5 ensemble to observations, Stroeve et al. (2012) showed, the CMIP5 models reproduced the seasonal cycle of the Arctic sea ice well, but the trend of the sea ice decline over the satellite era (1979-2011) was too low. Shu et al. (2015) showed a similar too low trend for the sea ice extent and volume, due to too thin sea ice. The CMIP5 multi-model mean ensemble of the Antarctic sea ice extent and volume trend were actually opposite of the observed Antarctic sea ice trend (positive). The spread among CMIP5 models is large, with a single model member in the RCP4.5 scenario predicting a seasonally ice-free Arctic by 2016 (i.e. three years ago) while the multi-model ensemble mean does not reach below the threshold of 1 million km^2 by 2100 (Stroeve et al. (2012)). Hence, the CMIP5 climate models are able to capture the seasonality of the Arctic sea ice extent and volume, but the sea ice is too thin and the sea ice loss too slow.

Notz and Stroeve (2016) explained this underestimation of the Arctic sea ice loss through a simple conceptual model of the sea ice edge. From this they showed, the location of the sea ice edge was determined by the balance between a decrease in incoming shortwave flux and the increase in incoming non-shortwave flux (due to increasing CO2 concentrations). Models underestimate the increase in incoming non-shortwave flux. This was observed when comparing the climate sensitivity (the magnitude of Arctic sea ice loss per metric ton of anthropogenic CO_2) between observations (3.0 ± 0.3 m^2) and the CMIP5 multi-model ensemble mean (1.75 ± 0.67 m^2).

As discussed in section 2.6.1, there are discrepancies between atmosphere-only models and coupled atmosphere-ocean models. The most important difference between these two is, the AGCM's does not capture the atmosphere-ocean feedbacks, hence does not capture remote effects. Further, Screen (2018) stated that AOGCM's generally agree more across models than AGCM's. AGCM's might differ from AOGCM's due to a tug-of-war between thermodynamic warming and dynamic cooling. This will be discussed below.

Climate models have difficulties in replicating the observed sea ice cover. This is a potential cause of discrepancy when comparing results across models (e.g. the CMIP5 project): despite being forced by the same emission scenario, different initial conditions will lead to different end results. As the climate response depends on the location and magnitude of the sea ice loss (see section 6.5), discrepancies in initial sea ice conditions can potentially lead to substantial differences in the end result. Therefore, being able to push the model toward the observed sea ice state, without breaking the energy conservation, would potentially decrease the uncertainty. Manuscript I focused on methods for constraining sea ice in coupled climate models, while maintaining energy conservation. The Earth is a closed system, where energy, water and mass are conserved. This is replicated by the coupled climate models: energy is redistributed in the Earth system, not created or destroyed. As the energy is already conserved in the climate models, it is desirable to maintain this energy conservation. Additionally, constraining sea ice without conserving energy would potentially lead to each model loosing or gaining a different amount of energy, thereby introducing a new source of uncertainty. By keeping the energy conserved, the energy would be redistributed in the Earth system, ensuring all models remained in radiative balance.

6.5 The impact of regional sea ice loss vs. pan-Arctic sea ice loss

Sea ice loss in different regions has different impacts on the climate. Pedersen et al. (2016) showed that the location of the northern center of the NAO shifted eastward for sea ice loss in the Pacific, while it shifted westward for sea ice loss in the Atlantic. This was further supported in Screen (2017b). They showed that sea ice loss in some regions induced a thermodynamic warming. In other regions, sea ice loss induced a dynamical cooling (e.g. BAKA). Despite this, the sum of the regional responses was a cooling of the mid- and high-latitudes, whereas the response to a pan-Arctic sea ice loss was dominated by warming. Screen (2017b) suggested that this discrepancy was due to a tug-of-war between the direct thermodynamic warming and the dynamical cooling (Screen et al. (2015b), Deser et al. (2016) and Screen (2017a)). The thermodynamic warming is a direct effect of the increased oceanic heat release to the atmosphere, as the sea ice does not shield the ocean anymore. The dynamical cooling is due to a change in the atmospheric circulation, inducing a negative AO/NAO-like pattern. This implies that the magnitude of the sea ice loss determines the response, with smaller sea ice loss leading to cooling and larger sea ice loss leading to warming. From this follows, the transient response to sea ice loss will be different from the equilibrium response, thus resulting in a non-linear response to sea ice loss (Petoukhov and Semenov (2010), Screen (2017b), Peings and Magnusdottir (2014). The Arctic sea ice decline is projected to continue, resulting in an increasing amount of sea ice disappearing and subsequently leading to the thermodynamic warming winning over the dynamical cooling.

This tug-of-war between the thermodynamic warming and the dynamic cooling have been used to explain a lack of warming over Europe. McKenna et al. (2018) found that sea ice loss in Barents-Kara Seas and in Chukchi-Bering Seas had opposite tropospheric responses to a moderate sea ice loss (negative AO and positive AO, respectively), whereas both had a similar response (negative AO) for large sea ice reductions. They found that the sea ice reductions in Barents-Kara Seas (Chukchi-Bering Seas) induced cooling over North America (Eurasia) and warming over Northern Europe (North America). They explained the lack of cooling over Northern Europe (North America) to be due to the balance between the indirect, dynamical AO-induced cooling and the direct, thermodynamic warming from the local sea ice loss. Screen (2017a) also explained the 'missing' cooling over Europe, despite an intensification of the negative NAO, as the thermodynamic warming winning over the dynamical cooling. However, both these studies used an AGCM. Smith et al. (2017) showed, the response to sea ice loss in AGCM's is dominantly thermodynamic, whereas AOGCM's induce a more dynamical response, capturing the circulation changes as well. Hence, the magnitude of the sea ice loss in AOGCM's has to be relatively larger than in AGCM's before the thermodynamic warming wins over the dynamic cooling. This corresponds well with the AGCM's lacking atmosphere-ocean feedbacks as discussed in section 6.4.

In Study II, sea ice was only reduced in BAKA, a relatively small area. According to Screen (2017b), sea ice loss in this area will lead to dynamical cooling in the form of a negative NAO. This supports the results by Petoukhov and Semenov (2010), who found a negative NAO response to moderate sea ice reductions in BAKA, associated with a cooling over Europe. The mean temperature response in Study II showed a statistically significant cooling over eastern Europe, but the resulting circulation change were not a negative NAO. The response for the 5% coldest winters showed that equally cold winters required an intensification of the Scandinavian pattern. This is not equal to a negative NAO, but both induce advection of cold Arctic air toward Europe. According to the tug-of-war between the thermodynamic warming and the dynamical cooling discussed above, we expect the thermodynamic warming from a large sea ice loss to win over the dynamical cooling, hence leading to a warming over CEU, not cooling. This is also what was observed in Study III: the CEU mean temperature increased for all periods relative to P1. The missing intensification of the Aleutian Low in Study II relative to both Study III and Screen (2018) can also be explained by the discussion above: regional sea ice loss has the largest impact on the local area, or areas in close proximity to the sea ice loss. The Aleutian Low is simply too far away from BAKA to be greatly affected.

The discussions above highlight the potential issues when only modifying sea ice in a small region. Regional sea ice loss will not result in the same responses as a pan-Arctic sea ice loss.Regardless, there are a number of reasons for our choice in the experimental setup for Study II. First of all, the aim of Study II was not to investigate the effect of the observed or projected pan-Arctic sea ice loss, but to investigate the effect of BAKA sea ice loss. By excluding sea ice loss in other regions, we also excluded the impact from sea ice loss in these regions. Secondly, several studies showed that BAKA sea ice loss affects Europe the most (Petoukhov and Semenov (2010), Koenigk et al. (2016), Kretschmer et al. (2016)). Third reason combines the tug-of-war between thermodynamic warming and dynamical cooling with the underestimation of the observed cooling stated in Mori et al. (2019). If climate models underestimate the observed cooling, reducing sea ice in the entire Arctic might drown the dynamical cooling signal from BAKA sea ice loss. As BAKA sea ice loss is a main contributor to wintertime circulation changes over Europe, we should not loose to much information by ignoring sea ice loss in the remaining regions, while still avoiding drowning the cooling signal. The balance between thermodynamic and dynamical processes appear to be tipped toward the thermodynamic warming in the models. This effect is more pronounced for AGCM's: Mori et al. (2019) compared AGCM simulations to observations and Smith et al. (2017) found that AGCM's where dominantly thermodynamic. Even though coupled AOGCM's might have a tendency to induce more dynamical responses to sea ice loss, the dynamical cooling might still be cancelled out by the thermodynamic warming. This was not investigated further.

6.6 Abrupt change

The global mean temperature is projected to increase by approximately 10°C by year 2250, relative to the pre-industrial period. This is comparable in magnitude to the temperature change during the D-O events recorded in the Greenlandic ice cores (5-15°C; section 2.4.3). This similarity have led to the question: can D-O equivalent events occur in the present and the future, and how might this affect climate? This is one of the main questions of the Ice2ice project, which this PhD thesis is a part of. Defining abrupt change as more than 1°C warming per decade for at least four consecutive decades, Jansen et al. (2019, manuscript submitted) showed that the observed temperature change from 1978-2018 in the Eurasian Arctic was an abrupt climate change. They further showed that this criterion captured all the main D-O events in the Greenlandic NGRIP core. Hence, the current observed temperature change is not only comparable in size to the D-O events, but also in rate of change.
The abrupt temperature changes in the RCP8.5 scenario simulations were associated with areas of rapid sea ice loss (Jansen et al. (2019, manuscript submitted)). This is similar to the conclusions in Pedersen and Christensen (2019, manuscript submitted). Using the CMIP5 RCP8.5 emission scenario ensemble, they investigated the impact of the historical and projected sea ice loss on the temperature change on Greenland. They found, the resulting warming was largest for areas in close proximity of the sea ice loss, and only coastal areas on Greenland were affected by the projected sea ice loss. Since most of the Arctic sea ice is currently in the central Arctic, the largest sea ice reductions will occur here. Therefore, only a part of the warming on central Greenland is associated with the sea ice loss. In particular, they found that the warming on Greenland were mostly affected by sea ice loss in the Barents-Kara region, the Greenland Sea, the Canadian Archipelago and Baffin Bay, i.e. regions close to Greenland. The impact was largest on the coastal regions facing the sea ice loss region. This is partly supported by the mean temperature changes in Study II were sea ice was reduced only in the Barents-Kara Seas. Figure 5.4 show a statistically significant warming of the entire Greenland in C80, along the northern and eastern coast in C40 and the northern coast for C20. Statistically significant cooling is seen along the eastern coast for C60. This indicate a similar pattern to that found in Pedersen and Christensen (2019, manuscript submitted), although the magnitude of the sea ice loss and warming differs.

Study III found that the rate of changes shifted after the loss of the Arctic summer sea ice (P3). Up until P3, the trend of air temperature and the oceanic northward heat transport were increasing. As was the trend of the AA. The global mean temperature trend was largest for P3, but so was the GHG forcing trend, as discussed in section 6.3. This indicate that the temperature increase cannot solely be attributed to the sea ice loss. In fact, several studies have suggested that only a minor part of the temperature increase is caused by the sea ice loss (McCusker et al. (2017), Pedersen and Christensen (2019, manuscript submitted)). The rest is caused by the increasing GHG emissions. McCusker et al. (2017) showed that the response to sea ice loss and increasing CO_2 concentrations are clearly separated in winter, adding up to give the full (sea ice loss + increasing CO_2) circulation response. They also showed, the response to either sea ice loss or increasing GHG emissions are insensitive to the background climate state. That is, the temperature increase from Arctic sea ice loss was the same for pre-industrial CO_2 concentrations as when doubling the CO_2 concentrations ($2\times CO_2$). The response from $2\times CO_2$ was the same for the pre-industrial sea ice cover and for the $2\times CO_2$ sea ice cover. If this relationship holds for the past as well, how can the temperature changes during D-O events be comparable in magnitude to the current observed global mean temperature change, when the first was driven by sea ice loss, and the second by sea ice loss and increasing GHG emissions? This is most likely due to the location of the sea ice loss as discussed above: temperature changes over areas with sea ice loss are larger than over areas with no sea ice loss. The sea ice retreat during the D-O events were in the Nordic Seas, in close proximity to Greenland. Hence, this sea ice loss affected the temperature in Greenland and subsequently the temperature reconstructions from the Greenlandic ice cores. The current observed global mean temperature could potentially have larger temperature changes over areas of sea ice loss, but Jansen et al. (2019, manuscript submitted) showed that climate models have difficulties in simulating the abruptness of the projected temperature change.

Chapter 7

Conclusion

The overall aim of this PhD thesis was to analyze the sensitivity of the climate to sea ice changes in the coupled climate model EC-Earth. The following conclusions are based on the work of the three separate manuscripts presented.

Study I concluded that nudging sea ice in a coupled climate model via the surface sensible heat flux is a suitable approach. However, maintaining energy conservation is tricky and requires more research. In this study, sea ice was nudged indirectly by nudging the sensible heat flux in EC-Earth, redistributing the extra energy ΔHF in the atmosphere. Method 1 succeeded in reaching the target sea ice cover, yet it did not redistribute ΔHF in the atmosphere. Instead, ΔHF disappeared into space. Hence, this method was not energy conserving. Implementing a manual energy distribution of the extra energy ΔHF in the atmospheric component of EC-Earth lead to a nudging that was energy conserving, but it warmed/cooled the atmosphere too much. This caused the model to crash within a few years. Several ideas on how to circumvent this issue was proposed, the most realistic solution being to redistribute the energy in the ocean instead of the atmosphere. This idea was not tested. We concluded that the idea of nudging the heat flux instead of the sea ice directly is a suitable method for nudging sea ice in a coupled model, but instead of redistributing the energy ΔHF in the atmosphere, the best method for nudging sea ice is to remove ΔHF.

Study II concluded that although the mean temperature over all years showed a weak cooling over eastern Europe for a target of 60% sea ice concentration relative to climatology, this was not observed for the 5% coldest winters. Here, our results showed that to obtain equally cold Central European winters required an intensification of the Scandinavian pattern with reduced Barents-Kara sea ice. Study II reduced sea ice concentration in the BAKA region to a target of 100% (C100), 80% (C80), 60% (C60), 40% (C40) and 20% (C20). The mean temperature response showed a weak non-linear cooling for C60 for a small area over eastern Europe. Averaging over a larger area of Europe, the statistical significance disappeared, resulting in only C40 and C20 being significantly different from C100. The temperature over Central Europe for the 5% coldest winters were not significantly different from C100 for either of the four sea ice reduced simulations. However, the temperature difference between C40 and C80 were significantly different. The circulation also differed between the mean response and response for the 5% coldest winters. The mean response showed a low pressure anomaly over BAKA, deepening with sea ice reductions. The 5% coldest winters response showed an intensification of the high pressure anomaly over Scandinavia, i.e. the Scandinavian pattern. Other studies have shown, climate models tend to underestimate the observed cooling over Europe, possibly explaining the weak cooling in C60.

Preliminary results from Study III suggested that the sea ice state have an impact on the climate. There appeared to be a shift in trends for some parameters after the Arctic became seasonally ice-free, however this coincided with changes in the radiative forcing. The rising global temperature led to increased temperature variability over low and mid-latitudes and decreased variability over high latitudes. Extreme temperatures were overall projected to become less extreme, except for European summers. Here, they were projected to become more extreme. The north-south temperature gradient (the Arctic Amplification) was projected to decrease, but not disappear entirely, when the Arctic sea ice disappeared.
Increased temperatures led to intensified precipitation patterns: wet-get-wetter and dry-get-drier. Further, an increase in variability and extremes were observed. Extreme precipitation (low and high precipitation) especially increased over Southeast Asia, Indicating larger interannual variability for the Asian monsoon. Our results also indicate an equatorward shift of the ITCZ.
The projected atmospheric circulation showed three things: 1) a trend toward more positive AO patterns in autumn, 2) an intensification of the Aleutian Low in winter and spring and 3) a weaker Hadley circulation.
The Arctic Ocean and the Barents Sea were projected to become warmer and fresher, strengthening the stratification. An exception to was a preliminary weakening of the stratification in the Barents Sea due to atlantification (a shallower Atlantic Water core, increased vertical mixing). The freshening of the Arctic Ocean was most likely due to increased net precipitation (P-E), not increased fresh water input from the Greenland Ice Sheet. The warming of the Arctic Ocean were associated with an increased heat transport into the Arctic Ocean.
Manuscript III is still ongoing work. The preliminary results discussed above have led to several ideas for further analyses: do the strong stratification in the Arctic Ocean lead to reduced heat release? And how does Greenland react to the sea ice changes? The later were only briefly investigated.

The three manuscripts presented above all investigate the sensitivity of sea ice changes on the climate. They find that the magnitude, location and rate of the sea ice loss plays a large role in the impact on the climate (Study II and III). As we are currently experiencing an accelerating Arctic sea ice loss, it is important to simulate the impact from sea ice changes correctly in climate models. However, current climate models have difficulties replicating the observed sea ice loss. Correcting this by assimilation or nudging might introduce new issues (Study I). Several approaches for nudging sea ice in coupled climate models, while maintaining energy conservation, are proposed in this thesis. This could potentially improve the coupled climate models, leading to even better model predictions in the future.

Chapter 8

Bibliography

K. Aagaard, L. K. Coachman, and E. Carmack. On the halocline of the Arctic Ocean. *Deep-Sea Research*, 28A:529–545, 1981.

M. Aarthun and T. Eldevik. Quantifying the influence of Atlantic heat and Barents sea ice variability and retreat. *Journal of Climate*, 25:4736–4743, 2012.

J. P. Abraham, M. Baringer, N. L. Bindoff, T. Boyer, L. J. Cheng, J. A. Church, J. L. Conroy, C. M. Domingues, J. T. Fasullo, J. Gilson, G. Goni, S. A. Good, J. M. Gorman, V. Gouretski, M. Ishii, G. C. Johnson, S. Kizu, J. M. Lyman, A. M. Macdonald, W. J. Minkowycz, S. E. Moffitt, M. D. Palmer, A. R. Piola, F. Reseghetti, K. Schuckmann, K. E. Trenberth, I. Velicogna, and J. K. Willis. A review of global ocean temperature observations: implications for ocean heat content estimates and climate change. *Reviews of Geophysics*, 51, 2013.

O. Adam, T. Bischoff, and T. Schneider. Seasonal and interannual variations of the energy flux equator and ITCZ. Part 1: Zonally averaged ITCZ position. *Journal of Climate*, 29, 2016.

T. Albrecht, A. Aschwanden, J. Brown, E. Bueler, D. DellaGiustina, M. Haselhoff, R. Hock, C. Khroulev, C. Lingle, M. Martin, D. Maxwell, N. Shemonski, R. Winkelmann, and F. Ziemen. Pism, a Parallel Ice Sheet Model: User's Manual. 2012.

R. J. Allen and C. S. Zender. Forcing of the Arctic Ocean by Eurasian snow cover. *Journal of Climate*, 224:6528–6539, 2011.

AMAP. *AMAP Assesment Report: Arctic Pollution Issues. Arctic Monitoring and Assesment Programme (AMAP)*. 1998. Oslo, Norway. xii+859 pp.

M. A. Balmaseda, L. Ferranti, F. Molteni, and T. N. Palmer. Impact of 2007 and 2008 arctic ice anomalies on the atmospheric circulation: Implications for long-range predictions. *Quarterly Journal of the Royal Meteorological Society*, 136(652):1655–1664, 2010. doi: 10.1002/qj.661. URL https://rmets.onlinelibrary.wiley.com/doi/abs/10.1002/qj.661.

A. G. Barnston and R. E. Livezey. Classification, seasonality and persistence of low-frequency atmospheric circulation patterns. *Monthly Weather Review*, 115(6):1083–1126, 1987. doi: 10.1175/1520-0493(1987)115<1083:CSAPOL>2.0.CO;2. URL https://doi.org/10.1175/1520-0493(1987)115<1083:CSAPOL>2.0.CO;2.

R. Blackport and P. J. Kushner. The transient equilibrium climate response to rapid summertime sea ice loss in CCSM4. *Journal of Climate*, 29:401–417, 2016.

R. Blackport and P. J. Kushner. Isolating the atmospheric circulation response to Arctic sea ice loss in the coupled climate system. *Journal of Climate*, 30:2163–2185, 2017.

L. Brodeau and T. Koenigk. Extinction of the northern oceanic deep convection in an ensemble of climate model simulations of the 20th and 21st centuries. *Climate Dynamics*, 2015.

K. D. Burke, J. W. Williams, M. A. Chandler, A. M. Haywood, D. J. Lunt, and B. L. Otto-Bliesner. Pliocene and Eocene provide best analogs for near-future climates. *PNAS*, 115:13288–13293, 2018.

R. Caballero and P. L. Langen. The dynamic range of poleward energy transport in an atmospheric general circulation model. *Geophysical Research Letters - GEOPHYS RES LETT*, 32, 01 2005. doi: 10.1029/2004GL021581.

J. Cattiaux, R. Vautard, C. Cassou, P. Yiou, V. Masson-Delmotte, and F. Codron. Winter 2010 in europe: A cold extreme in a warming climate. *Geophysical Research Letters*, 37 (20), 2010. doi: 10.1029/2010GL044613. URL `https://agupubs.onlinelibrary.wiley.com/doi/abs/10.1029/2010GL044613`.

W. Cheng, J. C. H. Chiang, and D. Zhang. Atlantic meridional overturning circulation (amoc) in cmip5 models: Rcp and historical simulations. *Journal of Climate*, 26(18):7187–7197, 2013. doi: 10.1175/JCLI-D-12-00496.1.

J. Cohen, M. Barlow, P. J. Kushner, and K. Saito. Stratosphere-troposphere coupling and links with Eurasian land surface variability. *Journal of Climate*, 20:5335–5343, 2007.

J. Cohen, J. Foster, M. Barlow, K. Saito, and J. Jones. Winter 2009–2010: A case study of an extreme arctic oscillation event. *Geophysical Research Letters*, 37(17), 2010. doi: 10.1029/2010GL044256. URL `https://agupubs.onlinelibrary.wiley.com/doi/abs/10.1029/2010GL044256`.

J. Cohen, J. C. Furtado, M. Barlow, V. A. Alexeev, and J. E. Cherry. Arctic warming, increasing snow cover and widespread boreal winter cooling. *Environmental Research Letters*, 7, 2012.

J. Cohen, J. A. Screen, J. C. Furtado, M. Barlow, D. Whittleston, D. Coumou, J. Francis, K. Dethloff, D. Entekhabi, J. Overland, and J. Jones. Recent Arctic amplifictaion and extreme mid-latitude weather. *Nature Geoscience*, 7:627–637, 2014.

A. Dai, D. Luo, M. Song, and J. Liu. Arctic amplification is caused by sea-ice loss under increasing CO_2. *Nature Communications*, 10, 2019.

W. Dansgaard, S. J. Johnson, H. B. Clausen, D. Dahl-Jensen, N. S. Gundestrup, C. U. Hammer, C. S. Hvidberg, J. P. Steffensen, A. E. Sveinbjörnsdottir, J. Jouzel, and G. Bond. Evidence for general instability of past climate from a 250-kyr ice-core record. *Nature*, 364:218–220, 1993.

S. D. L. J. C. U. Dean Roemmich | Scripps Institution of Oceanography, University of California, N. O. Gregory C. Johnson | Ocean Climate Research Division, Pacific Marine Environmental Laboratory, W. U. Atmospheric Administration (NOAA), Seattle, S. W. U. Stephen

Riser | University of Washington, School of Oceanography, U. L. J. C. U. Russ Davis | Instrument Development Group, Scripps Institution of Oceanography, S. D. L. J. C. U. John Gilson | Scripps Institution of Oceanography, University of California, M. U. W. Brechner Owens | Woods Hole Oceanographic Institution, Woods Hole, A. O. Silvia L. Garzoli | Physical Oceanography Division, M. F. U. Meteorological Laboratory, NOAA, A. O. Claudia Schmid | Physical Oceanography Division, M. F. U. Meteorological Laboratory, NOAA, M. I. . U. N. F. N. Meteorological, and C. U. Oceanography Center, Monterey. The argo program: Observing the global ocean with profiling floats. *Oceanography*, 22, June 2009. URL `https://doi.org/10.5670/oceanog.2009.36`.

C. Deser, R. A. Tomas, and L. Sun. The role of the ocean-atmosphere coupling in the zonal-mean atmospheric response to arctic sea ice loss. *Journal of Climate*, 28:2168–2186, 2015.

C. Deser, L. Sun, R. A. Tomas, and J. Screen. Does ocean coupling matter for the northern extratropical response to projected Arctic sea ice loss? *Geophysical Research Letters*, 43, 2016.

Q. Ding, A. Schweiger, M. L'Heureux, E. J. Steig, D. S. Battisti, N. C. Johnson, E. Blanchard-Wrigglesworth, S. Po-Chedley, Q. Zhang, K. Harnos, M. Bushuk, B. Markle, and I. Baxter. Fingerprints of internal drivers of Arctic sea ice loss in observations and model simulations. *Nature Geoscience*, 12:28–33, 2019.

T. M. Dokken, K. H. Nisancioglu, C. Li, D. S. Battisti, and C. Kissel. Dansgaard-Oeschger cycles: Interactions between ocean and sea ice intrinsic to the Nordic seas. *Paleoceanography*, 28: 491–502, 2013.

EC-Earth Consortium. EC-Earth. `http://www.ec-earth.org`. Accessed: 2019-05-09.

ECMWF. *Part IV: Physical Processes*. Number 4 in IFS Documentation. ECMWF, 2010 2010. URL `https://www.ecmwf.int/node/9233`. Operational implementation 26 January 2010.

T. Fichefet and M. M. Maqueda. Sensitivity of a global sea ice model to the treatment of ice thermodynamics and dynamics. *Journal of Geophysical Research*, 102(C6):12609–12646, 1997.

J. Francis and S. J. Vavrus. Evidence for a wavier jet stream in response to rapid arctic warming. *Environmental Research Letters*, 10, 2015.

D. M. W. Frierson and Y.-T. Hwang. Extratropical influence on ITCZ shifts in slab ocean simulations of global warming. *Journal of Climate, volume =*, 2012.

J. Garcia-Serrano, C. Frankignoul, and G. Gastineau. On the predictability of the winter Euro-Atlantic climate: Lagged influence of autumn Arctic sea ice. *Journal of Climate*, 28:5195–5216, 2015.

G. Gastineau, J. Garcia-Serrano, and C. Frankignoul. The influence of autumnal Eurasian snow cover on climate and its link with Arctic sea ice cover. *Journal of Climate*, 30:7599–7619, 2017.

P. D. Gingerich. Temporal scaling of carbon emission and accumulation rates: Modern anthropogenic emissions compared to estimates of petm onset accumulation. *Paleoceanography and Paleoclimatology*, 34(3):329–335, 2019. doi: 10.1029/2018PA003379. URL `https://agupubs.onlinelibrary.wiley.com/doi/abs/10.1029/2018PA003379`.

K. Guirguis, A. Gershunov, R. Schwartz, and S. Bennett. Recent warm and cold daily winter temperature extremes in the northern hemisphere. *Geophys. Res. Lett*, 38, 09 2011. doi: 10.1029/2011GL048762.

C. Guo, K. Nisancioglu, H. Sadatzki, T. Dokken, and E. Jensen. Dynamical sequences of ocean, atmosphere and sea ice processes over an abrupt cold-to-warm climate transition in the marine istope stage 3. 2019, manuscript in preparation.

K. Hartung, G. Svensson, H. Struthers, A.-L. Deppenmeier, and W. Hazeleger. An ec-earth coupled atmosphere-ocean single-column model (aoscm) for studying coupled marine and polar processes. *Geoscientific Model Development Discussions*, pages 1–35, 03 2018. doi: 10.5194/gmd-2018-66.

W. Hazeleger, X. Wang, C. Severijns, S. Stefanscu, R. Bintanja, A. Sterl, K. Wyser, T. Semmler, S. Yang, B. van den Hurk, T. van Noije E. van der Linden, and K. van der Wiel. EC-Earth: A seamless Earth-system prediction approach in action. *Bull. Am. Meteorol. Soc.*, 91:1357–1363, 2010.

W. Hazeleger, C. Severijns, T. Semmler, S. Stefanscu, S. Yang, X. Wang, K. Wyser, E. Dutra, J. M. Baldasano, R. Bintanja, P. Bougeault, R. Caballero, A. N. L. Ekman, J. . H. Christensen, B. van den Hurk, P. Jimenez, C. Jones, P. Kållberg, T. Koenigk, R. McGrath, P. Miranda, T. van Noije, T. Palmer, J. A. Parodi, T. Schmith, F. Selten, T. Storelvmo, A. Sterl, H. Tapamo, M. Vancoppenolle, P. Viterbo, and U. Willén. EC-Earth V2.2: description and validation of a new seamless earth system prediction model. *Climate Dynamics*, 39:2611–2629, 2012.

R. X. Huang. *Ocean Circulation: Wind-driven and Thermohaline processes*. Cambridge University Press, 2010.

J. W. Hurrell, Y. Kushnir, G. Ottersen, and M. Visbeck. *An Overview of the North Atlantic Oscillation*, pages 1–35. American Geophysical Union (AGU), 2013. ISBN 9781118669037. doi: 10.1029/134GM01. URL `https://agupubs.onlinelibrary.wiley.com/doi/abs/10.1029/134GM01`.

IPCC. *Climate Change 2013: The Physical Science Basis. Contribution of Working Group I to the Fifth Assessment Report of the Intergovernmental Panel on Climate Change*. Cambridge University Press, Cambridge, United Kingdom and New York, NY, USA, 2013. ISBN ISBN 978-1-107-66182-0. doi: 10.1017/CBO9781107415324. URL `www.climatechange2013.org`.

E. Jansen, J. H. Christensen, T. Dokken, K. H. Nisancioglu, B. M. Vinther, E. Capron, C. Guo, M. F. Jens, P. L. Langen, R. A. Pedersen, S. Yang, M. Bentsen, H. A. Kjær, H. Sadatzki, E. Sessford, and M. Stendel. The start of a new era of abrupt climate change - perspectives from the past. 2019, manuscript submitted.

M. F. Jensen, K. H. Nisancioglu, and M. A. Spall. Large changes in sea ice triggered by small changes in Atlantic water temperature. *Journal of Climate*, 31(12):4847–4863, 2018.

E. Kalnay. *Atmospheric modeling, data assimilation and predictability*. Cambridge University Press, Cambridge, UK, 2012.

B.-M. Kim, S.-W. Son, S.-K. Min, J.-H. Jeong, S.-J. Kim, X. Zhang, T. Shim, and J.-H. Yoon. Weakening of the stratospheric polar vortex by Arctic sea ice. *Nature Communications*, 5:4646, 2014.

M. Kimmritz, F. Counillon, C. M. Bitz, F. Massonnet, I. Bethke, and Y. Gao. Optimising assimilation of sea ice concentration in an Earth system model with a multicategory sea ice model. *Tellu A: Dynamic Meteorology and Oceanography*, 70, 2018.

P. Kindler, M. Guillevic, M. Baumgartner, J. Schwander, A. Landais, and M. Leuenberger. Temperature reconstruction from 10 to 120 kyr b2k from the ngrip ice core. *Climate of the Past*, 10(2):887–902, 2014. doi: 10.5194/cp-10-887-2014. URL `https://www.clim-past.net/10/887/2014/`.

K. Kjeldsen, N. Korsgaard, A. Bjørk, S. Khan, J. Box, S. Funder, N. Larsen, J. Bamber, W. Colgan, M. van den Broeke, M.-L. Siggaard-Andersen, C. Nuth, A. Schomacker, C. Andresen, E. Willerslev, and K. Kjær. Spatial and temporal distribution of mass loss from the greenland ice sheet since ad 1900. *Nature*, 528, 2015. doi: 10.1038/nature16183.

J. A. Knauss. *Introduction to physical oceanography*. Waveland Press, Inc, 1997.

T. Koenigk, L. Brodeau, R. G. Graversen, J. Kalrsson, G. Svensson, micheal Tjernström, U. Willén, and K. Wyser. Arctic climate change in 21st century CMIP5 simulations with EC-Earth. *Climate Dynamics*, 40:2719–2743, 2013.

T. Koenigk, M. Calan, G. Nikulin, and S. Schimanke. Regional Arctic sea ice variations as predictor for winter climate conditions. *Climate Dynamics*, 46:317–337, 2016.

E. W. Kolstad, T. Breiteig, and A. A. Scaife. The association between stratospheric weak polar vortex events and cold air outbreaks in the Northern Hemisphere. *Q. J. R. Meteorol. Soc.*, 136: 886–893, 2010.

M. Kretschmer, D. Coumou, J. F. Donges, and J. Runge. Using causal effect networks to analyze different Arctic drivers of midlatitude winter circulation. *Journal of Climate*, 29(11):4069–4081, 2016. doi: 10.1175/JCLI-D-15-0654.1.

M. Kretschmer, J. Cohen, V. Matthias, J. Runge, and D. Coumou. The different stratospheric influence on cold-extremes in Eurasia and North America. *Climate and Atmospheric Science*, 1, 2018.

P. L. Langen and V. A. Alexeev. Polar amplification as a preferred response in an idealized aquaplanet GCM. *Climate Dynamics*, 29:305–317, 2007.

M. S. Lozier, F. Li, S. Bacon, F. Bahr, A. S. Bower, S. A. Cunningham, M. F. de Jong, L. de Steur, B. deYoung, J. Fischer, S. F. Gary, B. J. W. Greenan, N. P. Holliday, A. Houk, L. Houpert, M. E. Inall, W. E. Johns, H. L. Johnson, C. Johnson, J. Karstensen, G. Koman, I. A. Le Bras, X. Lin, N. Mackay, D. P. Marshall, H. Mercier, M. Oltmanns, R. S. Pickart, A. L. Ramsey, D. Rayner, F. Straneo, V. Thierry, D. J. Torres, R. G. Williams, C. Wilson, J. Yang, I. Yashayaev, and J. Zhao. A sea change in our view of overturning in the subpolar north atlantic. *Science*, 363(6426):516–521, 2019. ISSN 0036-8075. doi: 10.1126/science.aau6592. URL `https://science.sciencemag.org/content/363/6426/516`.

G. Madec and the NEMO team. *NEMO ocean engine*. Note du Pôle de modélisation de l'Institut Pierre-Simon Laplace, France, No 27, 2008.

M. S. Madsen, S. Yang, G. Adalgeirsdottir, S. H. Svendsen, C. Rodehacke, and I. M. Ringgaard. Interactions of the greenland ice sheet with the climate system in warm scenarios as simulated in ec-earth-pism. 2019, manuscript in preparation.

K. E. McCusker, J. C. Fyfe, and M. Sigmond. Twenty-five winters of unexpected Eurasian cooling unlikely due to Arctic sea-ice loss. *Nature Geoscience*, 9:838–843, 2016.

K. E. McCusker, P. J. Kushner, J. C. Fyfe, M. Sigmond, V. V. Kharin, and C. M. Bitz. Remarkable separability of circulation response to Arctic sea ice loss and greenhouse gas forcing. *Geophysical Research Letters*, 44:7955–7964, 2017.

C. M. McKenna, T. J. Bracegirdle, E. F. Shuckburgh, P. H. Haynes, and M. M. Joshi. Arctic sea ice loss in different regions leads to contrasting Northern hemisphere impacts. *Geophysical Research Letters*, 45:945–954, 2018.

M. Meinshausen, S. J. Smith, K. Calvin, J. S. Daniel, M. L. T. Kainuma, J.-F. Lamarque, K. Matsumoto, S. A. Montzka, S. C. B. Raper, K. Riahi, A. Thomson, G. J. M. Velders, and D. P. P. van Vuuren. The RCP greenhouse gas concentrations and their extensions from 1765-2300. *Climatic Change*, 109:213–241, 2011.

V. P. Meleshko, V. M. Kattsov, V. M. Mirvis, A. V. Baidin, T. V. Pavlova, and V. A. Govorkova. Is there a link between arctic sea ice loss and increasing frequency of extremely cold winters in eurasia and north america? synthesis of current research. *Russian Meteorology and Hydrology*, 43(11):743–755, Nov 2018. ISSN 1934-8096. doi: 10.3103/S1068373918110055. URL `https://doi.org/10.3103/S1068373918110055`.

M. Mori, M. Watanabe, H. Shiogama, J. Inoue, and M. Kimoto. Robust Arctic sea-ice influence on the frequent Eurasian cold winters in past decades. *Nature Geoscience Letters*, 7, 2014.

M. Mori, Y. Kosaka, M. Watanabe, H. Nakamura, and M. Kimoto. A reconciled estimate of the influence of Arctic sea-ice loss on recent Eurasian cooling. *Nature Climate Change*, 9:123–129, 2019.

J. Müller, A. WAgner, K. Fahl, R. Stein, M. Prange, and G. Lohmann. Towards quantitative sea ice reconstructions in the northern North Atlantic: a combined biomarker and numerical modelling approach. *Earth and Planetary Science Letters*, 306:137–148, 2011.

T. Nakamura, K. Yamazaki, K. Iwamoto, M. Honda, Y. Miyoshi, Y. Ogawa, and J. Ukita. A negative phase shift of the winter AO/NAO due to recent Arctic sea-ice reduction in late autumn. *Journal of Geophysical Research: Atmospheres*, 120:3209–3227, 2015.

A. L. Niederdrenk and D. Notz. Arctic sea ice in a 1.5°C warmer world. *Geophysical Research Letters*, 45(4):1963–1971, 2018. doi: 10.1002/2017GL076159. URL `https://agupubs.onlinelibrary.wiley.com/doi/abs/10.1002/2017GL076159`.

D. Notz and J. Stroeve. Observed Arctic sea-ice loss directly follows anthropogenic CO_2 emission. *Science*, 354:747–750, 2016.

F. Ogawa, N. Keenlyside, Y. Gao, T. Koenigk, S. Yang, L. Suo, T. Wang, G. Gastineau, T. Nakamura, H. N. Cheung, N.-E. Omrani, J. Ukita, and V. Semenov. Evaluating impacts of recent Arctic sea ice loss on the Northern hemisphere winter climate change. *Geophysical Research Letters*, 45(7):3255–3263, 2018. doi: 10.1002/2017GL076502.

I. H. Onarheim, T. Eldevik, and L. H. Smedsrud. Seasonal and regional manifestation of Arctic sea ice loss. *Journal of Climate*, 31, 2018.

J. M. Osborne, J. A. Screen, and M. Collins. Ocean–atmosphere state dependence of the atmospheric response to arctic sea ice loss. *Journal of Climate*, 30(5):1537–1552, 2017. doi: 10.1175/JCLI-D-16-0531.1. URL `https://doi.org/10.1175/JCLI-D-16-0531.1`.

OSISAF. Osi-450: Sea ice concentration data record of the eumetsat ocean and sea ice satellite application facility (osi saf), 2017. URL `http://www.osi-saf.org/?q=content/global-sea-ice-concentration-data-record-smmrssmissmis`. Accessed: 2019-04-08.

T. Oudar, E. Sanchez-Gomez, F. Chauvin, and J. Cattiaux. Respective roles of the direct GHG radiative forcing and induced Arctic sea ice loss on the Northern hemisphere atmospheric circulation. *Clim. Dyn.*, 49:3693–3713, 2017.

S. D. Outten and I. Esau. A link between Arctic sea ice and recent cooling trends over Eurasia. *Climate Change*, 110:1069–1075, 2012.

PAGES2k Consortium. A global multiproxy database for temperature reconstructions of the common era. *Scientific Data*, 4, 2017. doi: 10.1038/sdata.2017.88.

W. Paterson. 15 - ice core studies. In W. Paterson, editor, *The Physics of Glaciers (Third Edition)*, pages 378 – 409. Pergamon, Amsterdam, third edition edition, 1994. ISBN 978-0-08-037944-9. doi: https://doi.org/10.1016/B978-0-08-037944-9.50021-2. URL `http://www.sciencedirect.com/science/article/pii/B9780080379449500212`.

R. A. Pedersen and J. H. Christensen. Attributing Greenland warming patterns to regional Arctic sea ice loss. 2019, manuscript submitted.

R. A. Pedersen, I. Cvijanovic, P. L. Langen, and B. M. Vinther. The impact of regional Arctic sea ice loss on atmospheric circulation and NAO. *Journal of Climate*, 29:889–902, 2016.

Y. Peings and G. Magnusdottir. Response of the wintertime Northern hemisphere atmospheric circulation to current and projected Arctic sea ice decline: A numerical study with CAM5. *Journal of Climate*, 27:244–264, 2014.

V. Petoukhov and V. A. Semenov. A link between reduced Barents-Kara sea ice and cold winter extremes over Northern continents. *Journal of Geophysical Research*, 115, 2010.

R. E. Petrie, L. C. Shaffrey, and R. T. Sutton. Atmospheric impact of Arctic sea ice loss in a coupled ocean-atmosphere simulation. *Journal of Climate*, 28:9606–9622, 2015.

F. Pithan and T. Mauritsen. Arctic amplification dominated by temperature feedbacks in contemporary climate models. *Nature Geoscience*, 2014.

I. V. Polyakov, A. V. Pnyushkov, M. B. Alkire, I. N. Ashik, T. M. Baumann, E. C. Carmack, I. Goszczko, J. Guthrie, V. V. I. andTorsten Kanzow, R. Krishfield, R. Kwok, A. Sundfjord, J. Morison, R. Rember, and A. Yulin. Greater role for Atlantic inflows on sea-ice loss in the Eurasian Basin and the Arctic Ocean. *Science*, 356:285–291, 2017.

D. Randall. *Introduction to the Global Circulation of the Atmosphere (ARC).* Princeton University Press, 2015. ISBN 9781400897445. URL `https://books.google.dk/books?id=3MZHAQAACAAJ`.

I. M. Ringgaard, S. Yang, E. Kaas, and J. H. Christensen. Nudging sea ice in the coupled climate model ec-earth. 2019a. Manuscript ready for submission.

I. M. Ringgaard, S. Yang, E. Kaas, and J. H. Christensen. Barents-kara sea ice and european winters in ec-earth. 2019b. Manuscript is in review for Climate Dynamics.

I. M. Ringgaard, S. Yang, E. Kaas, and J. H. Christensen. Rcp8.5?? 2019c. Manuscript in submission.

W. F. Ruddiman. *Earth's climate: Past and future*. W. H. Freeman and Company, New York, 2008.

B. Rudels, L. G. Anderson, and E. P. Jones. Formation and evolution of the surface mixed layer and halocline of the Arctic Ocean. *Journal of Geophysical Research*, 101:8807–8821, 1996.

B. Rudels, E. P. Jones, U. Schauer, and P. Eriksson. Atlantic sources of the Arctic Ocean surface and halocline waters. *Polar Research*, 23(2):181–208, 2004.

P. Ruggieri, R. Buizza, and G. Visconti. On the link between Barents-Kara sea ice variability and European blocking. *Journal of Geophysical Research: Atmospheres*, 121:5664–5679, 2016.

H. Sadatzki, T. M. Dokken, S. M. P. Berben, F. Muschitiello, R. Stein, K. Fahl, L. Menviel, A. Timmermann, and E. Jansen. Sea ice variability in the southern Norwegian Sea during glacial Dansgaard-Oeschger climate cycles. *Science Advances*, 5, 2019.

A. A. Scaife and J. R. Knight. Ensemble simulations of the cold european winter of 2005-2006. *Quarterly Journal of the Royal Meteorological Society*, 134(636):1647–1659, 2008. doi: 10.1002/qj.312. URL `https://rmets.onlinelibrary.wiley.com/doi/abs/10.1002/qj.312`.

J. A. Screen. Influence of Arctic sea ice on European summer precipitation. *Environmental Research Letters*, 8, 2013.

J. A. Screen. The missing Northern European winter cooling response to Arctic sea ice loss. *Nature Communications*, 2017a.

J. A. Screen. Simulated atmospheric response to regional and pan-Arctic sea ice loss. *Journal of Climate*, 30:3945–3962, 2017b.

J. A. Screen. Consistency and discrepancy in the atmospheric response to Arctic sea-ice loss across climate models. *Nature Geoscience*, 2018.

J. A. Screen and I. Simmonds. The central role of diminishing sea ice in recent Arctic temperature amplification. *Nature Letters*, 2010.

J. A. Screen, C. Deser, and L. Sun. Projected changes in regional climate extremes arising from Arctic sea ice loss. *Environmental Research Letters*, 10, 2015a.

J. A. Screen, C. Deser, and L. Sun. Reduced risk of North American cold extremes due to continued Arctic sea ice loss. *American Meteorological Society*, 2015b.

T. Semmler, L. Stulic, T. Jung, N. Tilinina, C. Campos, S. Gulev, and D. Koracin. Seasonal atmospheric responses to reduced Arctic sea ice in an ensemble of coupled model simulations. *Journal of Climate*, 29:5893–5913, 2016.

M. C. Serreze, A. P. Barrett, J. C. Stroeve, D. N. Kindig, and M. M. Holland. The emergence of surface-based Arctic amplification. *The Cryosphere*, 3:11–19, 2009.

Q. Shu, Z. Song, and F. Qiao. Assessment of sea ice simulations in the cmip5 models. *The Cryosphere*, 9(1):399–409, 2015. doi: 10.5194/tc-9-399-2015. URL `https://www.the-cryosphere.net/9/399/2015/`.

D. A. Smeed, S. A. Josey, C. Beaulieu, W. E. Johns, B. I. Moat, E. Frajka-Williams, D. Rayner, C. S. Meinen, M. O. Baringer, H. L. Bryden, and G. D. McCarthy. The north atlantic ocean is in a state of reduced overturning. *Geophysical Research Letters*, 45(3):1527–1533.

D. M. Smith, N. J. Dunstone, A. A. Scaife, E. K. Fiedler, D. Copsey, and S. C. Hardman. Atmospheric response to Arctic and Antarctic sea ice: The importance of ocean-atmosphere coupling and background state. *Journal of Climate*, 30:4547–4565, 2017.

S. Sorokina, C. Li, J. J. Weitstein, and N. G. Kvamstø. Observed atmospheric coupling between Barents Sea ice and the Warm-Arctic Cold-Siberia anomaly pattern. *Journal of Climate*, 29: 495–511, 2016.

A. Sterl, R. Bintanja, L. Brodeau, E. Gleeson, T. Koenigk, T. Schmith, T. Semmler, C. Severijns, K. Wyser, and S. Yang. A look at the ocean in the EC-Earth climate model. *Climate Dynamics*, 39:2631–2657, 2012.

T. F. Stocker and S. J. Johnsen. A minimum thermodynamic model for the bipolar seesaw. *Paleoceanography*, 18(4), 2003. doi: 10.1029/2003PA000920. URL `https://agupubs.onlinelibrary.wiley.com/doi/abs/10.1029/2003PA000920`.

J. Stroeve and D. Notz. Changing state of Arctic sea ice across all seasons. *Environmental Research Letters*, 13, 2018.

J. C. Stroeve, V. Kattsov, A. Barrett, M. Serreze, T. Pavlova, M. Holland, and W. N. Meier. Trends in arctic sea ice extent from cmip5, cmip3 and observations. *Geophysical Research Letters*, 39 (16), 2012. doi: 10.1029/2012GL052676. URL `https://agupubs.onlinelibrary.wiley.com/doi/abs/10.1029/2012GL052676`.

S. H. Svendsen, M. S. Madsen, S. Yang, C. Rodehacke, and G. Adalgeirsdóttir. An introduction to the coupled EC-Earth-PISM model system. *DMI Scientific Report*, 15-05, 2015.

N. C. Swart, J. C. Fyfe, E. Hawkins, J. E. Kay, and A. Jahn. Influence of internal variability on Arctic sea-ice trends. *Nature Climate Change*, 5, 2015.

K. E. Taylor, R. J. Stouffer, and G. A. Meehl. An overview of CMIP5 and the experiment design. *American Meteorological Society*, 93:485–498, 2012.

D. W. J. Thompson and J. M. Wallace. The arctic oscillation signature in the wintertime geopotential height and temperature fields. *Geophysical Research Letters*, 25(9):1297–1300, 1998. doi: 10.1029/98GL00950. URL `https://agupubs.onlinelibrary.wiley.com/doi/abs/10.1029/98GL00950`.

S. Tietsche, D. Notz, J. H. Jungclaus, and J. Marotzke. Assimilation of sea-ice concentration in a global climate model - physical and statistical aspects. *Ocean Science*, 9:19–36, 2013.

K. Vaage, L. Papritz, L. Haavik, M. A. Spall, and G. W. K. Moore. Ocean convection linked to the recent ice edge retreat along east greenland. *Nature Communications*, 9:19–36, 2018.

S. Valcke. The oasis3 coupler: a european climate modelling community software. *Geoscientific Model Development*, 6:373–388, 2013.

G. J. Van Oldenborgh, R. Haarsma, H. De Vries, and M. R. Allen. Cold extremes in north america vs. mild weather in europe: The winter of 2013–14 in the context of a warming world. *Bulletin of the American Meteorological Society*, 96(5):707–714, 2015. doi: 10.1175/BAMS-D-14-00036.1. URL `https://doi.org/10.1175/BAMS-D-14-00036.1`.

M. Vancoppenolle, S. Bouillon, T. Fichefet, H. Goosse, O. Lecomte, M. A. M. Maqueda, and G. Madec. *LIM The Louvain-la-Neuve sea Ice Model*. Note du Pôle de modélisation de l'Institut Pierre-Simon Laplace, France, No 31, 2012.

T. Vihma. Effects of arctic sea ice decline on weather and climate: A review. *Surveys in Geophysics*, 35(5):1175–1214, Sep 2014. ISSN 1573-0956. doi: 10.1007/s10712-014-9284-0. URL `https://doi.org/10.1007/s10712-014-9284-0`.

J. M. Wallace and P. V. Hobbs. *Atmospheric Science - An introductory survey*. Academic Press, Massachusetts, USA, 2006.

S. Yang and J. H. Christensen. Arctic sea ice reduction and European cold winters in CMIP5 climate change experiments. *Geophysical Research Letters*, 39, 2012.

List of Abbreviations

AA	Arctic Amplification.
AGCM	Atmosphere General Circulation model.
AMOC	Atlantic Meridional Overturning Circulation.
AO	Arctic Oscillation.
AOGCM	Atmosphere-Ocean General Circulation model.
AW	Atlantic Water.
CEU	Central Europe.
D-O	Dansgaard-Oeshger.
ECMWF	European Centre of Medium-Range Weather Forecasts.
ECP	Extended Concentration Pathway.
EU	Europe.
GCM	General Circulation model.
GHG	Greenhouse Gas.
GIS	Greenland Ice Sheet.
IFS	ECMWF's Integrated Forecast System.
ITCZ	Intertropical Convergence Zone.
LIM	Louvain-la-Neuve sea Ice Model.
LWR	Long Wave Radiation.
MIS3	Marine Isotope Stage 3.
NAO	North Atlantic Oscillation.
NEMO	Nucleus for European Modelling of the Ocean.
NH	Northern Hemisphere.
OGCM	Ocean General Circulation model.

RCP	Representative Concentration Pathway.
SD	Standard Deviation.
SIC	Sea Ice Concentration.
SLHF	Surface Latent Heat Flux.
SMHI	Swedish Meteorological and Hydrological Institute.
SSHF	Surface Sensible Heat Flux.
SST	Sea Surface Temperature.
SWR	Short Wave Radiation.

List of Figures

List of Tables

Appendix A

Manuscript I

Nudging sea ice in the coupled climate model EC-Earth

Ida M. Ringgaard, Shuting Yang, Eigil Kaas and Jens H. Christensen

May 15, 2019

Abstract

Constraining sea ice in coupled climate models, while maintaining energy conservation, have been achieved for short time periods or with a seasonal dependence. A method that works year round and can continue for several years, have not been developed. It was the aim of this study to develop a method for nudging sea ice in coupled climate models, while conserving energy. Two methods are presented here, both nudge sea ice by modifying the surface heat flux between the atmosphere and the ice/ocean surface. In the first method, a additional heat (positive or negative) was added to the sensible heat was used to force the coupled climate model EC-Earth to form or melt sea ice. This method achieved the target sea ice, but it turned out not to be energy conserving, as the atmospheric component in EC-Earth (IFS) did not 'see' the modified heat flux. The second method was based on the first method, but here the additional heat was manually redistributed in the atmosphere. This method reached the sea ice target, if the target was close to the models own sea ice state. If the discrepancies between the target and the models sea ice state, this method failed by either becoming unstable or by heating the atmosphere so much, that it became impossible to sustain a sea ice cover. The results presented here highlight the difficulties there is with nudging sea ice in coupled climate models while maintaining energy conservation. Redistributing heat in the climate system could still work, but redistributing it in the atmosphere requires a very delicate balance between reaching the sea ice target and avoiding model instabilities.

1 Introduction

Improved understanding of the climate system can be achieved via observations or by dedicated model experiments. The latter allow us to isolate a single component of the system, and investigate its impact. This is of course not possible with the real climatic system considering its space and time scales: there we cannot reverse the experiment or isolate parts of the system and observe the impacts. Therefore, we have to rely on computer models to perform our climate experiments.

Modifying climate models can be achieved by modifying the external forcing (orbital parameters, green house gases etc.), prescribing parameters to a target value, or by pushing the model toward a target (toward observations for example). The latter may be viewed as a kind of assimilation of data/information. Assimilation covers a large fan of methods, including *Newtonian relaxation* or *nudging*, where a nudging term is added to the prognostic equations (Kalnay (2012)). The nudging term depends on a target value, for example an observation, and is normally given as $\frac{x_{obs}-x}{\tau_x}$, where x is a parameter, x_{obs} is an observation of this parameter and τ_x is the relaxation time scale. In this study we focus on how to nudge sea ice in a coupled climate model. This means energy has to be added or removed from the system to form or melt sea ice in certain areas. For Atmosphere Global Circulation Models (AGCM's) this is not an issue, since the sea ice is prescribed anyway. However, this becomes an issue when using coupled climate models. In these, water, mass and energy are conserved between the atmosphere and ice/ocean modules. So far, most methods for constraining sea ice in coupled models have not been energy-conserving. Those that are only work for shorter time periods or depends on the season. This study aims at developing a method for nudging sea ice in a coupled climate model, keeping the energy and water conserved. Section 2 discusses various methods for constraining sea ice in other studies. Sections 3.3 and 3.4 presents 2 methods for nudging sea ice in a coupled model.

2 Methods for constraining sea ice

One part of the climate system that has been investigated intensively in the last decades is the declining Arctic sea ice and its impact on the atmospheric climate, both locally and remotely. As the observational sea ice record is relatively short (continues and Arctic-wide observations only started with the satellites in 1979), climate models can be used to investigate hypotheses about the recent decline as well as future projections. Additionally, the isolated impact of sea ice changes can be tested. Studies investigating the impact of sea ice on the climate by perturbing the sea ice have often used AGCM's. In recent years the importance of modeling the coupled system, i.e. activating atmosphere/ocean feedbacks in the model as well, have been documented, thus highlighting the need for constraining sea ice in Atmosphere-Ocean Global Circulation models (AOGCM's) (Deser et al. (2015)). Sections 2.1 and 2.2 discuss various methods for constraining sea ice in AGCM's and AOGCM's.

2.1 Atmosphere-only models (AGCM)

Many studies uses AGCM's to investigate the atmospheric response of Arctic sea ice variations (Petoukhov and Semenov (2010), Screen (2013), Pedersen et al. (2016), Lang et al. (2017)). As AGCM's are not coupled to the ocean, sea ice is prescribed to the atmosphere. Nudging sea ice then simply means to prescribe a target sea ice cover and or thickness instead, since the energy and water is not conserved between the atmosphere and ocean anyway. AGCM's have been widely used, partly because they are much faster to run than fully coupled models, partly because atmospheric time scales are much shorter than those in the oceans. This means that for shorter experiments the ocean will not have changed too much, and is therefore neglected. However, Deser et al. (2015) showed that the atmosphere/ocean feedbacks are crucial for capturing remote impacts of climatic changes. They performed several experiments with different ocean model complexity (no interactive ocean, slab ocean and full-depth ocean) and with sea ice conditions representing late twenty-century and late twenty-first-century sea ice cover. They conclude that including an interactive ocean (i.e. a full-depth ocean and not just a slab ocean) is necessary to obtain a response outside the northern extra-tropics. Further, using a dynamical full-depth ocean, instead of a thermodynamical slab ocean, produces the equatorial symmetry observed. The thermodynamic atmosphere-ocean coupling (slab ocean) exaggerates the thermodynamic response compared to a full-depth ocean. Hence, AGCM's might underestimate not only the strength of the warming, but also the spatial coverage. Both Petrie et al. (2015) and Screen (2018) suggest that the atmospheric circulation discrepancies across AGCM's are larger than for AOGCM's. Therefore, being able to constrain sea ice in coupled climate models is vital.

2.2 Atmosphere-Ocean coupled models (AOGCM)

Sea ice has been constrained in coupled climate models in numerous ways. Screen (2018) summarizes some of these methods, and below is a brief discussion of these. Petrie et al. (2015) and Semmler et al. (2016) both used an energy-conserving, although time limited, approach where the initial sea ice thickness is reduced. This results in a decrease of sea ice throughout the year due to increased heat flux through the ice and increased melting. As these experiments only perturb the initial fields, these simulations will relatively fast return to the unperturbed state. A different approach is to modify the sea ice albedo (Graversen and Wang (2009), Blackport and Kushner (2016) and Blackport and Kushner (2017)). Modifying the albedo modifies the amount of solar radiation received by the sea ice. Although this method is water and energy conserving, it is seasonally skewed, as it only works in the sunlit part of the year. A third approach is to perturb a surface heat flux in order to constrain sea ice. Deser et al. (2015), McCusker et al. (2017) and Oudar et al. (2017) all applied a surface heat flux (a 'ghost' flux) in order to reach a certain sea ice target. The term 'ghost' flux refers to the fact that the flux is only seen by a single component of the coupled model (to the sea ice component in the first two studies and to the ice/ocean component in the latter study). The remaining components only see the indirect effect.

This last approach, perturbing the sea ice indirectly by adding a surface heat flux to either the ice or the ocean component, has at least two advantages. First, it conserves water. If sea ice was nudged directly, ice, i.e. water, would be added or removed from the system. This is avoided by nudging by proxy (by heat flux). Secondly, all the processes related to forming and melting sea ice is being handled by the model and does not have to be computed manually (brine rejection, ice velocity and, for some sea ice models: distributing sea ice in the respective sea ice thickness categories). However, it is not energy conserving. That is the aim of the present study, to develop an energy conserving method for nudging sea ice, based on the approaches in Deser et al. (2015), McCusker et al. (2017) and Oudar et al. (2017).

3 Methods and model

Forcing the climate model to form or melt sea ice on its own requires the energy in the system to be redistributed accordingly.

First, lets consider how to form or melt sea ice. To form sea ice, the ocean has to be cooled to the freezing point. For ice to melt, heat has to be added to the sea ice. To have an energy conserving nudging method, this heat has to come from somewhere. Deser et al. (2015) used longwave radiation (LWR) to force their model to change the sea ice cover, thereby conserving water. However, changing the LWR essentially means sending more or less heat to space via the atmospheric window under cloud free conditions. This is not energy conserving. The two methods presented in this study are both based on this idea of modifying the heat flux between the atmosphere and the ice/ocean. Instead of modifying the LWR, we modify the surface sensible heat flux (SSHF). As the SSHF is given by the difference in temperature between the atmosphere and the ocean (eq. 1), modifying SSHF only redistributes the heat between the atmosphere and the ocean.

$$SSHF = C_H|V|(T_s - T_{air}) \tag{1}$$

where C_H is a bulk transfer coefficient for heat, V is the wind speed, T_s is the skin temperature and T_{air} is the air temperature Wallace and Hobbs (2006). Hence, nudging SSHF conserves energy.
In section 3.3 and 3.4 two methods for nudging sea ice are presented, but first the coupled climate model used in this study is presented in section 3.1.

3.1 Model

The fully coupled global climate model used in this study is EC-Earth (Hazeleger et al. (2010)). EC-Earth couples the atmosphere, with the land, ocean and sea ice via the OASIS-3 coupler. The atmospheric component is the ECMWF's Integrated Forecast System (IFS) cycle 36r4 with a spectral resolution of T255 (equivalent to ∼80 km) and 91 vertical levels (ECMWF (2010)). The ocean component is the Nucleus for European Modelling of the Ocean version 3.6 (NEMO, Madec and the NEMO team (2008)), embedded with the sea ice component the Louvain-la-Neuve sea Ice Model (LIM3, Vancoppenolle et al. (2012)). Both are on the ORCA1 tripolar grid (1°x1°) and with 75 vertical levels. IFS and NEMO are coupled through the OASIS3 coupler (Valcke (2013)). By coupling the two components, information is exchanged between the two components at a certain frequency. For our setup of EC-Earth, the time step is 2700s for both IFS and NEMO, thus they are coupled every time step. Additionally, IFS and NEMO are not on the same grid, so OASIS3 have to interpolate the variables between the two grids, before sending them. Not all computed variables are coupled, only the variables needed for the other component. NEMO for example needs the ocean surface conditions in the form of the surface heat fluxes, fresh water fluxes and wind stress, whereas IFS needs the sea surface temperature and sea ice conditions. One of the variables send from the atmosphere to the ocean is the non-solar heat flux Q_{ns}. This is the sum of the LWR, the surface latent heat flux (SLHF) and SSHF, i.e. NEMO does not receive a separate SSHF. This will be used later on. IFS computes the contributors separately (see the IFS manual (ECMWF (2010))) and sums them up right before sending them to NEMO through OASIS3.

3.2 Experimental setup

The methods presented in this study are tested for two target sea ice covers. Target70N is an idealized cover of 100% sea ice concentration from the North Pole down to 70°N. South of this latitude sea ice will be nudged toward 0%. This idealized area is chosen to test how the nudging method behaves for areas were the target is to grow sea ice (Barents Sea, BS) and areas were sea ice has to be melted (Baffin Bay, BB). Target50N is used for Method 2. This is similar to Target70N, but with 100% sea ice concentration down to 50°N. This allow us to test how our methods react when they are being pushed far away from realistic sea ice covers.

3.3 Method 1

In Method 1 sea ice is indirectly nudged by modifying the SSHF at each time step. Pushing the model to form or melt sea ice requires large amounts of energy. This extra energy (ΔHF) is added to the SSHF computed by IFS (eq. 2).

$$SSHF_{new} = SSHF + \Delta HF \tag{2}$$

The magnitude and direction of ΔHF depends on three factors: 1) The size of the heat flux received by the ocean, 2) if the target is to form or melt sea ice and 3) if the model and the target are opposing each other. The latter could for example be if the target is to form sea ice in summer. As for 1), the size of the total surface heat flux received by the ocean is $HF_{Total} = SWR + LWR + SLHF + SSHF$, where SWR is the Short Wave Radiation. In the following it is assumed that the target is to form sea ice, but the method is the same for melting sea ice. Either way, there are two cases: in Case 1, the model and the target are opposing each other, i.e. forming sea ice in summer. In Case 2, the model and the target are complementing each other, i.e. forming sea ice in winter. Starting with Case 1, energy is being transported from the atmosphere into the ocean, heating the ocean and melting any sea ice. To form sea ice, the ocean has to cool, i.e. loose heat. This can be achieved by reverting the energy received from the atmosphere back into the atmosphere. This gives the first term of the nudging factor ΔHF:

$$\Delta HF = (-1) \cdot THF \tag{3}$$

Now the ocean does not receive any surface heat flux, but to form sea ice it needs to cool even further. This is achieved by increasing the heat flux from the ocean to the atmosphere. The magnitude of this extra energy is defined as the difference between the simulated sea ice concentration and the target sea ice concentration times the HF_{Total}:

$$HF_{Total} \cdot \Delta SIC = HF_{Total} \cdot (SIC_{Model} - SIC_{Target})/\tau \tag{4}$$

ΔSIC is weighted by the actual HF_{Total}, to make sure the ΔHF is large enough to be seen by the ocean. τ is the relaxation time scale, which here is set to 1, and is therefore ignored in the following. Combining equations 3 and 4 results in the following definition for the nudging factor ΔHF:

$$\Delta HF = (-1) \cdot HF_{Total} + ABS(HF_{Total}) \cdot \Delta SIC \tag{5}$$

The closer the target sea ice concentration is to the simulated sea ice, the weaker the nudging.
For Case 2, ΔHF only differs from Case 1 in one aspect: Since the HF_{Total} has the correct direction already (upwards into the atmosphere in winter), equation 3 can be neglected. Put in another way, whether or not to include HF_{Total} depends on the sign of HF_{Total} as well as ΔSIC:

$$\begin{aligned} SIGN(HF_{Total}) &= SIGN(\Delta SIC) \rightarrow 0 \\ SIGN(HF_{Total}) &\neq SIGN(\Delta SIC) \rightarrow -1 \end{aligned} \tag{6}$$

Therefore, the final equation for the nudging factor ΔHF is:

$$\Delta HF = \begin{Bmatrix} 0 \\ -1 \end{Bmatrix} \cdot HF_{Total} + ABS(HF_{Total}) \cdot \Delta SIC \tag{7}$$

ΔHF will be non-zero as long as there is the slightest difference between the simulated and the target sea ice. This can lead to instabilities, so in the results below a lower threshold of 5% is used, where no nudging is done for ΔSIC below this value.

3.3.1 Results

To test Method 1, a model simulation (M1) is nudged toward an idealistic sea ice concentration of 100% from the North Pole down to 70°N. South of this latitude sea ice will be nudged toward 0%. This idealized area is chosen to test how the nudging method behaves for areas were the target is to grow sea ice (Barents Sea, BS) and areas were sea ice has to be melted (Baffin Bay, BB). The effect of the nudging method is evaluated by comparing to a control run (CTRL) with no nudging performed. The resulting mean nudging factor ΔHF for each month are shown in figure 1a. In the Barents Sea, ΔHF is positive upwards, meaning SSHF is removed from the ocean to cool it down. In Baffin Bay it is the opposite. The nudging lead to changes in the sea ice as well as in the air temperature. Figures 1b and 1c shows the monthly mean 2m temperature anomaly and the sea ice concentration anomaly (M1-CTRL) for the first model year. South of 70°N, Method 1 succeeds in removing sea ice almost to the target. The now ice-free areas experience a large increase in temperature, compared to CTRL (more than 10°C). This large temperature increase is what can be expected when the ocean is not covered by sea ice anymore. Forming sea ice north of 70°N is not as easy. Focusing on the Barents Sea, the sea ice target is not fully reached, but more sea ice is formed by the end of the year, compared to CTRL. A small area is still not ice-covered, and the ΔHF over this ice-free area is on the order of 300-400 Wm^{-2}. This should lead to a large increase in the air temperature, but the air above only warms $\sim$2°C in January and even cools in periods (fig. 1b). This discrepancy between the simulated output and our expectations lead us to focus on shorter time periods, more precisely every time step of the first simulated day. The temperature anomalies for each model level for the first six time steps are shown in figure 2a. In Baffin Bay, the air temperature increases from the second time step. As energy should be taken from the atmosphere and added to the sea ice in this point, we would expect to see an air temperature decrease, not an increase as is shown. In the Barents Sea, energy should be taken from the ocean and send to the atmosphere, thus causing a temperature decrease in the ocean and a temperature increase in the atmosphere, as is observed from the second time step (fig. 2a). The counterintuitive behaviour in Baffin Bay led us to check the energy balance:

$$
\begin{aligned}
\frac{d\overline{E_{tot}}}{dt} &= \frac{1}{4\pi}\frac{d}{dt}\int_{-\pi/2}^{\pi/2}\int_{0}^{2\pi} E_{tot}cos(\phi)d\lambda d\phi \\
\frac{d\overline{E_{tot}}}{dt} &= \frac{1}{4\pi}\frac{d}{dt}\int_{-\pi/2}^{\pi/2}\int_{0}^{2\pi} (SH + LW + SW_{surf} + LW_{surf})cos(\phi)d\lambda d\phi \\
&- \frac{1}{4\pi}\frac{d}{dt}\int_{-\pi/2}^{\pi/2}\int_{0}^{2\pi} (SW_{toa} + LW_{toa})cos(\phi)d\lambda d\phi
\end{aligned}
\tag{8}
$$

Computing the energy change in a column of air (left side in equation 8) and the corresponding energy in and out of that column (i.e. the heat flux coming in at the top of the atmosphere (TOA), minus what goes out at the Earth surface as well as lateral changes) right side in equation 8) shows that Method 1 is not energy conserving. Returning to the atmospheric module of revealed that IFS does not use the SSHF it computes, except for minor corrections in the cloud parameterization. IFS computes SSHF as a diagnostic parameter based on the computed air and sea surface temperatures. That is, the atmospheric temperature profile have already been updated correspondingly earlier in the time step, but without explicitly computing SSHF. Therefore, when SSHF is computed in IFS, it will not be used in IFS so as to not use it twice. This is an issue for Method 1, since only the original, unmodified amount of energy equivalent to SSHF is distributed in the atmosphere. Nudging SSHF by adding ΔHF will thus not be 'seen' by the atmosphere, only the ocean. For the nudging method to be energy conserving, the atmosphere needs to see ΔHF as well, not only the unmodified SSHF. Since IFS does not do this, we manually distributed the extra energy in the atmosphere, as described below in Method 2.

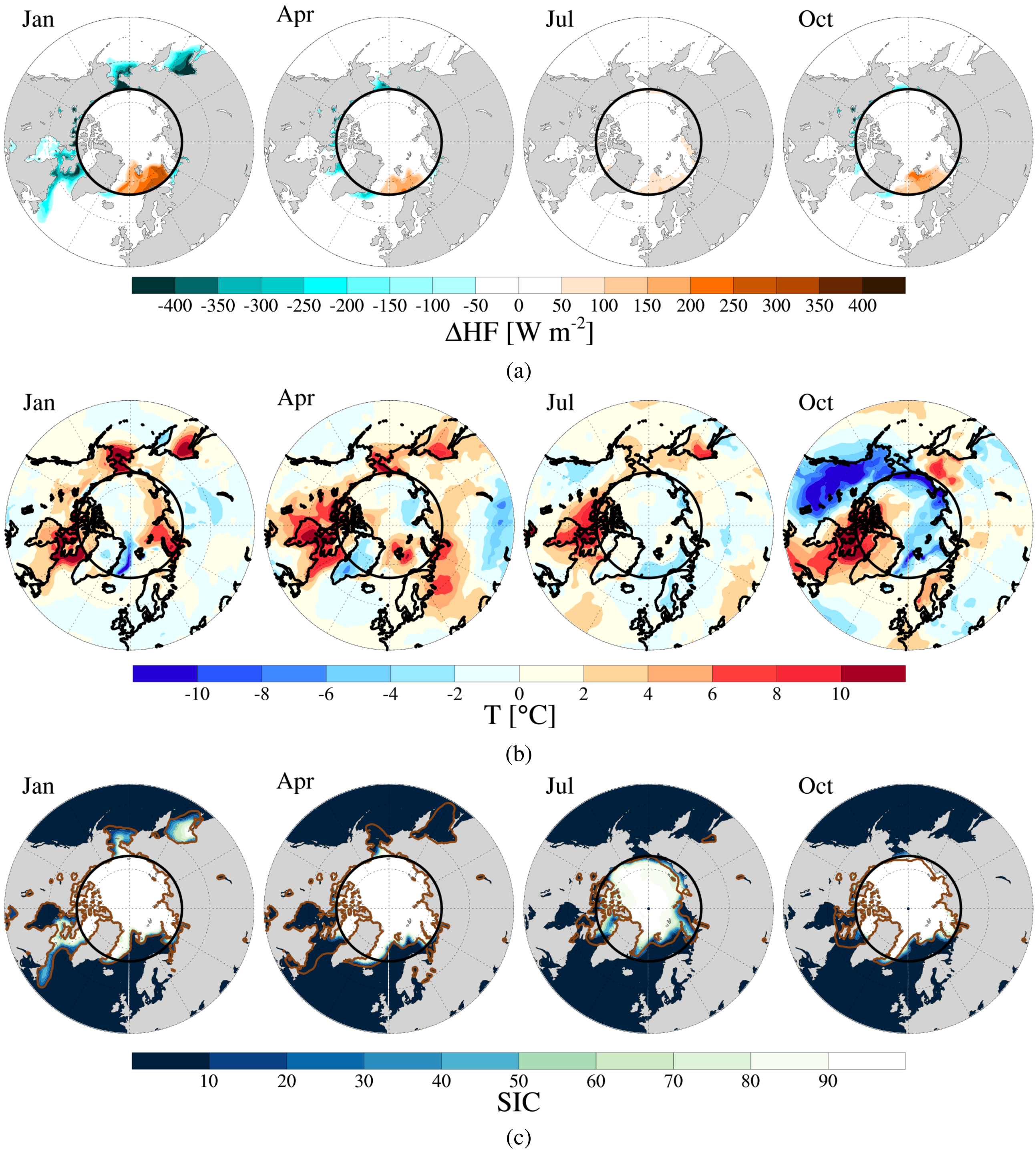

Figure 1: M1 monthly mean (a) ΔHF (in W m^{-2}), (b) temperature anomaly (M1-CTRL; in °C) and (c) sea ice concentration (in %) for January, April, July and October. Brown line in (c) indicate the climatological sea ice edge (SIC>=15%) from CTRL. Black line indicate the target sea ice edge at 70°N.

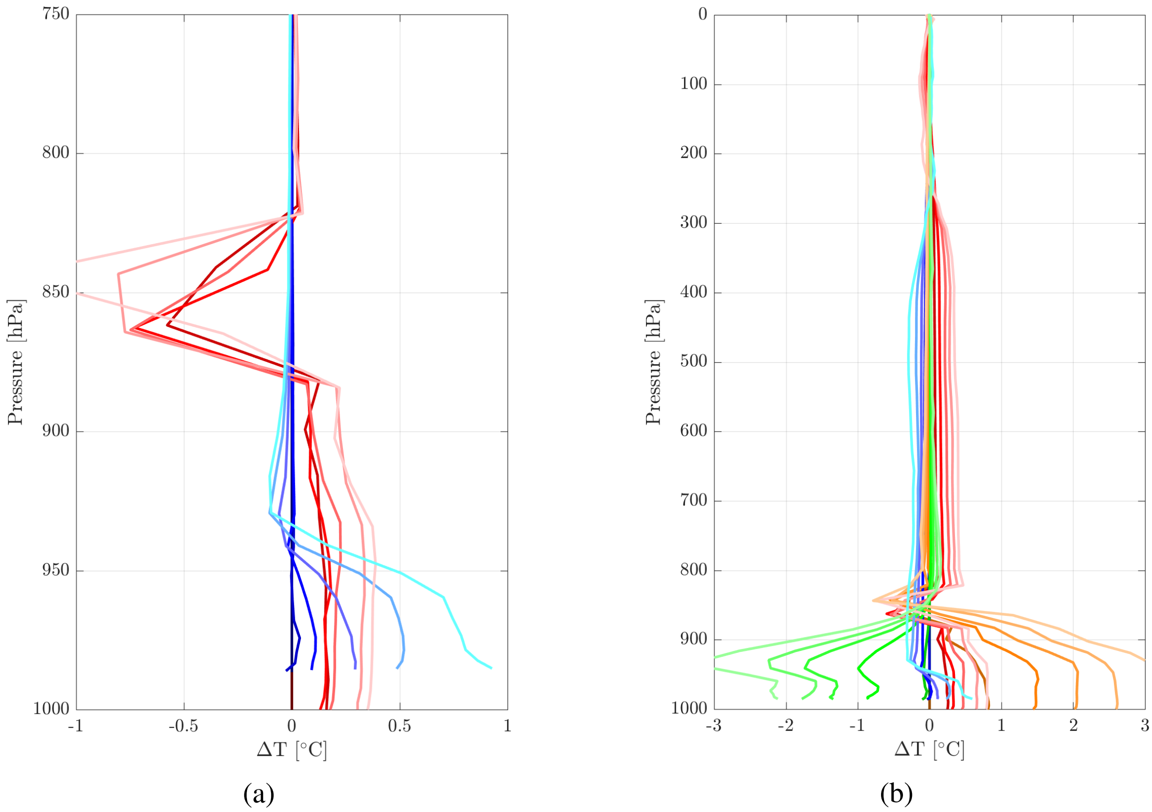

Figure 2: (a) Temperature anomaly (M1-CTRL; in °C) at each model level for the first 6 time steps at single grid point in the Barents Sea (red and orange) and Baffin Bay (blue and green). The lighter the color, the later in the simulation. (b) The same but for (M2-CTRL). ΔHF is either distributed in the entire air column (red and blue) or only in the bottom 700 hPa (orange and green). Please note the different y-axis.

3.4 Method 2 - Redistribute the heat in the atmosphere

Method 2 builds on Method 1 in the sense that the energy needed to form or melt sea ice (ΔHF) is computed in IFS and then send to the ocean. In order to conserve energy, ΔHF needs to be redistributed in the atmosphere. As IFS does not do this on its own, this has to be implemented manually. In the real world, changes in SSHF affects the air temperature. Therefore, the aim is to modify the temperature of the air. This is achieved by modifying the instantaneous total atmospheric energy E_{tot} in each air column above areas of nudging, given in equation 9:

$$E_{tot} = \int_{z_s}^{\infty} (E_{kin} + s + Lq_v)\rho \, dz \tag{9}$$

where E_{kin} is the kinetic energy, $s = c_pT + gz$ is the dry static energy, c_p is the specific heat capacity at constant pressure, T is temperature, g is the gravitational acceleration, z is height, L is the latent heat of vaporization, q_v is the specific humidity and ρ is the density of air. Dividing this into separate integrals gives:

$$E_{tot} = \int_{z_s}^{\infty} (E_{kin} + Lq_v)\rho \, dz + \int_{z_s}^{\infty} gz\rho \, dz + \int_{z_s}^{\infty} c_pT\rho \, dz \tag{10}$$

The potential energy, can be rewritten using hydrostatic balance, $\frac{\partial p}{\partial z} = -\rho g$:

$$\int_{z_s}^{\infty} gz\rho \, dz = -\int_{z_s}^{\infty} \frac{\partial p}{\partial z} z \, dz \tag{11}$$

Using integration by parts:

$$E_{tot} = -\int_{z_s}^{\infty} \left(\frac{\partial}{\partial z}(pz) - p\frac{\partial z}{\partial z} \right) dz = -\left[pz\right]_{z_s}^{\infty} + \int_{z_s}^{\infty} p \, dz = p_s z_s + \int_{z_s}^{\infty} p \, dz \tag{12}$$

Using the ideal gas las the last term can be rewritten as:

$$\int_{z_s}^{\infty} p \, dz = \int_{z_s}^{\infty} \rho RT \, dz = 0 \tag{13}$$

which gives

$$E_{tot} = \int_{z_s}^{\infty} (E_{kin} + Lq_v + c_pT)\rho \, dz + p_s z_s \tag{14}$$

Using hydrostatic balance again to change the limits:

$$E_{tot} = -\frac{1}{g} \int_{p_s}^{0} (E_{kin} + Lq_v + c_pT) \, dp + p_s z_s \tag{15}$$

As the aim is to pretend SSHF has been changed, thus only modifying the temperature in the air column, the change in energy of the air column only depends on the 3rd term:

$$\Delta E = -\frac{1}{g}\sum_{klev=1}^{Nlev} c_p \Delta T_{klev} \Delta p_{klev} \tag{16}$$

where p_{klev} is the pressure at each model layer. The sum of ΔE over all layers must equal ΔHF computed in section 3.3. The simplest way would be to distribute ΔHF equally up through the atmosphere, giving each layer the same amount of energy. In reality, the lower layers would receive the sensible heat, gradually declining with height. The amount of energy received in each model layer can be depicted by a vertical profile (T_{prof}) and an amplitude A, (eq. 17). T_{prof} is independent of time and horizontal location, going from 0 to 1, whereas A depends on both time and space.

$$T^t(i, j, klev) = A^t(i, j) \cdot T^t_{prof}(klev) \tag{17}$$

where (i, j) is the horizontal grid, $klev$ is the layers in the atmosphere and t is time. Putting this into eq. 16:

$$\Delta E = -\frac{1}{g}\sum_{klev=1}^{Nlev} c_p A T_{prof}(klev)\Delta p(klev) = -\frac{1}{g} A c_p \sum_{klev=1}^{Nlev} T_{prof}(klev)\Delta p(klev) \tag{18}$$

The amplitude A of is then given by:

$$A = -\frac{g\Delta E}{c_p \sum_{klev=1}^{Nlev}(T_{prof}(klev)\Delta p(klev))} \tag{19}$$

Using A and a predetermined profile T_{prof} (in the following we use $T_{prof} = \frac{1}{1+exp(-x)}$), the energy ΔHF can be redistributed in the atmosphere (eq. 20).

$$\frac{dT}{dt} = \frac{dT}{dt} + \Delta T \tag{20}$$

As SSHF is send to the ocean at the end of each time step, the redistribution of ΔHF is done by updating the air temperature at the beginning of the next time step. The results using this energy conserving nudging method are shown in section 3.4.1 below.

3.4.1 Results

Method 2 is tested by nudging toward Target70N. This experiment is named M2. First step is to check if the energy is redistributed in the atmosphere as it is supposed to. Figure 2b show the atmospheric profiles for the same two locations and time steps as in figure 2a. For each location, the extra energy

ΔHF is either distributed over the entire atmosphere (red and blue lines) or over the bottom 20 layers (equivalent to around 700 hPa, orange and green lines). In the real world, the sensible heat flux from the land/ocean surface would be redistributed in the atmospheric boundary layer, not the entire atmosphere. However, this means adding/removing a large amount of heat in the relatively shallow boundary layer which might lead to instabilities or rapid and large temperature changes. To smooth the effect of the ΔHF, we also test the response when redistributing ΔHF in the entire atmosphere. As expected, redistributing the energy below 700 hPa, increases (decreases) the air temperature above the Barents Sea (Baffin Bay) rapidly compared to CTRL (figure 2b, orange and green lines). In Baffin Bay, the surface temperature decreases by 7.1°C during the first day, compared to CTRL (not shown). In the Barents Sea the surface temperature increases more than 4.6°C during the first day (not shown). Redistributing the energy in the entire atmosphere slow down the rapid increase/decrease in temperature (fig. 2b, blue and red lines). By the end of the first day, the surface temperature increase above the Barents Sea is now 1.3°C and 4.5°C above Baffin Bay (not shown). The 1°C change over the Barents Sea is not an unrealistic increase. Redistributing ΔHF in the entire atmosphere (orange experiment) lead to an increase in the surface temperature after a few time steps, whereas only redistributing ΔHF below 700hPa (green experiment) results in cooling the surface. This discrepancy occurs as both experiments starts to melt the sea ice, leading to a warmer ocean/ice surface. The heat removed from the atmosphere to achieve this can only be taken from the bottom of the atmosphere in the green experiment, hence the cooling of this layer. In the orange experiment, the cooling can be distributed over the entire atmosphere, allowing for the warmer surface to warm the lowest part of the atmosphere. Hence the different responses. From figure 2b it is clear the Method 2 succeeds in redistributing the energy in the atmosphere.

The monthly mean temperature and sea ice concentration for the first year (fig. 3b and 3c, respectively) show that the target sea ice cover is close to being reached, and the temperature anomalies compared to CTRL are realistic, with temperature changes in some areas around ±10°C and much lower for others. However, Target70N (sea ice down to 70°N) is not too far away from the present day sea ice cover. The sea ice in the Barents Sea is further south than the observed sea ice cover, but the target is almost reached here. Melting sea ice takes less energy than forming sea ice, due to difference in heat capacity of ice compared to ocean and that the ocean has to be cooled before sea ice can be formed, but melting sea ice can start immediately. Therefore, melting sea ice south of 70°N is achieved faster. However, after 1 model year the model becomes unstable and crashes. Using stronger nudging causes the model to crash faster, using weaker nudging keeps the model stable, but does not succeed in reaching the target sea ice cover.

As this nudging method should work for a variety of sea ice covers, a new experiment with a much larger target sea ice cover (SIC down to 50°N) is performed, hereafter referred to as M2_{50N}. The resulting temperature anomaly and sea ice concentration for the second modelled year can bee seen in figures 4a and 4b. From this it is clear that by targeting a large sea ice cover, the atmosphere heats up so much (more than 10°C over large parts of the Northern Hemisphere), that it counteracts the effort to form sea ice. Slowing down the process by using a weaker ΔHF results in the nudging not being large enough to have an effect.

The issue of the large temperature changes in the atmosphere due to the nudging can be explained by a simple back-of-the-envelope calculation of the amount of energy needed to melt ice. Melting 1m^3 of ice requires an amount of energy (Q) equal to $306.3 \cdot 10^3$ kJ. Distributing this evenly in a unit column over the entire atmosphere results in a temperature increase of: $Q = g^{-1}C_pTdp \rightarrow$ T = 30K, where $g = 9.82$m s^{-2}, $dp = 1000$hPa is the pressure difference from top to bottom of the atmosphere and $C_{p,air} = 1004$ J K^{-1} kg^{-1} is the heat capacity of the atmosphere. Warming a unit ocean column by the the same temperature and energy would result in a unit column with a depth of: $dz = \frac{Q}{\rho_{ocean}C_{p,ocean}\Delta T} = 2.4$m, where $\rho_{ocean} = 10^3$ kg m^{-3} and $C_{p,ocean} = 4220$ J K^{-1} kg^{-1}. That is, the amount of energy warming the entire atmospheric column by 30K only warm 2.4m of the ocean column up to 30K. From this it is clear that the amount of energy added to the atmosphere in areas of target sea ice growth is huge and will warm the atmosphere too much, as was seen in figure 4a. Hence, energy is conserved, but the atmosphere becomes too warm to allow for sea ice growth.

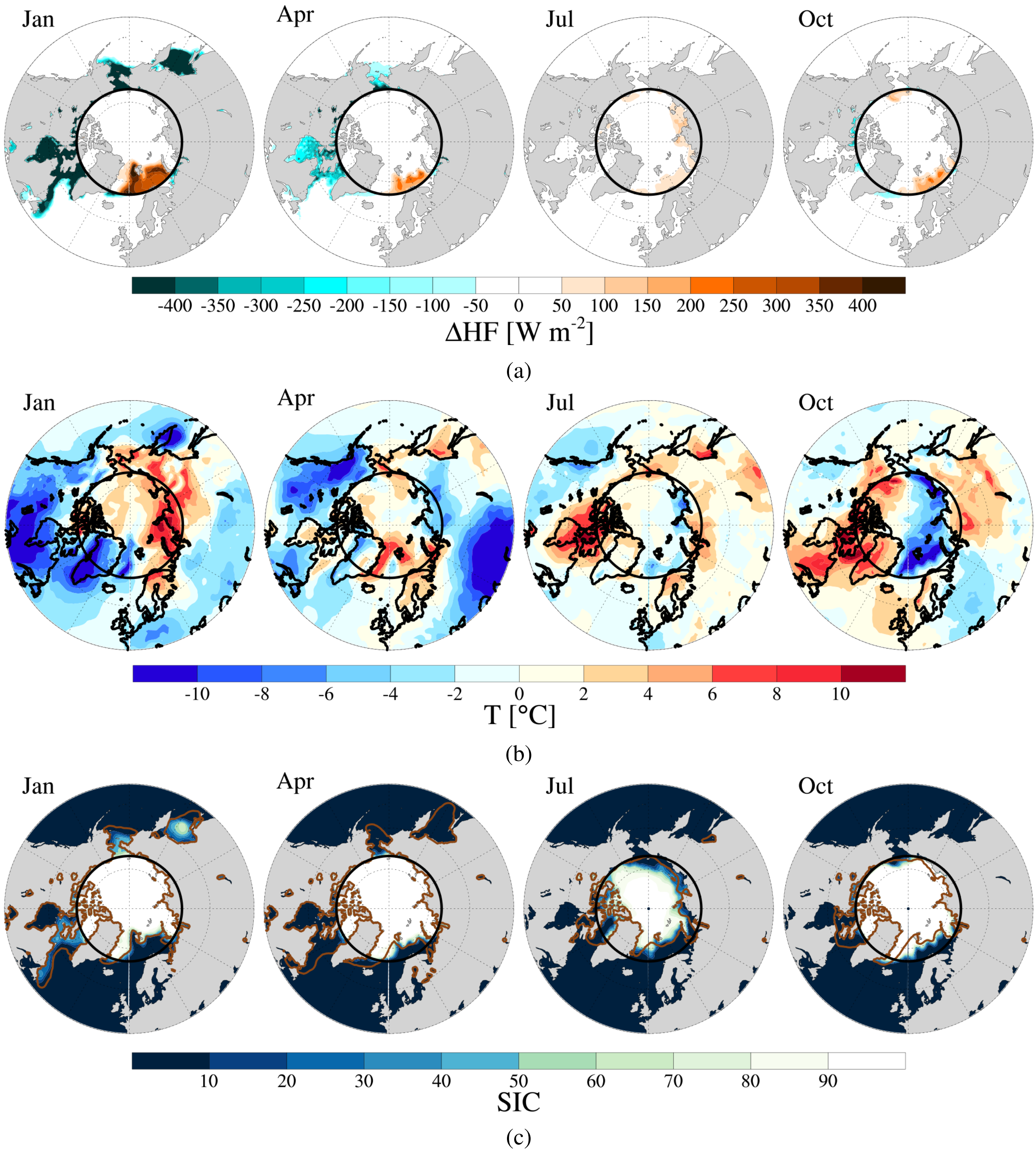

Figure 3: M2 monthly mean (a) ΔHF (in W m^{-2}) (b) temperature anomaly (M2-CTRL; in °C) and (c) sea ice concentration (in $\%$) for M2 for January, April, July and October. Brown line in (c) indicate the climatological sea ice edge (SIC>=15$\%$) from CTRL. Black line indicate the target sea ice edge at 70°N.

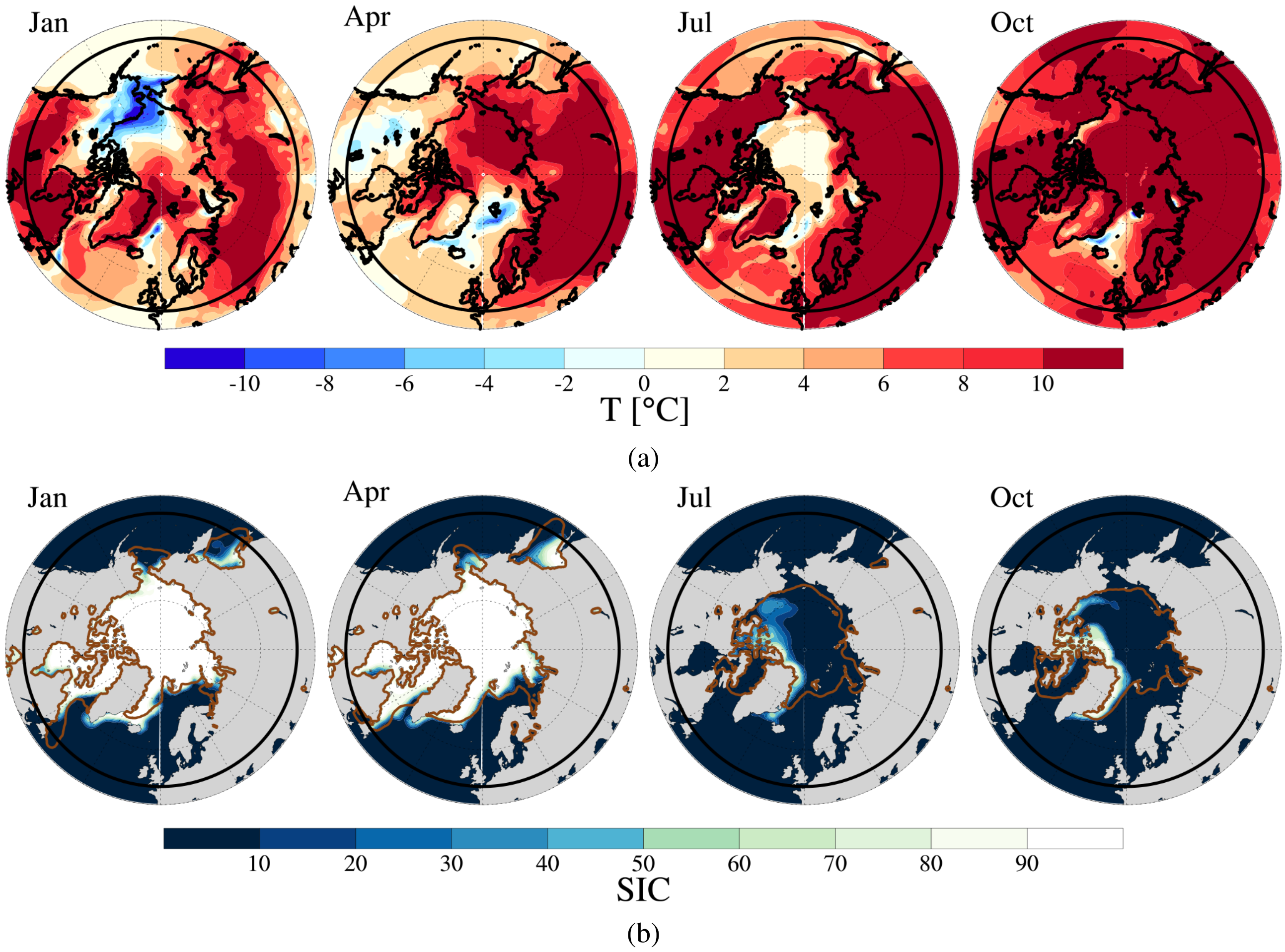

Figure 4: $M2_{50N}$ monthly mean (a) temperature anomaly ($M2_{50N}$-CTRL; in °C) and (b) sea ice concentration (in %) for January, April, July and October for 2nd model year. Brown line in (b) indicate the climatological sea ice edge (SIC>=15%) from CTRL. Black line indicate the target sea ice edge at 50°N.

4 Discussion

This study aims at developing a method for nudging sea ice, while conserving energy. Method 1 succeeds in forming and melting sea ice close to the target, but it is not energy conserving. Method 2 on the other hand is energy conserving, but only succeeds in coming close to the target for small sea ice changes, relative to the models own sea ice state. For larger changes, M2 does not succeed in reaching the sea ice target because the atmospheric temperature increases too much and too rapidly.
The idea behind simply moving heat from the ice/ocean to the atmosphere is that the heat will be advected away from the nudging area, allowing for sea ice to form. However, the amount of energy put into the atmosphere to form sea ice is too large to be advected away fast enough. A potential solution for this is to use a weaker nudging, thus sending less heat to the atmosphere. This is a very delicate balance between cooling the ocean enough to form sea ice and not warming the atmosphere too much, thus warming the ocean again. A balance we did not succeed in finding. The nudging was either too weak to form any sea ice, the atmosphere heated up too much or the model became unstable.
Another solution is to 'go with the flow', i.e. only nudge toward more sea ice in the growing season and toward less sea ice in the melting season. Although this results in smaller ΔHF, the issues are the same as before: finding the balance between cooling the ocean enough and not warming the atmosphere too much. Easing the nudging can also be achieved by setting the relaxation time scale $\tau \neq 1$ in equation 4. This was tested, revealing the same issues with finding the correct balance.
A third possibility is to collect all the extra energy ΔHF in a buffer, slowly releasing it over time to the atmosphere. This might work, but it will only be energy conserving over a longer time period, not for every time step. This erodes the idea of energy conservation.
Fourthly, the heat ΔHF could be redistributed in the ocean instead of the atmosphere. As the heat capacity of the ocean is larger than that of the atmosphere, equal amounts of heat added to the ocean and the atmosphere would not result in equal heating. The extra heat would modify the stratification, but so does it in the atmosphere. In the Arctic Ocean the stratification is dominantly dependent on salinity, not temperature, so it could potentially work here. This method have not been tested in the present study.
An alternative method could be to modify the mixing coefficient in the ocean, allowing for more mixing, thus bringing up heat from below when the target was to melt sea ice. For a target of forming sea ice, mixing could be inhibited, thus preventing warm water from mixing into the surface mixed layer. This method was not tested either.
Finally, a solution could be to not send ΔHF to the atmosphere directly above the nudging area, but somewhere else for example distribute it evenly in the global atmosphere or send it to the bottom of the ocean. Especially the last point would not affect the climate system for some time, due to the large heat capacity of the ocean. Again, if the climate system practically does not see ΔHF or it is send somewhere non-physical, it erodes the idea of energy conservation.
To keep the nudging experiments as close to reality as possible, it might be better then to simply make ΔHF disappear. This way, it does not modify the climate system somewhere unintentionally. This not energy conserving method of nudging a heat flux to indirectly modify sea ice or temperature has

been proposed by Deser et al. (2015) and Oudar et al. (2017) and is discussed in section 2. In our case, the ΔHF is then not added to the SSHF but to Q_{ns}, as NEMO does not receive a separate SSHF, but a combined Q_{ns} (see section 3.1). This results in Method 1 becoming similar to the flux correction proposed in Oudar et al. (2017). The only difference is determining the magnitude of the flux.

Due to the technical setup of EC-Earth, where the atmosphere/ocean sensible heat flux is computed as prognostic variables in the atmospheric component and then send to the ocean, any changes in the surface sensible heat fluxes have to be redistributed manually in the atmosphere. This might not be an issue in other models. The Norwegian Earth System Model (NorESM), the Community Climate System Model (CCSM) and the Community Earth System Model (CESM) all uses the coupler CPL7. In these models, the atmosphere/ocean fluxes are computed in the coupler and then send to the atmosphere and the ocean (Craig et al. (2012), Bentsen et al. (2013)). Therefore, Method 1 could potentially work for these models.

5 Conclusion

In this study two methods for nudging sea ice in the coupled climate model EC-Earth are presented. Both methods aim at nudging sea ice indirectly by nudging the heat flux between the atmosphere and the ocean, hence forcing the model to form or melt sea ice by it self. This should redistribute the energy in the atmosphere, while conserving water and energy. In Method 1, the sensible heat flux is modified, resulting in the target sea ice cover. However, as the atmospheric component of EC-Earth (IFS) does not actually use the extra sensible heat flux (ΔHF) it computes and send to the ocean, this method turned out not to be energy conserving. In Method 2, SSHF is again modified and send to the ocean, but here ΔHF is manually distributed in the atmosphere above. Although this is now energy conserving, Method 2 only works well for weak, small sea ice nudging experiments. For experiments with larger discrepancies between the modelled sea ice concentration and a target sea ice cover, the atmosphere warms up too much (>10°C over most of the Northern Hemisphere for a target sea ice down to 50°N). Hence, this method is not suitable. Therefore, the water, but not energy conserving, Method 1 where surface heat flux is used to nudge sea ice, is a useful alternative. This is similar to the flux correction technique proposed in Oudar et al. (2017).
Our results show that the energy conserving approach of modifying the sensible heat flux and redistributing the energy in the atmosphere, is probably not the way to go. At least not for sea ice targets far away from the models own sea ice state, as this results in large, unrealistic temperature changes, and/or an unstable model. However, the methods presented here have only been tested for idealized sea ice targets. Therefore, it could be interesting to test them on more realistic sea ice targets, for example by only nudging in small areas. Alternatively, it could be tested on sea ice targets smaller than the models own sea ice state, as melting sea ice proved to be easier than forming sea ice.

References

Bentsen, M., Bethke, I., Debernard, J. B., Iversen, T., Kirkevag, A., Seland, Ã., Drange, H., Roelandt, C., Seierstad, I. A., Hoose, C., and Kristjánsson, J. E. (2013). The norwegian earth system model, noresm1-m - part 1: Description and basic evaluation of the physical climate. *Geoscientific Model Development*, 6:687–720.

Blackport, R. and Kushner, P. J. (2016). The transient equilibrium climate response to rapid summertime sea ice loss in ccsm4. *Journal of Climate*, 29:401–417.

Blackport, R. and Kushner, P. J. (2017). Isolating the atmospheric circulation response to arctic sea ice loss in the coupled climate system. *Journal of Climate*, 30:2163–2185.

Craig, A. P., Vertenstein, M., and Jacob, R. (2012). A new flexible coupler for earth system modeling developed for ccsm4 and cesm1. *Int. J. High Perform. Comput. Appl.*, 26:31–42.

Deser, C., Tomas, R. A., and Sun, L. (2015). The role of the ocean-atmosphere coupling in the zonal-mean atmospheric response to arctic sea ice loss. *Journal of Climate*, 28:2168–2186.

ECMWF (2010). *Part IV: Physical Processes*. Number 4 in IFS Documentation. ECMWF. Operational implementation 26 January 2010.

Graversen, R. G. and Wang, M. (2009). Polar amplification in a coupled climate model with locked albedo. *Climate Dynamics*, 33:629–643.

Hazeleger, W., Wang, X., Severijns, C., Stefanscu, S., Bintanja, R., Sterl, A., Wyser, K., Semmler, T., Yang, S., van den Hurk, B., van Noije E. van der Linden, T., and van der Wiel, K. (2010). Ec-earth: A seamless earth-system prediction approach in action. *Bull. Am. Meteorol. Soc.*, 91:1357–1363.

Kalnay, E. (2012). *Atmospheric modeling, data assimilation and predictability*. Cambridge University Press, Cambridge, UK.

Lang, A., Yang, S., and Kaas, E. (2017). Sea ice thickness and recent arctic warming. *Geophysical Research Letters*.

Madec, G. and the NEMO team (2008). *NEMO ocean engine*. Note du Pôle de modélisation de l'Institut Pierre-Simon Laplace, France, No 27.

McCusker, K. E., Kushner, P. J., Fyfe, J. C., Sigmond, M., Kharin, V. V., and Bitz, C. M. (2017). Remarkable separability of circulation response to arctic sea ice loss and greenhouse gas forcing. *Geophysical Research Letters*, 44:7955–7964.

Oudar, T., Sanchez-Gomez, E., Chauvin, F., and Cattiaux, J. (2017). Respective roles of the direct ghg radiative forcing and induced arctic sea ice loss on the northern hemisphere atmospheric circulation. *Clim. Dyn.*, 49:3693–3713.

Pedersen, R. A., Cvijanovic, I., Langen, P. L., and Vinther, B. M. (2016). The impact of regional arctic sea ice loss on atmospheric circulation and nao. *Journal of Climate*, 29:889–902.

Petoukhov, V. and Semenov, V. A. (2010). A link between reduced barents-kara sea ice and cold winter extremes over northern continents. *Journal of Geophysical Research*, 115.

Petrie, R. E., Shaffrey, L. C., and Sutton, R. T. (2015). Atmospheric impact of arctic sea ice loss in a coupled ocean-atmosphere simulation. *Journal of Climate*, 28:9606–9622.

Screen, J. A. (2013). Influence of arctic sea ice on european summer precipitation. *Environmental Research Letters*, 8.

Screen, J. A. (2018). Consistency and discrepancy in the atmospheric response to arctic sea-ice loss across climate models. *Nature Geoscience*.

Semmler, T., Stulic, L., Jung, T., Tilinina, N., Campos, C., Gulev, S., and Koracin, D. (2016). Seasonal atmospheric responses to reduced arctic sea ice in an ensemble of coupled model simulations. *Journal of Climate*, 29:5893–5913.

Valcke, S. (2013). The oasis3 coupler: a european climate modelling community software. *Geoscientific Model Development*, 6:373–388.

Vancoppenolle, M., Bouillon, S., Fichefet, T., Goosse, H., Lecomte, O., Maqueda, M. A. M., and Madec, G. (2012). *LIM The Louvain-la-Neuve sea Ice Model*. Note du Pôle de modélisation de l'Institut Pierre-Simon Laplace, France, No 31.

Wallace, J. M. and Hobbs, P. V. (2006). *Atmospheric Science - An introductory survey*. Academic Press, Massachusetts, USA.

Appendix B

Manuscript II

Noname manuscript No.
(will be inserted by the editor)

Barents-Kara sea ice and European winters in EC-Earth

Ida Margrethe Ringgaard · Shuting Yang · Eigil Kaas · Jens Hesselbjerg Christensen

Received: date / Accepted: date

Abstract The potential link between decreasing Barents-Kara sea ice and cold winters in Europe is investigated using the enhanced resolution (horizontal atmospheric resolution of ∼80 km) global, coupled climate model EC-Earth. Nudging sea ice only in the Barents and Kara Seas, five configurations of sea ice covers are used to assess the importance of the amount of sea ice in this region. Nudging in the coupled model is achieved by modifying the non-solar surface heat flux into the ice/ocean interface. The mean winter temperature response suggests a weak but statistically significant non-linear response with cooling over eastern Europe for moderate sea ice reductions in the Barents-Kara Seas, a weaker but still cold anomaly for minor reductions and warming for major reductions. However, this non-linear response is not reflected in the circulation. Instead, a negative mean sea level pressure anomaly over Barents-Kara Seas intensifies with sea ice reduction. In contrast to this, is the response in the coldest winters over central Europe: the larger the sea ice reduction, the stronger the Scandinavian pattern and the associated easterlies has to be to obtain cold winters over central Europe. The use of a coupled climate model is a potential explanation for the link between the intensified Scandinavian pattern and the cooling over Europe observed in this study, that is not observed in some atmosphere-only model studies.

Keywords Sea ice · Barents-Kara Seas · Arctic sea ice loss · Coupled global climate model · Cold European winters

1 Introduction

Arctic sea ice has declined over the last decades (Stroeve and Notz (2018)). This decline has been observed over the whole Arctic, however it is fastest in the Barents-Kara Seas (BAKA) (Onarheim et al. (2015), Onarheim et al. (2018)). At the same time a

Ida Margrethe Ringgaard
Univsersity of Copenhagen, Juliane Maries vej 30, DK-2100 Copenhagen, Denmark
Danish Meteorological Institute, Lyngbyvej 100, DK-2100 Copenhagen, Denmark
Tel.: +45 39 15 72 73
E-mail: iri@dmi.dk

Shuting Yang
Danish Meteorological Institute, Lyngbyvej 100, 2100 Copenhagen, Denmark

Eigil Kaas
Univsersity of Copenhagen, Juliane Maries vej 30, DK-2100 Copenhagen, Denmark

Jens Hesselbjerg Christensen
Univsersity of Copenhagen, Juliane Maries vej 30, DK-2100 Copenhagen, Denmark
NORCE, Norwegian Research Centre AS, Bergen, Norway
Danish Meteorological Institute, Lyngbyvej 100, DK-2100 Copenhagen, Denmark

number of unusual cold winter events have been observed over Eurasia (Cohen et al. (2012), Liu et al. (2012)). These apparent counter-intuitive developments have induced a number of hypotheses related to a possible causality between declining Arctic sea ice and cold extreme winters over Eurasia. In particular, how a rapid decline of BAKA sea ice could have an impact on the latter. Several studies based on observations and model results have suggested that there is a link between low sea ice in BAKA and cold winter conditions over Eurasia. According to Mori et al. (2014), the probability of severe winters in central Eurasia has more than doubled due to sea ice reductions in BAKA. Yang and Christensen (2012) analyzed the CMIP5 multi-model ensemble and found that despite an overall warming of Europe in the near future, cold winters (compared to the period 1971-2000) are still likely to occur.

Some observational studies find a link between BAKA sea ice loss and cold Eurasian winters. Some observational studies even suggest Arctic sea ice loss as a driver of cold Eurasian winter. Koenigk et al. (2016) used reanalysis (ERA-Interim) and satellite sea ice data (OSI-SAF) to pinpoint autumn Barents Sea sea ice variations as the best predictor for the following winters NAO (low sea ice linked to negative NAO). The observed warming over BAKA has also been linked to cooling over East Asia (Kug et al. (2015)). Outten and Esau (2012) showed a co-variability between the observed negative temperature trends over Eurasia and the Arctic sea ice loss. However, co-variability does not show causality. Determining a potential driver of the Eurasian wintertime cooling was undertaken by Kretschmer et al. (2016). By using causal effects networks to analyze observational data, they showed that the BAKA sea ice reduction induces a weaker winter AO leading to wintertime cooling, thus being an important driver of the mid-latitude winter circulation. Further, Kretschmer et al. (2018) showed that cold winters in Eurasia and in North America are governed by different stratospheric patterns. Using cluster analysis, they showed that cold winters in northern Eurasia are linked to a weak polar vortex, upward propagating waves into the stratosphere leading to a negative NAO and resulting in cold spells over Eurasia.

Not only observational studies show this potential link and pathway. Using climate models, several model studies have investigated the effect of sea ice reduction on Eurasian winter temperatures. Petoukhov and Semenov (2010) used an atmosphere-only model (AGCM) at a coarse resolution ($2.8^\circ \times 2.8^\circ$) to investigate the effect of step wise sea ice reduction in BAKA. They found a non-linear response to sea ice reduction, showing that a moderate sea ice reduction (40-80%) induced an enhanced anticyclonic anomaly over the Arctic Ocean and thus a strong easterly flow leading to cooling over Europe. In an AGCM study by Nakamura et al. (2015), sea ice reduction in BAKA induced a stationary Rossby wave leading to a negative AO/NAO like pattern, inducing prolonged Arctic cold air advection toward continental mid-latitudes.

Several mechanisms linking Arctic sea ice reduction, and in particular BAKA sea ice reduction, to cold Eurasian winter anomalies have been proposed. A typical proposed chain of events is: negative sea ice anomalies over BAKA in late autumn cause a larger surface heat flux from the ocean to the atmosphere, hence warming over BAKA; this induces upward propagating waves, leading to a weaker polar vortex, as well as weaker westerlies; downward propagation of the signal from the stratosphere back to the troposphere; the weaker polar vortex induces a negative AO/NAO like pattern linked to cold anomalies over Europe (Ruggieri et al. (2016), Garcia-Serrano et al. (2015), Kretschmer et al. (2018)).

This potential link is still being widely discussed, as other studies have not been able to identify such a link. McCusker et al. (2016) compared the trend in BAKA sea ice decline to the trend of Eurasian winter temperatures for two time periods: 1979-1989 and 2002-2012. They found that although the Eurasian cooling over this period was exceptional, the BAKA sea ice loss was not, hence suggesting that BAKA sea ice is not the main driver of Eurasian cooling. Instead, the observed cooling over Eurasia was most likely driven by internal atmospheric variability. The same conclusion was reached by Sorokina et al. (2016), based on ERA-Interim with no apparent correlation between Barents sea ice, turbulent heat fluxes over Barents Sea and the 'warm-Arctic cold Continents' pattern. Using an AGCM, Screen (2017a) reached a similar conclusion analyzing the link between NAO and Arctic sea ice loss and found that even though Arctic sea ice loss does intensify negative NAO events, this does not have a strong effect on the winter temperatures over Europe: the winter temperatures remain constant or even warm slightly. This 'missing' cooling is the result of the dynamical cooling due to the negative NAO being offset or exceeded by the thermodynamic warming due to the sea ice loss itself. Ogawa et al. (2018) also used AGCM's to investigate the impact of recent Arctic sea ice decline on winter climate, reaching the same conclusion as Screen (2017a) that the observed cooling over Siberia in winter is caused by internal atmospheric dynamics.

The above clearly shows that there is no consensus among neither observational nor climate model studies as to whether there is a link between BAKA sea ice reductions and Eurasian wintertime cooling. The discrepancy between observations and model studies might be caused by an underestimation of the cooling in climate models (Mori et al. (2019)). The discrepancy among

modelling studies might be related to the use of AGCM's and coupled GCM's. As sea ice is often prescribed to AGCM's as new boundary conditions, atmosphere-ocean feedbacks are not included in the model. Further, the model sensitivity to sea ice perturbations may be offset due to circulation biases in the basic state. Deser et al. (2015) showed that including the oceanic feedbacks by coupling the atmosphere to the ocean results in global responses, as opposed to locally, poleward confined responses in AGCM's. Further, Screen (2018) states that coupled atmosphere-ocean models seem to agree more across models than atmosphere-only models. This implies that coupled climate models are needed to obtain a more complete picture. As opposed to many of the studies presented above using AGCM's, we aim at using a coupled climate model, as this will capture the atmosphere-ocean feedbacks, thus capturing remote responses as well.
The aim of this study is to answer the following questions:

1. Using a coupled climate model and only modifying sea ice in the Barents-Kara Seas, are we able to find resulting colder winters in Europe?
2. Is the response, if identified, linearly related to the extent of the sea ice cover in Barents-Kara Seas? Or is it non-linear as Petoukhov and Semenov (2010) suggest?

2 Method

2.1 Methods for constraining sea ice

Screen (2018) discussed some of the methods used to modify sea ice in a coupled climate model. Sea ice can be modified by changing the sea ice concentration (SIC) in the model, overwriting the models own SIC using brute force. However, this is neither energy- nor (fresh-)water conserving. This can be improved by changing SIC over time, using assimilation and Newtonian relaxation (e.g. Tietsche et al. (2013)). A different approach of energy and water conserving was used by Petrie et al. (2015) and Semmler et al. (2016). Both studies reduced sea ice thickness just before, or early in, the melt season, which induced a smaller summer sea ice extent. However, this approach only works for short time periods, as the system will quickly return to normal again.
To avoid these constraints, some studies have used a 'ghost' flux to perturb sea ice in coupled climate models. Deser et al. (2015) adds to the ice module a seasonally, but not spatially, varying long-wave (LW) radiative flux (LRF), which is computed according to a target sea ice cover. They simulated scenarios with different LRF and from the resulting sea ice covers, estimated which magnitude of LRF results in the target sea ice cover. Oudar et al. (2017) compute the 'ghost' flux as the difference in non-solar (LW+turbulent) heat flux between a control simulation and target simulation. That is, they use the non-solar flux generated due to a specific sea ice cover. A slightly different approach is taken by McCusker et al. (2017). Their 'ghost' flux is computed as the amount of heat needed to melt (or create) a certain mass of sea ice. This heat is then added to/removed from the ice model. To form sea ice, heat is also removed from the ocean, in order to cool it down.

Our approach is similar to McCusker et al. (2017): the difference in sea ice concentration in a specific grid cell at each time step is used to compute a 'ghost' flux. However, our method differs in two ways: 1) instead of computing the heat needed to melt/form a certain mass of sea ice, we use the difference between the instantaneous SIC and a target SIC ($\Delta SIC = SIC_{model} - SIC_{target}$) as a weight on the magnitude of the instantaneous non-solar heat flux received by the ocean (HF):

$$\Delta HF = HF \cdot \Delta SIC \cdot A \tag{1}$$

where A is an empirical constant. We have used a value of 5, as the resulting ΔHF were too small to make a difference when using a smaller value. Using 5 ensures a large enough adjustment every time step, without causing the model to become unstable. If ΔSIC exceeds a threshold value (here set to 5%), the correction term is added to the instantaneous non-solar flux, HF. 2) The heat added to melt sea ice is superimposed at the atmosphere/ocean boundary.

2.2 Experimental setup

In this study we use the fully coupled climate model EC-Earth V3.2. The atmosphere component of EC-Earth used here is the ECMWF's Integrated Forecast System (IFS) cycle 36r4 with a spectral resolution of T255 (equivalent to 80km) and 91 vertical levels. The ocean component is the Nucleus for European Modelling of the Ocean (NEMO) version 3.6 on the ORCA1 tripolar grid (1°x1°) and with 75 vertical levels. NEMO is embedded with the sea ice component the Louvain-la-Neuve sea Ice Model (LIM3). IFS and NEMO are coupled through the OASIS-3 coupler. The older version EC-Earth V2.2 is presented and validated in Hazeleger et al. (2010) and Hazeleger et al. (2012). The older version, V2.2 differs from V3.2 by using IFS cycle 31r1 with horizontal resolution T159, NEMO version 2 and LIM2. These have all been updated since V2.2. One of the main differences is in the sea ice component LIM, as LIM3 has five sea ice thickness categories whereas LIM2 only has one. Validating EC-Earth V3.2 against ERA-Interim, similar to Hazeleger et al. (2012), show a general warm shift and reduction of the biases in most regions in V3.2, except over Sahara where the cold bias in V2.2 seems intensified in winter (DJF) (see the Supplementary figure S1). The systematic errors in the Arctic has shifted from a large cold bias in V2.2 to a slightly warm bias. The bias in summer (JJA) is also smaller in general than in V2.2, with a shift toward a warmer bias. Bias in the tropics have been reduced compared to V2.2. The cold bias over Greenland has decreased, as has the bias over Europe. A band across central Eurasia has a warmer bias in V3.2. The mean sea level pressure bias in V3.2 show similar patterns to that in V2.2 (Supplementary figure S2). In general, the bias shifted towards a more positive bias, i.e. higher pressure. To focus on a few areas, we note the bias is smaller over the North Atlantic in both summer and winter relative to V2.2. Over Sahara has the high pressure bias increased. The Aleutian Low bias has shifted from being positive to negative. Hence, V3.2 have similar bias patterns to those of V2.2, with smaller, but slightly more positive values.

Six simulations were carried out, each 100 years long: one freely running model and five experiments, where sea ice concentrations were nudged. The freely running, unforced model simulation under present day conditions (GHG, aerosols etc) was run after an initial spin-up period of 350 years, hereafter referred to as CFree. This model simulation is used to generate the model sea ice concentration climatology (CFree$^{Clim}_{SIC}$) and the sea ice area climatology (CFree$^{Clim}_{SIA}$). There is still a drift (global mean surface (2m) temperature trend of ∼0.2°C over 100 years) in CFree even after the spin-up. All model results are therefore linearly detrended before being analyzed. The five perturbed experiments are equal to CFree except the sea ice in BAKA (30-80°E, 65-80°N, see figure 1), where the SIC are nudged toward CFree$^{Clim}_{SIC}$, to a varying degree. Outside this region there is no nudging and the sea ice can evolve freely. When nudging applied, the SIC in BAKA is only reduced in the winter half year from November through April, as November sea ice have been shown to be correlated to the sign of the NAO (Koenigk et al. (2016)). The rest of the year, SIC is nudged toward CFree$^{Clim}_{SIC}$. Following the setup from Petoukhov and Semenov (2010), SIC is step wise reduced from 100% to 20% in steps of 20% in each simulation. This creates five perturbed sea ice covers for BAKA, all originating from the same initial conditions from CFree: C100 nudged toward 100% of CFree$^{Clim}_{SIC}$, C80 toward 80% (i.e. C80=0.8·CFree$^{Clim}_{SIC}$) and so forth. Comparing the long-term mean surface temperature for C100 and CFree, it is clear that only the local, perturbed region is affected by removing the internal SIC variability (not shown). Inside BAKA, C100 is up to 2°C warmer than CFree for the winter (DJFM) mean, but outside this region the differences are $\sim \pm 0.5$ °C. Comparing C100 SIC to the observed March SIC for the period 1979-2009 (OSISAF (2017)) it can be seen that C100 replicates the observed sea ice cover quite well, although with a smaller sea ice extent in the Barents Sea, the Bering Sea and the Sea of Okhotsk, see figure 1.

The monthly mean achieved sea ice area (SIA) for BAKA for each of the five perturbation experiments relative to the target SIA for C100 (CFree$^{Clim}_{SIA}$) are presented in table 1. Generally, the achieved winter SIA is larger than the target, and the summer SIA is lower, resulting in an annual mean close to the target SIA. The large difference between target and achieved SIA in summer is related to the fact that BAKA is almost ice-free in summer. Therefore, differences between the two concentrations will be relatively larger in summer. The achieved SIA is not equal to the target, as the nudging method compares every grid point to the target and is only activated if the difference is larger than ±5%. Although the target SIA is not reached exactly, table 1 shows a clear reduction going from C100 to C20.

Reducing sea ice in BAKA warms the local ocean underneath, and increases the surface salinity in summer and autumn for all four perturbed runs relative to C100. In winter and spring, the BAKA ocean surface layers are fresher than C100 (not shown). This is related to the reduced melting/forming of sea ice, leading to less fresh melt water release in summer and autumn, and less brine rejection in winter and spring, i.e. less salt being pushed out of the ice and into the ocean. Outside BAKA, there are no substantially changes to the ocean temperature and salinity profiles. Hence, this method does not induce noteworthy remote ocean impacts.

The atmospheric response of the reduced sea ice cover is assessed as the difference between the four experiments with reduced sea ice (C80, C60, C40, C20) and the control run C100. That is, the climatology of C100 have been subtracted from all experiments, so as to remove the seasonal cycle. Hence, results for C100 are presented as anomalies wrt the 100-year mean and ΔC20 to ΔC80 as changes of anomalies. As focus is on winter responses, we analyze the three bimonthly periods: early winter (December and January, DJ), mid winter (January and February (JF) and late winter (February and March, FM). By using bi-

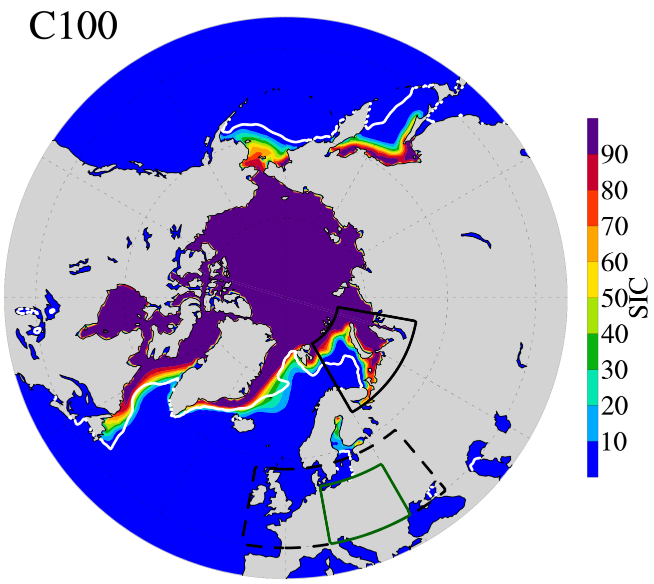

Fig. 1: 100-year mean sea ice concentration (SIC; in %) in March for C100. The observed March sea ice edge (SIC>15%) for the period 1979-2009 is shown in white (OSI-450, OSISAF (2017)). Black box indicates BAKA region [30-80°E, 65-80°N], black dashed box indicate Central Europe (CEU) region [-10°E-40°E, 45°N-58°N] (Screen et al. (2015a)) and green box indicate EU region [10°E-30°E, 45°N-55°N] (Petoukhov and Semenov (2010)).

Exp	**Target %**	**Jan**	**Feb**	**Mar**	**Apr**	**May**	**Jun**	**Jul**	**Aug**	**Sep**	**Oct**	**Nov**	**Dec**	**Annual mean**
C100	100	110.0	105.8	103.0	94.4	73.5	30.0	16.1	26.9	53.2	143.8	137.1	113.1	83.9
C80	80	96.9	95.0	90.6	81.6	55.9	23.9	15.8	20.1	45.7	105.0	113.6	98.2	70.2
C60	60	78.8	76.8	69.8	68.2	49.2	20.9	11.9	24.5	39.9	82.3	90.0	80.4	57.7
C40	40	55.8	54.6	48.2	54.1	43.9	17.6	9.41	6.75	15.2	54.7	61.9	56.5	39.9
C20	20	33.1	32.8	27.8	14.0	5.65	3.68	2.24	1.63	1.73	6.06	19.7	32.4	15.1

Table 1: Achieved BAKA SIA for each perturbed experiment relative to BAKA CFree$^{Clim}_{SIA}$ in % ($C80 = (SIA_{C80}/CFree^{Clim}_{SIA}) \cdot 100$) for each month and the annual mean. 100% is equal to the climatological BAKA SIA in CFree (CFree$^{Clim}_{SIA}$), i.e. the target for C100. The target percentage in the winter season for each of the five experiments is shown in column 2.

monthly periods instead of a mean over all winter months (DJFM), a potential cold signal of shorter duration will not that easily be averaged out by a compensating warmer period. This is essential, since very cold events are not necessarily cold throughout the entire winter. The coldest winters are represented by the 5th percentiles temperatures (T_{p5}), which is computed for each grid point as well as for the area mean of Central Europe (CEU, [-10°E-40°E, 45°N-58°N]). They are based on the monthly values of the detrended temperature anomalies for each subseason, i.e. the season JF consists of 200 months (2 months for each of the 100 years).

Statistical significance of the mean and percentiles are assessed by bootstrapping using Monte Carlo simulations with resampling (von Storch and Zwiers, 2003, chapter 5.5). Statistical significance is given at the 95% confidence level. The significance of the percentiles are computed by bootstrapping the percentiles of the C100 experiment, then testing the percentiles of the sea ice reduced experiments toward this.

3 Results

Results are discussed below for all three bimonthly periods (early, mid and late winter), but only results from mid winter are shown. In general, anomalies relative to C100 are shown.

3.1 Mean atmospheric responses

We first focus on examining the change of the mean states as sea ice is reduced. Reducing sea ice in a certain area allows for more heat to escape from the ocean into the atmosphere. Therefore, the surface air temperature above and in the surrounding area is expected to increase. This is confirmed by the surface temperature distribution (figures 2). Comparing to the temperature mean of C100, it is seen that over the BAKA nudging region there is an increase in temperature of 3°C or more. The more the sea ice is reduced, i.e. going from ΔC80 to ΔC20, the larger this area becomes. For all four reductions and for each bimonthly period, the general picture is of a warming Northern Hemisphere (NH), largest increase in temperature over BAKA and adjacent areas of Eurasia and North America. Standing out is the simulation C60 with 60% of climatological sea ice, which shows significantly lower temperatures over an area of eastern Europe between Scandinavia and the Black Sea of about 1°C as well as the North Atlantic (around <0.5°C), as seen in figure 2(c). A smaller, but still significantly cold area over eastern Europe is present in late winter as well (not shown). For smaller sea ice reductions than this (C80), there is a lack of warming, but not statistically significantly different from the control run anywhere over Europe (figure 2(b)). Larger sea ice reductions (C40 and C20), does not exhibit colder areas over Europe, but rather statistically significant warming (fig. 2(d)-(e)). It is interesting to note that the warmest winters appear to occur in C40, not in C20. The non-linearity of the surface temperature with BAKA sea ice reductions for all three bimonthly winter periods is visualized in figure 3, which shows the area mean temperature anomalies (i.e. fig. 2) for two areas over Europe (areas shown in figure 1): CEU (black circles) and EU (red triangles) which is the same area used in Petoukhov and Semenov (2010). The colder temperatures in C60 relative to C80, C40 and C20 are present in all three bimonthly periods and for both areas over Europe. For these area averaged values, only C20 and C40 are significantly different (warmer) from C100. However, the difference between the minimum and the maximum temperature (i.e. C60 and C40) is statistically significant for both EU and CEU in all three subseasons. Averaging over a larger area suppress the relatively small statistically significant colder area over eastern Europe seen in figure 2 for C60.

The mean absolute mean sea level pressure (MSLP) for the control simulation (C100) is shown in figure 4(a). Similar to the observed winter MSLP pattern, two low pressure systems are identified over Iceland and the Bering Sea, while a high pressure system is located over Siberia and central Asia. The mean response to sea ice reductions for all four perturbed experiments are quite similar: a low pressure anomaly appear over the BAKA region and downstream thereof (figures 4(b)-(e)), with increase in strength as sea ice reduces. This tendency seems to saturate around a 40% sea ice reduction (C40), consistent with the maximum warming response in C40 (fig. 2(d)). The low pressure anomaly is consistent with removing sea ice, which warms the surface and the air above, hence leading to expansion and rise of the air (a 'heat low'). It results in an overall southward displacement of the high pressure system over Siberia in conjunction with the development of the local pressure anomaly over and downstream of the forcing region. The linearity of the MSLP anomaly across reduction scenarios can be seen more clearly in figure 5. It shows the area mean root-mean-square-error (RMSE) of the MSLP for each perturbed experiment relative to C100 for the area north of 50°N, encompassing the MSLP anomaly seen in figures 4(b)-(e). In general, we see an increasing RMSE following the reduction in sea ice, going from 0.7 for C80 to 2.1 for C40 and 2.0 for C20. Hence, the MSLP anomaly in figure 4 becomes increasingly less like the C100 pattern as BAKA sea ice is reduced. Similar to the mean temperature response, the MSLP seems to saturate around C40.

The changes in the pressure systems are reflected in the wind patterns (not shown): the control run C100 shows the dominating westerlies over Europe, and all four perturbed experiments show a cyclonic wind anomaly over BAKA, associated to the low pressure anomaly discussed above. Also, as the low pressure anomaly increases (from ΔC80 through ΔC20), the wind anomaly over Europe increases. The results above indicate a potential link between cold winters and moderate sea ice reductions in BAKA.

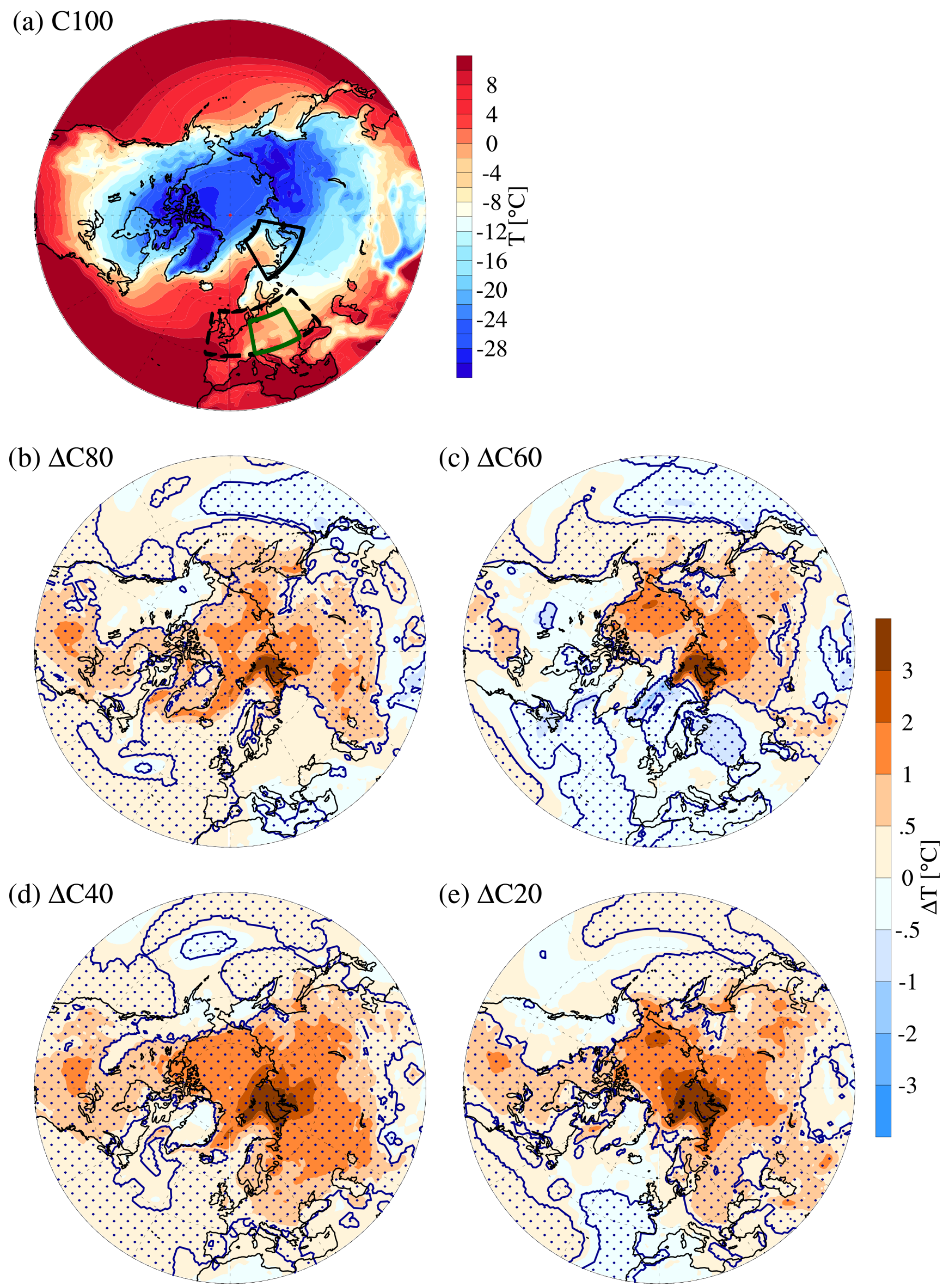

Fig. 2: (a) Mid winter (JF) mean absolute surface (2m) temperature (in °C) for C100. The difference in mean JF surface temperature for (b) ΔC80, (c) ΔC60, (d) ΔC40 and (e) ΔC20. Black box indicates BAKA area. Dots indicate significance at 5% level, black dashed box indicate CEU region and green box indicate EU region.

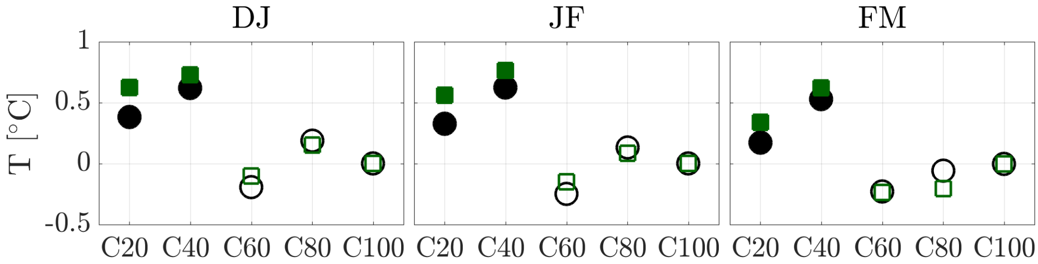

Fig. 3: The area mean of the 100-year mean surface air temperature anomaly (in °C) for two areas over Europe for each of the five perturbed simulations. The two areas CEU (black circles) and EU (green squares) are shown in figure 1. Filled markers indicate temperatures significantly different from C100 at a 5% level. The temperature difference between C60 and C40 (i.e. minimum and maximum) is significantly different at a 5% level for both EU and CEU for all three subseasons.

3.2 Abnormally cold winters

After examining the mean atmospheric responses through all 100 years we will take a closer look at the coldest winters. There are several ways to investigate the response in the occurrence of the coldest winters. Here we first analyze the temperature distribution in each grid point, to identify geographical regions of interest. Afterwards, we focus at larger regions covering Europe.

3.2.1 Grid point wise percentiles

The coldest winters are shown as the 5th percentile temperature (T_{p5}) in each grid point in figure 6. Figure 6(a) shows T_{p5} for C100 (T_{p5}^{C100}). The difference between the control simulation and the four perturbed experiments are shown in figure 6(b)-(e) for mid winter. Clearly, large parts of the Northern Hemisphere experience warmer cold winters (orange colors), especially over the perturbed region (BAKA). The magnitude and spatial extent of these warmed areas increase as more sea ice is removed in BAKA (i.e. going from ΔC80 to ΔC20). This is similar to the 100-year mean atmospheric response seen in figure 2. However, there are also areas where T_{p5}^{Cx} is colder than T_{p5}^{C100}. In ΔC60 (fig. 6(c)), Europe experiences a lack of warming, with small areas of statistically significant cooling over Eurasia, including parts of the area over eastern Europe that was significantly cold in the mean response (fig. 2(c)). The temperature anomalies over eastern Europe reach 1-2°C lower than that of the climatological run (C100). The 5% warmest winters demonstrate a similar pattern (not shown), with a lack of warming over Europe in C60. Combining this with the mean temperature response shown in section 3.1 indicates that the temperature distribution for C60 is shifted toward lower temperatures compared to C100. This shows that C60 is statistically significant colder than C100 in some small areas and colder, but not statistically significant colder, in larger areas. This suggests that a moderate reduction of sea ice may link to statistically significant lower temperatures, but only for some small areas of Europe. For C80, there is not significant change over Europe, whereas C40 and C20 show a statistically significant warming over Europe. Quantifying the area averaged coldest temperatures over CEU and EU, the same non-linearity as for the mean response is implied in figure 7, but neither of the four reduction experiments are statistically significantly different from C100. However, the temperature difference between the minimum and the maximum (i.e. C80 and C40) is statistically significant for EU, but not for CEU, for JF and FM, indicating the non-linear behavior.
The analysis in figure 6 is performed at each grid cell separately, meaning that the coldest temperature in neighboring grid points are not necessarily from the same winter months, thus not necessarily caused by the same weather systems. Lining up all the winter months chronologically and extracting the coldest month in each grid point reveals larger coherent areas, as depicted in figure 8. Further, looking at the second, third, fourth (and so on) coldest winter months results in a much messier picture with no large coherent areas showing up (not shown). Therefore, the above figures suggest that there might be a link between reduced BAKA sea ice and Eurasian winter temperatures, but it does not show why they occur.

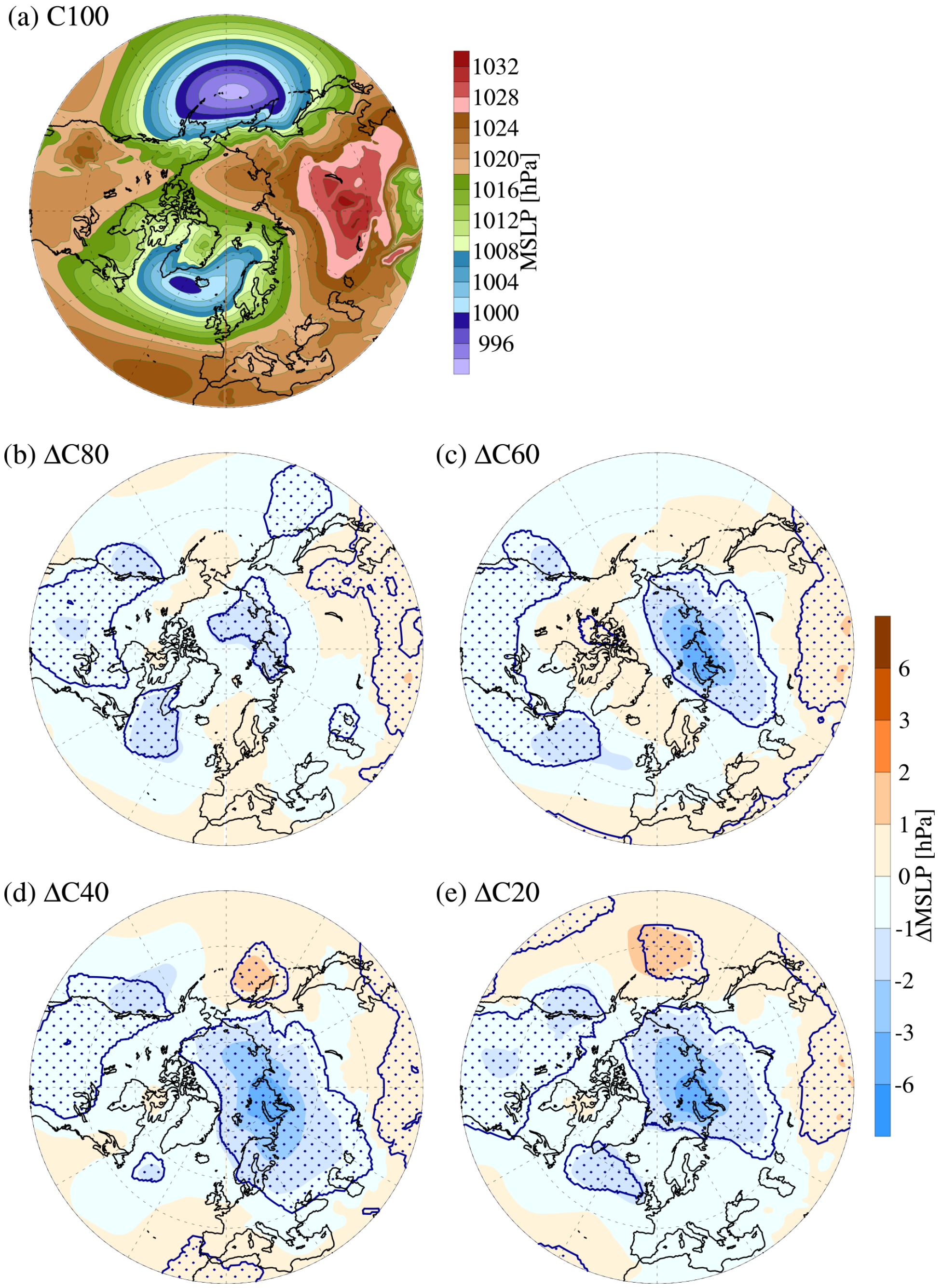

Fig. 4: (a) Mid winter (JF) mean absolute mean sea level pressure (in hPa) for C100. The difference compared to C100 for (b) ΔC80, (c) ΔC60, (d) ΔC40 and (e) ΔC20. Dots indicate significance at 5% level.

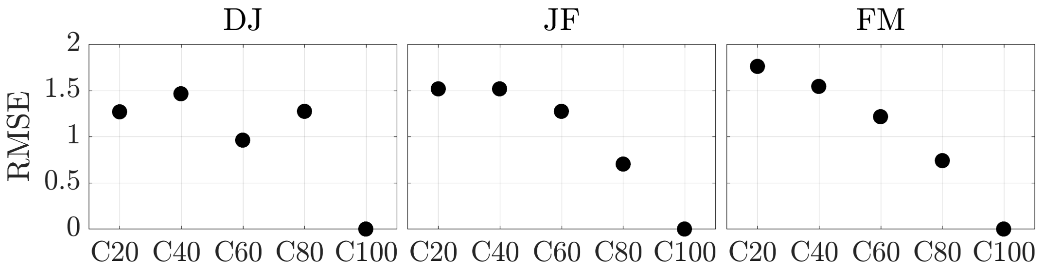

Fig. 5: The root-mean-square-error (RMSE) of the mean sea level pressure (in hPa) for each perturbed experiment relative to C100 over the area north of 50°N.

3.2.2 Cold winter months composite of larger regions

Focusing on larger regions, the area mean winter temperature for CEU is used to determine the 5% coldest winter months, in each bimonthly period. These months are then used to construct composites of surface temperature and MSLP. The composite surface temperatures for cold CEU are shown in figure 9. The resulting composites of surface temperature anomalies for C100 demonstrates a cold anomaly of more than -5°C in a large area of Europe and Western Asia, accompanied by a warm anomaly of above 2°C over Greenland (fig. 9(a)). Reducing sea ice in BAKA results in a general warming over most of the Arctic for the cold winter months for all three subseasons (figs. 9(b)-(e)). However, it is worth noting that all four perturbed experiments have a similar, cold response in early and mid winter over the northern part of CEU and Scandinavia, as well as parts of Asia and North America, with respect to C100 (early winter not shown). The southern part of CEU warms relative to C100 for C40 and C20. The area mean temperature response over CEU show no statistically significant change as the BAKA sea ice is reduced (blue circles in figure 7).

The corresponding circulation responses are shown in figure 10. For the 5% coldest winter months in CEU in figure 10(a), the overall MSLP is higher than the time average over the Nordic Seas and Scandinavia in C100, resembling the Scandinavian pattern (Barnston and Livezey (1987)). Reducing the sea ice in BAKA expands this high pressure anomaly northward while strengthening the anticyclonic anomalies, saturating around C40. This implies that as sea ice is reduced, cold winters in CEU are accompanied by an increasingly stronger Scandinavian pattern and hence stronger easterlies bringing cold air from Siberia into Central Europe. The strengthening of the Scandinavian pattern can be visualized by looking at the spatial sum of the MSLP anomalies for the reduced experiments (C20-C80) projected onto the MSLP anomalies for the control simulation (C100). Equation 2 shows the case for C80

$$P = \frac{\sum_{\phi}\sum_{\lambda}(\Delta MSLP_{C80} \cdot \Delta MSLP_{C100} \cdot \cos\phi \Delta\phi \Delta\lambda)}{\sum_{\phi}\sum_{\lambda}(\Delta MSLP_{C100} \cdot \Delta MSLP_{C100} \cdot \cos\phi \Delta\phi \Delta\lambda)} \tag{2}$$

where, λ and ϕ are the longitudinal and latitudinal coordinates,$\Delta MSLP_{C80}$ is the temporal mean of the detrended MSLP anomaly (i.e. fig. 10(b)) and $\Delta MSLP_{C100}$ is the same but for C100. The sum is taken over the region (40°W-60°E, 45°N-90°N), the green box in figure 10(a). The result for each experiment and for each of the 3 bimonthly winter periods can be seen in figure 11. For DJ and JF, P are generally above 1, indicating that the Scandinavian pattern intensifies when sea ice is removed in BAKA. For C40, the high pressure anomaly over Scandinavia has shifted northward and expanded (fig. 10(d)), leading to a P value closer to 1 compared to C20, C60 and C80.

This high pressure anomaly over Scandinavia is in contrast to the low pressure anomaly over BAKA observed for the mean response. This imply that even though the mean response is a low pressure anomaly, the 5% coldest winters (10 months out of the 200 months for each bimonthly period) occur when cold air is being advected from the North, associated with the Scandinavian pattern.

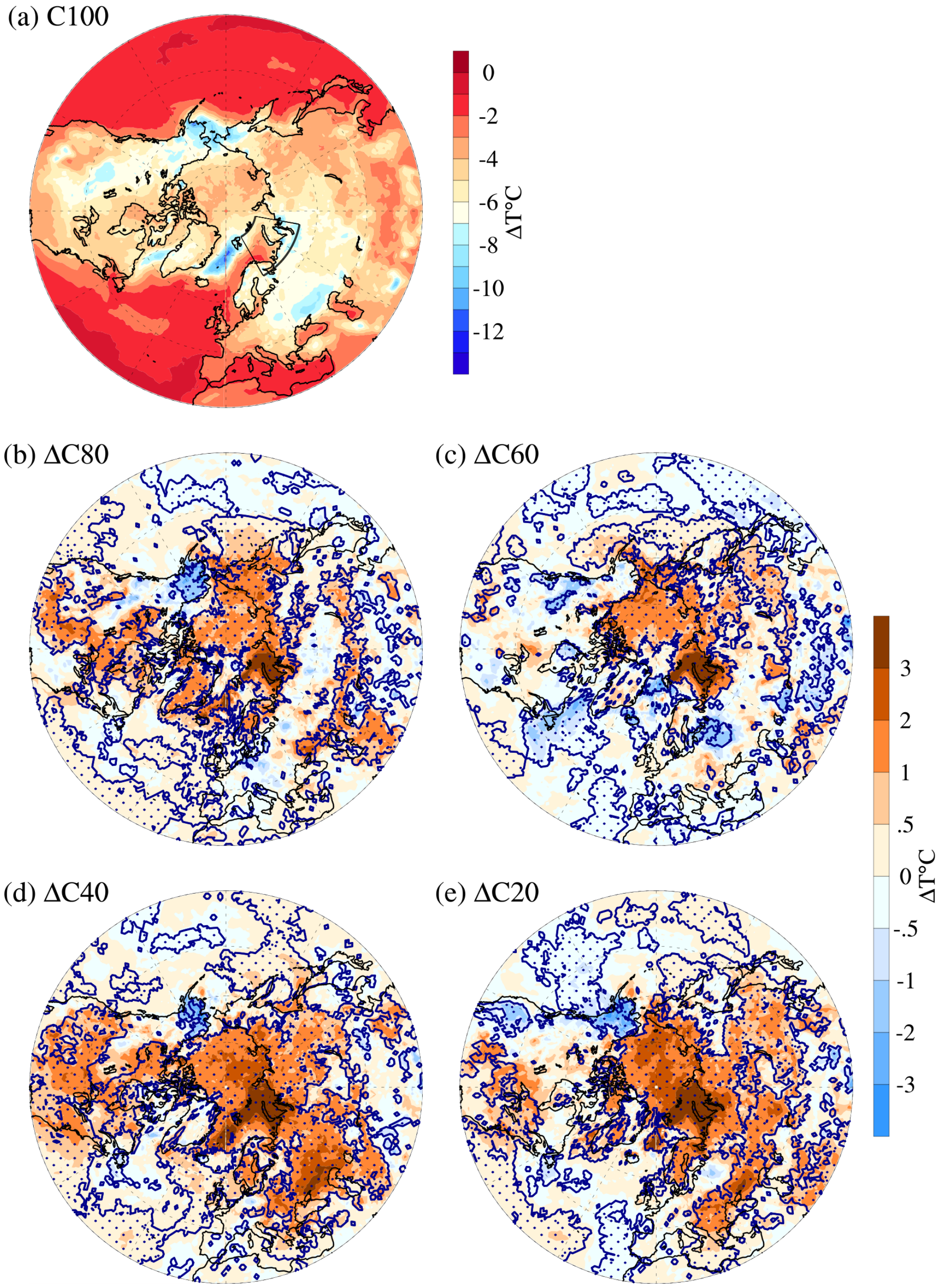

Fig. 6: (a) Mid winter (JF) composite of the surface temperature (in °C) for the 5% coldest winters at each grid cell for C100. The difference compared to C100 for (b) ΔC80, (c) ΔC60, (d) ΔC40 and (e) ΔC20. Orange/brown colors indicate warmer 5th percentiles (warmer coldest winter months) and blue colors indicate colder 5th percentiles (colder cold winter months) in the perturbed experiments wrt to C100. Dots indicate significance at 5% level.

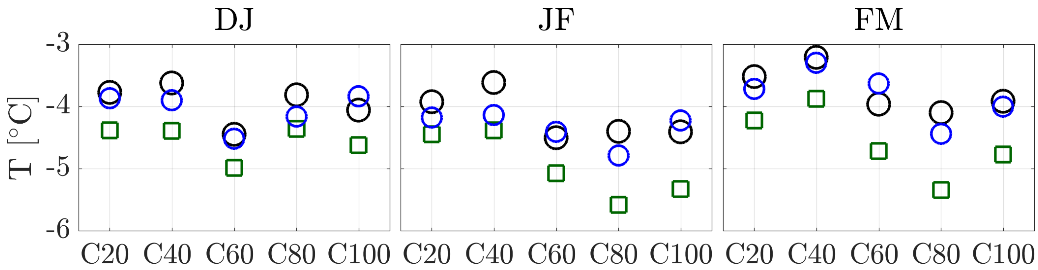

Fig. 7: The area and temporal mean surface temperature (in °C) of the 5% coldest winter months in each grid cell (black circles (CEU) and green squares (EU)) and the mean of the 5% coldest winter months in CEU (blue circles). None of the perturbed simulations are significantly different from C100 at a 5% level. The temperature difference between C80 and C40 (i.e. minimum and maximum) is significantly different at a 5% level in JF and FM for EU, but not for CEU.

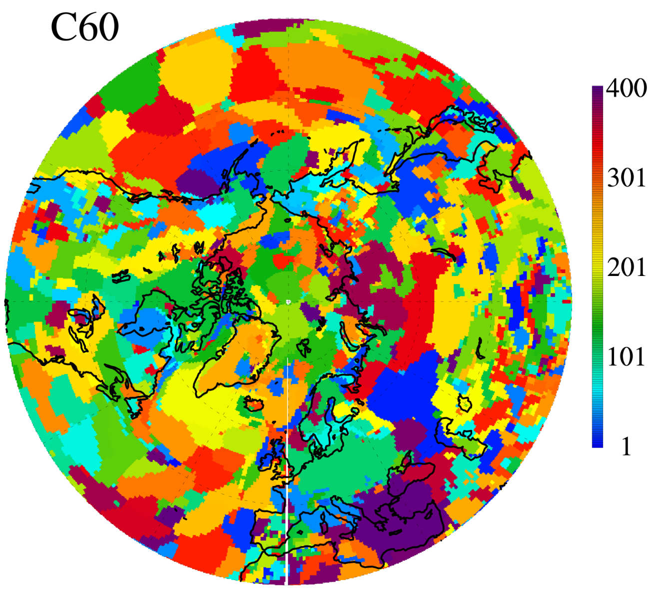

Fig. 8: The month with the coldest surface air temperature occurring during 100 years at each grid cell for C60. The numbering is constructed by taking the four winter months (DJFM) and lining them up chronologically. Hence, month #1 is January of the first year, #2 is February, #3 is March and #4 is December etc.

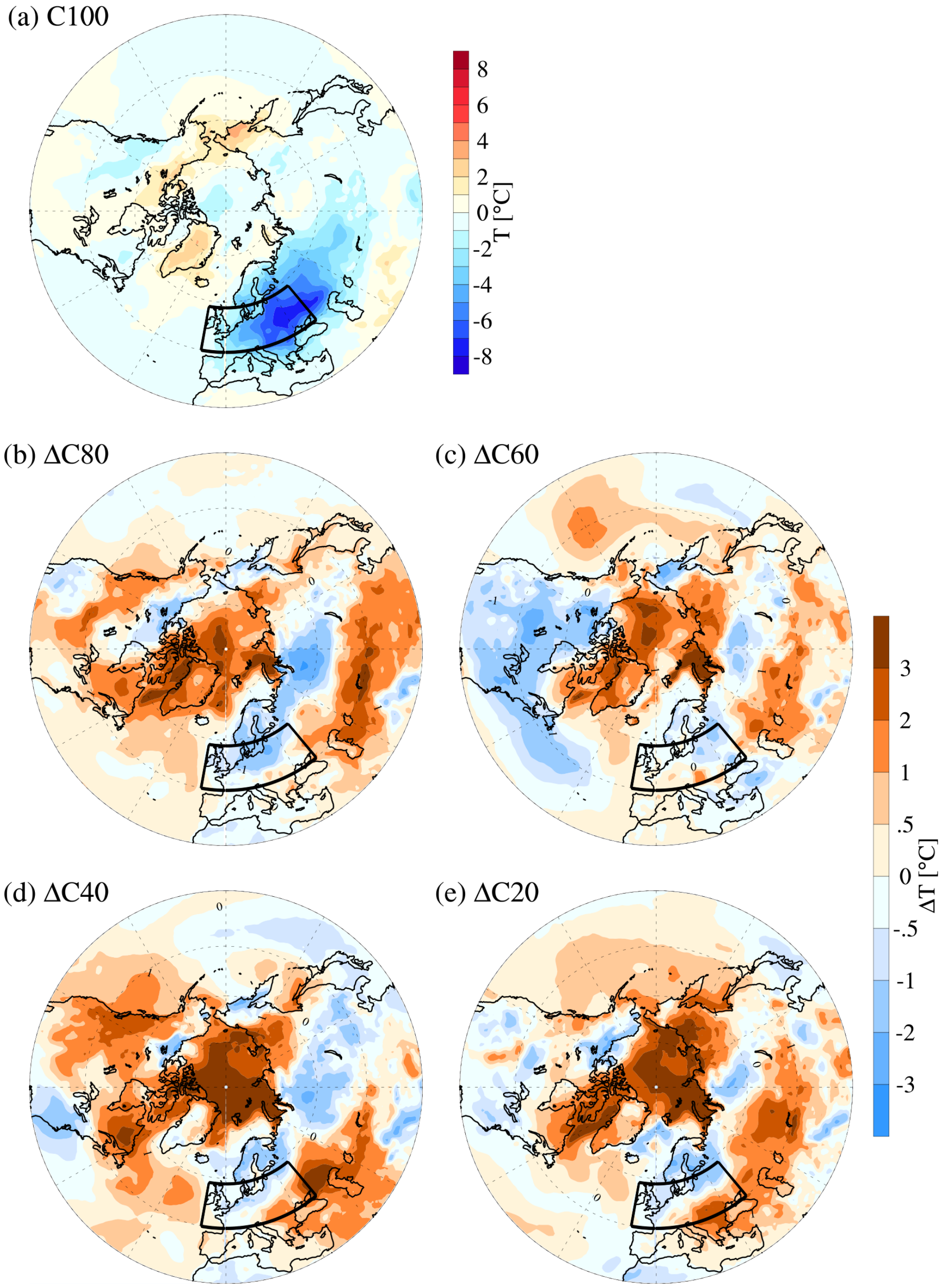

Fig. 9: Mid winter (JF) composite of the surface temperature (in °C) for the 5% coldest winters in CEU (black box). (a) Temperature difference in C100 ($T_{C100} - T_{C100,clim}$) and the response as changes of anomalies in (b) $\varDelta$C80, (c) $\varDelta$C60, (d) $\varDelta$C40 and (e) $\varDelta$C20. Orange colors indicate warmer than C100 and blue colors colder.

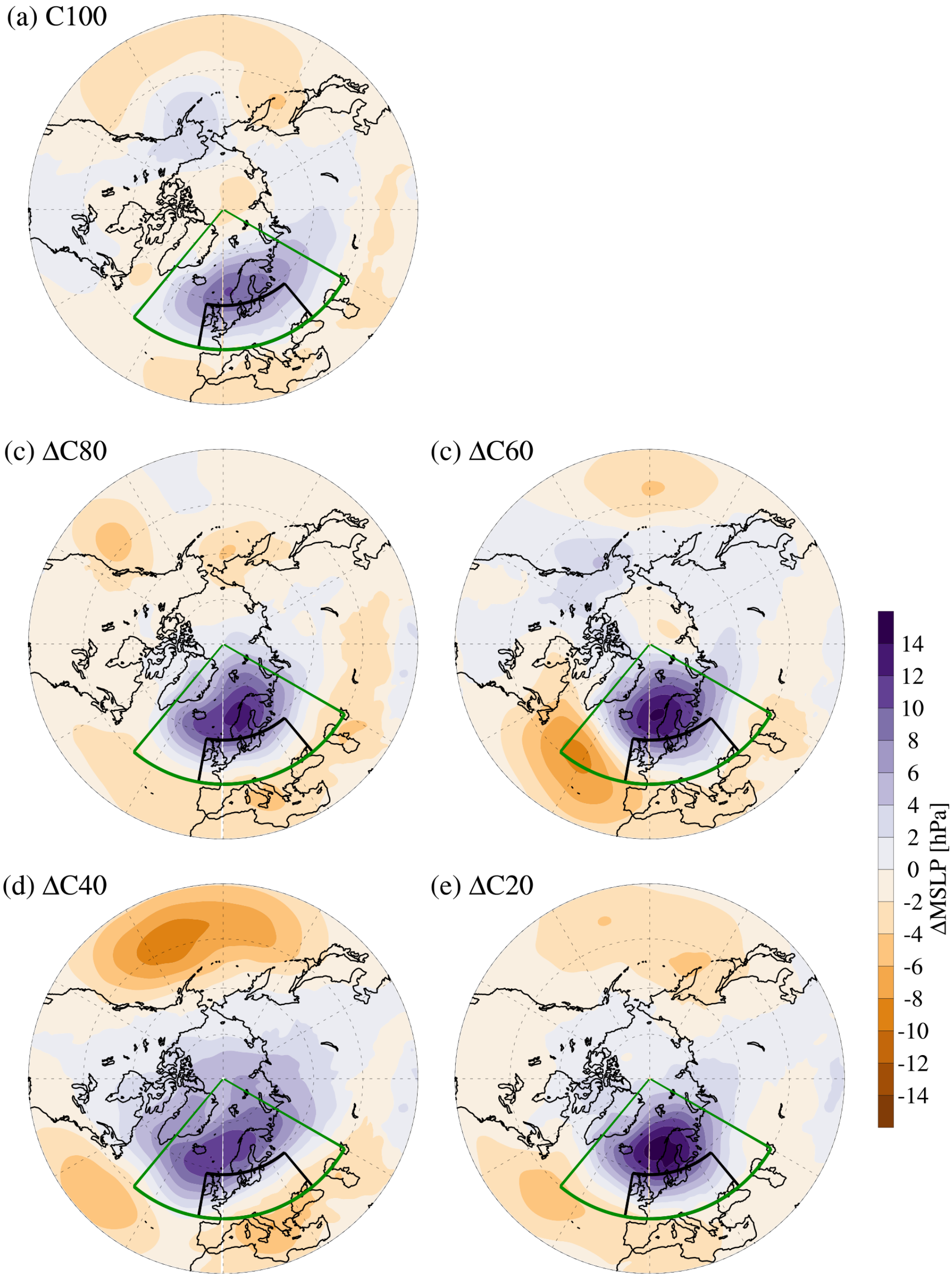

Fig. 10: Mid winter (JF) composite of mean sea level pressure (in hPa) difference wrt the climatology of C100 for the 5% coldest winters in CEU (black box) for a) C100, (b) C80, (c) C60, (d) C40 and (e) C20. Green box indicate the region used to compute P in figure 11 [40°W-60°E, 45°N-90°N]. Black box indicate CEU.

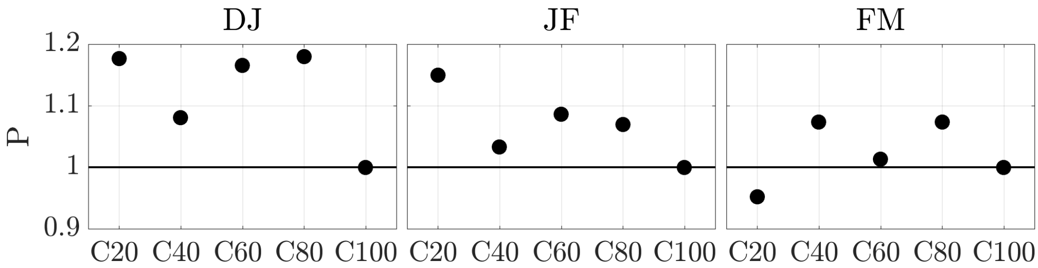

Fig. 11: P of the sea ice reduced MSLP patterns relative to the C100 MSLP pattern in fig. 10(a). P is unitless. The method for computing P is shown in eq. 2. P=1 indicate that the Scandinavian pattern in C20 to C80 is equal to the one in C100. P>1 indicate a stronger Scandinavian pattern relative to C100, and P<1 indicate a weaker Scandinavian pattern.

4 Discussion and conclusion

The link between sea ice reduction in BAKA and cold European winter months have been investigated by step wise reducing sea ice in BAKA in an A-O coupled, global climate model at enhanced resolution. Our setup is based on Petoukhov and Semenov (2010), but differs as they use an AGCM. For the mean temperature responses we find a statistically significant, non-linear response to linear BAKA sea ice reductions, with limited areas of negative temperature anomalies over eastern Europe for moderate reductions and small warm anomalies for minor reductions (80%) and for major reductions (20-40%) (figure 2). The same non-linear behavior is found when focusing on the coldest winter months in each grid cell, although the regions where this is statistically significant are smaller. Averaging over Central Europe indicate the non-linear behavior, but only C20 and C40 are statistically significantly different from C100, as the areas of significance over CEU are relatively small. This is somewhat similar to what Petoukhov and Semenov (2010) found: a shift from warm anomalies over Europe for small sea ice reductions to cold anomalies for moderate (40-80%) and warm again for large reductions. However, they also saw a clear shift from cyclonic to anticyclonic circulation and back again with the step wise reduction in sea ice. Our results do not show this clear shift. In contrast, the mean negative MSLP anomalies over BAKA intensify with sea ice reduction. The difference between their results and ours could be model related: firstly, they use an AGCM with fixed SST patterns, whereas we use a coupled model. Secondly, our horizontal and vertical model resolution is higher (a horizontal resolution of 0.7° in and 91 vertical levels in T255 compared to 2.8° in T42 and 19 vertical levels). In our setup, both aspects of the model configuration are consistent with a more adequate representation of physical processes. Although AGCM's have smaller biases relative to observations, due to AGCM's being forced by observed SST's, coupled models capture the atmosphere/ocean feedbacks. These feedbacks have been proved to be important for capturing global wide responses to local changes in the climate system (Deser et al. (2015)). We therefore interpret our results to offer a more realistic sensitivity of real-world response to BAKA sea ice modifications. We shall return to this discrepancy later. Despite the partial agreement with the 100-year averages from Petoukhov and Semenov (2010) on the non-linearity of the overall CEU winter temperature dependence to BAKA sea ice change, our stratification into the coldest winters do not show quite the same statistically convincing shift towards pronounced colder winters. The CEU winters in the perturbed simulations are not statistically significantly colder than C100, and the circulation responses is that of an intensification of the Scandinavian pattern, leading to stronger easterlies. The overall shift towards colder winters when sea ice is moderately reduced, implies that the shift in the mean winter temperature is also related to less warm winters occurring (not shown).

Focusing on the 5% coldest winters for CEU relative to C100, our results imply that to obtain equally cold CEU winters, the strength of the Scandinavian pattern associated with cold winters over CEU must intensify with the sea ice reduction in BAKA. Hence, we neither see the non-linear temperature response nor a negative pressure anomaly, as was seen for the mean responses. This suggests that the mean response to BAKA sea ice reductions differs from the response for the coldest winters.

The link between BAKA sea ice loss and cold Eurasian winters have mostly been investigated using observational data sets or AGCM's, but there are some studies using coupled climate models as well. Currently, there are no consensus among either observational studies, AGCM' studies or AOGCM studies. Most studies using coupled AOGCM's have investigated the link between an Arctic-wide sea ice decline and its effect on climate, not a sea ice decline confined to BAKA, for example by analyzing the CMIP5 ensemble mean or by modifying the sea ice as discussed in section 2.1. To our knowledge, modifying only BAKA sea ice in a coupled climate model have not been done in other studies. As the response to sea ice reduction depends on its spatial location (Pedersen et al. (2016), Screen (2017b)), an Arctic-wide sea ice decline will most likely have a spatially larger response compared to only BAKA sea ice decline. Therefore, comparing our study to those with an Arctic-wide decline, we do not expect equal results.

Screen (2018) compared six coupled GCM's, all simulating the projected 21st century sea ice decline (Blackport and Kushner (2016), Blackport and Kushner (2017), Deser et al. (2015), McCusker et al. (2017), Oudar et al. (2017)). They find that the circulation response is relatively similar between the six models: an intensification of the Aleutian Low, an increase in sea level pressure over Eurasia, weakening of the Icelandic Low and a reduction of the mid-latitude westerlies. Our results for the coldest winters show the intensification of the MSLP over Eurasia (more Presley over Scandinavia), but not the intensification of the Aleutian Low. This discrepancy is most likely related to the difference in area of sea ice reduction. Neither of these six studies found a significant cooling over Eurasia as a response to Arctic sea ice loss and associated circulation changes. Only Blackport and Kushner (2016), who modified the sea ice albedo to nudge sea ice (which is most effective during summer and not winter), found a weak Eurasian cooling associated with the increased high pressure anomaly off the coast of Eurasia. This response they found for some, but not all, of their eight simulations, and the response was strongest for their transient, not their equilibrium, simulations. This imply that the cooling over Eurasia was strongest as the climate was adjusting to the new sea ice albedo. The high pressure anomaly and associated weak Eurasian cooling is similar to our findings, although the high pressure anomaly is not located in exactly the same place.

Another study that simulated the observed Arctic-wide sea ice loss, but focused on the BAKA/Eurasia link was McCusker et al. (2016). In an ensemble of coupled AOGCM simulations, they replicated the observed BAKA sea ice loss, but not the cooling over central Europe. From this they concluded that the cooling over Eurasia is due to an internally driven trend toward anti-cyclonic circulation over BAKA. They found the same result using AGCM simulations. Their study differs from ours in two ways: first, they used the observed sea ice loss across the Arctic which amounts to about 11% in BAKA SIC from 1979-1989 to 2002-2012, whereas in our study larger sea ice reductions are studied. Secondly, they compared BAKA sea ice loss to Eurasia temperature trends, whereas we focused on the mean response and the 5% coldest winters. Sun et al. (2016) did not find that sea ice loss led to colder continents either. They based this on the ensemble mean of both AGCM and AOGCM model simulations. However, taking the ensemble mean will smooth out the extreme events, which might explain the lack of cooling over the continents. In contrast to these two studies, Kug et al. (2015) associated anomalous warming over BAKA with anomalous cooling over East Asia, using observations and the CMIP5 coupled multi-model ensemble. Yang and Christensen (2012) also concluded from the CMIP5 ensemble that abnormally cold European winters will continue to occur as the BAKA sea ice declines in the future. The above imply that there are not consensus among AOGCM's although most of the studies that do find a link between Arctic/BAKA sea ice loss and cold Eurasian winters only find a weak cooling.

The discrepancy between AGCM's are even larger, as was also suggested by Screen (2018). In addition to the AGCM study by Petoukhov and Semenov (2010) discussed above, Honda et al. (2009) found a link between BAKA sea ice reduction and abnormally cold winter over East Asia in AGCM simulations. Mori et al. (2014) concluded from an ensemble of AGCM simulations that the probability of severe winters in central Eurasia have more than doubled due to BAKA sea ice reductions. Nakamura et al. (2015) found that BAKA sea ice loss induced a negative AO/NAO, leading to cold winter events. Not all studies identify cooling over Europe as a response to a negative AO/NAO-type pattern. McKenna et al. (2018) showed that even though sea ice reductions in BAKA led to a negative NAO, this did not lead too cooling over Europe. On the contrary, it led to warming. They explain this as a balance between the direct, local warming over BAKA due to sea ice loss and the indirect cooling induced by a negative AO. They found that the direct warming was larger than the indirect cooling, hence leading to a warming of Europe. This conclusion of the 'missing' cooling response to a negative NAO was also reached by Screen (2017a). They compared negative NAO events for periods of low Arctic sea ice covers and high Arctic sea ice covers. They suggest, similar to McKenna et al. (2018), that the dynamical cooling related to the negative NAO is overcome by the thermodynamic warming.

Finally, observational studies have also divergent results. As discussed in section 1, Outten and Esau (2012), Garcia-Serrano et al. (2015) and Koenigk et al. (2016) all found a link between BAKA sea ice loss and wintertime circulation. Kretschmer et al. (2016) even found that BAKA sea ice reductions was a main driver of the observed wintertime negative AO and associated cooling over Eurasia. Sorokina et al. (2016) did not find a link, stating that the observed Eurasian cooling were caused by atmospheric internal variability, not BAKA sea ice reductions.

The discrepancies between observational studies, AGCM's and AOGCM's might be related to the fact that they are observational studies, AGCM studies and AOGCM studies. Mori et al. (2019) suggests that extremes in model simulations may not be able to reach an extreme level comparable to observations. Comparing AGCM's to reanalysis, Mori et al. (2019) showed that the models systematically underestimated the Eurasian cooling due to a weaker 'warm Arctic-cold Eurasia' (WACE) pattern, relative to observations. They attributed the weaker WACE pattern to a too weak response to BAKA sea ice loss. Corrected for this bias by enhancing the WACE pattern, they conclude that $\sim$44% of the central Eurasian cooling observed from 1995-2014 was caused by BAKA sea ice loss. This might explain why some model studies lack a cooling over Eurasia e.g. McCusker et al. (2016).

The discrepancies between atmosphere-only and coupled atmosphere-ocean model studies might be explained by the tug-of-war between thermodynamic warming and dynamical cooling suggested by Screen et al. (2015b), Deser et al. (2016) and Screen (2017a). Smith et al. (2017) found that the response to sea ice reduction in AGCM's was dominantly a thermodynamic response to local warming, whereas the dominant response in coupled models was the dynamical response related to the AO/NAO. They suggest that the dynamic response does occur in AGCM's, but somewhat delayed compared to within the coupled models. Thus, a potential explanation for the *not* missing cooling in our mean results, could be that the dynamical cooling from the circulation pattern is stronger in the coupled models than in AGCM's. Thus, AOGCM's can overcome a larger thermodynamic warming

caused by sea ice reductions, i.e. it can overcome larger sea ice reductions.
The balance between the thermodynamic warming and the dynamical cooling have been proposed to also be related to the location and magnitude of the sea ice loss. Several studies have shown that the atmospheric response to sea ice loss depends greatly on the location of the sea ice loss. Koenigk et al. (2016) used reanalysis data and satellite sea ice data to show that the temperature over Central and Western Europe was influenced by the sea ice variability in the Greenland Sea, but the sign of the NAO was linked to the Barents Sea sea ice (negative NAO following sea ice loss). Pedersen et al. (2016) used an AGCM to show that the location of the NAO is very sensitive to the geographical location of the sea ice loss. The study by Screen (2017b) investigated this geographical dependence further, by dividing the Arctic into 9 regions. It was shown that some regions induce large-scale dynamical changes while other regions only induce a thermodynamic response from the local sea ice loss. One of the regions in which sea ice loss induced large-scale circulation changes in winter was BAKA . Sea ice loss in this region led to reduced NAO.
Additionally, it was shown that the sum of the response from each region is not the same as pan-Arctic sea ice loss: the former leads to cooling over the mid- and high latitudes, while the latter leads to warming. They propose, the regional sea ice loss works on shorter time-scales and induces dynamical cooling, whereas the pan-Arctic sea ice loss is indicative of the longer time-scale sea ice loss resulting in thermodynamic warming winning over the dynamical cooling. As BAKA has highly variable thin sea ice, it is the region currently experiencing the largest sea ice loss and likely to become ice free in the near future (around year 2050), it goes in the category of short time-scales (Onarheim et al. (2018), Stroeve and Notz (2018)). Hence, the response should be dominated by dynamical cooling.
The Arctic sea ice loss up until now has been most pronounced in BAKA, but is projected to cover more regions in the future. This indicates that the importance of the short time-scale regional sea ice loss (leading to dynamical cooling) will diminish as the longer time-scale pan-Arctic sea ice loss (leading to thermodynamic warming) takes over. Hence, the response to the sea ice loss observed until now will most likely be a transient response and not the same response as will be seen for Arctic sea ice loss in the future, i.e. it is a non-linear response, as suggested by several studies including Screen (2017b) and Peings and Magnusdottir (2014). In our study, the region of the sea ice reductions might be too small for the thermodynamic warming to compensate for the dynamical cooling. Whether this will occur for pan-Arctic sea ice loss in a coupled model is an interesting question, but beyond the scope of this study.
While winter sea ice has been fast declining in the BAKA, the Arctic has been loosing winter sea ice elsewhere. We chose not to simulate an Arctic-wide sea ice loss to investigate if the BAKA sea ice loss alone could induce Eurasian cooling. Including the rest of the Arctic sea ice loss would have disturbed this response by including processes and responses from the other Arctic regions. As discussed above, whether or not Eurasian wintertime cooling occurs seems to be a battle between thermodynamic warming and dynamical cooling. As Screen (2017b) suggests, including the pan-Arctic sea ice loss would most likely have increased the thermodynamic warming, resulting in the warming winning over the cooling. Although this would be have been more realistic, the balance between warming and cooling might not be. As Mori et al. (2019) showed, climate models tend to underestimate the cooling. This implies that climate models might overestimate the impact from the thermodynamic warming, hence they might not able to simulate the balance between the dynamical cooling and thermodynamic warming correctly. Thus, by reducing sea ice across the Arctic, the warming might overwhelm the already too weak cooling. As BAKA have been shown to be the region with the largest influence on Europe, the overwhelming Arctic-wide warming might be counteracted by ignoring the pan-Arctic sea ice loss, as the response from this should only have a minor impact on Europe. Our choice to not simulate the pan-Arctic sea ice loss is most likely the reason we do not observe the intensification of the Aleutian Low observed for the six coupled models in Screen (2018). Due to the limitations of our study by only simulating BAKA sea ice loss, not Arctic sea ice loss, our results can 'only' be used to imply a link between reduced BAKA sea ice and a temporal mean Eurasian cooling.

In addition to the choice of location and extent of sea ice nudging, the method used for nudging sea ice can also affect our results. As described in section 2.2, the sea ice is reduced in each grid cell to a certain percentage of the climatology, i.e. the maximum SIC in C60 is 60%. Another possible method for changing the sea ice cover in a certain region is to change the overall volume of sea ice in each grid cell. This would allow for sea ice to cover a grid cell by 100% which is more physical than the entire region being covered by up to, and not exceeding, for example 60% sea ice. However, this would require removing sea ice in certain regions and not others, i.e. making assumptions about the location of the sea ice reduction. Thus, reducing the sea ice concentration in each grid cell is less realistic, but avoid further assumptions. Such additional sensitivity experiments are however well beyond the scope of the present work.

Acknowledgements The research leading to these results has received funding from the European Research Council under the European Community's Seventh Framework Programme (FP7/2007-2013) / ERC grant agreement 610055 as part of the ice2ice project.

References

Barnston AG, Livezey RE (1987) Classification, seasonality and persistence of low-frequency atmospheric circulation patterns. Monthly Weather Review 115(6):1083–1126, DOI 10.1175/1520-0493(1987)115<1083:CSAPOL>2.0.CO;2, URL https://doi.org/10.1175/1520-0493(1987)115<1083:CSAPOL>2.0.CO;2

Blackport R, Kushner PJ (2016) The transient equilibrium climate response to rapid summertime sea ice loss in ccsm4. Journal of Climate 29:401–417

Blackport R, Kushner PJ (2017) Isolating the atmospheric circulation response to arctic sea ice loss in the coupled climate system. Journal of Climate 30:2163–2185

Cohen J, Furtado JC, Barlow M, Alexeev VA, Cherry JE (2012) Arctic warming, increasing snow cover and widespread boreal winter cooling. Environmental Research Letters 7

Deser C, Tomas RA, Sun L (2015) The role of the ocean-atmosphere coupling in the zonal-mean atmospheric response to arctic sea ice loss. Journal of Climate 28:2168–2186

Deser C, Sun L, Tomas RA, Screen J (2016) Does ocean coupling matter for the northern extratropical response to projected Arctic sea ice loss? Geophysical Research Letters 43

Garcia-Serrano J, Frankignoul C, Gastineau G (2015) On the predictability of the winter euro-atlantic climate: Lagged influence of autumn arctic sea ice. Journal of Climate 28:5195–5216

Hazeleger W, Wang X, Severijns C, Stefanscu S, Bintanja R, Sterl A, Wyser K, Semmler T, Yang S, van den Hurk B, van Noije E van der Linden T, van der Wiel K (2010) Ec-earth: A seamless earth-system prediction approach in action. Bull Am Meteorol Soc 91:1357–1363

Hazeleger W, Severijns C, Semmler T, Stefanscu S, Yang S, Wang X, Wyser K, Dutra E, Baldasano JM, Bintanja R, Bougeault P, Caballero R, Ekman ANL, Christensen JH, van den Hurk B, Jimenez P, Jones C, KÃěllberg P, Koenigk T, McGrath R, Miranda P, van Noije T, Palmer T, Parodi JA, Schmith T, Selten F, Storelvmo T, Sterl A, Tapamo H, Vancoppenolle M, Viterbo P, WillÃl'n U (2012) Ec-earth v2.2: description and validation of a new seamless earth system prediction model. Climate Dynamics 39:2611–2629

Honda M, Inoue J, Yamane S (2009) Influence of low arctic sea-ice minima on anomalously cold eurasian winters. Geophysical Research Letters 36

Koenigk T, Calan M, Nikulin G, Schimanke S (2016) Regional arctic sea ice variations as predictor for winter climate conditions. Climate Dynamics 46:317–337

Kretschmer M, Coumou D, Donges JF, Runge J (2016) Using causal effect networks to analyze different arctic drivers of midlatitude winter circulation. Journal of Climate 29(11):4069–4081, DOI 10.1175/JCLI-D-15-0654.1

Kretschmer M, Cohen J, Matthias V, Runge J, Coumou D (2018) The different stratospheric influence on cold-extremes in eurasia and north america. Climate and Atmospheric Science 1

Kug JS, Jeong JH, Jang YS, Kim BM, Folland CK, Min SK, Son SW (2015) Two distinct influences of arctic warming on cold winters over north america and east asia. Nature Geoscience Letters

Liu J, Curry JA, Wang H, Song M, Horton RM (2012) Impact of declining arctic sea ice on winter snowfall. Proc Natl Acad Sci USA

McCusker KE, Fyfe JC, Sigmond M (2016) Twenty-five winters of unexpected eurasian cooling unlikely due to arctic sea-ice loss. Nature Geoscience 9:838–843

McCusker KE, Kushner PJ, Fyfe JC, Sigmond M, Kharin VV, Bitz CM (2017) Remarkable separability of circulation response to arctic sea ice loss and greenhouse gas forcing. Geophysical Research Letters 44:7955–7964

McKenna CM, Bracegirdle TJ, Shuckburgh EF, Haynes PH, Joshi MM (2018) Arctic sea ice loss in different regions leads to contrasting northern hemisphere impacts. Geophysical Research Letters 45:945–954

Mori M, Watanabe M, Shiogama H, Inoue J, Kimoto M (2014) Robust arctic sea-ice influence on the frequent eurasian cold winters in past decades. Nature Geoscience Letters 7

Mori M, Kosaka Y, Watanabe M, Nakamura H, Kimoto M (2019) A reconciled estimate of the influence of arctic sea-ice loss on recent eurasian cooling. Nature Climate Change 9:123–129

Nakamura T, Yamazaki K, Iwamoto K, Honda M, Miyoshi Y, Ogawa Y, Ukita J (2015) A negative phase shift of the winter ao/nao due to recent arctic sea-ice reduction in late autumn. Journal of Geophysical Research: Atmospheres 120:3209–3227

Ogawa F, Keenlyside N, Gao Y, Koenigk T, Yang S, Suo L, Wang T, Gastineau G, Nakamura T, Cheung HN, Omrani NE, Ukita J, Semenov V (2018) Evaluating impacts of recent arctic sea ice loss on the northern hemisphere winter climate change. Geophysical Research Letters 45(7):3255–3263, DOI 10.1002/2017GL076502

Onarheim IH, Eldevik T, ÃĚrthun M, Ingvaldsen RB, Smedsrud LH (2015) Skillful prediction of barents sea ice cover. Geophysical Research Letters 42

Onarheim IH, Eldevik T, Smedsrud LH (2018) Seasonal and regional manifestation of arctic sea ice loss. Journal of Climate 31

OSISAF (2017) Osi-450: Sea ice concentration data record of the eumetsat ocean and sea ice satellite application facility (osi saf). URL `http://www.osi-saf.org/?q=content/global-sea-ice-concentration-data-record-smmrssmissmis`, accessed: 2019-04-08

Oudar T, Sanchez-Gomez E, Chauvin F, Cattiaux J (2017) Respective roles of the direct ghg radiative forcing and induced arctic sea ice loss on the northern hemisphere atmospheric circulation. Clim Dyn 49:3693–3713

Outten SD, Esau I (2012) A link between arctic sea ice and recent cooling trends over eurasia. Climate Change 110:1069–1075

Pedersen RA, Cvijanovic I, Langen PL, Vinther BM (2016) The impact of regional arctic sea ice loss on atmospheric circulation and nao. Journal of Climate 29:889–902

Peings Y, Magnusdottir G (2014) Response of the wintertime northern hemisphere atmospheric circulation to current and projected arctic sea ice decline: A numerical study with cam5. Journal of Climate 27:244–264

Petoukhov V, Semenov VA (2010) A link between reduced barents-kara sea ice and cold winter extremes over northern continents. Journal of Geophysical Research 115

Petrie RE, Shaffrey LC, Sutton RT (2015) Atmospheric impact of arctic sea ice loss in a coupled ocean-atmosphere simulation. Journal of Climate 28:9606–9622

Ruggieri P, Buizza R, Visconti G (2016) On the link between barents-kara sea ice variability and european blocking. Journal of Geophysical Research: Atmospheres 121:5664–5679

Screen JA (2017a) The missing northern european winter cooling response to arctic sea ice loss. Nature Communications

Screen JA (2017b) Simulated atmospheric response to regional and pan-arctic sea ice loss. Journal of Climate

Screen JA (2018) Consistency and discrepancy in the atmospheric response to arctic sea-ice loss across climate models. Nature Geoscience

Screen JA, Deser C, Sun L (2015a) Projected changes in regional climate extremes arising form arctic sea ice loss. Environmental Research Letters 10

Screen JA, Deser C, Sun L (2015b) Reduced risk of North American cold extremes due to continued Arctic sea ice loss. American Meteorological Society

Semmler T, Stulic L, Jung T, Tilinina N, Campos C, Gulev S, Koracin D (2016) Seasonal atmospheric responses to reduced arctic sea ice in an ensemble of coupled model simulations. Journal of Climate 29:5893–5913

Smith DM, Dunstone NJ, Scaife AA, Fiedler EK, Copsey D, Hardman SC (2017) Atmospheric response to arctic and antarctic sea ice: The importance of ocean-atmosphere coupling and background state. Journal of Climate 30:4547–4565

Sorokina S, Li C, Weitstein JJ, KvamstÃÿ NG (2016) Observed atmospheric coupling between barents sea ice and the warm-arctic cold-siberia anomaly pattern. Journal of Climate 29:495–511

von Storch H, Zwiers FW (2003) Statistical analysis in climate research. Cambridge University Press

Stroeve J, Notz D (2018) Changing state of arctic sea ice across all seasons. Environmental Research Letters 13

Sun L, Perlwitz J, Hoerling M (2016) What caused the recent warm arctic, cold continents trend pattern in winter temperatures? Geophysical Research Letters 43:5345–5352

Tietsche S, Notz D, Jungclaus JH, Marotzke J (2013) Assimilation of sea-ice concentration in a global climate model - physical and statistical aspects. Ocean Science 9:19–36

Yang S, Christensen JH (2012) Arctic sea ice reduction and european cold winters in cmip5 climate change experiments. Geophysical Research Letters 39

Supplementary figures

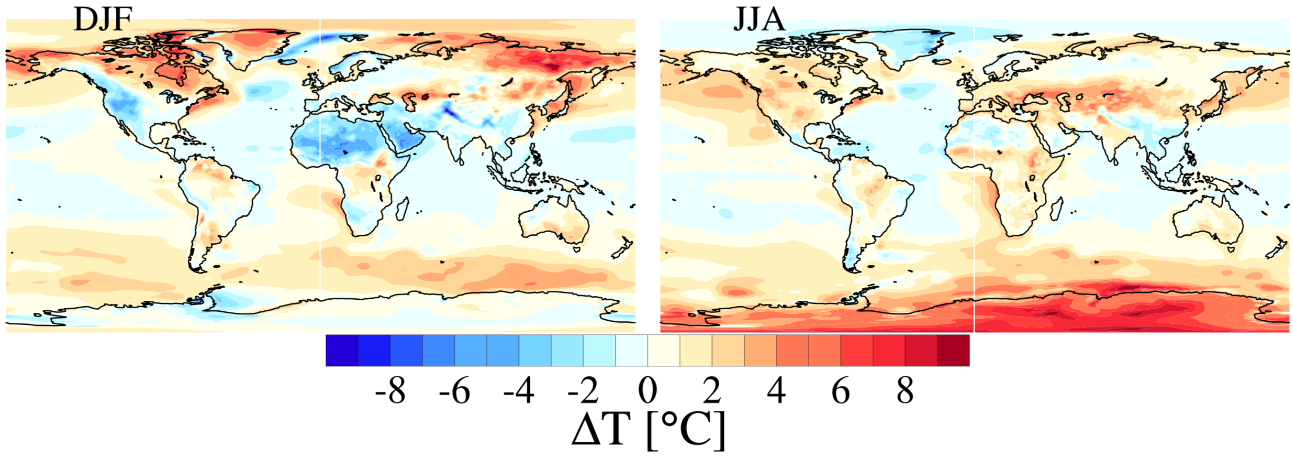

Fig. S1: Mean winter (left) and summer (right) surface (2m) air temperature (in °C) difference between EC-Earth V3.2 and ERA-Interim data for the period 1979-2009.

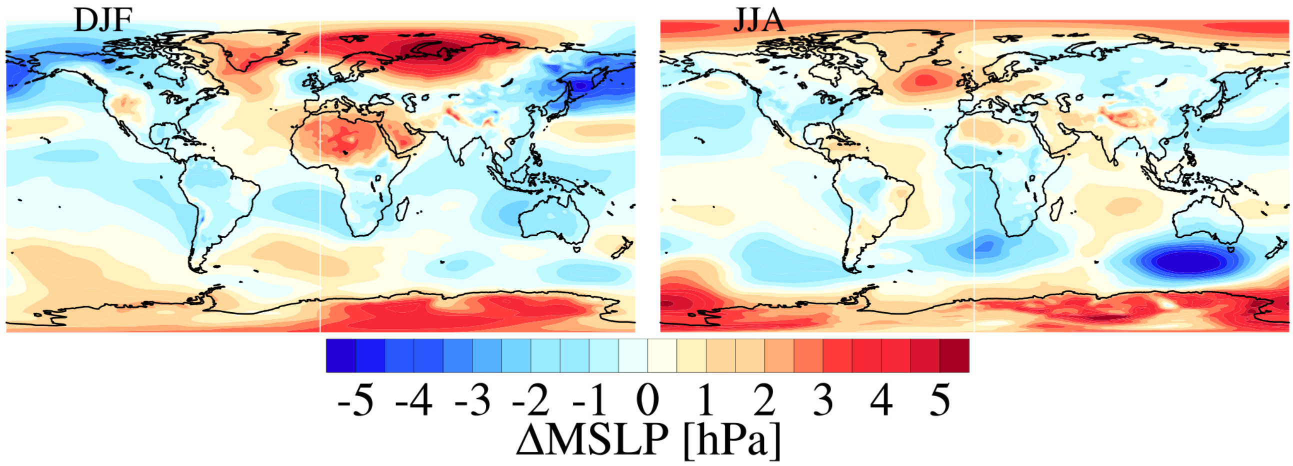

Fig. S2: Winter (left) and summer (right) mean sea level pressure (in hPa) difference between EC-Earth V3.2 and ERA-Interim data for the period 1979-2009.

Appendix C

Manuscript III

Climate change associated with sea ice loss in extended EC-Earth-PISM RCP8.5 simulation

Ida M. Ringgaard, Shuting Yang, Eigil Kaas and Jens H. Christensen

May 15, 2019

Abstract

The ongoing decline of the Arctic sea ice is projected to continue in the future. Potential implications on climate due to the transition from a perennial Arctic sea ice cover, to as seasonal ice cover and finally to an ice-free Arctic Ocean was investigated using a 1350 year (years 1850-3200) long RCP8.5 scenario simulation. This simulation was carried out using the model EC-Earth-PISM: the atmosphere-ocean general circulation model EC-Earth coupled to an interactive Greenland Ice Sheet through the ice sheet model PISM. The overall evolution of the RCP8.5 simulation follows that of the CMIP5 ensemble: a decreasing Arctic Amplification, intensified precipitation patterns and an equatorward shift of the ITCZ, a weakening of the AMOC and a strengthening of the Arctic Ocean stratification. The results indicate a potential shift in trends around the time the Arctic becomes seasonally ice-free and subsequently completely ice-free. However, this coincides with the stabilization of the radiative forcing. Further analysis is required to separate the effects, as well as investigating the potential impact of different sea ice states on climate.

1 Introduction

In the recent past, the climate has changed due to increased anthropogenic emission of greenhouse gases (GHG) (IPCC (2013)). This has manifested itself through increased global air and ocean temperatures, a decline in snow and sea ice, and a rise in global sea level. As the GHG emissions continue to rise, these trends are expected to continue as well. The Arctic sea ice has declined since the start of the satellite records, however the decline is not equally distributed over either time or space. The September sea ice extent have declined by 14% since 1979, but the second half of the period declined 3.5 times faster than the first part (Stroeve and Notz (2018)). The March sea ice loss increased from -2.4% per decade over the period 1979-1999 to -3.4 % per decade from 2000-2018 (Stroeve and Notz (2018)). The sea ice loss manifests it self during winter in the seasonally ice-covered regions, whereas the summer sea ice loss occurs in the perennial sea ice regions (Onarheim et al. (2018)). The Kara Sea is most likely the first part of the Arctic Ocean to become ice free in September and the Arctic as a whole is projected to become seasonally ice-free by the middle of this century (following the RCP8.5 emission scenario; Koenigk et al. (2013)). As the projected global temperature to continues to rise, the Arctic Ocean will most likely become ice-free year round at some point after year 2100. Hence, the climate system will transition from a perennially ice-covered Arctic Ocean over a seasonally ice-free state to a perennially ice-free Arctic Ocean. This might leads to large changes in the climate system. A reduced Arctic sea ice cover will have many different impacts on the climate system. The ice-free Arctic Ocean can absorb more of the incoming solar radiation, leading to a warmer Arctic Ocean. With the sea ice gone, the wind can reach the ocean surface, leading to stronger mixing. Additionally, Brodeau and Koenigk (2015) found that the deep water formation follows the sea ice edge. As this retreats northward, so does the areas of deep water formation, shoaling the mixed layer depth and thus weakening the deep water formation. Above the ocean, will the Arctic Amplification most likely change as well, as its main driver have been shown to be sea ice reductions (Serreze et al. (2009), Screen and Simmonds (2010), Pithan and Mauritsen (2014)). Hence, sea ice has the potential to impact the climate dramatically.

Large temperature and sea ice changes are not unprecedented in the Earths history. Using proxy records from Greenlandic ice cores, several abrupt warming events during the last glacial have been discovered (Dansgaard et al. (1993)). During these events, the temperature over Greenland increased by up to 15°C over decades to centuries (Huber et al. (2006), Kindler et al. (2014)), transitioning from a cold stadial into a warm interstadial. The abrupt warming was followed by a gradual cooling back to the cold stadial. These events are known as Dansgaard-Oeschger (D-O) events. The driver of these D-O events has been difficult to pinpoint due to the limited temporal resolution and spatial coverage of the paleo records. Dokken et al. (2013) hypothesized that a potential driver of the D-O events could be sea ice changes. Comparing the air temperature proxy δ^{18}O over Greenland from the NGRIP ice core during the Marine Isotope Stage 3 (MIS3) with several proxies from a marine sediment core in the Nordic Seas, they found that during the cold stadials, the Nordic Seas were ice-covered, but during the warmer interstadials the Nordic Seas were mostly ice-free. They proposed, that inflowing warm Atlantic Water gradually built up in the Nordic Seas during the cold stadials, weakening the

ocean stratification. At a certain point, the stratification broke down, allowing for warm subsurface water to mix with surface water, leading to a rapid melting of sea ice. The now ice-free ocean released vast amounts of heat to the atmosphere, thus leading to the abrupt temperature increases observed in Greenland. This hypothesis was supported by Sadatzki et al. (2019). Using the same two cores with a different proxy for sea ice they could constrain the timing of the abrupt warming over Greenland relative to changes in sea ice and the oceanic circulation. They conclude that the sea ice variability occurs first, due to increased warm subsurface waters. This is followed by an overturning pulse mixing the entire water column in the Norwegian Sea and reinvigorating the deep-water formation. This releases vast amounts of heat to the atmosphere, subsequently leading to abrupt warming over Greenland.
Proxy records reveal the mixed end-result of all processes that have occurred at a specific time. The records show the relative timing of processes, if they are constrained well enough and the temporal resolution is high enough, but they cannot show a causal relationship. For example, they cannot tell if sea ice reductions are able to cause a temperature change large enough as observed over Greenland, only that a sea ice retreat occurred prior to a temperature increase. To test this, climate models can be used. Guo et al. (2019, manuscript in preparation) simulated the MIS3 period using the coupled general circulation model NorESM. By adding fresh water to the simulation (a hosing experiment), they simulated a sea ice cover down to Bay of Biscay. This represented the cold stadial period. Stopping the input of extra fresh water, the sea ice cover rapidly retreated to a state similar to the present day winter sea ice cover, with an ice-free Nordic Seas, equivalent to the warm interstadial of the D-O events. This rapid sea ice retreat led to increased temperatures over Greenland of approximately 10°C, similar in magnitude to the observed temperature changes in the NGRIP ice core (Huber et al. (2006), Kindler et al. (2014)).

The above imply that large and rapid changes in sea ice cover had large impacts in the past. If a retreat of the Arctic sea ice cover can induce such abrupt and large changes as D-O events, what might occur when the Arctic sea ice completely disappears? And what happens when the Greenland Ice Sheet (GIS) starts to melt? This study aims at investigating these questions by analyzing a RCP8.5 scenario simulation, focusing on the periods just after the Arctic summer sea ice disappears, when the Arctic winter sea ice disappears and when the GIS is disappearing.

2 Experiment and Method

2.1 Experiment

In this study, the model EC-Earth-PISM is used (Svendsen et al. (2015), Madsen et al. (2019, manuscript in preparation)). EC-Earth-PISM combines the global coupled atmosphere-ocean general circulation model EC-Earth V2.3 (Hazeleger et al. (2012)) with the Ice Sheet Model PISM (Albrecht et al. (2012)).

EC-Earth V2.3 consists of the atmospheric component IFS (ECMWF's Integrated Forecast System; ECMWF (2010)) and the ocean component NEMO2.0 (Nucleus for European Modelling of the Ocean; Madec and the NEMO team (2008)) embedded with the sea ice component LIM2 (Louvain-la-Neuve sea Ice Model; Vancoppenolle et al. (2012)). The horizontal resolution for IFS cycle 31r1 is approximately 80 km (T159L62). NEMO and LIM2 uses the ORCA1 grid (horizontal resolution of $1°\text{x}1°$) and NEMO has 42 vertical layers. This is the version of EC-Earth used for the Coupled Model Intercomparison Project Phase 5 (CMIP5; Taylor et al. (2012)).

EC-Earth-PISM has an interactive Greenland Ice Sheet (GIS) through coupling to the ice sheet model PISM. The GIS has a horizontal resolution of 20 km. This coupling allows for GIS to interact with the atmosphere and the ocean, as well as changing the topography (ice area and volume) of GIS. This allow for GIS to shrink.

EC-Earth-PISM is run using the CMIP5 protocol: starting from a pre-industrial control state, a historical simulation is run until year 2005, followed by the Radiative Concentration Pathway 8.5 (RCP8.5) emission scenario and the Extended Concentration Pathway (ECP8.5; Taylor et al. (2012), Meinshausen et al. (2011)). The whole experiment is simulated for 1350 years, from 1850 to 3200. The radiative forcing for RCP8.5 is shown in figure 1a. RCP8.5 is the high-end emission scenario where the radiative forcing is projected to reach 8.5 Wm^{-2} by 2100, continuing up to 12 Wm^{-2} by year 2250, after which it stabilizes.

2.2 Sea ice states

This study focuses on the climatic impact of five different Arctic sea ice states. As can be seen in figure 1b, the Northern Hemisphere (NH) sea ice area (SIA) is relatively stable from 1850 to the 1970's. After this, SIA starts to decline more rapidly. EC-Earth-PISM predicts a seasonally ice-free Arctic Ocean by year 2060 and completely ice-free by year 2154. The annual global mean temperature increases rapidly during most of the 1900's, up until the middle of the 23rd century, after which it stabilizes. This stabilization occurs due to the stabilization of the projected GHG emissions (fig. 1a). The GIS volume is stable until around year 2060 after which it declines linearly (fig. 1b). By the end of the simulation in year 3200, the GIS volume has declined by 62% from 3.59 million km^3 to 1.38 million km^3.

Five 30-year time slices representing five different Arctic sea ice states are chosen to be investigated (gray boxes in fig. 1b): the pre-industrial period (years 1850-1879, hereafter referred to as P1),

Table 1: 30-year mean of the global mean (2m) surface air temperature (T; in °C) and its change relative to P1, Arctic sea ice area (SIA; in million km^2) for March (September), and global mean precipitation (P; mm day^{-1}) for each of the five periods.

	Period	**Years**	**T (ΔT)** [°C]	**SIA Mar (Sep)** [million km^2]	**P** [mm day^{-1}]
P1	Pre-industrial	1850 - 1879	12.7 (0)	7.84 (15.4)	2.84
P2	Present day	1976 - 2005	13.4 (0.61)	6.38 (14.5)	2.85
P3	Loss of Arctic summer sea ice	2060 - 2089	16.2 (3.56)	0.164 (10.4)	3.00
P4	Loss of Arctic winter sea ice	2154 - 2183	20.5 (7.82)	0 (0.418)	3.24
P5	Loss of Greenland Ice Sheet	3170 - 3199	25.4 (12.7)	0 (0)	3.60

present day (years 1976-2005, P2), just after the loss of Arctic summer sea ice (years 2060-2089, P3), just after the loss of Arctic winter sea ice (years 2154-2183, P4) and the end of the simulation where the GIS have declined by 62% (years 3170-3199, P5), see Table 1. P3 and P4 are chosen as the first consecutive 30-year period where the Arctic summer and winter SIA is below one million km^2, respectively. The monthly mean March and September sea ice concentration for the five regimes are shown in figure 2.

2.3 Methods

The results from each of the five preiods have been detrended relative to their respective 30-year period due to the rapid increase in global mean temperature for some of the periods (see fig. 1b). Results are shown as the changes relative to the pre-industrial period P1 (e.g. ΔP2 = P2-P1), unless otherwise stated. Additionally, they are shown for the four boreal seasons (winter = DJF, spring = MAM, summer = JJA and autumn = SON).
The 30-year seasonal mean change for temperature and precipitation have been pattern scaled by dividing each parameter in each grid cell by the annual global mean surface air temperature anomaly, i.e. ΔT for the specific time slice (Santer et al. (1990), Mitchell (2003)). The units are then (°C)/(°C) for temperature and (mm/day)/(°C) for precipitation changes. This is done so as to be able to exclude the almost linear change due to the global warming. For temperature, a value smaller than 1 indicates that the temperature change is smaller than that of the global mean average change. Similarly, a value larger than 1 indicates a temperature change larger than the global mean average change. For precipitation, positive values indicate an increase in precipitation per degree global warming, and negative values indicate a decrease in precipitation per degree global warming.

The temporal variability is represented by the change in standard deviation (SD) relative to P1, i.e. $\Delta P_2 = SD_{P2}$-SD_{P1}. The standard deviation is computed for monthly means in each season for each 30-year period, hence over 90 months for each season.

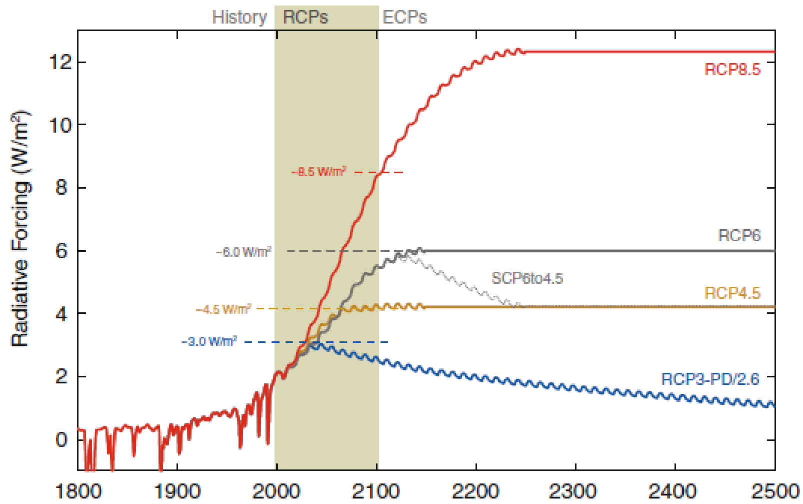

(a)

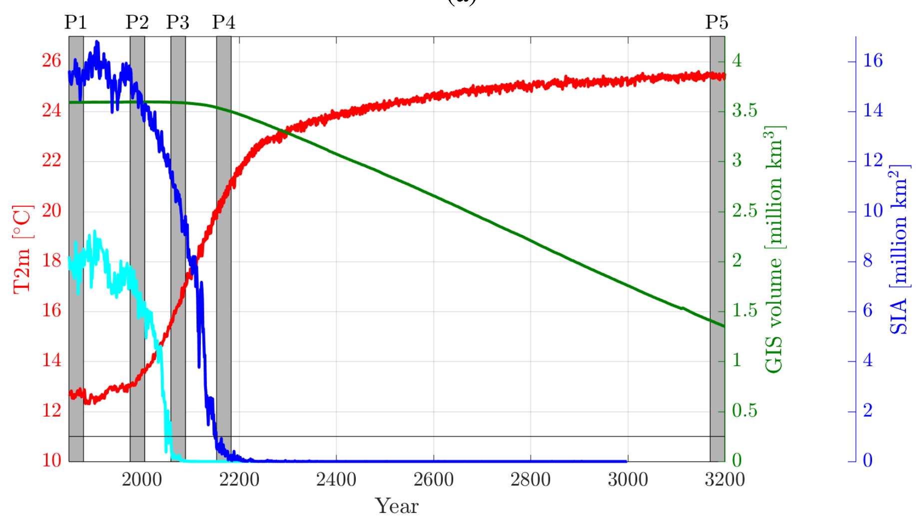

(b)

Figure 1: (a) Radiative forcing for CMIP5. Figure from Meinshausen et al. (2011). (b) Annual global mean surface (2m) air temperature (red; in °C), annual Greenland Ice Sheet Volume (green; in million km^3) and mean NH SIA (in million km^2) for March (dark blue) and September (light blue) in the EC-Earth-PISM RCP8.5 simulation. Horizontal line indicate SIA equal to one million km^2. The 5 grey boxes indicate the 5 periods defined in table 1. The temperature for year 2571 has been removed, as there was a spurious spike in temperature for this year. The spike occurred due to an error in the forcing setup.

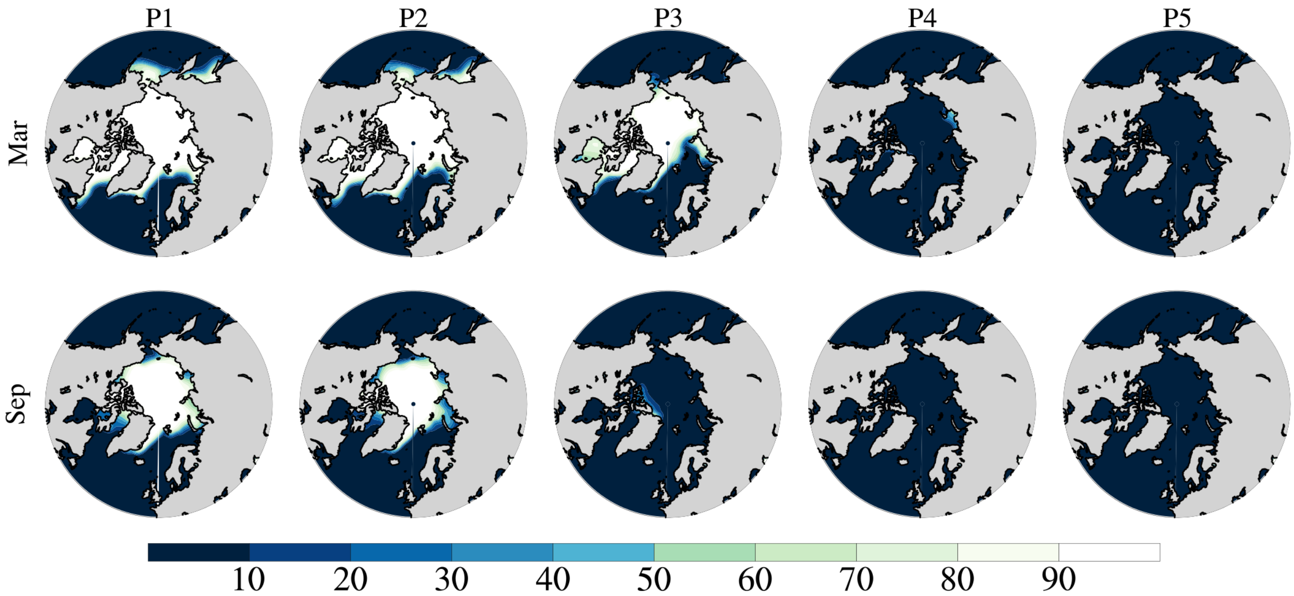

Figure 2: 30-year mean sea ice concentration (in %) for March and September for each of the five periods.

3 Results

3.1 The atmosphere

3.1.1 Changes in surface climate

The 30-year detrended seasonal mean pattern scaled surface air temperature change is shown in figure 3. As the temperature has been pattern scaled, the overall global warming is suppressed in these plots. The most pronounced feature is the large warming of the Arctic relative to the global warming, i.e. Arctic Amplification (AA). Note that the amplified warming is only seen over the Arctic, not the Antarctic. Looking at the pattern scaled temperature, the largest change is seen in winter and autumn, peaking in P3 with up to 6°C/°C warming. Summer experiences the weakest temperature change and no AA, i.e. the temperature change in the Arctic is similar in magnitude to the global mean temperature change. The strength of the warming in winter and autumn is not constant through the five regimes, peaking in P3 just after the Arctic becomes seasonally ice-free. After P3, the annual global mean temperature seems to 'catch up' with the Arctic temperatures. For P4, just after the Arctic becomes ice-free year round, the Arctic winter temperature is approximately 4°C/°C, and at the end of the simulation when GIS is shrinking, it is approximately 3°C/°C. Another feature to note is that the warming is stronger over land relative to the ocean.
The AA can be visualized more clearly computing the ratio between the mean temperature trend of the Arctic (60-90°N) relative to the global mean temperature. This is shown in figure 4 for periods P2-P5, using P1 as the reference period. From this it does not appear that AA peaks at P3, but rather that it decreases with the decreasing Arctic sea ice cover, going from 4.4 in December in P2 to 2.3 in P5. The temperature change over land areas north of 60°N (e.g. Siberia) is larger in P2 than in P3, hence the discrepancy in AA between figures 3 and 4.

The detrended mean pattern scaled total precipitation change show an increase in precipitation for areas with high precipitation in P1 and a decrease for areas with low precipitation in P1 (figure 5). That is, wet areas get wetter and dry areas get drier. An increase in precipitation is to be expected as a warmer atmosphere can contain more water vapor than cold air. Please note that the largest anomalies appear to occur for present day (ΔP2). This is related to the pattern scaling, as the precipitation is scaled by the global mean temperature anomaly relative to P1, and for P2 that is <1°C (see table 1). An interesting feature is that Europe is projected to get drier in summer and the Amazones drier in autumn (the end of the dry season June-November).
The green band around Equator in figure 5 indicates that the Intertropical Convergence Zone (ITCZ) sharpens around Equator as the world warms. The same feature (an intensification in precipitation near Equator and a decline in precipitation on the poleward sides) is seen for the zonal area-integrated detrended precipitation in figure 6a, indicating an equatorward shift of the ITCZ. This potential shift is investigated further by locating the latitude of the maximum area-integrated precipitation between 20°S and 20°N (ϕ_{max}), as well as the the latitude of the precipitation centroid (ϕ_{cent}), i.e. the latitude where equal amounts of precipitation falls to the north and the south (Frierson and Hwang (2012),

Adam et al. (2016)), see figure 6a. Going from P1 to P5, the location of ϕ_{max} and ϕ_{cent} converges toward Equator and each other. Plotting ϕ_{max} and ϕ_{cent} for each time regime highlights this (fig. 6b). Going from P1 to P5, ϕ_{max} moves toward Equator in winter and spring (6b top row). The ϕ_{cent} is also moving toward Equator in winter, but in spring it is moving away from Equator and toward ϕ_{max} instead. In summer, ϕ_{max} is stationary at 8.5°N until all the Arctic sea ice has melted, after which it starts to move toward Equator (6b bottom left). The same is partly seen for the ϕ_{cent}, after an initial northward shift for P2 and P3. In autumn, the ϕ_{max} is quite stable, only starting to move equatorward for P5, whereas the ϕ_{cent} moves northward going from P1 to P5.

The variability of temperature and precipitation is illustrated by the change in standard deviation (SD) for each 30-year period using monthly means, relative to P1 (see section 2.3). For temperature, a pattern of decreased SD at the poles and increased SD in the mid-latitude and tropical continents emerges as the global mean temperature rises (fig. 7). The green areas over the continents imply larger variability in temperatures over land than over the ocean. The decrease in SD is mostly related to the disappearance of the sea ice, reflected by the large decrease in SD in autumn, winter and spring over areas formerly covered by sea ice. The green areas indicating increase in SD over the Arctic Ocean in P2 and P3 reflect the large temperature differences caused by even a small sea ice cover. The decrease in SD over high latitudes migrates down over land regions previously affected by sea ice changes (Eurasia and North America in winter). Summer is dominated by an increase in SD, except for Antarctica and eventually Greenland.

The SD of the precipitation is similar to the mean precipitation change: areas with much precipitation have larger SD as well (compare fig. 8 to fig. 5). Areas with little precipitation have a smaller SD.

3.1.2 Change in extremes

Changes in the SD reveal changes in the variability, but not changes in the extremes. Potential changes in extremes are investigated by analyzing the 5th and 95 percentiles of the detrended monthly mean temperatures and precipitation for each season and for four areas: Greenland, Europe, Southeast Asia and South America (areas shown in figure 9a).
As sea ice disappears and the global mean temperature rises, the coldest temperatures over Greenland and Europe become warmer and the warm extremes become colder, i.e. the extremes become less extreme (fig. 9b, black and dark blue lines). This hold throughout the year, except for European summers. Here, the cold extremes become colder and the warm extremes become warmer. For Southeast Asia and South America the trend is the same; extremes become more extreme (fig. 9b, red and green lines).
The precipitation percentiles reveal more extreme precipitation for all four areas for all seasons, both for extreme low and extreme high precipitation (fig. 9c). The largest changes can be seen in Southeast Asia, while the change in Europe is moderate. This indicates large interannual variability in the Asian monsoon. The shift in extremes appears to occur at P3 in summer and at P4 in winter.

3.1.3 Changes in circulation

The change in detrended mean sea level pressure (MSLP) shows two main features (figure 10). The first is a strengthening of the Aleutian Low in winter and spring. This anomaly intensifies from around -2 hPa (P2), over -6 hPa and -10 hPa (P3 and P4), to -17 hPa (P5). The second is a decrease in the MSLP above the Arctic Ocean and an increase of in MSLP north of the Azores High in autumn. This pattern resembles the positive Arctic Oscillation (AO), indicating a shift toward more positive AO. The weaker North-South temperature gradient implied by the weaker AA in figures 3 and 4 suggests changes to the overall atmospheric circulation as well. This can be represented by the stream function ψ reflecting the flow of the air (along the stream lines). ψ is given by equation (1), using the gravitational acceleration g, the zonal mean of the meridional velocity $\bar{v}^{\lambda}$ at the pressure layer p and the latitude ϕ.

$$g\frac{\partial \psi_p}{\partial p} = \bar{v}^{\lambda} 2\pi a \cos\phi \tag{1}$$

The stream functions and the anomalies of P2 to P5 relative to P1 for winter and summer are shown in figure 11. The two Hadley Cells and Ferrel Cells are clearly seen. The strongest Hadley Cell has a rising branch in the tropics in the summer hemisphere and a sinking branch in the subtropics in the winter hemisphere. Several changes occur due to the rising global temperature. First, a weakening of the Hadley Cell. In winter, ψ decreases from approximately 200×10^9kg s^{-1} in P1 to 170×10^9kg s^{-1} in P5. In summer, ψ decreases from around 240×10^9kg s^{-1} in P1 to 200×10^9kg s^{-1} in P5. Second, the rising branch of the Hadley Cell is displaced equatorward and the sinking branch widens toward the poles. This contraction around Equator supports the sharpening of the ITCZ seen in figure 6a. The Ferrel Cell, on the poleward side of the Hadley Cells, appear to shift slightly toward the poles.
The change in MSLP variability is shown in figure 12. As sea ice disappears, the SD increases over the Arctic and decreases over Antarctica. additionally, the SD decreases over Europe in autumn and winter. Generally, the SD increases over northern mid and high latitudes, and decreases SD over the southern mid and high latitudes. This is most clear for P4 and P5.

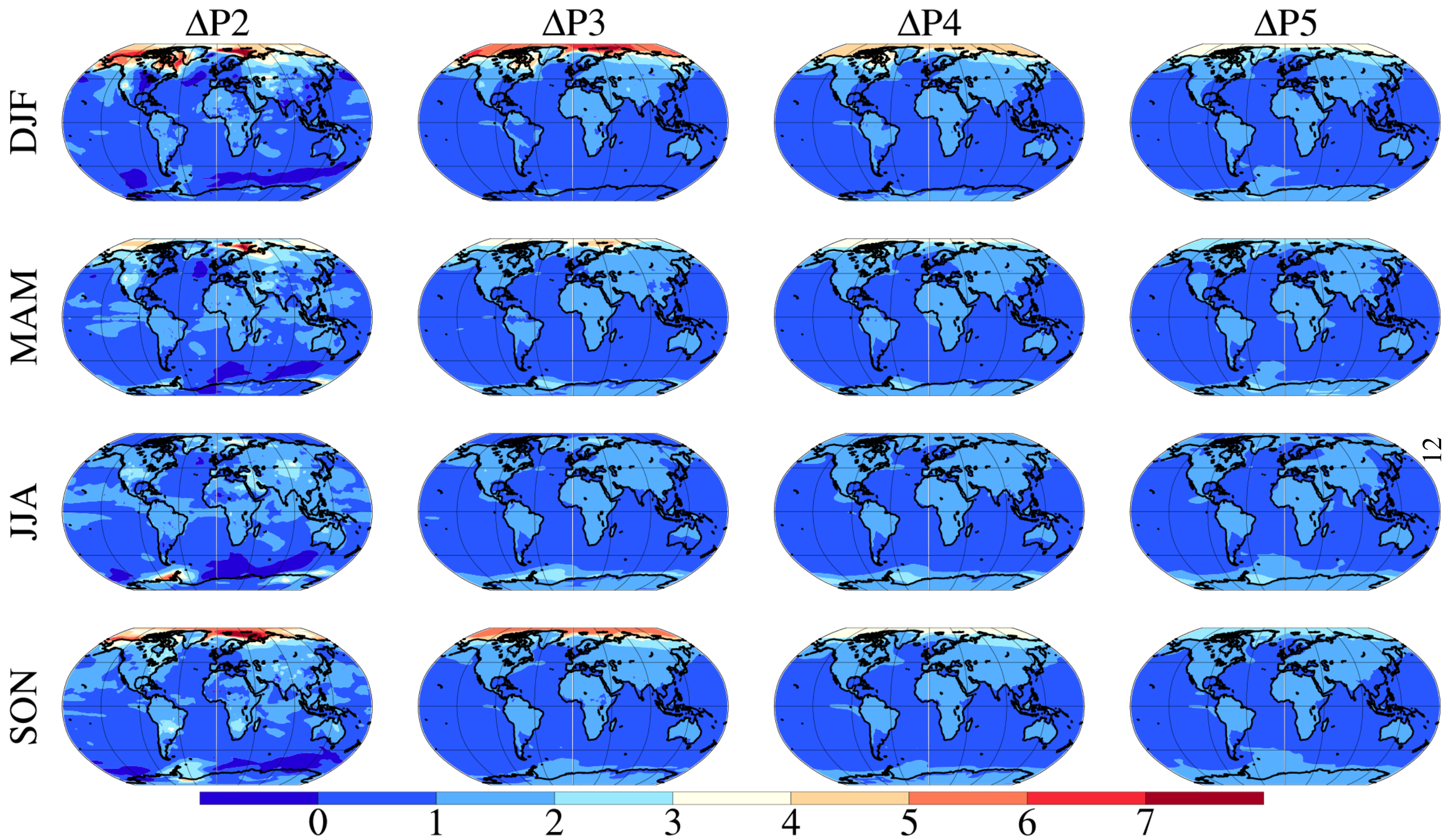

Figure 3: Pattern scaled temperature [°C/°C] for each season (rows) and each time period relative to P1 (columns).

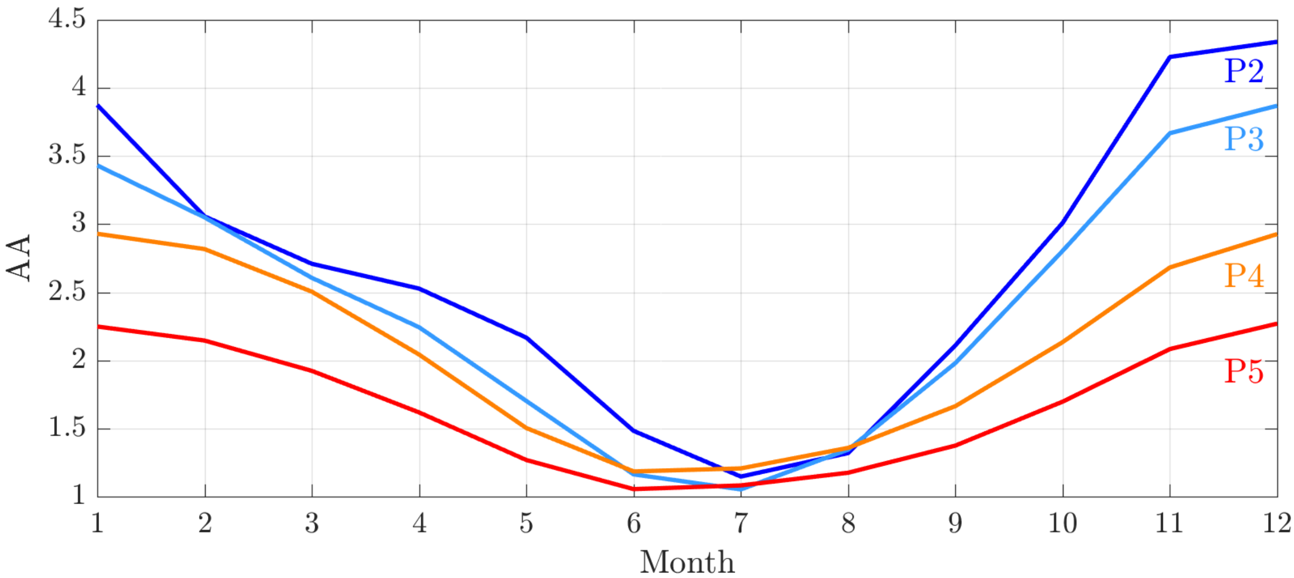

Figure 4: Arctic amplification, relative to P1 (1850-1879) for P2 (dark blue), P3 (light blue), P4 (orange) and P5 (red). AA is computed as: $(\overline{T^{P2}_{Arc}} - \overline{T^{P1}_{Arc}})/(\overline{T^{P2}_{Glo}} - \overline{T^{P1}_{Glo}})$.

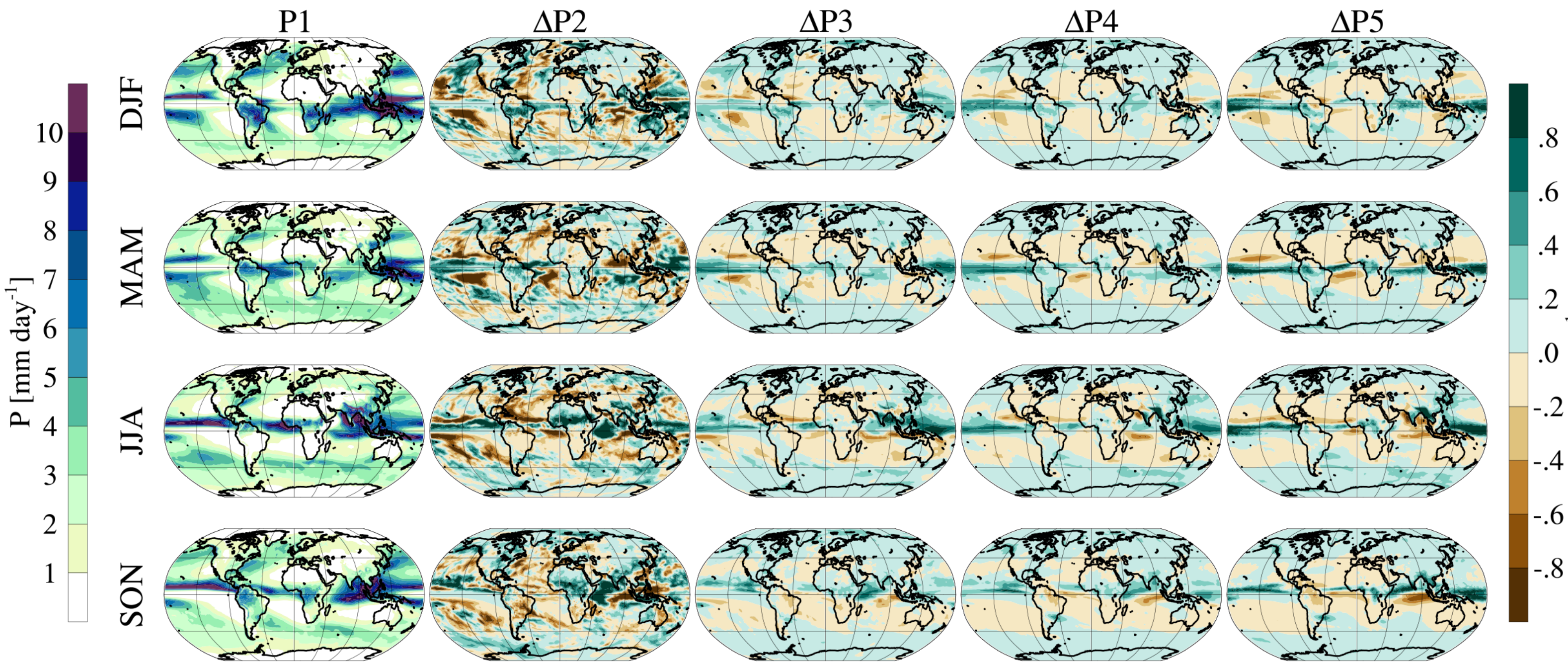

Figure 5: Absolute precipitation for P1 (in mm day^{-1}) (left column) and the pattern scaled precipitation (in (mm day^{-1})/(°C)) for P2 to P5 and for each season (four right columns).

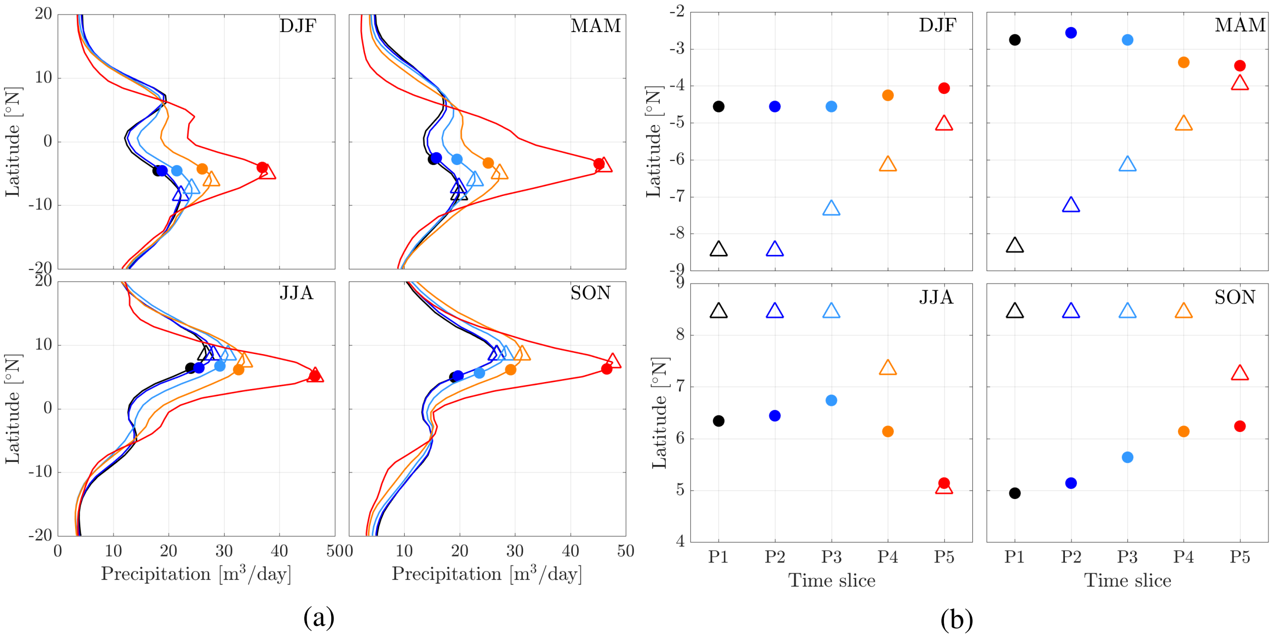

Figure 6: (a) Zonal area-integrated detrended precipitation. Circles show the latitude of the precipitation centroid (ϕ_{cent}, latitude of the median precipitation) and triangles show the latitude of the maximum precipitation (ϕ_{max}). (b) The latitude of the precipitation centroid (ϕ_{cent}, circle) and maximum precipitation (ϕ_{max}, triangles) for each time slice.

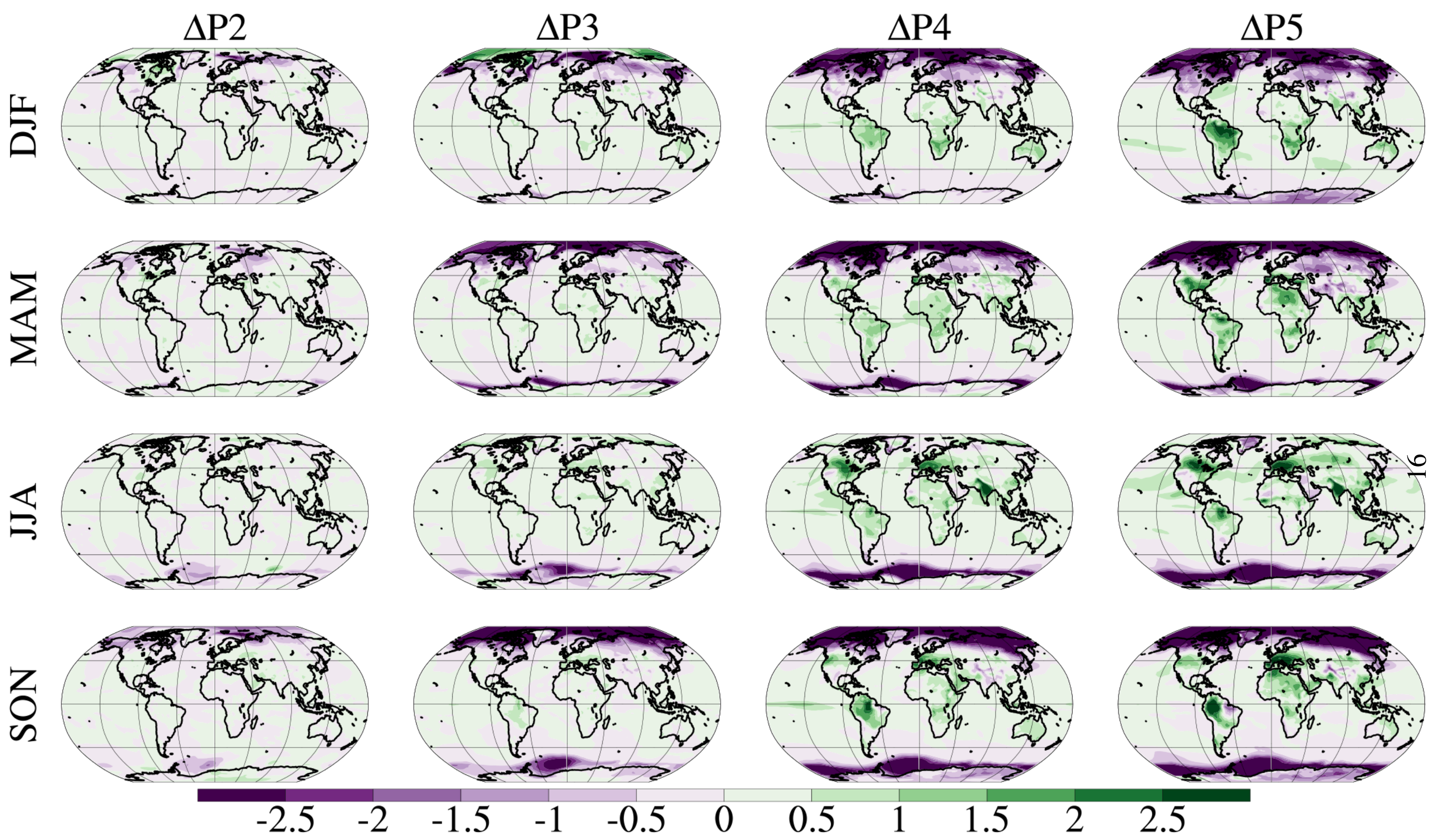

Figure 7: Standard deviation difference of the detrended surface air temperatures (in °C) for P2 to P5, relative to P1, for each season (rows) and each time period relative to P1 (columns).

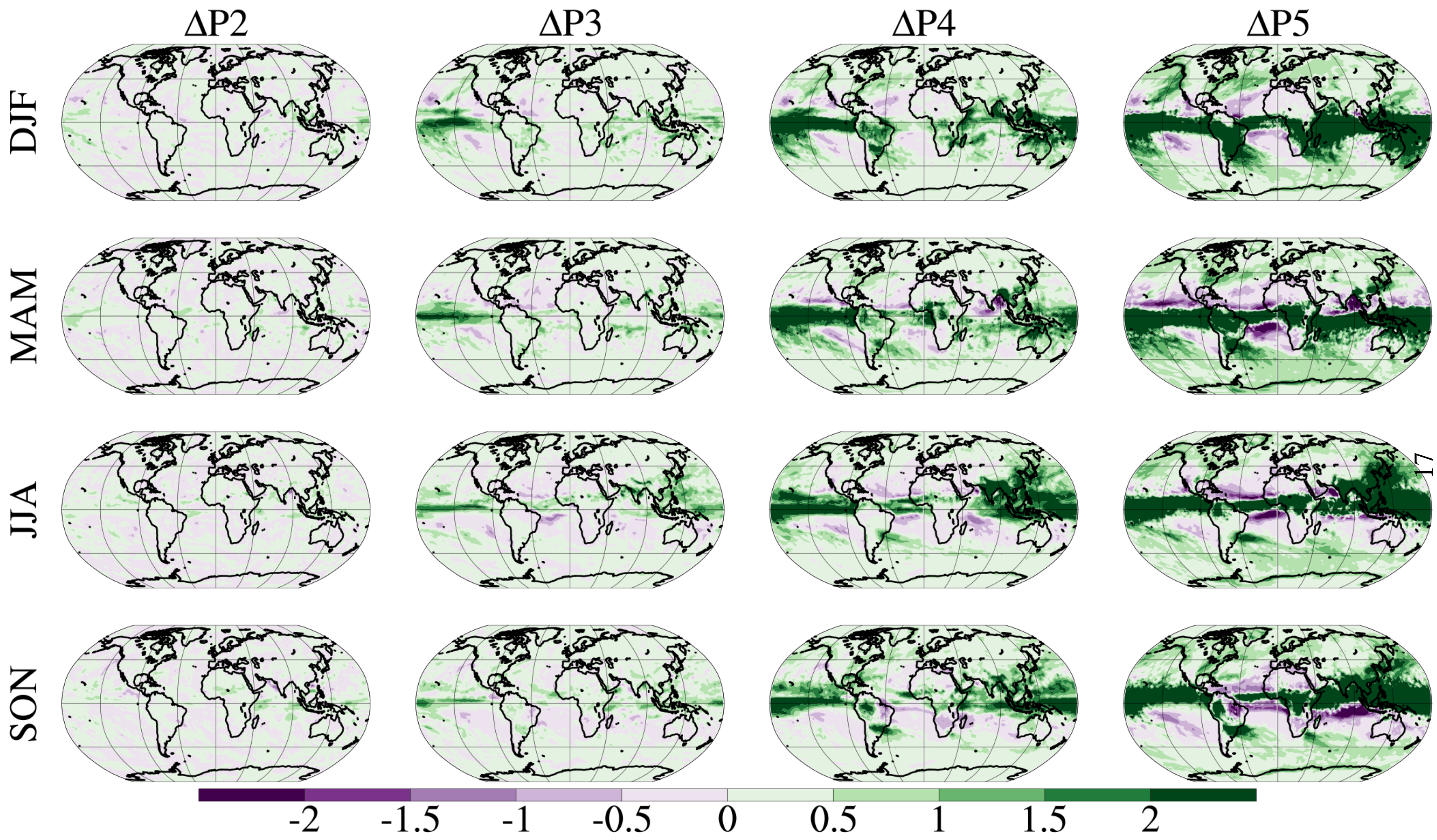

Figure 8: Standard deviation difference of the detrended precipitation (in mm day^{-1}) for P2 to P5, relative to P1, for each season (rows) and each time period relative to P1 (columns).

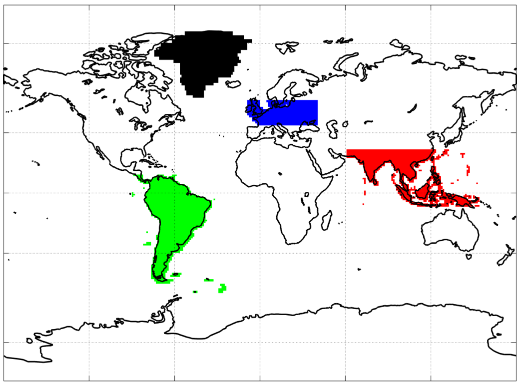

(a)

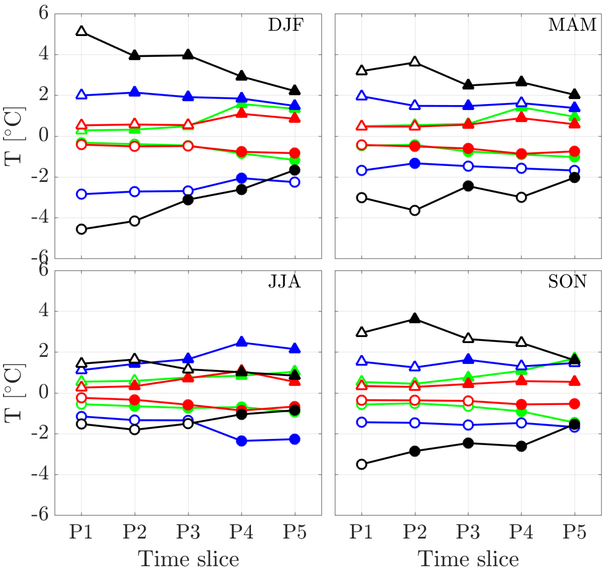

(b)

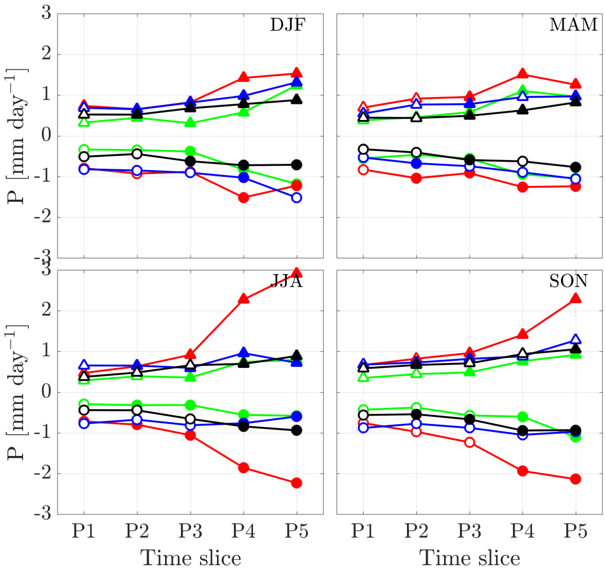

(c)

Figure 9: (a) Map showing the four areas Greenland (black), Europe (blue), Southeast Asia (red) and South America (green) used in (b) and (c). The 5th (circles) and 95th (triangles) percentile of the area mean detrended seasonal temperature (b) and precipitation (c).

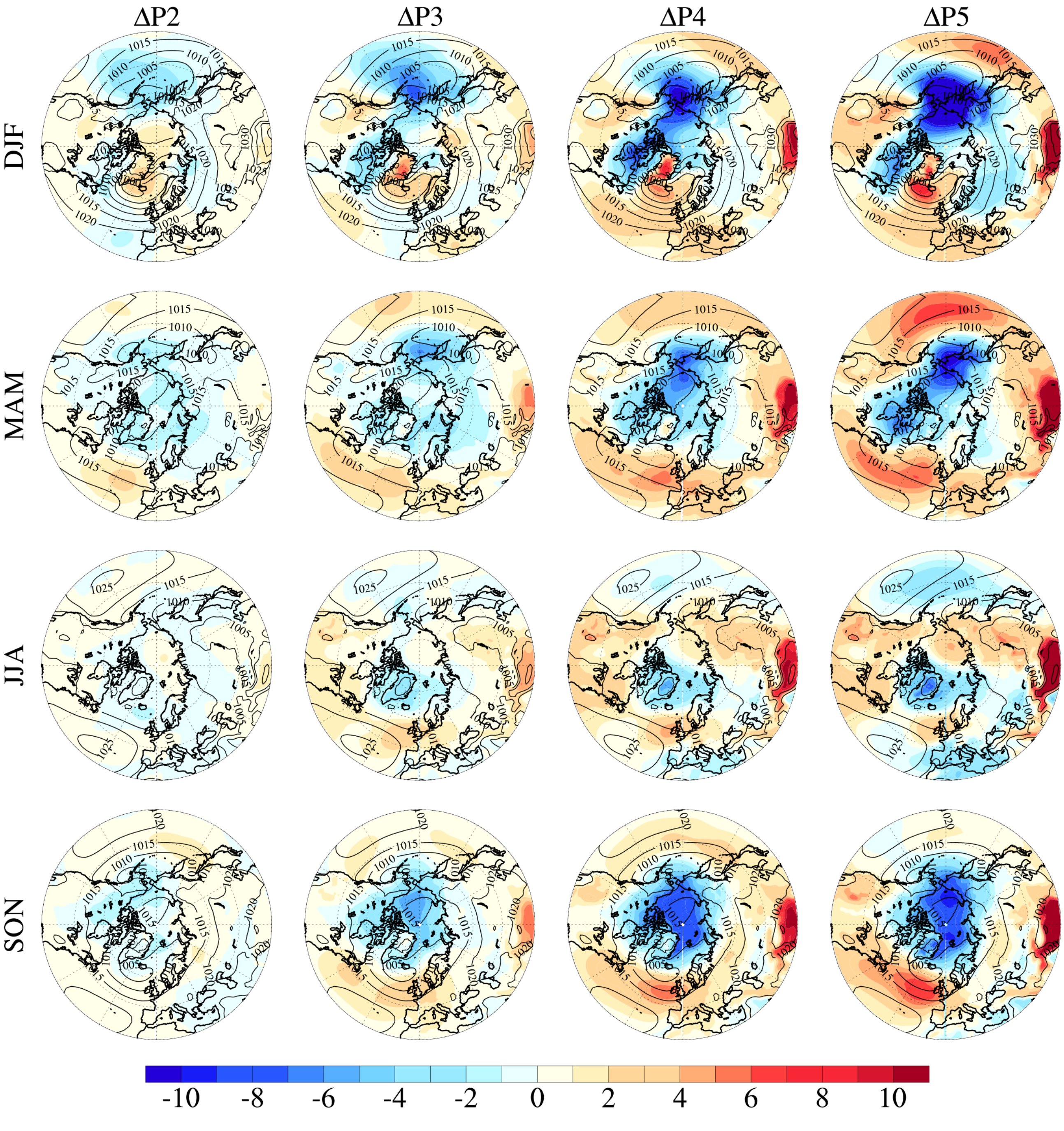

Figure 10: Mean sea level pressure (in hPa) for P1 (contours) and the changes for P2 to P5 relative to P1 (shading) for each season.

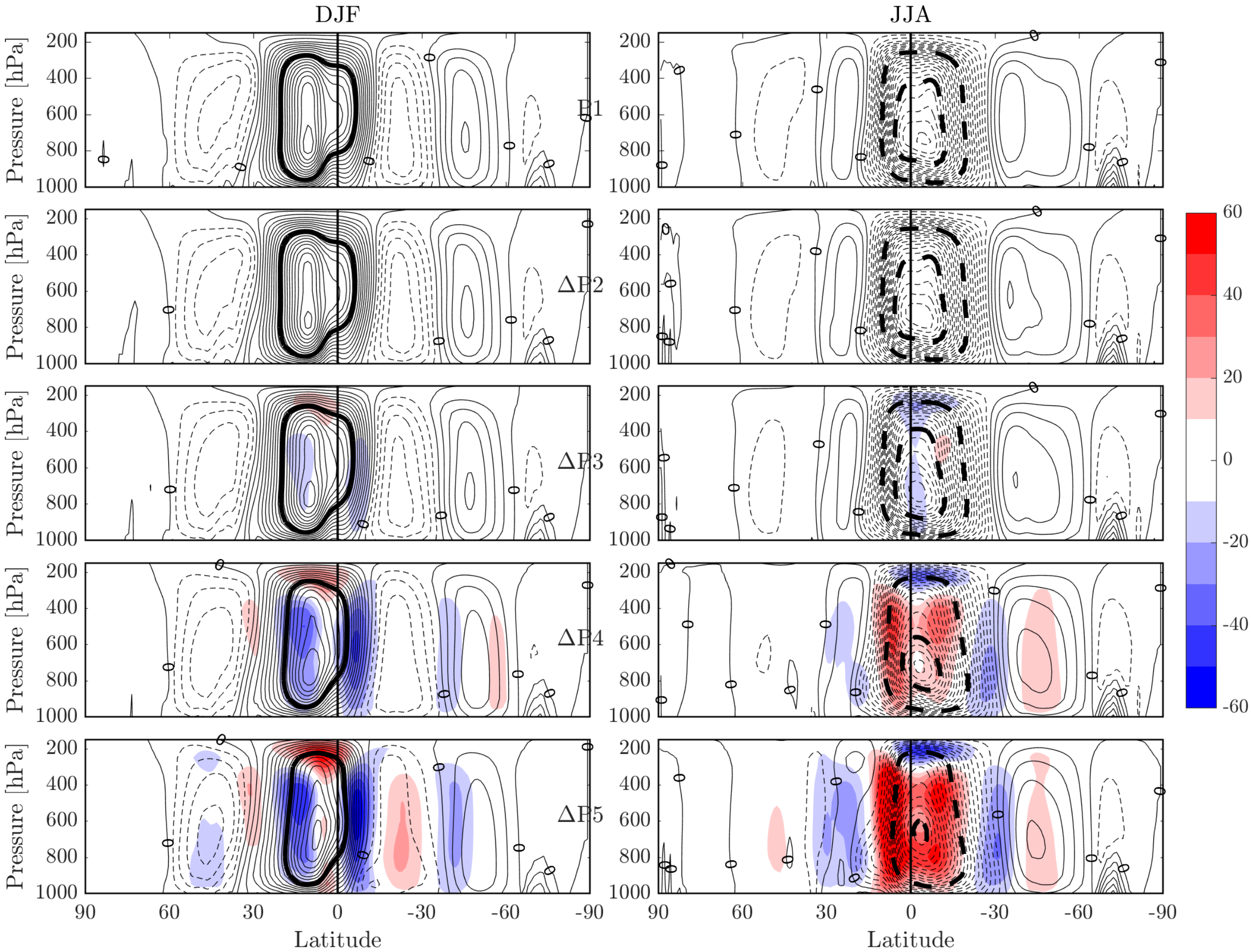

Figure 11: Stream function (in 10^9kg s^{-1}) for P1 (top row) for DJF (left column) and JJA (right column). The four rows below show the stream functions for P2 to P5 (contours) and the difference relative to P1 (shading; in 10^9kg s^{-1}). The interval for the thin contour lines is 10×10^9kg s^{-1} and 100×10^9kg s^{-1} for the thick contour lines. Positive is counterclockwise flow (solid lines + red shading) and negative is clockwise flow (dashed lines + blue shading).

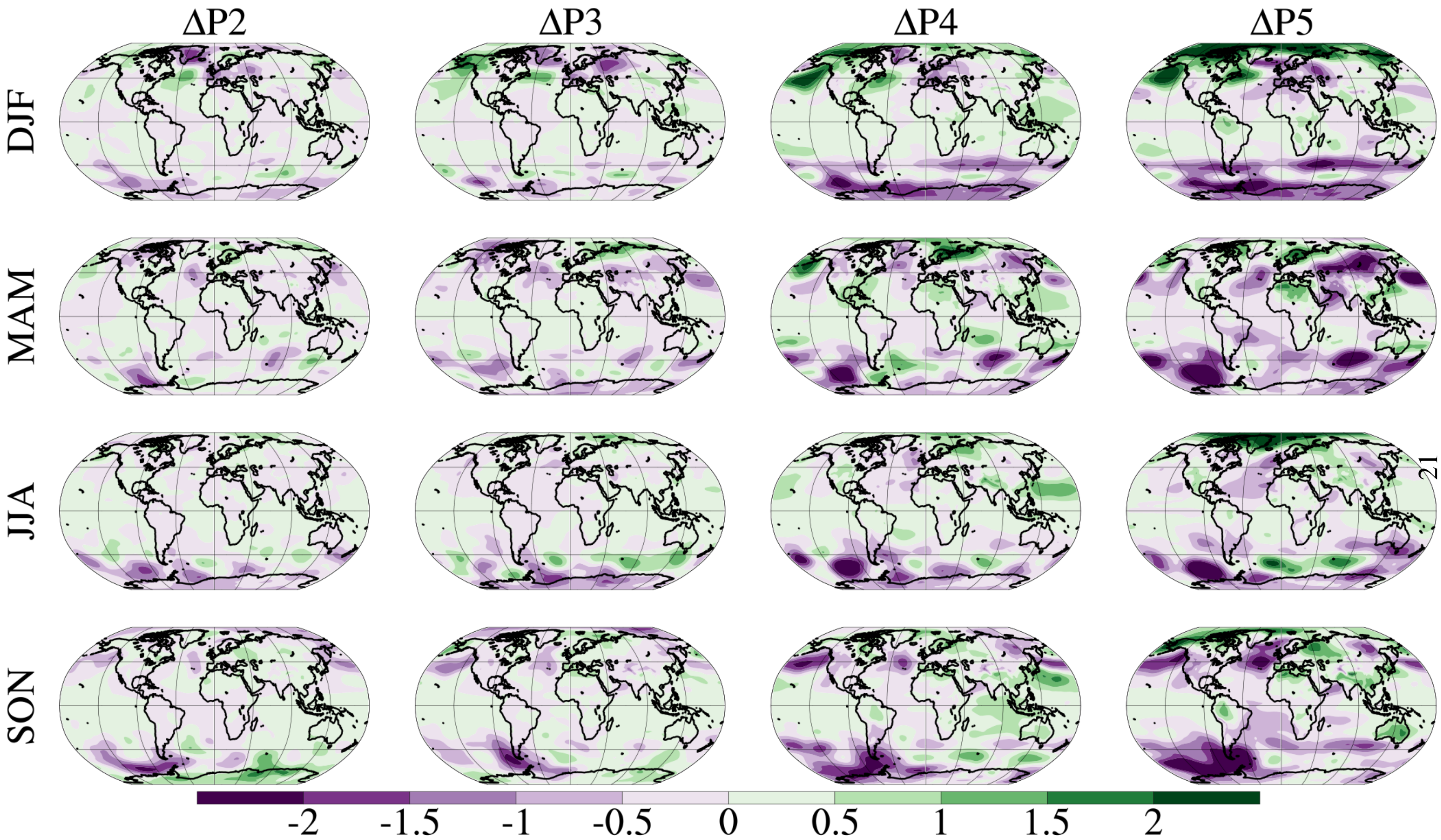

Figure 12: Standard deviation difference of the detrended mean sea level pressure (in hPa) for P2 to P5, relative to P1, for each season (rows) and each time period relative to P1 (columns).

3.2 The ocean

3.2.1 Temperature, salinity and stratification

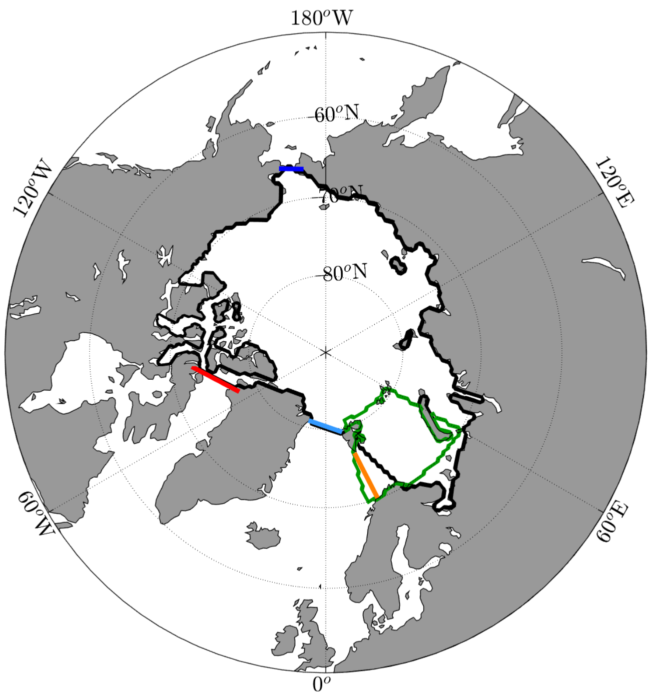

Figure 13: Map of the regions used for the Arctic Ocean (black) and the Barents Sea (green) and the four gateways: Fram Strait (FS, light blue), Barents Sea Opening (BSO, orange), Canadian Archipelago (CAA, red) and Bering Strait (BS, dark blue).

During the 1350-year long RCP8.5 simulation, the Arctic Ocean undergoes large changes as well. It transitions from a perennial ice covered ocean (P1 and P2) to an ice-free ocean (P4 and P5). The seasonal mean of the upper 1000m of the Arctic Ocean (see region in figure 13) temperature and salinity profiles are shown in figure 14. Overall, the Arctic Ocean becomes warmer and fresher throughout all seasons, as sea ice retreats. While there still is sea ice in the Arctic, the ocean only warms by 0.1-0.4°C from P1 to P2 in the surface mixed layer (black and dark blue curves in fig. 14, left column). The seasonal cycle is clear with the surface mixed layer being warmer than the underlying thermocline in summer and autumn, and colder in winter and spring. During the seasonally ice-free period, the Arctic ocean surface mixed layer warms by up to 1.0-3.7°C over the course of the year (light blue curve in fig. 14). As the Arctic become ice-free (P4; orange curve), the surface mixed layer temperature increases even further: more than 6.0°C (10.0°C) in winter (summer). For the last period when the GIS is melting (P5) the maximum increase in temperature in winter and spring does not occur at the surface, but at a depth of 500m (red curve in fig. 14). Here, the temperature increases by 12.5°C relative to P1. At the surface, the increase in temperature range from 8.31°C in spring to 14.4°C in summer. The seasonal temperature cycle appear to increase.

A similar change, but opposite in sign, is seen for the salinity. The Arctic Ocean becomes fresher by 1.8-2.3 psu for P2, 1.0-1.01 psu in P3, 1.6-2.1 psu in P4 and as much as 5.2-5.7 psu in P5, relative to P1 (fig. 14, middle column). Unlike temperature, salinity has little seasonal change.

The strengthened thermo- and halocline with increasing global temperature indicate a strengthening of the ocean stratification (fig. 14). In cold regions, the stratification is mostly governed by salinity. The stratification is illustrated by the strength of the Brunt-Vaisala frequency N^2, with a strong stratification given by a large N^2 (Knauss (1997)). The N^2 for the Arctic Ocean is shown in the right column of figure 14. Here, the expected strengthening of the stratification is evident.

The same tendency is seen for the Barents Sea, although with significant differences (fig. 15, region shown in green in figure 13). The surface mixed layer in P2 increased by 0.6-1.7°C relative to P1 over the course of the year. This warming continues as the Arctic becomes seasonally ice-free (P3), with the surface mixed layer warming by 4.8-7.6°C through the year (light blue curve in left column of fig. 15). For an ice-free Arctic Ocean (P4), the Barents Sea surface mixed layer temperature increases by 9.2°C in spring to 12.1°C in summer. Finally, for the last period P5, the temperature increases by as much as 15.1°C in summer. Similar to the Arctic Ocean, the maximum temperature increase in winter and spring ($\sim$13.7°C) is not at the surface, but at a depth around 250-300m. This warm sub-surface layer is the Atlantic Water (AW). Comparing the depth of the maximum sub-surface temperature for P1 to P5 shows that the depth decreases, implying that the core of the AW shoals (black and red curve in right column of fig. 15).
The salinity profile of the Barents Sea differs from that of the Arctic Ocean, with a less pronounced halocline in the Barents Sea (fig. 15; middle column). The change from the pre-industrial period P1 to present day conditions P2 is a small increase in surface mixed layer salinity (up to 0.09 psu in summer and 0.052 psu in winter) and a small decrease in salinity with depth (up to 0.06 psu). Loosing the Arctic summer sea ice (P3) enhances this trend with a saltier mixed layer. In summer, the salinity increases by 0.66 psu and in winter it decreases by 0.27 psu, relative to P1. The maximum decrease with depth is around 0.14 psu at a depth of 800m. This increasing saline surface mixed layer and fresher sub-surface layer weakens the gradient between the two, i.e. the halocline weakens. This implies that the stratification weakens as well. This destabilizing trend is only seen in the Barents Sea as long as there is sea ice in the Arctic, i.e. P3. When all the sea ice is gone (P4), the upper 400m freshens much more (orange curve in fig. 15). The surface mixed layer salinity decreases by 0.15-0.61 psu, with minimum change in spring and maximum change in summer. In contrast to P2 and P3, the change in salinity is not primarily confined to the mixed layer, but is present throughout the water column. A noticeable exception is the increase in salinity at a depth of 400-500m, indicating the AW layer. During the next 1000 years until P5, the Barents Sea continues to freshen, with the larger surface salinity decrease (2.51-2.94 psu) than in the sub-surface AW layer (0.63 psu). This large decrease in surface mixed layer salinity and smaller decrease (or even increase) in salinity of the AW layer implies a strengthening of the stratification. This is also what is observed in the right column of figure 15.

Deep water formation occurs in areas with large convection, since deep water is formed by dense surface water sinking toward the bottom. Therefore, the mixed layer depth is often used as an indicator of deep water formation, with a deep mixed layer indicating a strong deep water formation. Deep water formation occurs along the sea ice edge in winter, peaking in March. The main location for deep water formation is the Labrador Sea (Knauss (1997)). As the sea ice retreats, the areas with a large mixed layer depth follows the sea ice northward, shoaling on the way (not shown). By P4, the mixed layer depth is shallower than 1000m, indicating a weakening of the deep water formation. This is similar to the findings by Brodeau and Koenigk (2015).

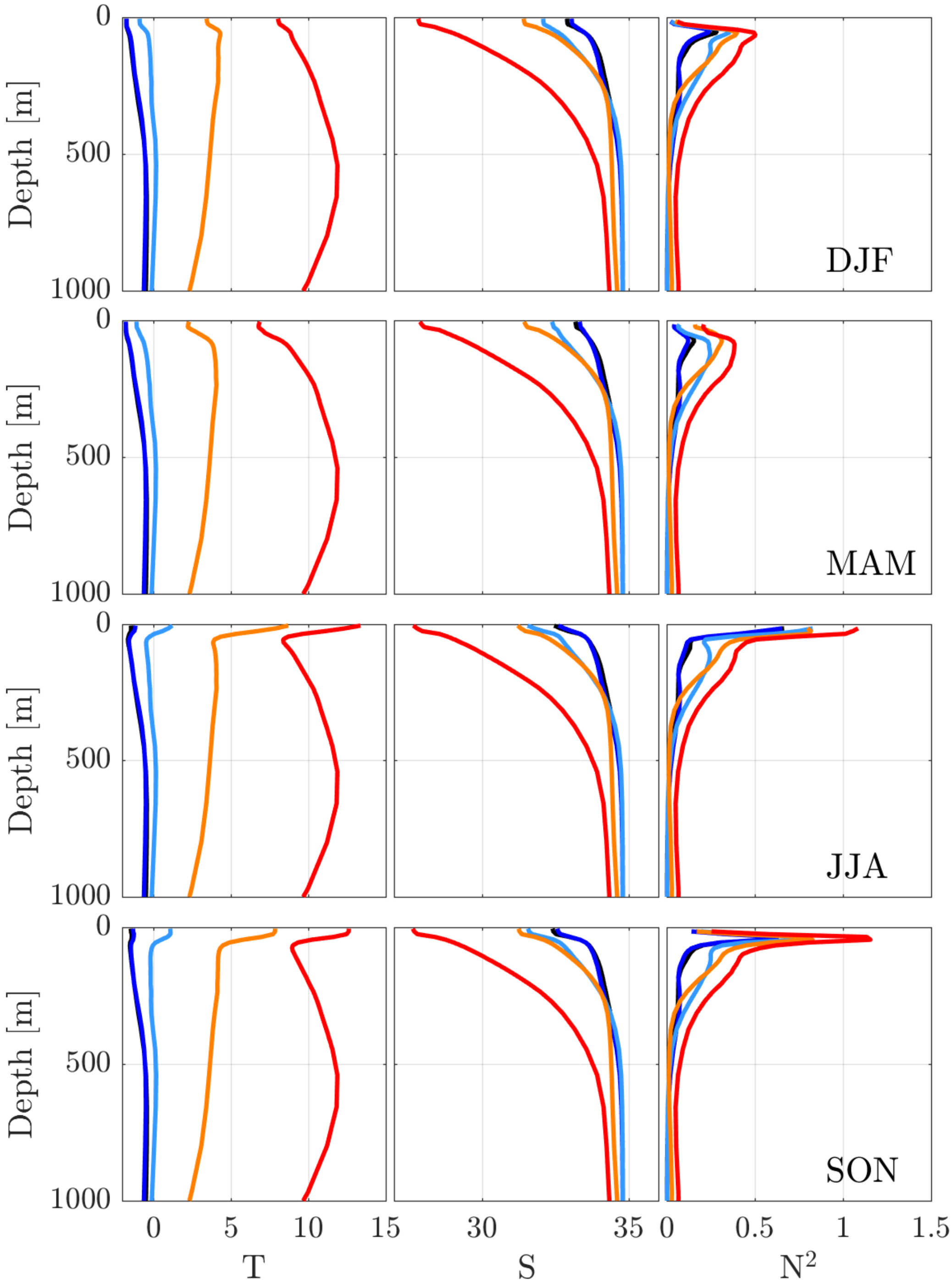

Figure 14: The upper 1000m of the area mean temperature (left; in °C), salinity (middle; in psu) and Brunt-Vaisala frequency (right; N^2; in hr^{-1}) for the Arctic Ocean. P1 (black), P2 (blue), P3 (yellow), P4 (orange), P5 (red).

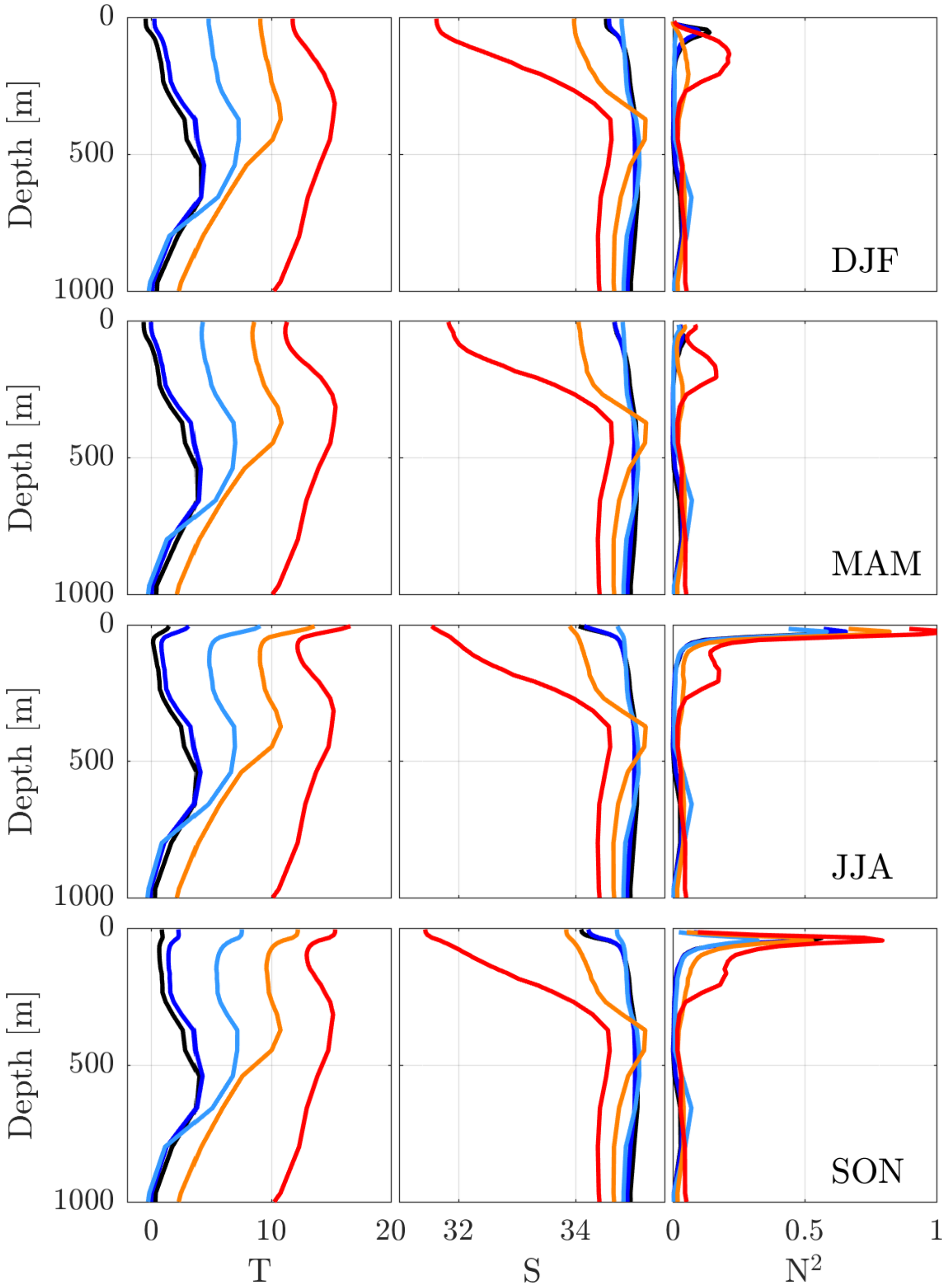

Figure 15: The upper 1000m of the area mean temperature (left; in °C), salinity (middle; in psu) and Brunt-Vaisala frequency (right; N^2; in hr^{-1}) for the Barents Sea. P1 (black), P2 (blue), P3 (yellow), P4 (orange), P5 (red).

3.2.2 Ocean circulation

The strength of the ocean circulation is quantified by the The Atlantic Meridional Overturning Circulation (AMOC) in figure 16. Going from P1 to P5, the AMOC weakens from a maximum of approximately 16 Sv in P1, to around 7 Sv in P5. Coinciding with this is a shallowing of the AMOC. The weakening of the AMOC continues until P4. Between P4 and P5, the AMOC increases slightly in the upper 500m between 10°N and 25°N. A detail worth noting in figure 16 is the increase in strength north of Iceland (∼64°N) in P3. This implies a stronger northward transport across the Iceland-Scotland Ridge for P3. When the Arctic becomes ice-free year round, this transport weakens again. The maximum value with depth of the AMOC between several latitudinal bands are shown in figure 17. The weakening of the AMOC until P4 is seen clearly. The slight recovery of the AMOC after P4 observed in figure 16 is only observed for the two most southern latitudinal bands (30°S-90°N and 20-°).
The core of the warm and saline Atlantic Water (AW) was seen at a depth approximately 500m in figures 14 and 15. The warm increase in this layer indicates either an increased northward heat or volume transport. The total volume transport is stable through the 1350 year simulation, but the individual contributions from each of the four gateways Fram Strait (FS), Barents Sea Opening (BSO), Bering Strait (BS) and the Canadian Archipelago (CAA) changes (fig. 18, top panel; gateways shown in fig. 13). The most pronounced changes are through FS and BSO. The northward BSO volume flux increases into the Barents Sea and the FS volume flux increases southwatd. The volume transport peaks after the Arctic becomes ice-free in summer (P3). After this is stabilizes around 4 Sv for BSO and 3 Sv for FS. Comparing to the AMOC in figure 16, the increase in volume transport through FS and BSO coincidence with the increase in AMOC north of Iceland.
In contrast to the stable volume transport is the increasing total heat transport into the Arctic Ocean in figure 18. This increase continues until after P3, after which it gradually stabilizes around a northward heat transport of 100 TW. The distribution of this increased heat transport between four of the key gateways are shown in the middle row of figure 18 as well. The heat is transported into the Arctic Ocean through FS, BSO and CAA. Just after P3, the FS heat transport reverses from being a heat source to the Arctic Ocean (∼10 TW) to being a heat sink (∼-100 TW). This shift could be related to the ocean water reaching the reference temperature (0°C) used to compute the heat transport. That is, the southward volume transport was colder than 0°C for P1, P2 and P3 (fig. 18, middle row). This results in a net heat flux northward. As the ocean warms, the water passing through FS is now warmer than 0°C, resulting in a net southward heat transport. The BSO heat flux into the Barents Sea increases from ∼50 TW to 200-300 TW (fig. 18). This increase stabilizes around P4.
The total southward fresh water export is increasing (bottom row of figure 18). The increased FW export through FS and CAA is countered by an increased northward FW flux through BSO.

The large decrease in salinity by P5 in the Arctic Ocean indicates increased fresh water input into the Arctic Ocean. Fresh water can enter the Arctic Ocean through precipitation, river runoff from land, melt from GIS and fresh water transport into the Arctic Ocean. As was just shown, the latter is not the case, as fresh water is transported out of the Arctic Ocean (fig. 18, bottom). GIS melt water is most likely not a large contributor, as only melt water from the northern most tip of Greenland will flow into the Arctic Ocean region used here (fig. 13). Of the last two potential candidates, the net fresh water input from the atmosphere, i.e. precipitation-evaporation (P-E) over the Arctic Ocean, is the largest contributor. This is illustrated by the yearly mean fresh water input into the Arctic Ocean from river runoff and P-E in table 2.

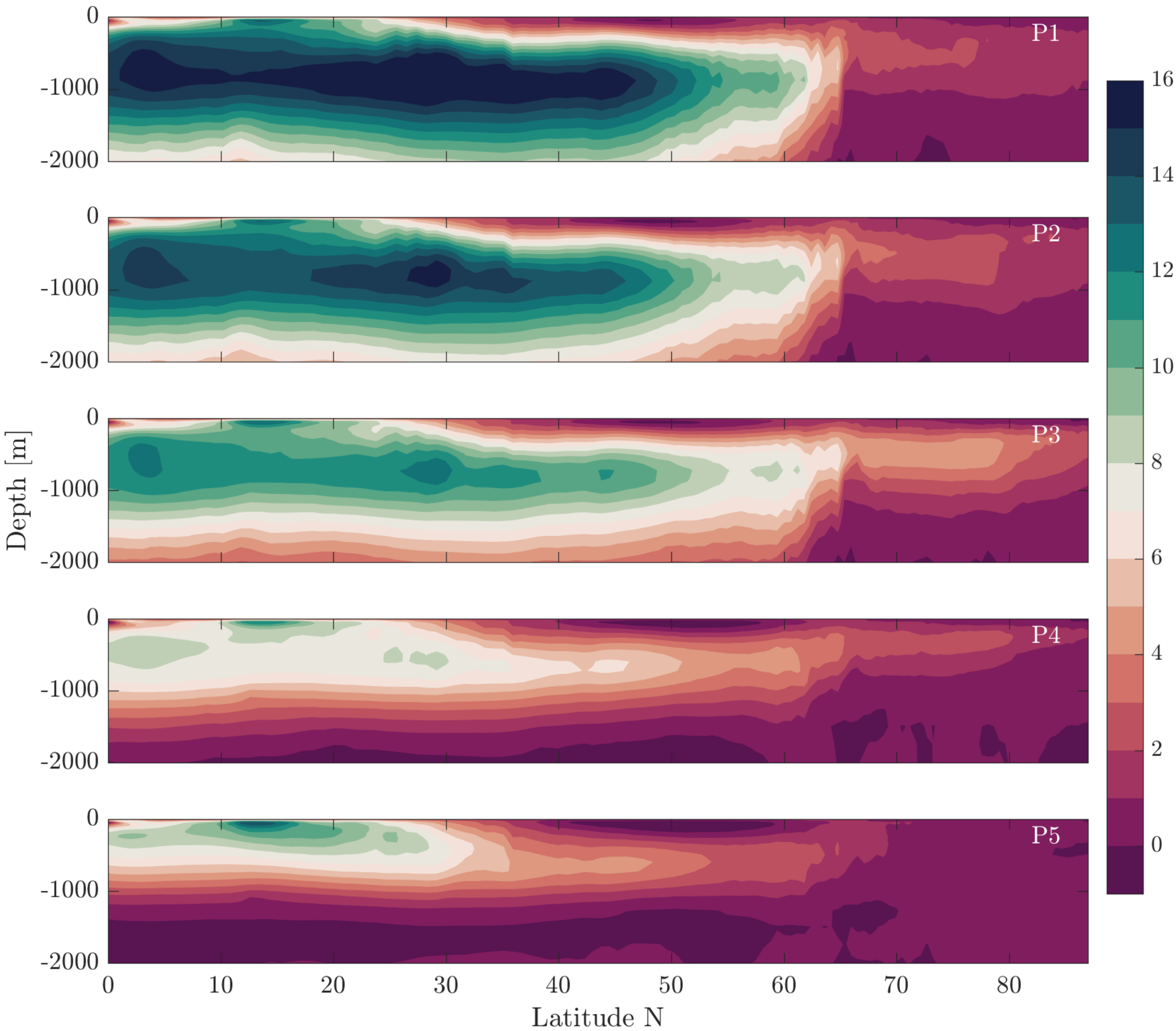

Figure 16: 30-year mean of the AMOC (in Sv) for in period.

Table 2: Annual mean river runoff and net freshwater flux (Precipitation-Evaporation; P-E) for the Arctic Ocean (in x10^{15} kg year^{-1}), for each of the five time regimes. Arctic Ocean region defined in figure 13.

	River runoff [x10^{15} kg year^{-1}]	**P-E** [x10^{15} kg year^{-1}]
P1	0.177	1.78
P2	0.183	1.77
P3	0.247	2.02
P4	0.439	2.53
P5	0.837	3.11

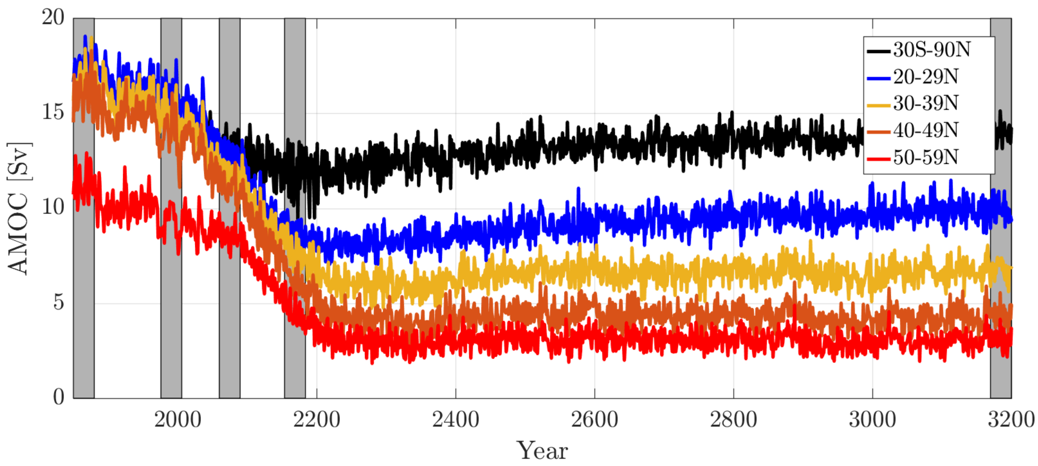

Figure 17: Maximum of AMOC with depth for different latitudinal bands (in Sv). Grey bars indicate the five periods.

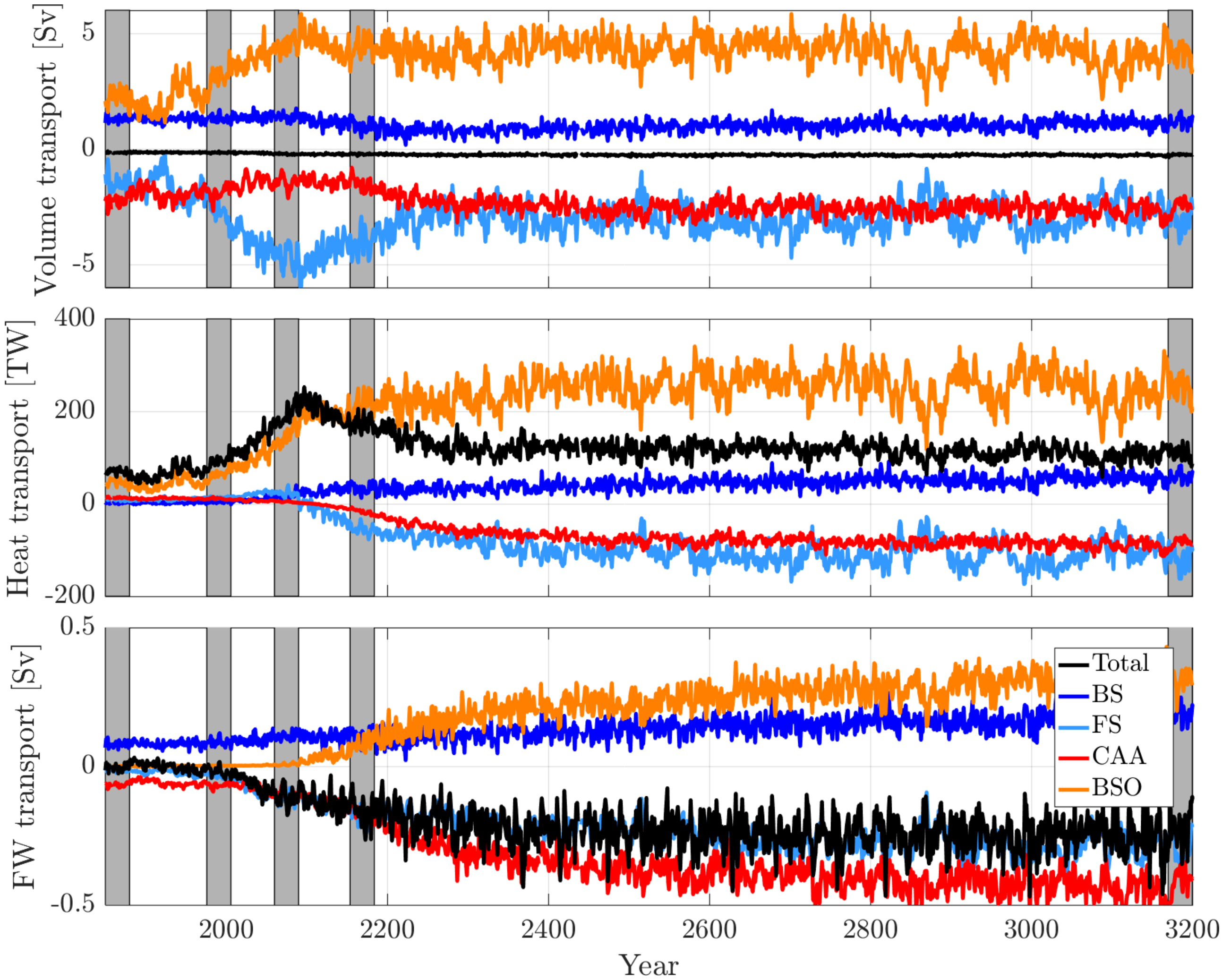

Figure 18: Monthly mean transport of volume (top; in Sv), heat (middle; in TW) and fresh water (bottom; in Sv) through Fram Strait (FS), Barents Sea Opening (BSO), Bering Strait (BS) and the Canadian Archipelago (CAA). Positive is into the Arctic Ocean. Grey bars indicate the five periods.

4 Discussion

The high-end emission scenario RCP8.5 presented in this study has been simulated by several other climate models as well, as part of the CMIP5 (Taylor et al. (2012)). Most of these projections run until year 2100, only about 8 model simulations continue on until year 2300. In CMIP5, the coupled atmosphere-ocean version of EC-Earth has been used to simulate RCP8.5 until 2100. However, the model version used for the CMIP5 differs from the model setup presented in the present study(i.e. EC-Earth-PISM), as this is interactively coupled to the Greenland Ice Sheet through the Ice Sheet Model PISM (see section 2.1). The comparison of EC-Earth with and without the coupling to PISM will not be discussed in this study, but we will just briefly mention that the RCP8.5 simulations are relatively similar between the two model configurations (Madsen et al. (2019, manuscript in preparation)). The RCP8.5 simulation of the standard EC-Earth model in the CMIP5 model ensemble has been analyzed and discussed in other studies. Therefore, the focus of our discussion will be on the transitions between sea ice states for key parameters.

4.1 The atmosphere

4.1.1 Temperature and Arctic Amplification

The global mean surface air temperature increased rapidly from present day and until around year 2250 (fig. 1b). This coincided with the rapid sea ice reduction in the Arctic. The temperature stabilized after 2250, as a result of the stabilization of the anthropogenic GHG forcings (figure 1a).
In addition to this rapid temperature increase, the main change of the projected temperature change following the RCP8.5 emission scenario was shown to be a stronger warming of the Arctic relative to the global mean temperature. This warming peaked just after the Arctic became seasonally ice-free (P3), after which the meridional north-south gradient slowly weakens (fig. 3). The AA (.i.e. the ratio of the mean Arctic temperature change to the global mean temperature change) did not show this peak at P3, but rather a graduel decrease in AA going from P2 to P5 (fig. 4). Several studies have suggested that the AA is driven by sea ice loss, increasing the upward heat flux from the ocean to the atmosphere (Serreze et al. (2009), Screen and Simmonds (2010), Dai et al. (2019)). This explains the observed seasonal asymmetry of the AA, i.e. strongest in winter and weakest in summer. Similar to our findings, Dai et al. (2019) found that as the sea ice disappeared in a GHG-induced warmer climate, the AA weakened. They analyzed CMIP5 model future projections up until year 2300, showing the strongest AA in the 21st and 22nd century. By the 23rd century, most of the Arctic sea ice was gone, resulting in a much weaker AA (equivalent to the summer AA in previous centuries). Further, they performed experiments with GHG induced warming and a fixed Arctic sea ice cover. As the global temperature increased, so did the Arctic temperature, but not amplified. From this they concluded that large AA cannot occur unless there were a sea ice decline. Our simulations continued for another 900 years, showing the same trend toward a weaker AA. However, there was still an increased warming over the Arctic relative to the global mean in P5. The temperature was still $\sim$3-4 times higher in the Arctic compared to the global mean temperature. Despite sea ice loss having been named the

main driver of AA, it can still exist in a world with no perennial sea ice. Langen and Alexeev (2007) showed that in a world with no land or sea ice (an aquaplanet), polar amplification is the preferred state.
As the world warms, the temperature at the high latitudes varied less, and the low and mid latitudes had larger variability. This was also reflected in the 5th and 95th percentiles of the temperatures for four areas, showing that in Europe the summers were projected to become more extreme with more extremely cold or extremely warm summers, relative to the respective period. For the rest of the year, and for Greenland, the temperatures became less extreme.

4.1.2 Precipitation and the shift of the ITCZ

The mean precipitation change showed an intensification of precipitation in areas with high precipitation and less precipitation in areas with low precipitation. This wet-gets-wetter and dry-gets-drier pattern is in good agreement with the CMIP5 model changes (IPCC (2013), chapter 12.4.5.2): the contrast between dry and wet regions will increase, mid and high latitudes will generally see an increase in precipitation, especially in winter, and the tropics will see an increase in precipitation in summer. There are some notable exceptions to this, for example the Amazon which appears to be getting drier, not wetter, in the future projections. This is observed both in our model simulation as well as in the CMIP5 ensemble. The change in the extreme precipitation appeared to increase after P3. The shift of the ITCZ toward Equator and the increase in equatorial rain observed in our model simulation are also similar to findings in IPCC (2013). There does not appear to be a clear shift in ϕ_{max} or ϕ_{cent} across seasons transitioning through the sea ice states. Overall, ϕ_{max} or ϕ_{cent} converged toward Equator and each other.

4.1.3 Atmospheric circulation

The mean change of the atmospheric circulation was a linear-like trend toward a pattern resembling the positive AO in autumn, and an intensification of the Aleutian Low in winter and spring. This pattern is similar to the CMIP5 ensemble, with the largest decreases in MSLP over the Barents Sea, Central Arctic Ocean and Bering Strait and an increase in MSLP over the North Atlantic and western Europe (Koenigk et al. (2013)). They found that the MSLP change pattern is robust across CMIP5 models, the magnitude of the change varies more. The same pattern was observed for an ensemble of CCSM4 simulations of the 21st century with the RCP8.5 scenario (Vavrus et al. (2012)). They also found that MSLP was the variable that varied the most across model ensembles. Both these studies simulated the 21st century. Our results indicate that the pattern they find, intensifies after year 2100.

4.2 The ocean

As the global mean air temperature rises, so does the Arctic ocean temperature (fig. 14). Further, increased precipitation and river runoff increased the fresh water input into the Arctic ocean, leading to a freshening. This is similar to findings in other studies of the RCP8.5 scenario. Koenigk et al.

(2013) analyzed the CMIP5 future scenarios for EC-Earth and found that the Arctic Ocean warms and freshens during the 21st century, the latter due to increased precipitation and river runoff.

Studies have shown that as the Arctic sea ice melts, the Barents Sea become more like the Atlantic Ocean and less like the Arctic Ocean (Aarthun and Eldevik (2012)). This process of a weakening stratification, increased vertical velocity, sea ice decline and shallowing of the AW is referred to as 'atlantification'. Polyakov et al. (2017) observed increased atlantification in the eastern Eurasian Basin as well. In our results, the Barents Sea did experience this atlantification, for some time. From the pre-industrial period (P1) until the seasonally ice-free Arctic Ocean (P3), the stratification weakened and the AW shallowed. However, after the last Arctic sea ice was gone (P4), the stratification increased again due to the large increase in fresh water. This indicates that the atlantification only endured as long as there was Arctic sea ice. Afterwards, the water column became increasingly stratified again.

4.2.1 Ocean circulation

The AMOC weakened as the Arctic sea ice disappeared (fig. 16). The weakest point of 7 Sv occurred around P4, when the Arctic sea ice was completely gone. After this, the southern part of the AMOC gradually strengthened until the end of the simulation at P5, but not reaching the pre-industrial levels around 16 Sv. The weakening of the AMOC has been observed by other studies as well (Cheng et al. (2013)). In addition to this, our results indicated an increase in the AMOC north of Iceland for P3. This coincided with an increase in volume transport through the Fram Strait and the Barents Sea Opening. However, the total volume transport did not change.
The increased heat transport through BSO into the Barents Sea in the results presented here is similar to results by Koenigk and Brodeau (2014). They found that the heat flux increased the heat content of the Barents Sea until around year 2040, where the heat flux through Frans Josef-Novaya Zemlya shifted from importing heat to the Barents Sea to exporting it. This was not because the current changed direction, but because the reference temperature (T_{ref}) used to compute the heat transport was reached due to the warming of the water, i.e. the northward water flow shifted from being colder than T_{ref} to becoming warmer than T_{ref}. This increased heat flux out of the Barents Sea through the Frans Josef-Novaya Zemlya transect balanced the increased heat flux through BSO and the net heat flux stabilizes, resulting in a net heat transport into the Arctic Ocean.

The above revealed that the largest changes in the ocean stratification occurred after P3, whereas the largest ocean circulation changes occurred before P4.

4.3 Transitions across sea ice states

The five time periods chosen in this study represent five different sea ice states. The global mean air temperature in figure 1b increases rapidly across the three middle regimes, P2-P4. The global mean temperature trend for each 30-year period is shown in figure 19a and for five regions (global mean,

Greenland, Europe, Southeast Asia and South America). This shows, the strongest positive trend occurring in P3. The temperature trend was positive throughout all five periods, except for Europe and South America for P1 and P5. In general, the four regions were close to the global mean trend, except for Greenland. For P2 and P3, the trend was 2.7 and 1.7 times higher for Greenland than the global mean, respectively. Hence, the temperature on Greenland increased 2.7 and 1.7 times faster than the global mean for these two periods. When all the Arctic sea ice was gone (P4), the temperature trend in Greenland was smaller than the global mean. The shift in temperature changes between sea ice states was also observed for the AA, where the AA was strongest for P2-P3.
Whereas the temperature rates peak at P3, is it not until after P3 that the temperature and precipitation variability start to increase (fig. 9). An exception to this is Greenland, which continuously decreases (increases) its temperature (precipitation) variability through the five time period. This all implies that the rate of the temperature change depends on the Arctic sea ice state.

The dependence of the Arctic sea ice cover was seen in the ocean as well. Here, some features changed more while the Arctic sea ice retreated (P2 and P3) and some when the Arctic sea ice was gone (P4 and P5). The first covers the atlantification of the Barents Sea. This was manifested through the weakening of the stratification and the shallowing of the AW until P3. After this point, the ocean stratification restrengthened, but the AW continued to shallow. The ocean circulation, represented by the AMOC, is also part of the first group, as it generally weakened until P4, after which the southern part slowly strengthened again. For P3, there was a small increase in northward transport north of Iceland, leading to an increase in volume transport through the Fram Strait and the Barents Sea Opening.
The changes in the temperature and salinity, hence the stratification, of the Arctic Ocean and the Barents Sea were most pronounced after the Arctic sea ice loss (P4). This continued increase in heat was partly due to the increased heat flux, partly due to the now ice-free ocean absorbing more of the incoming solar radiation. The continued freshening was mainly due increased precipitation.

Climate change has occurred before, as discussed in the Introduction. During the last glacial, several abrupt D-O events occurred, increasing the temperature on Greenland by up to 15° within decades (Kindler et al. (2014)). Sadatzki et al. (2019) showed that the D-O events were most likely driven by a rapid retreat of the Nordic Seas sea ice cover, causing a rapid temperature increase. Although the current observed and projected climate changes are caused by a different driver (increasing GHG emissions), there does seem to be some similarities between the two cases. Most pronounced is the rapid temperature increase as the Arctic sea ice retreats (P2 to P4), which in the RCP8.5 simulation stabilizes after all the Arctic sea ice is gone. However, this coincide with the increasing and subsequently stabilizing GHG emission. The 30-year trend of the GHG emissions are shown in figure 19b, illustrating a change in trends similar to that for temperature. McCusker et al. (2017) separated the effects of increased GHG emissions and Arctic sea ice loss. They showed that the mean global temperature change was the sum of the two, with the increased GHG emissions being the largest contributor (0.6-0.7° and 2.7-2.8°, respectively, out of the full effect of 3.6°). This additive behav-

ior was cleanest in winter. This indicates that the observed temperature increase in figure 1b is not solely driven by the sea ice retreat. McCusker et al. (2017) also showed that the climatic effects were insensitive to the background state, i.e. Arctic sea ice changes in a warm and a cold climate had similar effects. This implies that an equal magnitude of sea ice loss could potentially lead to a larger temperature increase today, due to the effect from the increasing GHG emissions, relative to a D-O event during the last glacial.
The location of the sea ice loss has been shown to be important (Pedersen et al. (2016), Screen (2017)). D-O events were triggered by a retreat of the Nordic Seas sea ice cover, whereas the current sea ice loss is located further north in the central Arctic. Areas closest to the sea ice loss is affected the most (Pedersen et al. (2016), Screen (2017)), the resulting effect of the two different sea ice retreats will likely be different.

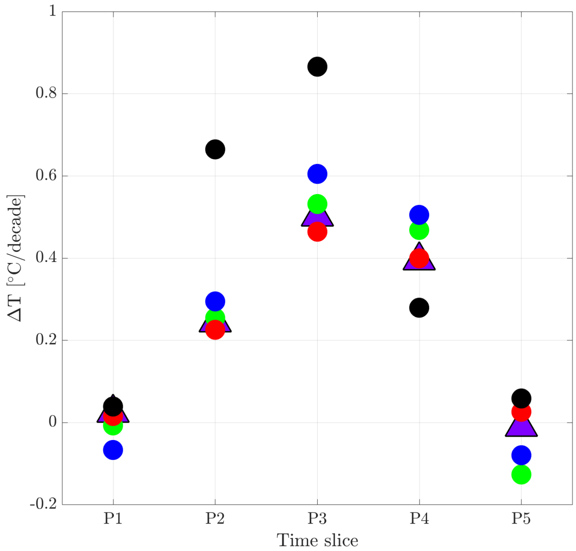

(a)

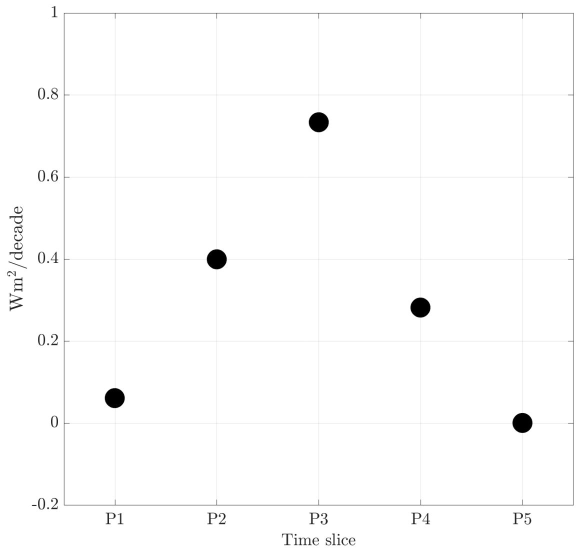

(b)

Figure 19: (a) Trend of the annual mean absolute temperature for each 30-year time regime [°C/decade] for the global mean (purple triangle), Greenland (black), Europe (blue), Southeast Asia (red) and South America (green). (b) Trend of the total anthropogenic GHG forcing for the RCP8.5 scenario for each of the five time periods.

5 Conclusion

This study aimed at investigating the climatic changes due to shifts in the Arctic sea ice state. This was achieved by assessing a 1350 year long simulation following the historical and RCP8.5 trajectories, run using the coupled atmosphere-ocean general circulation model EC-Earth with an interactive Greenland Ice Sheet via the PISM ice sheet model (EC-Earth-PISM). Five 30-year time periods were compared: the pre-industrial period (P1), the present day period (P2), the period just after the Arctic summer sea ice disappeared (P3), the period just after the Arctic winter sea ice disappeared (P4) and the end of the simulation when the GIS have shrunk by 62% (P5). In this simulation, the Arctic sea ice was projected to disappear in September in year 2060 and in March by year 2154. It was shown that the rate of the global mean temperature change was largest between P2 and P4, coinciding both with the largest rate of sea ice loss and increasing radiative forcing. The Arctic Amplification was shown to peak around P2 and P3, gradually weakening afterward, but not disappearing, by P5. Hence, the Pole-Equator tempetature gradient decreased as the Arctic sea ice disappeared. The temperature variability generally increased over low and mid-latitudes, while decreasing over high latitudes. An exception to this was Europe in summer, where temperatures were projected to become more extreme for P4 and P5.
The precipitation was projected to increase over wet areas and decrease over dry areas. Additionally, the ITCZ was projected to move toward Equator. The extreme precipitation (both high and low precipitation) increased after as the Arctic Ocean became seasonally ice-free. Especially, the variability of the Asian monsoon and the precipitation over South America increased after the Arctic became ice-free.
The atmospheric circulation changes revealed an intensified Aleutian Low in winter and spring. In autumn, the MSLP changes indicate a shift toward an enhanced positive AO pattern. A positive AO is associated with stronger westerlies, a stronger and less wavy jet stream, a warmer and wetter Northern Europe and a drier Mediterranean region.

The ocean changes were similar to those found by Koenigk et al. (2016): a warmer and fresher Arctic Ocean and increased heat transport into the Arctic Ocean through the Barents Sea. The freshening of the Arctic Ocean was most likely due to increased precipitation, not GIS melt. Further, a weakening of the AMOC was seen. The rate of change of these oceanic parameters was largest around P3 and P4, similar to the atmospheric changes. The ocean circulation stabilized after P4, while the temperature and salinity in the Arctic Ocean continued to increase and decrease, respectively.

Our preliminary results indicate that the sea ice state might impact the rate of some climatic changes. However, the rapid sea ice decline coincides with a rapid increase in global mean temperature and anthropogenic GHG emissions. Separating the influence of the sea ice loss, the increasing temperature and GHG emissions require further analysis. Additional analysis could be to investigate the impacts on Greenland more closely.

References

M. Aarthun and T. Eldevik. Quantifying the influence of Atlantic heat and Barents sea ice variability and retreat. *Journal of Climate*, 25:4736–4743, 2012.

O. Adam, T. Bischoff, and T. Schneider. Seasonal and interannual variations of the energy flux equator and ITCZ. Part 1: Zonally averaged ITCZ position. *Journal of Climate*, 29, 2016.

T. Albrecht, A. Aschwanden, J. Brown, E. Bueler, D. DellaGiustina, M. Haselhoff, R. Hock, C. Khroulev, C. Lingle, M. Martin, D. Maxwell, N. Shemonski, R. Winkelmann, and F. Ziemen. Pism, a Parallel Ice Sheet Model: User's Manual. 2012.

L. Brodeau and T. Koenigk. Extinction of the northern oceanic deep convection in an ensemble of climate model simulations of the 20th and 21st centuries. *Climate Dynamics*, 2015.

W. Cheng, J. C. H. Chiang, and D. Zhang. Atlantic meridional overturning circulation (amoc) in cmip5 models: Rcp and historical simulations. *Journal of Climate*, 26(18):7187–7197, 2013. doi: 10.1175/JCLI-D-12-00496.1.

A. Dai, D. Luo, M. Song, and J. Liu. Arctic amplification is caused by sea-ice loss under increasing CO_2. *Nature Communications*, 10, 2019.

W. Dansgaard, S. J. Johnson, H. B. Clausen, D. Dahl-Jensen, N. S. Gundestrup, C. U. Hammer, C. S. Hvidberg, J. P. Steffensen, A. E. Sveinbjörnsdottir, J. Jouzel, and G. Bond. Evidence for general instability of past climate from a 250-kyr ice-core record. *Nature*, 364:218–220, 1993.

T. M. Dokken, K. H. Nisancioglu, C. Li, D. S. Battisti, and C. Kissel. Dansgaard-Oeschger cycles: Interactions between ocean and sea ice intrinsic to the Nordic seas. *Paleoceanography*, 28:491–502, 2013.

ECMWF. *Part IV: Physical Processes*. Number 4 in IFS Documentation. ECMWF, 2010 2010. URL `https://www.ecmwf.int/node/9233`. Operational implementation 26 January 2010.

D. M. W. Frierson and Y.-T. Hwang. Extratropical influence on ITCZ shifts in slab ocean simulations of global warming. *Journal of Climate, volume =*, 2012.

C. Guo, K. Nisancioglu, H. Sadatzki, T. Dokken, and E. Jensen. Dynamical sequences of ocean, atmosphere and sea ice processes over an abrupt cold-to-warm climate transition in the marine istope stage 3. 2019, manuscript in preparation.

W. Hazeleger, C. Severijns, T. Semmler, S. Stefanscu, S. Yang, X. Wang, K. Wyser, E. Dutra, J. M. Baldasano, R. Bintanja, P. Bougeault, R. Caballero, A. N. L. Ekman, J. . H. Christensen, B. van den Hurk, P. Jimenez, C. Jones, P. Kållberg, T. Koenigk, R. McGrath, P. Miranda, T. van Noije,

T. Palmer, J. A. Parodi, T. Schmith, F. Selten, T. Storelvmo, A. Sterl, H. Tapamo, M. Vancoppenolle, P. Viterbo, and U. Willén. EC-Earth V2.2: description and validation of a new seamless earth system prediction model. *Climate Dynamics*, 39:2611–2629, 2012.

C. Huber, M. Leuenberger, R. Spahni, J. Flückiger, J. Schwander, T. F. Stocker, S. Johnsen, A. Landais, and J. Jouzel. Isotope calibrated greenland temperature record over marine isotope stage 3 and its relation to ch4. *Earth and Planetary Science Letters*, 243(3):504 – 519, 2006. ISSN 0012-821X. doi: https://doi.org/10.1016/j.epsl.2006.01.002. URL `http://www.sciencedirect.com/science/article/pii/S0012821X06000392`.

IPCC. *Climate Change 2013: The Physical Science Basis. Contribution of Working Group I to the Fifth Assessment Report of the Intergovernmental Panel on Climate Change*. Cambridge University Press, Cambridge, United Kingdom and New York, NY, USA, 2013. ISBN ISBN 978-1-107-66182-0. doi: 10.1017/CBO9781107415324. URL `www.climatechange2013.org`.

P. Kindler, M. Guillevic, M. Baumgartner, J. Schwander, A. Landais, and M. Leuenberger. Temperature reconstruction from 10 to 120 kyr b2k from the ngrip ice core. *Climate of the Past*, 10(2): 887–902, 2014. doi: 10.5194/cp-10-887-2014. URL `https://www.clim-past.net/10/887/2014/`.

J. A. Knauss. *Introduction to physical oceanography*. Waveland Press, Inc, 1997.

T. Koenigk and L. Brodeau. Ocean heat transport into the Arctic in the twentieth and twenty-first century in EC-Earth. *Climate Dynamics*, 42:3101–3120, 2014.

T. Koenigk, L. Brodeau, R. G. Graversen, J. Kalrsson, G. Svensson, micheal Tjernström, U. Willén, and K. Wyser. Arctic climate change in 21st century CMIP5 simulations with EC-Earth. *Climate Dynamics*, 40:2719–2743, 2013.

T. Koenigk, M. Calan, G. Nikulin, and S. Schimanke. Regional Arctic sea ice variations as predictor for winter climate conditions. *Climate Dynamics*, 46:317–337, 2016.

P. L. Langen and V. A. Alexeev. Polar amplification as a preferred response in an idealized aquaplanet GCM. *Climate Dynamics*, 29:305–317, 2007.

G. Madec and the NEMO team. *NEMO ocean engine*. Note du Pôle de modélisation de l'Institut Pierre-Simon Laplace, France, No 27, 2008.

M. S. Madsen, S. Yang, G. Adalgeirsdottir, S. H. Svendsen, C. Rodehacke, and I. M. Ringgaard. Interactions of the greenland ice sheet with the climate system in warm scenarios as simulated in ec-earth-pism. 2019, manuscript in preparation.

K. E. McCusker, P. J. Kushner, J. C. Fyfe, M. Sigmond, V. V. Kharin, and C. M. Bitz. Remarkable separability of circulation response to Arctic sea ice loss and greenhouse gas forcing. *Geophysical Research Letters*, 44:7955–7964, 2017.

M. Meinshausen, S. J. Smith, K. Calvin, J. S. Daniel, M. L. T. Kainuma, J.-F. Lamarque, K. Matsumoto, S. A. Montzka, S. C. B. Raper, K. Riahi, A. Thomson, G. J. M. Velders, and D. P. P. van Vuuren. The RCP greenhouse gas concentrations and their extensions from 1765-2300. *Climatic Change*, 109:213–241, 2011.

T. D. Mitchell. Pattern scaling. an examination of the accuracy of the technique for describing future climates. *Climatic Change*, 60:217–242, 2003.

I. H. Onarheim, T. Eldevik, and L. H. Smedsrud. Seasonal and regional manifestation of Arctic sea ice loss. *Journal of Climate*, 31, 2018.

R. A. Pedersen, I. Cvijanovic, P. L. Langen, and B. M. Vinther. The impact of regional Arctic sea ice loss on atmospheric circulation and NAO. *Journal of Climate*, 29:889–902, 2016.

F. Pithan and T. Mauritsen. Arctic amplification dominated by temperature feedbacks in contemporary climate models. *Nature Geoscience*, 2014.

I. V. Polyakov, A. V. Pnyushkov, M. B. Alkire, I. N. Ashik, T. M. Baumann, E. C. Carmack, I. Goszczko, J. Guthrie, V. V. I. andTorsten Kanzow, R. Krishfield, R. Kwok, A. Sundfjord, J. Morison, R. Rember, and A. Yulin. Greater role for Atlantic inflows on sea-ice loss in the Eurasian Basin and the Arctic Ocean. *Science*, 356:285–291, 2017.

H. Sadatzki, T. M. Dokken, S. M. P. Berben, F. Muschitiello, R. Stein, K. Fahl, L. Menviel, A. Timmermann, and E. Jansen. Sea ice variability in the southern Norwegian Sea during glacial Dansgaard-Oeschger climate cycles. *Science Advances*, 5, 2019.

B. D. Santer, T. M. L. Wigley, M. E. Schlesinger, and J. F. B. Mitchell. Developing climate scenarios from equilibrium GCM results. *MPI Report Number 47, Hamburg*, 1990.

J. A. Screen. Simulated atmospheric response to regional and pan-Arctic sea ice loss. *Journal of Climate*, 30:3945–3962, 2017.

J. A. Screen and I. Simmonds. The central role of diminishing sea ice in recent Arctic temperature amplification. *Nature Letters*, 2010.

M. C. Serreze, A. P. Barrett, J. C. Stroeve, D. N. Kindig, and M. M. Holland. The emergence of surface-based Arctic amplification. *The Cryosphere*, 3:11–19, 2009.

J. Stroeve and D. Notz. Changing state of Arctic sea ice across all seasons. *Environmental Research Letters*, 13, 2018.

S. H. Svendsen, M. S. Madsen, S. Yang, C. Rodehacke, and G. Adalgeirsdóttir. An introduction to the coupled EC-Earth-PISM model system. *DMI Scientific Report*, 15-05, 2015.

K. E. Taylor, R. J. Stouffer, and G. A. Meehl. An overview of CMIP5 and the experiment design. *American Meteorological Society*, 93:485–498, 2012.

M. Vancoppenolle, S. Bouillon, T. Fichefet, H. Goosse, O. Lecomte, M. A. M. Maqueda, and G. Madec. *LIM The Louvain-la-Neuve sea Ice Model*. Note du Pôle de modélisation de l'Institut Pierre-Simon Laplace, France, No 31, 2012.

S. J. Vavrus, M. M. Holland, A. Jahn, D. A. Bailey, and B. A. Blazey. Twenty-first-century Artic climate change in CCSM4. *Journal of Climate*, 25:2696–2710, 2012.